Developing Multiscale Models of Dynamic Blood Flow and Control in the Cerebral Micorvasculature

Ali Daher

Supervisors: Professors Stephen Payne and Daniel Bulte

Department of Engineering Science

University of Oxford

A Thesis Submitted for the Degree of

Doctor of Philosophy

Hilary Term 2024

Abstract

A healthy brain possesses an intrinsic collection of mechanisms, known as dynamic cerebral autoregulation, that allow it to withstand physiological disturbances and maintain a sufficient and continuous supply of blood required to perform its functions. Abnormalities in cerebral autoregulation have been implicated in various disease conditions, including ischaemic stroke, and more recently neurodegenerative diseases such as Alzheimer's. These protective mechanisms occur predominantly in the microvasculature, the site of exchange between the blood and the brain tissue. However, the microvasculature's role in diseases is poorly understood, primarily due to the current imaging gap between the scales of clinical imaging (mm) and the microvasculature (μm). Hence, models of blood flow in the microvasculature can play a key role in filling this gap and help achieve a better understanding of cerebrovascular pathologies. These conditions are often linked to structural modifications in the vessel network, alterations in blood flow patterns, as well as impairment in the autoregulatory responses, all of which are changes that the model should be able to address if it were to have any clinical value.

We use perturbation methods to derive a model of dynamic blood flow and control in the microvasculature, one that resolves the structure of the individual microvessels in the network, and the autoregulation mechanisms are incorporated via a feedback model that alters the compliance of the individual vessels. We then validate the model and use it to model blood flow in the cortical penetrating vessels, whereas we model the capillary bed of the cortex as a porous medium and geometrically discretise it using a novel finite volume algorithm that ensures numerical accuracy and computational feasibility of the numerical solver. We then appropriately couple the discrete and continuum parts of the networks, giving rise to a single multiscale system that characterises the dynamic pressure and flux variations throughout an MRI voxel-sized network.

We conduct parameter calibration and sensitivity analyses to ensure an accurate characterisation of the feedback model parameter space. Finally, to demonstrate the utility of the models, we use the constructed networks as *in-silico* vascular testing beds to explore the biophysical origins and mechanisms behind the hypercapnic response, which remain poorly understood due to the difficulties of investigating the response in a conventional experimental context. Drawing from the available experimental data, we propose a sequence of the signalling events underpinning the hypercapnic response, and use the models to test the hypothesis and provide compelling evidence that strongly corroborates its validity, thereby providing an important addition to our understanding of the blood flow control processes and motivating further *in-vivo* investigations.

Acknowledgements

First, I would like to thank my supervisor Professor Stephen Payne, who offered his supervision all the way from across the world in Taiwan. I would also like to thank my co-supervisor, Professor Daniel Bulte, who welcomed me to his group around halfway through my DPhil, supported me, and had my back while I was in Oxford. I am also grateful to Professors Helen Byrne and Joe-Pitt Francis from the Department of Mathematics, who guided me toward the Approximate Bayesian Computation schemes that I used in Chapter 5. I would also like to express gratitude to the Rhodes Trust, which financed my degree and provided me with the opportunity to meet great people from all around the world. In addition, I would like to thank the Oxford Advanced Research Computing staff, for their help throughout the years with troubleshooting the simulations run on the High Performance Computing clusters.

This thesis has been a challenging journey, not the least because of the health challenges I stumbled upon during my studies. Without the support of a wonderful group of people around me, I would likely not have been able to finish my research degree. In particular, I would like to thank the brilliant neurosurgeon, Dr Nidal Roussan, who has performed a complicated spinal surgery that relieved me from months of pain due to Cauda Equina Syndrome. I would also like to thank Dr Ghassan Khayatt for his help with my torn knee ACL and LCL. In addition, I would like to thank my physical rehabilitation specialists, Dominique and Yousef, for their continued dedication, support, and expertise to help me get back on my feet. I am also grateful to the Rhodes Trust for helping me cover the costs of the rehabilitation as well as my foot surgery. Finally, I am indebted to my parents for the care, patience, and support I received from them during my time in Jordan, especially during my recovery from long COVID after my sinus surgery. This thesis is a testament to the unwavering support of an amazing group of people.

To my biggest DPhil fan who showed the utmost support (and zero interest) in my research, my loving Teita (grandmother), who sadly passed away this year. She really wanted me to get that Dr title, and would have even been more excited about my DPhil completion than I am. And most importantly, to Maureen. Thank you for all your help. I would not be where I am without you. This thesis is dedicated to you.

Publications and Conferences

Journal Papers

A.Daher, S.Payne, A network-based model of dynamic cerebral autoregulation, Microvascular Research (ISSN:00262862) (2023)104503, http://dx.doi.org/10.1016/ j.mvr.2023.104503.

A. Daher, S.Payne, A dynamic multiscale model of cerebral blood flow and autoregulation in the microvasculature, Applied Mathematical Modelling (ISSN:0307-904X) 123(2023)213–240, http://dx.doi.org/10.1016/j.apm.2023.06.035.

A. Daher, S.Payne, The conducted vascular response as a mediator of hypercapnic cerebrovascular reactivity: A modelling study, Computers in Biology and Medicine (ISSN: 0010-4825), 170(2024)107985, https://doi.org/10.1016/j.compbiomed.2024.107985.

The first paper is based on the work in Chapter 3. The second paper is based on the work in Chapter 4. The third paper is based on the work in Chapter 6.

Conference Presentations

A.Daher, S.Payne, A Network Model of Dynamic Cerebral Autoregulation. Ninth World Congress in Biomechanics (2022).

A.Daher, S.Payne, A Dynamic Model of Autoregulation in the Cerebral Microvasculature. Seventh International Conference on Computational and Mathematical Biomedical Engineering (2022).

S.Payne, T.Jozsa, Y.Xue, J.Wang, J.Howman, M.Newsome, W.Wei, Y.Bing, X.Chen, **A.Daher**, Z.Tong, W.El-Bouri, Mathematical Models of The Cerebral Microcirculation In Health And Pathophysiology. Seventh International Conference on Computational and Mathematical Biomedical Engineering (2022).

A. Daher, Using Approximate Bayesian Computation To Calibrate The Model Parameters characterising The Autoregulatory Behaviour Of Microvessels . Eighth International Conference on Computational and Mathematical Biomedical Engineering (2024).

Contents

Glossary

ABC: Approximate Bayesian Computation

ABP: Arterial Blood Pressure

ACh: Acetylcholine

ACT: Arteriole-Capillary Transitional

BC: Boundary Conditions

BOLD: Blood Oxygen Level Dependent

CBF: Cerebral Blood Flow

CBV: Cerebral Blood Volume

CFD: Computational Fluid Dynamics

CFL: Courant-Friedrichs-Lewy

CN: Crank-Nicolson

CoW: Circle of Willis

CS: Cross-Sectional

CSF: Cerebrospinal Fluid

CV: Control Volume

CVR: Conducted Vascular Response

dCA: Dynamic Cerebral Autoregulation

DGEM: Direct Gradient Evaluation Method

DSC: Dynamic Susceptibility Contrast

EC: Endothelial Cell

EE: Elementary Effects

FD: Finite Difference

fMRI: Functional Magnetic Resonance Imaging

FV: Finite Volume

ICP: Intracranial Pressure

IP_3: Inositol Triphosphate

MAP: Mean Arterial Pressure

MC: Monte Carlo

MCF: Monte Carlo Filtering

MLCK: Myosin Light Chain Kinase

MRI: Magnetic Resonance Imaging

NVC: Neurovascular Coupling

ODE: Ordinary Differential Equation

PDF: Probability Distribution Function

PDE: Partial Differential Equation

RBC: Red Blood Cell

rCBF: Regional Cerebral Blood Flow

ROI: Region of Interest

SMA: Smooth Muscle Actin

SMC: Sequential Monte Carlo

VSM: Vascular Smooth Muscle

Chapter 1

Introduction

1.1 Autoregulation and Cerebrovascular Diseases

The brain is comprised of an intricate web of billions of neurons involved in information processing, which in turn enable us to experience the world. Supporting the neurons are approximately the same number of glial cells, the extracellular matrix, around 700 km of blood vessels, and the surrounding cerebrospinal fluid (CSF), which all together work to preserve the delicate environment of neurons and sustain the brain's functions.[1] To meet the high metabolic rate associated with information processing, the brain requires large amounts of oxygen and glucose: even though the brain represents only 2 % of the body weight, it accounts for 20 % of the body's total oxygen consumption and 14 % of the total cardiac output under resting conditions.[2],[3] Since the brain generally lacks reservoirs for storing energy substrates, it relies on a steady and reliable supply of oxygen and nutrients from the cerebral vascular system, and cannot afford to be subjected to significant and prolonged reductions in flow; if not mitigated, any disruptions in cerebral blood flow (CBF) would lead to rapid neuronal cell death and permanent damage to the brain regions, thereby affecting the functions of the brain and leading to death. Even subtle alterations in CBF can impact brain health and function and are linked to dementia and cognitive decline.[4] As such, cerebrovascular diseases continue to be among the leading causes of human morbidity and mortality, with a substantial burden on public health and the lives of the affected population.

A healthy brain can withstand physiological disturbances such as perturbations in blood pressure and maintain a sufficient and continuous supply of blood required to sustain its function. The mechanisms that perform this function are highly complex and are collectively known as dynamic cerebral autoregulation (dCA). The functional operation of these autoregulatory mechanisms over the lifespan preserves cerebrovascular health and supports brain longevity.[5] Conversely, it follows that any dysfunction or impairments in the robustness of the autoregulatory protective processes render the brain more susceptible to hypoperfusion, which can lead to metabolic deficit and precipitation of neuronal damage[5]; this is partic-

ularly true in the presence of risk factors such as hypertension and diabetes, in which the brain becomes particularly susceptible to damage in case of impairments in the dCA mechanisms.[6] Another widely accepted theory is that ischaemia and ischaemic strokes occur secondary to (that is, require) dysfunction in the functions of the microvessels supplying the brain parenchyma,[7] with functional deficits to CBF theorized to precede cognitive and structural atrophy.

Indeed, abnormalities in autoregulation have been reciprocally implicated in various disease conditions, including ischaemic stroke,[8] orthostatic hypotension,[9] vascular occlusions,[10] and neurological diseases such as Alzheimer's disease, the pathology of which has been traditionally attributed to the accumulation of amyloid plaques, but is now recognized to also involve a very strong vascular contribution to its onset and progression, including impairment in the autoregulatory response[11] and changes in the microvascular network;[12]–[14] these, in turn, could potentially impede the vasculature's ability to clear the accumulated proteins.[15]

A key requirement for understanding cerebrovascular diseases is the study of vascular behaviour, as well as structural changes in the vasculature, in response to physiological challenges and diseases.[16] More generally, as Bullit[17] has remarked, "almost every disease from cancer to the common cold affects blood vessel attributes (vessel number, radius, tortuosity, and branching pattern)." In particular, many of the brain pathological conditions, including small vessel obstruction during stroke, progressive capillary rarefaction, impaired regulation efficiency, neuropathologies such as Alzheimer's, and morphological changes during the development and treatment of brain tumours, occur in the cerebral microcirculation,[14],[18]–[23] where the majority of the cerebral vascular length is found.[24] Furthermore, it has been suggested that changes in the vascular geometry, and particularly that of the microvasculature, can provide early warning signs of pathological and neurological changes such as Alzheimer's disease,[25] and can potentially become one of the main biomarkers for the prevention and personalized treatment of stroke and other cerebrovascular diseases.[16]

Clearly, the cerebral microvascular architecture has profound implications for both health and disease.[26] However, due to issues pertaining to access, complexity, and scale, the microvasculature is also the portion of the vasculature where our understanding of blood flow control remains most incomplete.[27] In the context of whole-brain haemodynamic modelling, there

has been little focus on the microvasculature, and in most cases, its details are often lumped into a simplified compartmental representation for the sole purpose of providing the appropriate boundary conditions (BCs) for the larger cerebral circulation (see[28]–[35] for examples).

1.2 The Challenges of Studying the Cerebral Microvasculature

Clinical imaging techniques have resolutions that could be down to 0.8-0.9mm; hence, they are unable to capture the micron-scale anatomical features of the microvasculature. The scarce data available on the microvasculature's anatomical properties have been obtained either from *in-vivo* imaging of animal brains, primarily rodents, or through *ex-vivo* examination of post-mortem human brains. Most of the data has been obtained from the former, using high-resolution methods like two-photon microscopy, which requires highly invasive techniques like the generation of cranial windows for optical access to the cortex. It should also be noted that there are several significant and documented geometrical and anatomical differences between the microvasculature in humans and that in animals[36]; therefore, care must be taken when generalising any results across the species.

Perhaps the most prominent example and source of data for the microvasculature properties obtained from *ex-vivo* human brain imaging is the experiment conducted by Duvernoy et al.[37] In their experiment, detailed and high-quality images of the cortical penetrating arterioles and venules were obtained through the intravascular injection of India ink and gelatin as well as low-viscosity resin to outline the lumen of the vessels, which were then examined by stereoscopic and scanning electron microscopes, respectively. From these images, the statistical properties of a small section of the microvasculature, including the statistical distributions for the vessel diameter and length, volume and surface densities, branching angle, tortuosity, and diameter ratios, were quantified and recorded by Cassot et al.[38] The gathering and parameterization of such data enabled the generation of statistically accurate microcirculation networks, for example, via minimum spanning trees algorithms,[39],[40] which are based on matching the statistical properties of the generated networks with the measured and parameterised properties. The use of statistically generated networks bypasses the labour-intensive, time-consuming and error-prone method of experimentally extracting and reconstructing the dense and complex microvasculature structure.[41],[42] Note that there are other algorithms

and approaches for reconstructing the microvasculature network, such as constrained constructive optimization[43] and tissue metabolism-driven arterial tree generation,[44], but the trees generated via the method of minimum spanning trees are the only ones which relate directly to experimentally recorded the morphometrical properties of the microvasculature and are thus the ones used in this thesis.

Furthermore, it is extremely challenging to obtain any in-vivo measurements of the pressure fields in the cerebral microvasculature networks.[45] Commonly used micropipette measurements are limited to vessels close to the cortical surface and are only applicable to vessels with diameters $\gtrapprox 25\mu m$.[46],[47] If the flow through the vessels were to be calculated, then many pressure measurements at different locations would be needed to calculate the pressure gradients, which is not feasible in in-vivo studies.[45] The difficulty in obtaining in-vivo measurements inside the cerebral microcirculation, combined with the difficulty in obtaining accurate anatomical information on the network properties, render mathematical models as key for filling in the gap of our understanding of the microvasculature.

1.3 Using Mathematical Models to Bridge the Gap

This work aims to develop computational fluid dynamic (CFD) models that can then be combined with statistical models that capture the connectivity and anatomical features of the microvasculature, as well as with physiologically grounded feedback models of the blood flow control mechanisms, to provide large-scale models of CBF and regulation in the microvasculature. CFD models are well-suited for investigating the pressure and flow fields in the microvasculature, which are hard to obtain and assess using in-vivo techniques. The outputs from such large-scale models can then be compared with clinically observable measurements, thereby bridging the gap between the microvasculature and macroscale observable properties, such as CBF.

For instance, in functional magnetic resonance imaging (fMRI), Blood Oxygenation Level Dependent (BOLD) imaging is used to infer the changes in neuronal activity and determine which brain regions become activated and deactivated, for example, while performing particular tasks. The basic premise of the BOLD technique is that during heightened neuronal activity in a particular brain region, there is an increase in oxygen consumption and local

blood flow to that region, a process known as neurovascular coupling (NVC). The increase in blood flow normally exceeds that of oxygen consumption, leading to a relative increase in the concentration of oxygenated haemoglobin relative to the deoxygenated haemoglobin. Since oxygenated and deoxygenated haemoglobin have different paramagnetic properties, the magnetic signal recorded can then be used as a surrogate measure for delineating changes in neuronal activity across the different brain regions. Note that the recorded signal provides an indirect proxy measure of neuronal metabolism and activity. Furthermore, each voxel, which is the tiniest 3-D imaging unit from which a measurement can be obtained, contains thousands of microvessels. Hence, the usefulness of the BOLD technique in fMRI strongly depends on the understanding of the NVC process, as well as the underlying vascular architecture and function, which controls blood flow through its physical dilation and constriction.[48] Accordingly, spatially and temporally informed haemodynamic models of CBF and metabolism in the microcirculation can greatly contribute to the reconstruction of a coherent picture of the NVC process examined during fMRI and enable a better quantitative interpretation of the measured BOLD signal.

Unhampered by the limitations encountered by in-vivo experiments, in-silico models can also be used to formulate and test important hypotheses and elucidate the mechanisms behind important brain functions and processes (as we shall demonstrate in Chapter 6). The in-silico representations can also act as virtual safe, low-cost testing beds[49],[50] that offer preliminary assessments for the different outcomes before any clinical interventions or treatment plans, especially risky ones. For instance, in hypertensive patients with impaired autoregulation, it remains unclear which patients are ideal candidates for the administration of blood-pressure-lowering medications, and in which patients could reductions in blood pressure result in severe compromises in CBF.[51],[52] In such cases, in-silico models can facilitate the evaluation of the efficacy and risks of the treatment strategies,[53] which could, in turn, help guide clinicians towards the optimal, patient-specific treatment plan, as part of a new paradigm in medicine termed 'predictive medicine',[54] which entails predicting the probability of disease and introducing preventive measures to prevent or mitigate the effects of the disease.

With a wide range of numerical modelling techniques available, a computational approach for studying cerebral haemodynamics also offers the flexibility and the option of accommodating the modelling context, including scale, complexity, data availability and computational re-

sources available, as described in Section 2.6. This is of particular importance when studying the microvasculature, for two main reasons: first, as mentioned, there is limited data available on the network structure, on measurements quantifying the pressure and flow fields, and on the response and behaviour of the microvessels. Second, the microvasculature region is characterised by a very high vascular density that would preclude any upscaling of the model if the individual vessels are resolved; for instance, the capillary vessels in the cortex have a density of approximately 8000 $vessels/mm^3$.[55] This means that a network simulation on the scale of the whole cortex that accounts for every vessel would simply be computationally infeasible. Accordingly, the lack of anatomical data on the microvasculature and the computational infeasibility of stimulating every single microvessel necessitate a different approach. One option available with computational modelling, which is utilised in this thesis, is the use of a multiscale approach, in which numerical models of different resolution scales are combined into a single model to offer an accurate and computationally feasible characterisation of the overall system across its range of scales.

Computational haemodynamic models are playing an increasingly significant role in current vascular research and clinical practice,[56] with haemodynamic-based models for other organs like the heart, which have been extensively developed and successfully validated with experimental data, showing significant promise and value in model-based surgical and therapy planning (see[57]–[59] for examples). Cerebral haemodynamic models, on the other hand, are still relatively nascent and have received much less attention, but with the increased availability of experimental and imaging data, there has been rapid progress in the field in the last 15 years.[50] It is hoped that the models introduced in this thesis will help in filling in the gaps pertaining to the clinical imaging and computational modelling of the cerebral microvasculature and its autoregulatory behaviour, lay down the ground for future multiscale whole-brain dynamic simulations, and ultimately increase the translatability of haemodynamic models into the clinical environment.

What I found interesting and rewarding about this work are the various mathematical analyses and engineering techniques that I had to apply and learn about in order to inspect and analyse what might, from the first instance, be framed as a fundamentally physiological or biological problem. This is evident in the numerous approaches adopted in the main chapters of this thesis, which include: perturbation methods, control theory, time-frequency analy-

sis, ordinary differential equation (ODE) solvers, finite difference (FD) and finite volume (FV) solvers for hyperbolic, elliptic and parabolic partial differential equations (PDEs), stability analyses, method of characteristics, statistical analyses, parameter sensitivity analyses, Laplace transforms, Monte Carlo filtering (MCF), and Approximate Bayesian Computations (ABC) schemes. More importantly, these techniques and solvers have not been used in isolation; rather, their application has been physiologically grounded, whenever possible, with experimental and imaging data, and with knowledge of the histological and haematological properties and biological mechanisms in the cerebral microcirculation, which is of utmost importance if the models introduced here were to have any clinical utility in the future. Indeed, as Thomas[60] has remarked: "mathematics is playing an ever-important role in the physical and biological sciences, provoking a blurring of boundaries between scientific disciplines and a resurgence of interest in modern and classical techniques of applied mathematics."

1.4 Synposis

The literature review in Chapter 2 provides an overview of brain physiology and cerebral circulation, with a particular focus on the microvasculature. We examine the relevant microvascular and mural cell morphologies, and demonstrate how these features aid in the delineation of the different microvasculature zones. We discuss the mechanisms responsible for CBF control and regulation, which interact with one another and change the vascular smooth muscle (VSM) tone of the vessel walls and hence alter the pressure-radius relationship of the autoregulatory vessels. We look at the blood composition and its impact on blood flow in the microvasculature; in particular, we define the concept of apparent viscosity, describe the mathematical formulations used to calculate it, and discuss the important rheological considerations that emerge as a result of blood flow in the micron-scale microvasculature. We examine the general approaches available for haemodynamic modelling and outline the advantages, limitations and general usages of each. In particular, we illustrate an example of a compartmental representation of the vasculature, and how the CBF control and regulation mechanisms are incorporated into the model. We also introduce the theory of homogenisation and how it can be used to obtain an upscaled representation of the capillary bed.

In Chapter 3, we introduce the network model of dynamic CBF and autoregulation. We derive

the model from combining the three equations, or principles governing haemodynamic flow inside a compliant, autoregulatory vessel, giving rise to a second-order harmonic oscillator PDE, and obtain an approximate analytical solution for the PDE using perturbation analysis. This solution characterises the inlet and outlet flows in a vessel in terms of the pressure profile at the vessel ends, as well as the vessel and blood properties, via a simple ODE formulation. We then connect the vessels of the network by assuming conditions of mass conservation of blood and static pressure continuity at the nodes where vessels meet, resulting in a system of linear ODEs that characterises the pressure (and thus flow) throughout the whole network once the boundary node pressures are prescribed. The myogenic and endothelial mechanisms modify the vessel wall stiffness of the autoregulatory vessels via a first-order feedback equation emulating low-pass filter dynamics; the vessel stiffness is then non-linearly mapped into the vessel compliance to account for the effect of the dCA mechanisms on CBF. We apply the model to a simple microvascular network that functions as a vascular testing bed and examine its response to a drop in the inlet pressure. We find that the model reproduces the physiological features in terms of biphasic response that characterises the dCA mechanisms. We benchmark-validate the model by comparing the outputs of the developed model to the outputs obtained from the more elaborate 1-D CBF models, and find that the results of our model are in very good agreement with those obtained from the 1-D models, while significantly reducing the computational cost, thereby permitting the upscaling of network simulations for the microvasculature in which individual vessels are resolved. We also look at how the model can be used to examine the interplay between the myogenic and endothelial responses across the different generations. Finally, we conduct a variance-based global parameter sensitivity analysis to obtain important insights into the importance of each of the compliance feedback parameters, which in turn lay the grounds for the parameter calibration in Chapter 5.

If haemodynamic models were to be validated against clinical data, the model needs to be upscaled up to (at least) the size of an MRI voxel-sized network. Hence, in Chapter 4, we extend the model developed in Chapter 3 and devise a dynamic multiscale model of CBF and regulation in the cortical grey matter microvasculature. Owing to its net-like and periodic vascular structure, which is homogeneous and space-filling above a characteristic length of $25 - 75\mu m$, the capillary bed is homogenised and treated as a porous continuum, thereby eliminating the need for an explicit architectural representation of the complex and dense

capillary vessels and suppressing the strong impacts of the BC allocation. We model the flow in the capillary bed using Darcy's law, while that in the cortical penetrating vessels, which exhibit a fractal-like and hierarchical branching topology and thus cannot be homogenised, is modelled using the model developed in Chapter 3. We link the two representations using a distributed source flow formulation at the transition interface, one that ensures that the model is scale-invariant and does not give rise to physical and numerical singularities. We use the FV method to solve Poisson's equation characterising the flow in the capillary bed, which arises from combining Darcy's law with mass conservation, and discretise the capillary domain within the MRI voxel-sized network using a novel non-uniform grid that uses tighter meshing at the transition interface between the terminal vessels and the capillary continuum to ensure the numerical accuracy while maintaining the computational feasibility of the numerical solver. We test the model on a statistically generated MRI voxel-sized network, and examine the network's response to a drop in inlet pressure, similar to the approach adopted in Chapter 3. We perform an MCF analysis to enable us to efficiently obtain the permissible range of values for the parameters characterising the mesoscopic-scale properties of the homogenised capillary bed, as well as those of the arteriole-capillary and venule-capillary transition regions. We conduct an error analysis on the steady-state model output in order to verify the scale-invariance of our model, such that below a particular threshold for the size of the FV element, the pressure and flow fields become independent of the element size. Finally, we utilise the Elementary Effects (EE) method to conduct a sensitivity analysis of the compliance feedback model parameter values. This method permits screening of the parameters over their entire range, while also avoiding the large number of realizations required for the variance-based analysis conducted in Chapter 3 which for the multiscale model would render the sensitivity analysis as computationally prohibitive.

In Chapter 5, we use a class of ABC schemes, called sequential Monte Carlo (SMC) methods, to estimate the distribution of the compliance feedback model parameters used in Chapters 3 and 4 based on the experimental data available. Here, we introduce a prior distribution of the parameter space, one that is, whenever possible, physiologically grounded based on information on the possible range of the parameter values. We use the distribution to create a Monte Carlo (MC) ensemble of realizations, which we then feed into the dynamic model. The model output of a particular realization is then compared to the experimental data and the

realization is accepted if the discrepancy between the model output and the measured data is within a predefined error tolerance, after which the accepted realizations are mapped back into the input parameters and are used to obtain a posterior distribution of the parameter space. In SMC methods, the posterior distribution is used as a prior distribution for the next round of fitting, and the error tolerances are gradually reduced iteratively, allowing a gradual convergence towards the optimal distributions. We use the experimental data to calibrate the compliance feedback model and trace the diameter changes of individual isolated arteriolar vessels in response to changes in one or both of the transmural pressure and the pressure gradient, which elicit myogenic and endothelial responses, respectively. We create an *in-silico* representation of the experimental set-up and input conditions, and compare the output of the dynamic model to the measured experimental data within an ABC scheme; in this way, we ensure that the model is both physics-based and data-informed. Upon the parameter calibration, we find that the computationally low-cost compliance feedback model achieves very good agreement with the experimental data. We also demonstrate how the SMC parameter calibration process reveals valuable mechanistic insight into model dynamics, as evident in the significant differences in the obtained time constants between myogenic-induced vessel dilation and constriction.

Chapter 6 provides a case study that demonstrates how the models developed in Chapters 3 and 4 can play a vital role in clinical research. In this case, we use the models to test and validate a proposed mechanistic pathway that underlies the increase in CBF following increases in blood CO_2 gas levels, or what is known as the hypercapnic response, which remains poorly understood due to the challenges of *in-vivo* investigations in the microvasculature. Experimental data indicate that the release of Acetylcholine (ACh) in the cortex is a prerequisite for the occurrence of the hypercapnic response. Furthermore, it is known that Acetylcholine is an endothelial-dependent agonist of the conducted vascular response (CVR), in which local hyperpolarization of the endothelium as a result of ACh administration is conducted upstream of the vascular network. The hyperpolarizing current is also transmitted from the endothelial cells (ECs) to the adjacent VSM cells, eliciting their relaxation and hence causing vessel dilation. Finally, it has been experimentally demonstrated that the hypercapnic response is more strongly correlated with tissue rather than arterial or arteriolar CO_2 levels. Putting these pieces together, we propose a mechanistic pathway for the hypercapnic response, where

the increase in tissue CO_2 levels would trigger the local release of ACh, thereby eliciting the CVR that transmits the waves of hyperpolarization and dilation upstream, decreasing the vascular resistance and increasing CBF. Each of these mechanisms is encoded via a suitable mathematical model, after which the model parameters for each constituent mechanism are calibrated from experimental data. We test our model using both the simple network model developed in Chapter 3, as well as the multiscale model developed in Chapter 4 and obtain model outputs that are strongly aligned with the experimentally determined characteristics of the overall response, thereby supporting the proposition that these series of mechanisms are behind the hypercapnic response, prompting further *in-vivo* investigations, and opening the potential for the development and administration of better-targeted drugs and treatment plans for impaired cerebrovascular reactivity.

Finally, in Chapter 7, I summarise the findings of the thesis and conclude by discussing the potential future work that can be undertaken based on the work presented in this thesis.

Chapter 2

Literature Review

2.1 The General Structure of the Brain

The brain is composed of three regions that work in concert to carry out the brain's vital functions: the brain stem, cerebellum and cerebrum. The largest and most developed of these brain regions is the cerebrum; it is the structure that people have in mind when they visualize the brain. The cerebrum is composed of the right and the left hemispheres. It is the source of our thoughts and voluntary actions and is responsible for most of the brain's functions including memory, emotions, language, vision and hearing.

The surface of the cerebrum is coated by an important layer that is approximately 2-4mm thick, known as the cortex. The foldings in the cortex, known as the gyrus, increase the surface area of the brain to allow more neurons to fit inside the skull and thereby increase in information processing capacity of the brain. With around sixteen billion neurons arranged in six layers, the cortex plays a crucial role in the information-processing tasks of the brain, including perception, language, and memory. The cortex is made of grey matter, which consists primarily of neuronal cell bodies, or soma, with relatively few insulated (myelinated) axons. Underneath the cortical layers resides the white matter, which is comprised mostly of long-range myelinated axons that transmit signals across the different brain regions. The high concentrations of cell bodies in the grey matter and myelinated axons in the white matter give rise to the grey and white shading found in imaging data (hence the names). Figure 2.1 depicts the distribution of the grey and white manner in a cross-section of the cerebrum. The grey matter is much more vascularized and perfused than the white matter, due to the high energetic demand of the neurons.[37] In this thesis, we will focus on CBF and control in the cortical microvasculature.

The brain is also protected by several layers, which are the skull, pial matter, arachnoid matter and dura matter, with the CSF circulating between the arachnoid and pial matter to cushion it against the skull and absorb any shocks. The CSF also occupies the ventricular system where it is produced, and flows through the perivascular space around cerebral vessels, combining

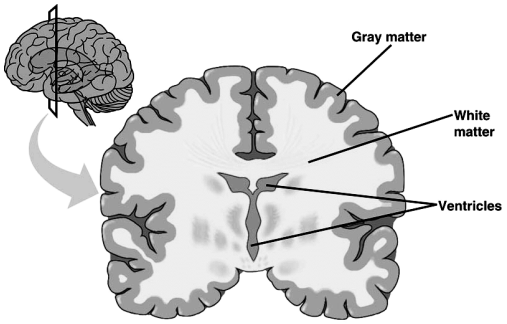

Figure 2.1: A cross-section of the brain. The outer section is the cortical grey matter, and underneath is the white matter, with CSF produced in the ventricles and pervading most of the brain. Reproduced without change from[61].

with the interstitial fluid as part of the glymphatic clearance pathway, the waste clearance system for the central nervous system.

2.2 Cerebral Circulation

The cerebral vasculature is a very complex, interconnected network of blood vessels across multiple length scales that provides a continuous supply of glucose and oxygen to the brain tissue.[50] Broadly speaking, the cerebral vasculature is sub-divided into different vessel types in the same manner as the rest of the circulatory system: arteries, arterioles, capillaries, venules and veins. At the largest scale, arteries form an efferent network of vessels that carry oxygenated blood at high pressure from the heart to the peripheral circulation. The vessel walls of the large arteries are compliant, allowing them to store blood volume during the systolic phase of the heartbeat and eject it during the diastolic phase, maintaining a more nearly steady flow than if the arteries were rigid.[49],[62] The distensibility of the arterial walls gives rise to the 'fluid-structure' interaction that is addressed in the thesis, and that is responsible for the propagation of the pulse pressure waves.[49]

The brain is supplied by four primary arteries: the left and right internal carotid arteries run anteriorly on the sides of the neck, and the left and right vertebral arteries supply the posterior part of the brain. The vertebral arteries join together to form the Basilar artery, which travels up the brain stem to join the internal carotid arteries through the interconnecting arteries, forming the Circle of Willis (CoW), shown in Figure 2.2. The CoW interconnects the major vessels that supply blood to different regions of the brain, which are the left and right middle cerebral arteries, posterior cerebral arteries, anterior cerebral arteries, as well

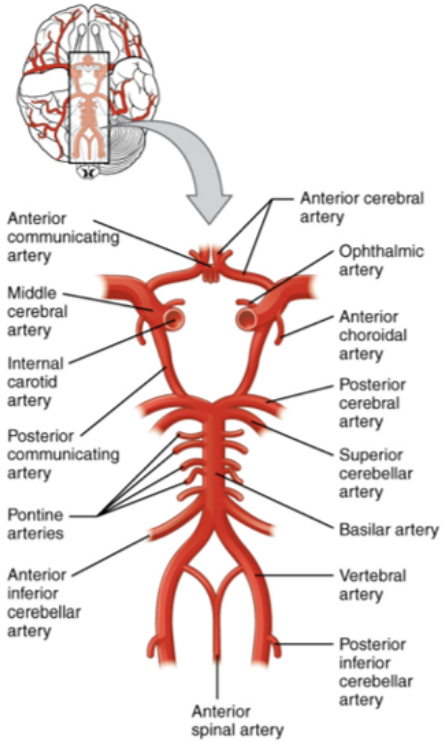

Figure 2.2: The blood supply to the brain enters through the internal carotid arteries and the vertebral arteries, eventually giving rise to the circle of Willis. Reproduced without change from[63].

as the anterior communicating artery. The interconnectivity between the vessels of the CoW provides a safety mechanism for perfusion through collateral flow; for instance, if one of the arteries becomes occluded and blood flow through it is reduced, retrograde flow from the other blood vessels can often preserve cerebral perfusion of the affected portion of the brain to avoid ischaemia. It is worth noting that various configurations for the CoW exist in the human population, with about half of the population having an incomplete circle.[55]

The arteries then bifurcate with strong branchings at ever-decreasing diameters and lengths[50] until reaching the pial arteries, which are situated in the subarachnoid space (between the arachnoid and pia matter) on the cortical space of the brain, as shown in Figure 2.3. The pial arteries then branch into the descending penetrating arterioles which bifurcate into gradually narrowing trees, transversing the six layers of the grey matter at different depths as shown in Figure 2.4(a), and are intimately in contact with the brain parenchyma, their astrocytic end feet, and the released metabolites.[64] The terminal arterioles then connect to the capillary bed, which forms a complex dense and interconnected network of narrow vessels, with diameters in the range of 5-10 μm. The capillary bed is the site where most of the nutrients and waste exchange between the vasculature and the brain tissue takes place, although recently the arteriolar vessels have also been recognized to play an important role in nutrient and oxygen

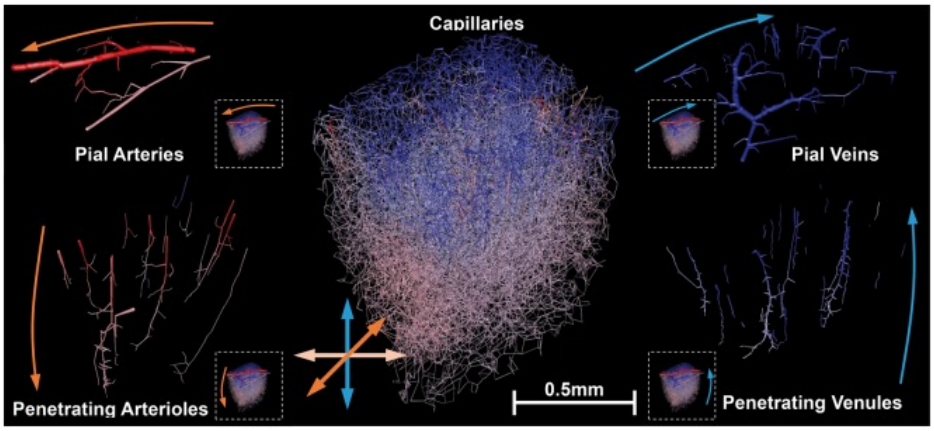

Figure 2.3: Depiction of the anatomical hierarchy of the arterial, arteriolar, venule and venous vessels in the cortex. The colour map represents the pressure distribution, with arteries in red and veins in blue. Large pial arteries distribute blood along the cortical surface, from which pial arterioles branch and feed the capillary bed across the cortical layers. Venules collect blood from the capillary vessels and return it to the cortical surface. Pial veins then carry the deoxygenated blood from the pial surface to the sinuses. Reproduced without change from[67].

exchange.[65],[66]

Similar to the descending arteriolar network, a parallel network of ascending venules (Figure 2.4(a)) drains the capillary bed and carries deoxygenated blood back to the pial veins on the cortical surface. The penetrating arteriole and venule networks are comprised of individual trees with conspicuous orthogonal columns[68] and a fractal branching topology[37] that lends itself to a hierarchical ordering analysis,[50] as shown in Figure 2.4(b). While different penetrating trees feed and drain different layers, the majority of the penetrating vessels terminate halfway through the grey matter.[37] Together, the penetrating vessels contribute to about 52% of the cerebrovascular volume.[69] In Chapter 4, we discuss the relevant statistical properties of the structure and distribution of the cortical penetrating trees in greater detail. Once in the venous circulation, blood then drains through the cerebral sinuses into the jugular veins in the neck, and back to the heart via the superior Vena Cava. In addition to their function as an afferent network returning blood to the heart, the veins also serve the purpose of a blood reservoir, since they are much more distensible than the arteries.

2.3 The Microvasculature: Vascular and Cellular Structure

The taxonomical subdivision of the vasculature introduced in Section 2.2 is reflective of the differential characteristics in terms of vessel size, physiological function, wall structure (including the surrounding mural cells), branching patterns, and CBF behaviour across the ves-

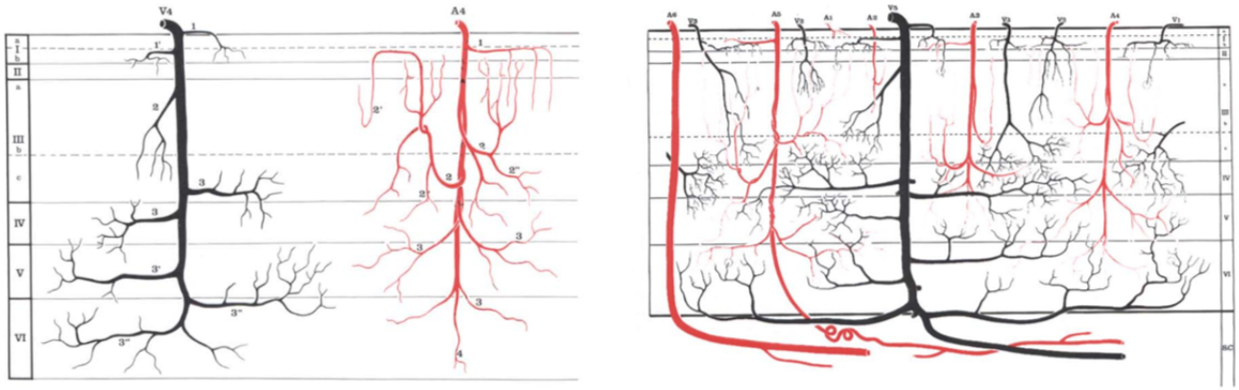

(a) (b)

Figure 2.4: Typical cortical arteriole (red) and venule (black) trees transversing the grey matter layers (a). The penetrating vessels form individual units (b). Reproduced without change from[37].

sel generations. Nonetheless, and particularly in the microvasculature, it is important to bear in mind that there are no strict borderlines between the vessel types based on the aforementioned properties, which change smoothly across the microvasculature. As Sims has put it: "a continuum of cell morphologies will occur in these regions so that discrepancies of cell names will inevitably arise."[70] Indeed, while recognizing the continuous transition in mural cell morphology, there are ongoing disagreements regarding how to refer to the different microvascular segments and their associated mural cells.[27]

In their excellent review paper, Hartmann et al.[27] addressed the nomenclature issues and attempted to reconcile the different classifications used in the literature. Drawing on the most recent findings from *in-vivo* optical imaging and single-cell transcriptomics, they delineated the different microvasculature zones based on the surrounding mural cells, including their morphology and cellular composition, gene expression, and control dynamics.[27] On that account, they have identified four types of mural cells, which accordingly define the major microvasculature zones in the cortex: 1) VSM cells on the arterioles, 2) Ensheathing pericytes on the arteriole-capillary transitional (ACT) zone, 3) capillary pericytes, exhibiting both mesh and thin stranded process on the capillaries, and 4) stellate VSM cells on venules. The four mural cell types and their associated microvasculature zones are illustrated in Figure 2.5.

Both the pial arteries and the penetrating arterioles are covered with a layer of concentric, ring-like VSM cells that are rich in alpha-smooth muscle actin filaments (α-SMA), an important component of the actomyosin contractile machinery, as discussed in Section 2.4. The vessel walls also include a layer of elastin, which together with the VSM cell layer permits

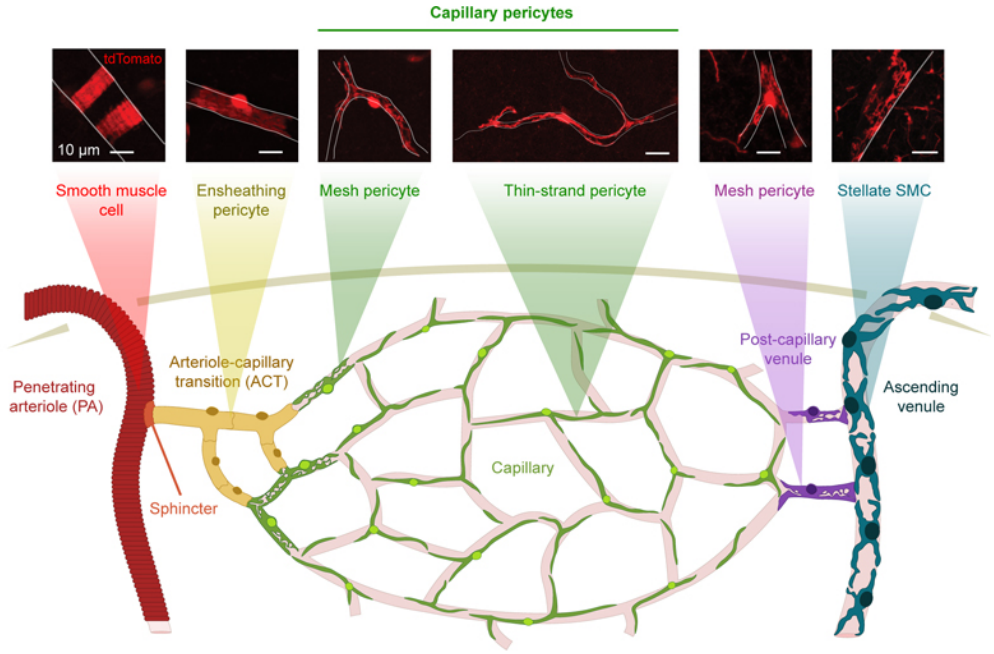

Figure 2.5: The different zones of the brain microvasculature and the associated mural cell types, according to the nomenclature proposed by Hartmann et al.[27] The microvasculature zones are divided as follows: pial arteriole, penetrating arteriole, arteriole-capillary transition (ACT), capillary, post-capillary venule, ascending venule, and pial venule. Reproduced without change from[27].

the vessel to rapidly dilate or constrict and hence facilitate a robust response from the vessels during CBF regulation.[27] Between the penetrating arterioles and the ACT, and positioned at the mouths of the offshoots from the penetrating arterioles, there often but not always exist annular, contractile sphincter cells which express α-SMA but lack an elastin layer.[71] The localized regions of constriction created by these sphincters provide a buffering capacity for the capillaries from any fluctuations in pressure occurring upstream.[71] Furthermore, those pre-capillary sphincters could dilate, thereby offering tighter control of and promoting CBF to the capillary bed during functional hyperemia.[71]

In the ACT zone, the vessels are covered by what is termed the ensheathing pericytes, which express α-SMA, similar to VSM cells, but also possess a hybrid morphology of both the VSM cells and the classic pericytes with their processes incompletely surrounding the capillary bed.[27] Similar to the VSM cells, the ensheathing pericytes wrap around the entire endothelial layer, yet at the same time they have processes that are elongated and exhibit protruding cell bodies like the classic pericytes.[72] With further branchings, α-SMA expression abruptly drops to levels that are very low or undetectable as the mural cells coverage transitions from ensheathing pericytes to the capillary pericytes, marking the start of the 'true' capillary zones.[27] If the orthogonal cortical column of the penetrating arteriole tree was assigned a branching

order of zero, and the branching order with each subsequent branching was increased by one, then the ACT-capillary junction would in most cases occur between the first and fourth branch orders, with higher orders possible in trees with larger diameter offshoot.[72] This means that most capillaries have branching orders in the range of three to six,[66],[73] while orders up to the ninth can be reliably traced from *in-vivo* imaging.[24]

The wall of the capillary vessels is made up of an endothelial layer and a thin basement membrane, and is, on average, $0.5\mu m$ thick. The walls are permeable to allow for the transport of nutrients and small molecules, like O_2 and CO_2, primarily via diffusion. Morphologically speaking, in the middle region of the capillary bed, which constitutes the majority of the capillary length, the capillary pericytes extend thin-strand, long processes that only partially cover the endothelium.[27] These processes may span multiple capillary segments, coordinating communication with the endothelial cells where the membrane thins.[74] These pericyte-endothelial communications play a crucial role in establishing the blood-brain barrier, CBF control, immune response regulation, and angiogenesis.[27] Closer to the ACT and in the post-capillary venule zone, the pericyte processes take on more of a mesh-like structure, still incompletely covering the endothelium,[27] as shown in Figure 2.5. Of course, the thin-strand and mesh-like capillary pericytes are difficult to unequivocally delineate, and represent a true continuum of morphologies.[27],[72]

An important and perceptive distinction in nomenclature proposed by Hartmann et al.[27] is that the ascribed function of the vessels is not factored in the designation of the microvascular zones, despite the strong apparent correlation between structure, location and function. This is because the ascribed functions can change over time as we learn more and develop more advanced technologies for experimental investigations. For instance, in the optogenetics experiment by Hill et al.,[75] while the VSM cells surrounding the arterioles contracted readily upon simulation, no changes in capillary diameter were recorded over the tens of seconds of capillary pericyte simulation, leading the authors to conclude that capillary pericytes lack the contractile ability and thus cannot possibly play a role in CBF regulation.[27],[75] A reassessment of the contractile ability of the capillary pericytes by another group of researchers[24] using the same technique found that the pericytes were indeed contractile, but required a much longer timescale and intense simulations, echoing the results of other recent experiments that demonstrate the contractile ability of pericytes. While the role of capillary pericytes in CBF

control and regulation is becoming increasingly recognised,[5],[76]–[78] their precise contribution towards CBF control, in terms of reactivity, timescale, and initiating stimulus, remains an important question and a source of controversy among researchers. On a similar note, while the capillary vessels mostly have diameters in the range of $5 - 10\mu m$,[62] basal diameters were not used regarded as a reliable metric to distinguish between the different vessel types and the microvascular zones, because the decrease in diameter as we move downstream is not necessarily strictly monotonic; for instance, due to the frequent presence of the sphincters between the arterioles and the ACT zone.

2.4 Mechanisms of Dynamic Cerebral Autoregulation and Blood Flow Control

The cerebral vascular bed is a highly dynamic active system that responds to multiple local and global stimuli over a range of lengths and time scales to ensure a tightly coupled relationship between the blood's local supply and demand.[50] During steady-state conditions, the flow (Q) of blood through a vessel can be assumed to be solely governed by the blood pressure difference (ΔP) between its two ends and the Hagen-Poiseuille resistance $(\mathcal{R})$, according to the linear relationship in Equation (2.1):

$$Q = \frac{\Delta P}{\mathcal{R}} \tag{2.1}$$

where $\mathcal{R}$ is the Poiseuille resistance, which depends on the vessel and blood properties, including the vessel length (L), internal radius (R), and the blood dynamic viscosity (μ), which in turn depends on vessel diameter and haematocrit levels, as explained in Section 2.5:

$$\mathcal{R} = \frac{8\mu L}{\pi R^4} \tag{2.2}$$

Of course, if we were to consider the dynamics of blood flow rather than assuming simple-steady state conditions, then it becomes necessary to incorporate the effects of blood inertia and wall compliance,[55],[79], as demonstrated in Chapters 3 and 4, but for the large part,

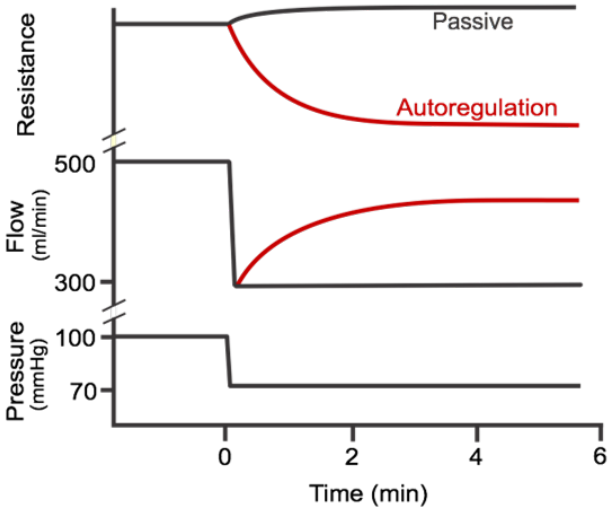

Figure 2.6: Response of the cerebral vasculature to a step decrease in arterial blood pressure (ABP). Reproduced without change from[2].

the flow through the microvessel is dictated by the Hagen-Poiseuille flow. Since the length of the vessel is largely invariant, and the blood haematocrit levels are generally adequately maintained in the cerebral circulation, the only way in which blood flow can be controlled is through changes in the vessel radius.[55] The dependence of the resistance on the radius to power four provides a fine degree of flow control since small changes in radius can lead to substantial changes in the resistance and thus the flow.

Considering the linear relationship between blood flow and the driving blood pressure in Equation (2.1), a decrease in the driving pressure will lead to a decrease in flow. Furthermore, given the compliant nature of the vessel walls, a decrease in the transmural pressure will also lead to vessel constriction, which in turn leads to an increase in the resistance according to Equation (2.2). This increase in resistance gives rise to a further decrease in blood flow in response to a pressure drop. To maintain blood flow, the passive response of the vessels needs to be counterbalanced by an active myogenic response, corresponding to a paradoxical vessel dilation in response pressure drop, as shown in Figure 2.6. Because this autoregulatory process takes time to occur, the passive response would start instantaneously when the pressure drops, leading to a slight drop in CBF, before the active response takes effect and restores blood flow, thereby giving rise to the biphasic autoregulatory response,[80] a schematic of which is shown in Figure 2.6.

Hence, on a fundamental level, blood flow is controlled by adjusting the radius of the vessels, which in turn modifies their resistance. Since it is the wall compliance (or its inverse, stiffness)

that sets the relationship between the vessel radius and transmural pressure, dCA is thus achieved through control of the vessel wall compliance.[81] By adjusting the compliance of the vessel, the relationship between pressure and radius is altered, and the vessel establishes a new equilibrium state in response to changes in the transmural pressure.[82] Indeed, almost all haemodynamic models of autoregulation, both on the scale of the individual vessel or in compartmental representations, incorporate the autoregulatory mechanisms via some form of a compliance feedback response, an example of which is described in Section 2.6.

The changes in the wall stiffness are brought by adjusting the level of activation and thus the tension in the VSM cells in the wall of the vessel. The VSM cells are in a partially contracted state under normal physiological conditions. From this baseline tone, the cells can then contract further or relax to modify the vessel stiffness. Since the small cerebral pial arteries and the arterioles have the largest fraction of VSM cells among blood vessels, they are the primary vessels that actively control blood flow (although the role of the capillary pericytes is becoming increasingly recognized (see[5],[76],[77]).

The pressure-induced myogenic response is not the only mechanism involved in maintaining CBF. CBF control can be roughly divided into four components: myogenic, metabolic, endothelial and neurogenic. The distinction is more of an artificial one, since the mechanisms are not independent but are in constant interaction to maintain CBF, and changes in one variable will affect all aspects of cerebral vasculature's behaviour,[81] as we shall demonstrate in the upcoming Chapters. Note that, strictly speaking, dCA refers to the vasculature's response to perturbations in the arterial blood pressure (ABP), or more accurately, in cerebral perfusion pressure (CPP), the net pressure gradient causing cerebral blood flow to the brain.[83] Hence, technically, dCA is only a subset of the larger umbrella of the dynamic CBF control mechanisms, which encompass feedback pathways that respond to other stimuli, including perturbations in blood gas levels (see Chapter 6). While the exact processes by which each component adjusts CBF are highly complex and different, they all converge to the same final mechanism: controlling the level of VSM tone.

The VSM cells are composed of thin actin and thick myosin filaments. Upon contraction, the two filaments slide over each other, shortening the length of the VSM cell and hence eliciting vessel wall constriction. Essentially, it is the intracellular concentration of the calcium ions,

modulated by the various CBF control mechanisms, that controls the degree of VSM cell contraction. The free calcium ions bind to a protein called calmodulin. The calcium-calmodulin complex then activates myosin light chain kinase (MLCK), an enzyme which, in the presence of ATP, phosphorylates the myosin light chains found on the myosin heads. The phosphorylation of the myosin light chains leads to the cross-bridge formation between the myosin heads and the actin filaments, thereby leading to smooth muscle contraction. In the same manner, vasodilation is achieved by the inhibition of myosin light chain phosphorylation.

The different CBF control mechanisms depend on different signalling mechanisms to modulate the intracellular calcium concentration. In the myogenic response, the stretch-induced activation of the potassium channels due to the changes in the VSM tension[84],[85] leads to an electrical depolarization that opens the voltage-gated calcium channels, leading to calcium influx. In the endothelial response, the shear stress on the endothelial lining as blood brushes against it stimulates the endothelial cells to synthesize several vasoactive substances such as Prostacyclin, endothelin-1, and, perhaps the most important of which, nitric oxide, that freely diffuse and bind to receptors on the VSM. Nitric oxide is then involved in the production of cyclic guanosine monophosphate (cGMP), which acts as a second messenger that eventually results in muscle relaxation. It activates protein kinases that decrease calcium entry, stimulates myosin light chain phosphatase, and decreases inositol trisphosphate (IP_3) levels required to release the stored calcium in the SR, ultimately decreasing levels of myosin phosphorylation and eliciting VSM relaxation.

In the case of the metabolic response, when the metabolic activity of the brain cells is not matched with an equivalent supply of oxygen and nutrients, vasodilating metabolites (such as adenosine, CO_2, H^+, and lactate) build up and are released into the bloodstream. They would then diffuse into VSM cells and activate signal transduction pathways that decrease intracellular calcium concentration, thereby stopping cross-bridge formation and inducing a relaxation response. For instance, Adenosine and H^+ activate ATP-sensitive potassium channels, which then leads to hyperpolarization and closing of voltage-gated calcium channels. In addition, Adenosine can bind to the adenosine A2A receptor, which leads to the formation of cyclic adenosine monophosphate (cAMP) inside the cell. Just like cGMP, cAMP acts as a second messenger that leads to the activation of protein kinases. The protein kinases result in the uptake of calcium by the sarcoplasmic reticulum (SR), the internal storage unit of the muscle

cell, and the opening of calcium-activated potassium channels leading to hyperpolarization and inhibition of calcium entry, thereby decreasing intracellular calcium concentrations.

In the case of the neurogenic response, the mechanisms can either be intrinsic or extrinsic. Intrinsically, cells such as neurons, astrocytes, and microglia release neurotransmitters with vasoactive properties, which affect the VSM tone in the walls of small and medium-sized arteries.[86] In Chapter 6 where we introduce and investigate a potential model of the vascular response to elevations in arterial CO_2 levels, termed the hypercapnic response, we examine the potential role of the intrinsic neurogenic release of ACh in mediating the hypercapnic response. As for the extrinsic response, despite the extensive autonomic innervation in the brain,[2],[87] experimental studies in humans have found only a modest and somewhat frequency-dependent role of sympathetic[88]–[90] and parasympathetic[89] activity in influencing dCA. Autoregulation was maintained in sympathetically and parasympathetically denervated animals, indicating that a major contribution of extrinsic neurogenic factors to autoregulation of cerebral blood flow is unlikely.[91] Hence, although the cerebral circulation is richly innervated with sympathetic nerve fibres,[92] the role of sympathetic nerve activity on CBF control and regulation remains controversial.[93] It is believed that the local response, incorporating the combination of the myogenic, metabolic, and intrinsic neurogenic mechanisms described above, is the dominant one, enabling the response to be adapted to local needs, with the extrinsic response merely providing a degree of coordination.[2],[55] Interestingly, the CBF control and regulation mechanisms have recently been shown to extend beyond the brain. The astrocytes surrounding the capillary web have been shown[5] to be able to monitor reductions in CPP and transmit signals to the central nervous system, which in turn results in increases ABP, heart rate and stroke volume. Hence, these glial cells function as intracranial baroreceptors of some sort, forming a homeostatic loop that maintains CBF and protects the brain from hypoperfusion.

2.5 Blood Properties

Blood makes up about 7 % of the human body weight or about 5L in volume. Plasma is the liquid part of blood. The solid part is made up primarily of three cell types: 1) erythrocytes, or red blood cells (RBCs), 2)leukocytes, or white blood cells, and 3) thrombocytes, or platelets.

Blood is therefore not a fluid in the traditional sense, but rather a suspension of the three cell types, along with ions and proteins, within the plasma fluid. RBCs essentially carry all of the haemoglobin, the iron-containing molecule that binds O_2, to supply the tissues with the O_2 needed for metabolism as blood flows through the microcirculation. With a typical concentration of approximately 4-6 million cells per mm^3 of blood,[94] RBCS comprise a large volume (approximately 45 %[95]) of the total blood volume. Because of their high concentrations, RBCs have a significant effect on the mechanical properties of blood,[95], particularly in the microvasculature, where the shear rates and the vessel diameters are lower than in the rest of the circulation.

RBCs are uniform in their shape and sizes, with human RBCs having a biconcave shape with a disk diameter of approximately $6.2 - 8.2\mu m$. However, they are very elastic and soft, allowing the outer membrane to deform and for the cell to squeeze through the capillary vessels, where they would flow in a single line, or what is referred to as 'single file.' At this smallest level in the capillaries, blood cannot be modelled as a homogeneous fluid anymore, since the RBC dimension is now of the same order as that of the vessel. In general, blood behaves as a non-Newtonian fluid, in which the dynamic viscosity depends on the vessel geometry and RBC content. In the macrocirculation, the non-Newtonian effects are negligible and blood is modelled as a homogenous fluid with a constant dynamic viscosity. In the microcirculation, however, the presence of the RBCs can have interesting and important implications on the rheology of blood, giving rise to three unique flow phenomena, as described below.

Even though blood behaves as a non-Newtonian fluid in the microcirculation, an 'apparent' dynamic viscosity (μ_{app}) characterising the rheology of blood in the microvessel can be obtained by combining and rearranging Equations (2.1) and (2.2) to get:

$$\mu_{app} = \frac{\pi R^4}{8QL}\Delta P \tag{2.3}$$

This observed or apparent viscosity is experimentally determined, and would thus take into consideration the geometry of the vessel and, if measured *in-vivo*, the interactions of the RBCs with the endothelial layer,[96],[97] thereby enabling us to model blood in the microvessel as a Newtonian fluid with a single effective viscosity. In vessels below $300\mu m$ in diameter, it

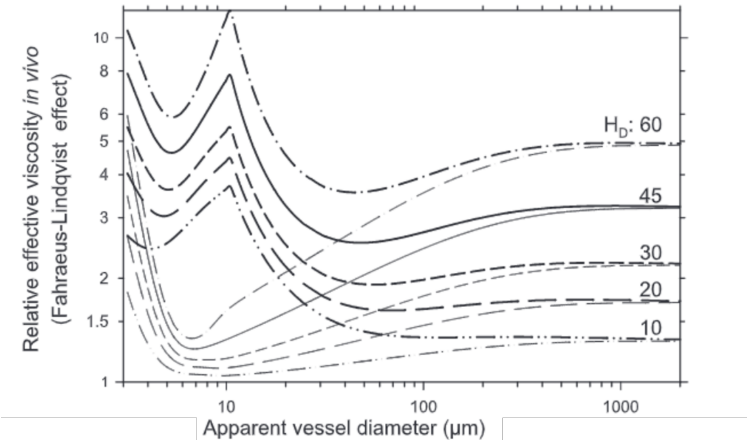

Figure 2.7: The dependence of the *in-vivo* measured apparent viscosity μ_{app} on the discharge haematocrit (H_D) and the vessel diameter. Reproduced without change from[97].

was found that this apparent viscosity decreases with vessel diameter, and this drop continues monotonically until reaching a diameter of around $10\mu m$, below which the apparent viscosity of blood exhibits a marked increase in viscosity up to a diameter of around $2.7\mu m$, which is regarded as the critical diameter below which deformable RBCs can no longer pass through the capillaries.[98],[99] This phenomenon is known as the Fåhræus-Lindqvist effect, and in such cases, empirical relationships are commonly used to determine the apparent viscosity of blood, which is calculated as a function of both the vessel diameter and the discharge haematocrit (defined as the volume flow rate of RBCs as a fraction of the total volume flow rate). Perhaps the most noteworthy of these empirical relationships are the ones developed by Pries et al., for both *in-vitro* and *in-vivo* conditions. In this thesis, we will be using *in-vivo* empirical model by Pries et al.[100] in Equation (2.4) to approximate the effective viscosity relative to plasma (μ_{rel}) based on the vessel diameter in μm (D) and the discharge haematocrit (H_D):

$$
\begin{aligned}
F &= \left(0.8 + e^{-0.057D}\right)\left(-1 + \frac{1}{1 + 10^{-11}D^{12}}\right) + \frac{1}{1 + 10^{-11}D^{12}} \\
\mu_{45} &= 6e^{-.0.85D} + 3.2 - .244e^{-0.06D^{0.645}} \\
\mu_{rel} &= \left[1 + (\mu_{0.45} - 1)\,\frac{(1 - H_D)^F - 1}{(1 - 0.45)^F - 1}\left(\frac{D}{D - 1.1}\right)^2\right]\left(\frac{D}{D - 1.1}\right)^2
\end{aligned}
\tag{2.4}
$$

Figure 2.7 illustrates the dependence of the *in-vivo* measured μ_{app} on H_D and the measured vessel diameter.

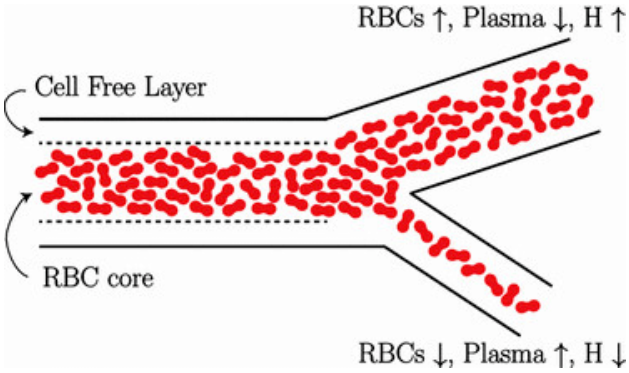

Figure 2.8: Phase separation (plasma skimming) at a bifurcation in the microcirculation. Reproduced without change from[102].

Two other important rheological phenomena in the microcirculation are the Fåhræus effect and phase separation. The Fåhræus effect refers to the decrease in haematocrit content inside the vessel or glass tube (referred to as tube haematocrit) as the diameter of the vessel or tube in which it is flowing decreases,[101] and is one of the reasons behind the Fåhræus-Lindqvist effect described above. This phenomenon arises because, in the microvessels, RBCs move over to the centre of the vessel, leaving only plasma near the surface of the vessel wall. Phase separation, or plasma skimming, refers to the uneven distribution of RBCs and plasma in the microcirculation as blood flows from a parent vessel to the daughter branches, and occurs due to the presence of the cell-free layer at the surface of the vessel walls,[102] as shown in Figure 2.8. Similar to the case of the Fåhræus-Lindqvist effect, empirical models have been developed to account for both the Fåhræus effect and plasma skimming. Phase separation empirical models tend to be non-linear, and thus require an iterative procedure that is normally solved in tandem with a model of CBF at the bifurcations or trifurcations to obtain the haematocrit distribution if phase separation were to be accounted for (see[103] for example).

2.6 Haemodynamic Modelling Landscape

There are various approaches available for modelling blood flow within a vascular network, which are summarised in Figure 2.9. The choice of which modelling approach(es) to use highly depends on the context of the modelling application and is dictated by multiple factors including the aims, scope, desired level of accuracy, and computational resources available.

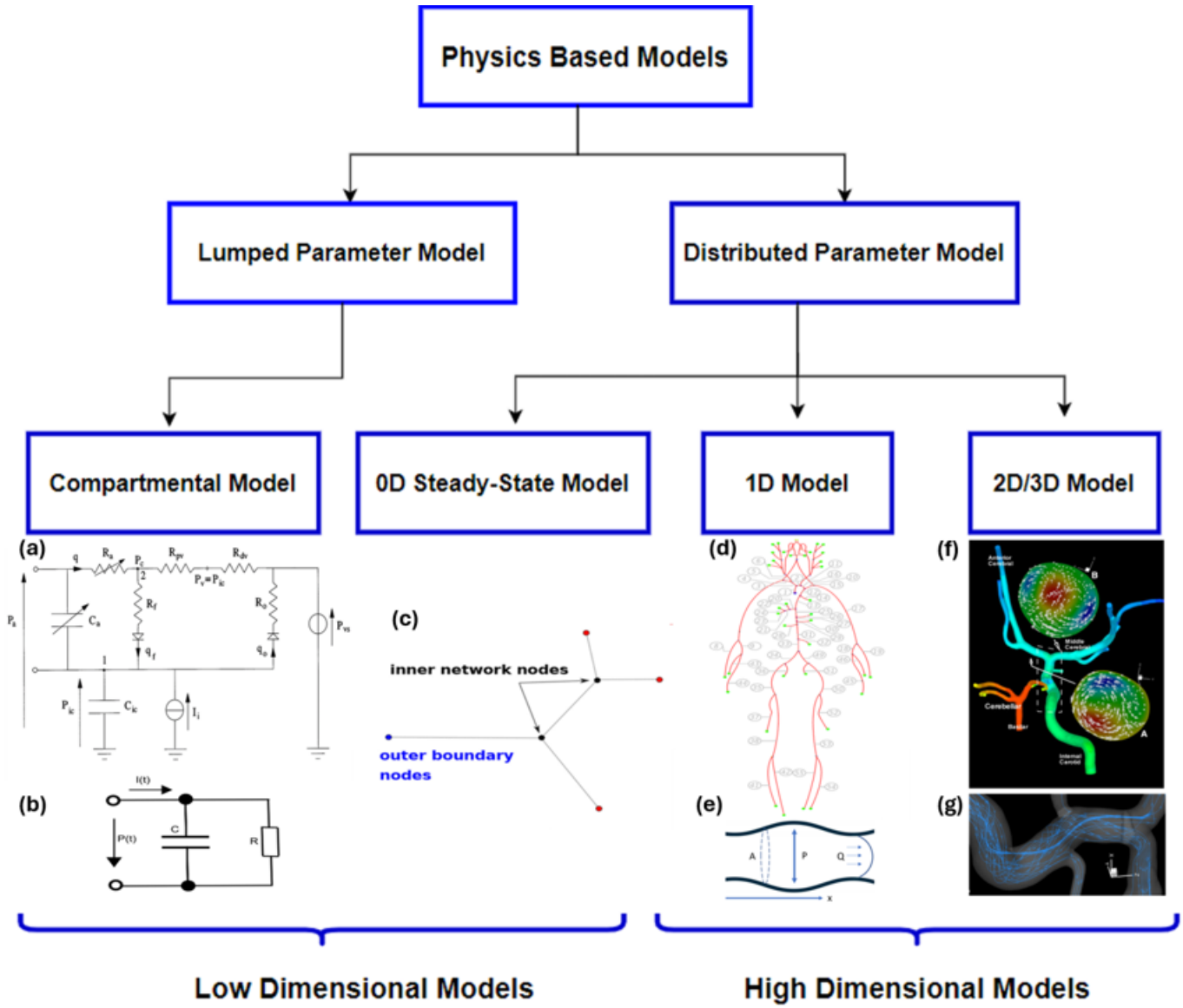

Figure 2.9: An overview of the haemodynamic modelling approaches used in literature. In 3-D models, the pressure distribution, and the velocity fields are calculated. In figure (f),[104] the pressure is indicated by the colourmap throughout the geometry of the CoW, and the velocity field is indicated by the white arrows along the 2D slices, with the colours inside the slices representing one of the inplane velocity components. From the velocity fields, the instantaneous streamlines can be computed, as shown in figure (g).[104]. Comparably, with only three primary variables to solve for, 1-D models permit the simulation of blood flow in a much larger number of arteries, as shown in the figure (d),[28] due to the reduced number of primary variables, which are depicted in figure (e). In 0-D steady-state models, the network is represented as a simple graph composed of edges and nodes as shown in figure (c),[65] and the steady-state Hagen-Poiseuille flow is calculated according to Equation (2.1). In compartmental models, multiple generations of blood vessels are lumped together into compartments, each of which is then composed of one or multiple components, as shown in figure (a).[105] The basic unit of compartmental models is the Windkessel model, one iteration of which is shown in figure (b), where a single compartment would be comprised of a resistor and capacitor. All images are reproduced with permission from the respective sources.

2.6.1 Three-Dimensional Models of Blood Flow

On one end of the computational spectrum, 3-D models employ some form of the Navier-Stokes momentum conversation and incompressible continuity equations, which, when combined with some form of a tube law that relates changes in transmural pressure to changes in the cross-sectional area (CSA) due to the wall's elastic (or viscoelastic) behaviour, give rise to a system of PDEs that characterises the 3-D velocity vector and pressure fields within the relevant domain of the distensible vessel. By using segmented images from imaging modalities such as MRI or computed tomography (CT) scans, a mesh can be generated for the domain on which the underlying PDE system is defined and solved, thereby allowing for the integration of patient-specific geometry into 3-D models.[30],[104]

2.6.2 One-Dimensional Models of Blood Flow

While 3-D models are the most comprehensive and accurate of the options in Figure 2.9, they are extremely computationally expensive, which is why their use is typically reserved for only small sections of the arterial system where the geometry of the underlying section is believed to have a significant effect on local haemodynamics; these include bends such as the ascending aorta and particular bifurcations like the common carotid bifurcation.[49],[62] For example, the calculated velocity vector and pressure fields near the vessel walls in the 3-D model can permit an accurate characterisation of the wall shear stress, the profile of which is widely regarded as an important contributor to vascular disease initiation and progression.[49],[95] Subject to certain simplifications, including the assumption of a specific radial velocity profile within the vessel and of a uniform pressure over the vessel's CSA, spatial 3-D models can reduced to uniaxial 1-D models. The list of the relevant simplifications and assumptions of the 1-D model can be found in Appendix D.

When benchmarked against their 3-D model counterparts[28],[29],[104],[106] as well as *in-vitro* measurements,[107]–[109] 1-D models have shown a great capacity for capturing the pressure and flow waveforms arising from the arterial pulse at a significantly reduced computational cost compared to 3-D models (by about three orders of magnitude[110]), thus allowing the haemodynamic simulations to be extended to larger sections of the arterial network. Nonethe-

less, the governing equations for the 1-D model are still in the form of a non-linear PDE system (see Section 3.3), and thus 1-D models remain a computationally intractable option for modelling blood flow within a network with a large number of vessels, such as in the microvasculature (see Chapter 3).

2.6.3 Zero-Dimensional Steady-State Models of Blood Flow

On the other end of the spectrum, low-dimensional models like the 0-D steady-state model and compartmental models require relatively modest computational resources. In the 0-D steady-state model, flow (Q) inside the vessel is assumed to be solely governed by the blood pressure difference (ΔP) between its two ends and the Hagen-Poiseuille resistance ($\mathcal{R}$), according to the linear relationship in Equation (2.1). The vessel network can then be represented as a graph comprising a collection of edges, denoting the vessels weighted by their resistances, each of which connects a pair of nodes representing the locations where vessels bifurcate, converge, or end. Coupling the linear Hagen-Poiseuille flow relationship with conditions of flow conversation and static pressure matching at the nodes then yields a simple linear system that can be used to solve for the steady-state pressure at the nodes, and thus for the steady-state flow through the vessels according to Equation (2.1), with a drastic reduction in geometry, computational complexity, and required number of variables when compared to the high-dimensional options. This approach, however, assumes a response that is instantaneous and fixed throughout the network, and thus cannot capture the dynamic effects of flow, such as the blood flow transit time arising due to the compliant behaviour of the vessel walls (*i.e.*, the ability of the vessel to expand or constrict), which have important implications on CBF characterisation (see Chapters 3 and 4).

2.6.4 Compartmental Models of Blood Flow

In compartmental (lumped parameter models), blood vessels with common attributes such as diameter, generation number, or structure of the vessel wall are effectively lumped together and partitioned into compartments. The compartmentalization can either be carried out over whole segments of the brain or only the terminal branches of the circulatory system; the latter case is utilised in a multiscale framework to provide appropriate terminal BCs for 1-D or

3-D vessel network models of the macrocirculation in lieu of a detailed representation of the microvasculature branchings. Owing to the similarities between the cardiovascular system and electric circuitry, well-established methods for electric circuit analysis are often applied in this context.[111] Perhaps the most popular member of this family is the Windkessel model, shown in Figure 2.9(b), where the relevant compartment is taken to be comprised of a resistance element to account for the viscous losses of the blood fluid, and a capacitance element accounts for the vessel's ability to 'store' or 'discharge' blood due to the movement of the elastic wall.

The aim behind these models is to develop the simplest representation that captures the complex behaviour of the haemodynamic system, typically via a coupled system of ODEs and algebraic equilibrium relations. Such a flexible and simple description makes it a powerful tool for cerebrovascular modelling, and indeed one that has been thoroughly utilised, establishing the first models of cerebral blood flow,[112] and helping explain evidence from clinical trials[105],[113] and measurements from functional imaging techniques.[114],[115] From the modelling approaches illustrated in Figure 2.9, the compartmental approach is the one that has been extensively, and to the best of our knowledge, exclusively utilised to model for the processes of dCA and CBF control in the vasculature (see[86],[116]–[124] for examples), where in response to perturbations in flow or pressure, the control feedback mechanisms would modify one of the compartments' lumped properties, typically the compliance.

We briefly describe one example of a compartmental model of cerebral haemodynamics that incorporates dCA through a compliance feedback response. We choose the model developed by Ursino et al.[123], because the models developed by Ursino and colleagues have been highly influential in providing a solid foundation for modelling cerebral haemodynamics, and because we use some of the proposed approaches and constitutive relations in our model. The model incorporates a simplified biomechanical representation of the cerebrovascular bed, including the large intracranial arteries, the pial arterial-arteriolar vessels, the cerebral veins, CSF production and reabsorption processes, and the craniospinal storage capacity. Figure 2.10 shows the mechanical analogue of intracranial dynamics according to the model.

Blood flow enters the large cranial arteries, at a pressure equal to the systemic arterial pressure (P_a). This segment consists of a constant resistance (R_{la}), which accounts for the pressure

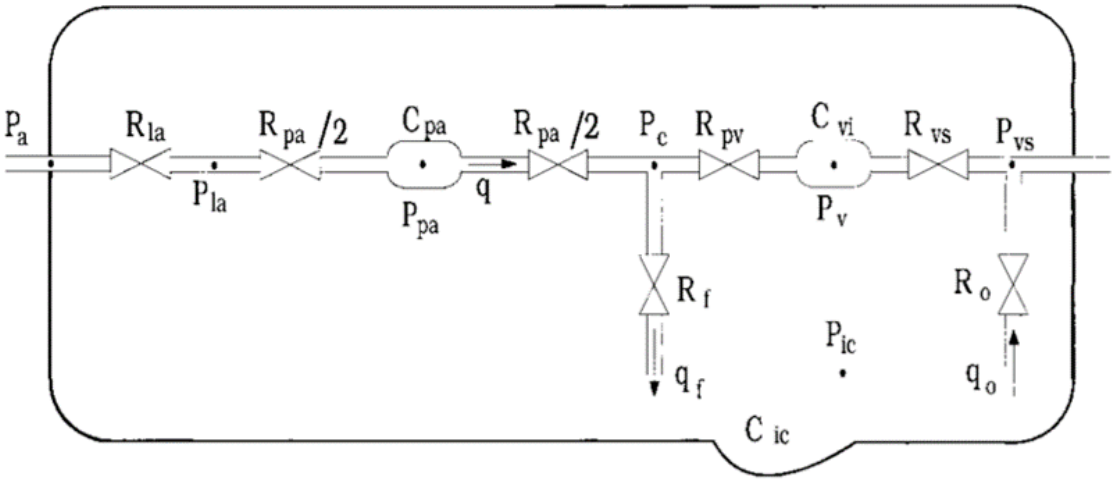

Figure 2.10: The mechanical analog of intracranial dynamics according to the presented model. Reproduced without change from[123].

drop in the pial arterial pressure (P_{la}). Blood then enters the pial arterial-arteriolar segment comprising multiple blood vessel generations, from the large pial arteries down to and including the small pial arteries and parenchymal arterioles. The whole segment is characterised by its values of compliance (C_{pa}) to account for the storage of cerebral blood volume (CBV), and hydraulic resistance (R_{pa}), which accounts for pressure drop to capillary pressure (P_c), and is where the CBF regulation is modelled to take effect.

At the capillary level, CSF is produced through a CSF formation resistance (R_f). Blood then passes through the venous cerebrovascular bed, described by the series arrangement of two segments. The first extends from the small postcapillary venules down to the large cerebral veins and includes the venous resistance (R_{pv}) and the intracranial venous capacity (C_{vi}). The second segment represents the terminal intracranial veins (lateral lakes and bridge veins) and is represented by a single hydraulic resistor (R_{vs}). Finally, CSF is reabsorbed at venous sinus pressure (P_{vs}) through CSF outflow resistance (R_o). The intracranial pressure (P_{ic}) is governed by the volume stored in the intracranial capacitor (C_{ic}), arising from the balance of CSF inflow (q_f), CSF outflow (q_o), and blood volume changes in pial arteries and veins.

Because cerebral veins behave passively, their blood volume (V_{vi}) variations can be solely ascribed to changes in transmural pressure:

$$\frac{dV_{vi}}{dt} = C_{vi}\left(\frac{dP_v}{dt} - \frac{dP_{ic}}{dt}\right) \tag{2.5}$$

In contrast, changes in the CBV in the arterial-arteriolar pial segment (V_{pa}) can be ascribed to both transmural pressure changes and the action of cerebrovascular control mechanisms:

$$\frac{dV_{pa}}{dt} = C_{pa}\left(\frac{dP_{pa}}{dt} - \frac{dP_{ic}}{dt}\right) + \frac{dC_{pa}}{dt}\left(P_{pa} - P_{ic}\right) \tag{2.6}$$

The first term in the right-hand side of Equation (2.6) corresponds to passive blood volume changes, ascribed to transmural pressure alterations, whereas the second term accounts for active volume changes as a result of the autoregulatory control mechanisms that modify the pial arterial-arteriolar compliance.

In this model, two distinct control mechanisms are considered: flow-mediated dCA, to account for the metabolic response, and CO_2 reactivity to account for the response of the cerebral vasculature to CO_2 gas levels, as illustrated in Figure 2.11. The input quantity for autoregulation is flow percentage change (ΔCBF), while the input quantity for CO_2 reactivity is the logarithm of CO_2 partial pressure ($\Delta P_{aCO_2} = log_{10}\frac{P_{aCO_2}}{P_{aCO_2 n}}$). The dynamics of each mechanism are reproduced by means of a gain factor (G) and a first-order low-pass filter with time constant τ. The gain factor of CO_2 reactivity is multiplied by the corrective factor A_{CO_2} to account for the dependency of the strength of CO_2 reactivity on CBF levels during ischaemia. Finally, autoregulation and the CO_2 reactivity response interact nonlinearly through a sigmoidal static relationship, thus producing changes in pial arterial-arteriolar compliance. The sigmoidal relationship accounts for the existence of maximal limits for the vascular response. The volume, and thus the resistance of the arterial-arteriolar pial segment (since the two are related by geometrical laws), is then set by the relationship in Equation (2.6).

Ultimately, however, compartmental models do drastically simplify the brain geometry and do not include any morphological details about the interconnectivity of the vessel network, or the attributes and responses of the individual vessels, the characterisation of which is crucial, given the strong coupling between the haemodynamics of blood flow, and the precise vascular architecture[26],[125]. Hence, compartmental models do come with their limitations, particularly regarding modelling the microvasculature comprising the sub-cortical arterioles, capillaries, and venules, where the majority of the brain's vascular length is found, and where our understanding of blood flow control remains incomplete.[27] As Cassot et al.[26] have re-

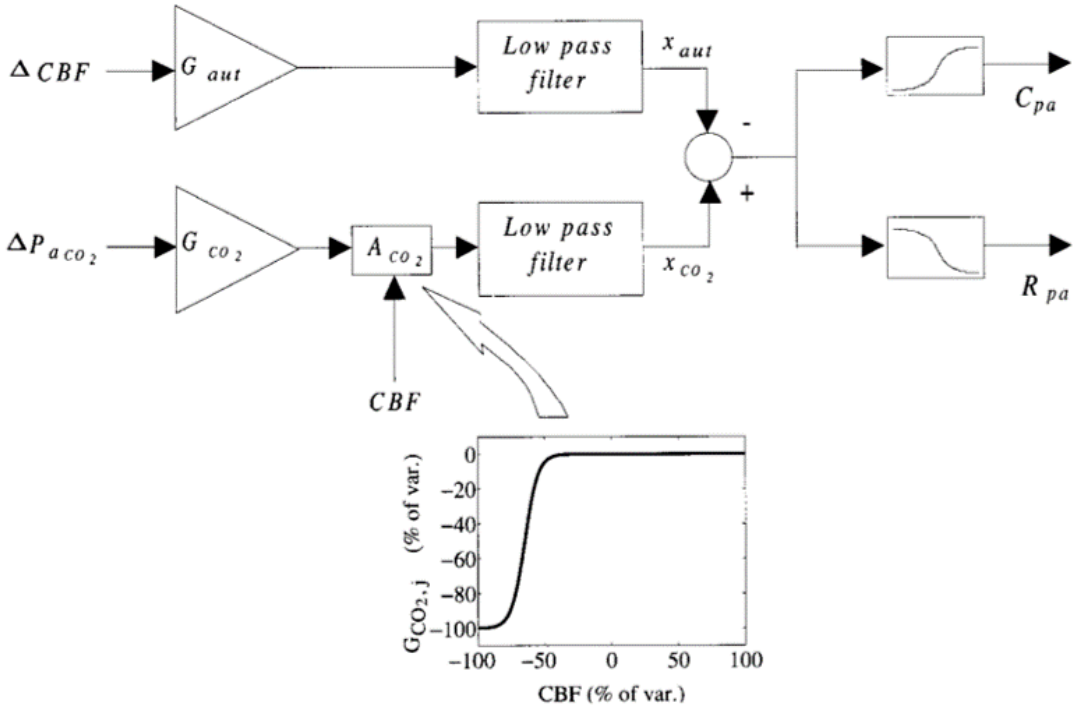

Figure 2.11: Block diagram describing the action of cerebrovascular regulation mechanisms. The upper branch describes autoregulation, while the lower branch indicates CO_2 reactivity. Reproduced without change from[123].

marked: "All the details of the vascular geometry, including the capillary net, the arterial and venous trees, need to be considered to analyse the flow field in the organ." The limitations and drawbacks of compartmental models in the particular context of modelling the dCA mechanisms are discussed in Chapter 3.

2.6.5 Continuum Models Using Homogenisation theory

Finally, one more relevant approach for modelling CBF in the cortical capillary bed is homogenisation. With homogenisation, the microscopic properties and details of the capillary architecture are implicitly represented via an effective parameter, the permeability tensor ($\mathbf{K}$), that characterises the aggregate of small-scale contributions of the capillary vessels on the flow and pressure fields at a larger mesoscopic scale. Homogenisation eliminates the need for an explicit, discrete representation of the capillary bed architecture at the level of the individual vessel, and suppresses the effects of BC allocation[126],[127] which have a strong impact on the haemodynamic simulations,[43],[67] thereby permitting the assembly of larger models of the capillary bed that could be compared with results from imaging data. Homogenisation theory has been previously used[41],[128],[129] to model the capillary bed as a porous medium,

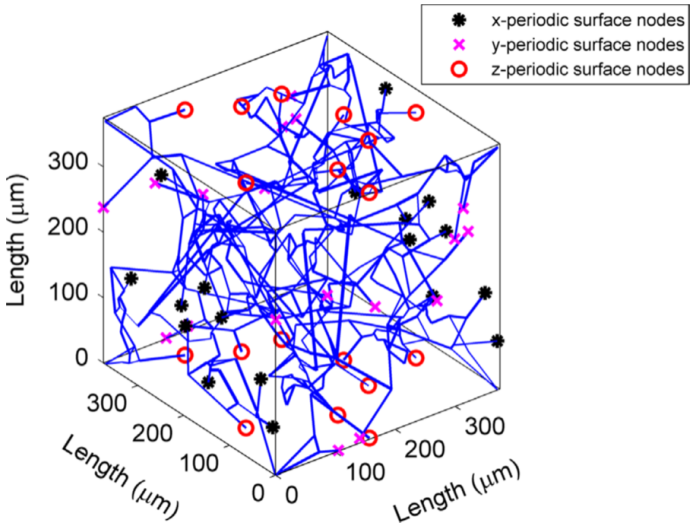

Figure 2.12: A statistically generated capillary network in a cube with 375 μm side length with the additional constraint of spatial heterogeneity. Reproduced without change from[41].

in which the macroscale flow is described using a volume-averaged form of Darcy's law[128]:

$$\mathbf{u}_c = -\mathbf{K}\nabla P \tag{2.7}$$

where $\mathbf{u}_c$ is the volume averaged capillary velocity, $\mathbf{K}$ is the capillary permeability tensor $(m^3 s/kg)$, and ∇P is the gradient of the spatially averaged pressure field at the mesoscopic scale. Such averaged representation is valid for the capillary bed since it exhibits a mesh-like, interconnected periodic structure with no structural correlation to the location of the cortical penetrating columns, one that is homogeneous and space-filling above a characteristic length of $25 - 75\mu m$,[130]–[132] as is required by the homogenisation procedure.[41],[128] One of the advantages of such representations is that they lend themselves nicely to the assimilation of numerical or experimental data obtained over small volumes[133]; for instance, values for the $\mathbf{K}$ entries have been acquired via numerical simulations over small periodic cubes which are anatomically representative of networks of the capillary bed,[41] one example of which is shown in Figure 2.12. The numerical simulations have revealed that $\mathbf{K}$ is isotropic and diagonally dominant, which greatly simplifies the FV numerical derivations in Chapter 4

2.7 Summary

In this literature review, we have provided a brief overview of the structure and function of the human brain, before describing the cerebral circulation, with a particular focus on the microvasculature. We have outlined the different zones of the microvasculature, which are distinguished from one another primarily by the morphology of the mural cells surrounding the vessels, and with the understanding that these zones do not form discretised regions but rather represent a continuum of vascular and mural cell morphologies. We then described the processes governing CBF control in the arteriolar vessels, including the myogenic, endothelial, metabolic and neurogenic mechanisms, which alter the VSM tone in the vascular walls and thus modify the pressure-radius relationship of the vessels. Next, we examined the composition of blood, and the important rheological implications arising from the interactions of the RBCs with the fluid plasma and the vessel walls. In particular, we described how an effective, or apparent viscosity can be obtained as a function of the vessel diameter and haematocrit content from *in-vivo* empirical formulations, which are to be used in the next chapters. Finally, we outlined the general modelling approaches available for conducting haemodynamic simulations, which include 3-D, 1-D, steady-state 0-D, and compartmental models, as well as upscaled homogenised representations of the capillary bed, and outlined the advantages, limitations, and general uses of each. We described one example of a compartmental model that incorporates CBF and regulation feedback mechanisms, which in turn paves the way for discussing the models of dynamic CBF and control in the next chapters.

Chapter 3

A Network-Based Model of Dynamic Cerebral Blood Flow and Autoregulation

Abstract

Cerebrovascular diseases continue to be among the leading causes of morbidity and mortality in humans. Abnormalities in dCA have been implicated in many of these disease conditions. Accurate models are therefore needed to better understand the complex pathophysiology behind impaired dCA. We thus present here a simple framework for modelling a vessel-driven network model of dCA in the microvasculature, as opposed to the conventional compartmental modelling approach. Network models incorporate the actual connectivity and anatomy of the vasculature, thereby allowing us to include and trace changes in the calibre and morphology of individual vessels, investigate the spatial specificity and heterogeneity of the various control mechanisms to help disentangle their contributions, and link the model parameters to the actual network physiology. We incorporate the proposed control feedback mechanisms at the level of the individual vessel, and solve for the dynamic pressure and flow fields within a simple vessel network. In response to an upstream pressure drop, the network is found to be able to recover CBF while exhibiting the characteristic autoregulatory behaviour in terms of changes in vessel calibre and the biphasic flow response. We assess the feasibility of our formulation in larger networks by comparing the simulation results to those obtained using a one-dimensional (1-D) model of CBF applied to the same microvasculature network and find that our model results are in very good agreement with the 1-D solution, while significantly reducing the computational cost, thus enabling more detailed models of network behaviour to be adopted in the future. Accurate and computationally feasible models of dCA that are more representative of the vasculature can help increase the translatability of haemodynamic models into the clinical environment, which would help develop more informed treatment guidelines for patients with cerebrovascular diseases.

3.1 Introduction

Abnormalities in dCA have been implicated in various cerebrovascular diseases. A thorough understanding of the processes that govern dCA is thus required to gain greater insight into the link between dCA impairment and the associated cerebrovascular pathologies. This is particularly true in the microvasculature, an area that has received relatively little attention due to issues pertaining to access, complexity, and scale.

In response to physiological perturbations, the dCA feedback mechanisms act to change the wall stiffness (or its inverse, the compliance),[2] and hence the diameter, of the autoregulatory microvessels. Models of dCA within a vascular network have adopted a wide range of complexity, but they all more or less rely on the same fundamental compartmental approach described in Section 2.6. Compartmental models, however, do not include any morphological details regarding the attributes and responses of individual microvessels, which become relevant when attempting to model the mechanisms responsible for dCA, as well as the associated pathological conditions, such as vessel occlusion or remodelling of mural cell coverage, all of which predominantly occur at the level of the individual vessel.[2],[17],[27] A key requirement for the understanding of cerebrovascular diseases is studying the vascular response, as well as the acute and chronic changes in the vasculature structure, in response to physiological challenges and diseases.[16] Altered vascular properties, including diameter, branching pattern, and tortuosity, are closely and reciprocally correlated with cerebrovascular diseases such as atherosclerosis and stroke,[134],[135] with altered brain vessel status shown to be both a potent biomarker and predictor[18],[136] as well as a potential outcome[17],[137] of cerebral pathologies.

Consistent with this concept, compartmental models are also unable to account for the microvasculature's spatial heterogeneity (see[78],[138]–[140]) and its complex interconnectivity, and thus cannot be used to investigate the complex interplay between the various CBF regulating mechanisms across the different vessel generations covering a wide range of length scales. In addition, lumped models cannot be used to examine the flow patterns in the microvasculature, alterations in which have been theorized and shown to be implicated in disease conditions.[141]–[144] Network models of the microvasculature can help to predict the pressure and flow profiles in the smaller vessels, thereby shifting the role of microvasculature modelling from merely providing the BCs for the larger vessels, to being actively studied in normal and

diseased conditions, when examined either in isolation or as part of multi-scale efforts that is aimed towards capturing the strong interactions between components at different length scales.

Even when the focus is on the physically measurable waveforms in the larger vessels, such as the pressure and flow waveforms, which are of a high diagnostic significance,[62] an accurate characterisation of the local microcirculation topology, with its specific wave transmission and reflection properties, is still crucial, given the strong coupling between the global haemodynamics of CBF, and the precise vascular architecture.[26],[108],[125],[145] A proper representation of the terminal branches is warranted to ensure accurate wave propagation and reflection at the macro-micro circulation interface. Indeed, elementary lumped models of the microvasculature were unable to capture important features such as pressure wave propagation effects[62],[146]–[148] when compared to their arterial tree counterparts, even when including a compliant element to account for the delay in response or when directly specifying the equivalent reflection coefficient. In the particular context of cerebral haemodynamic modelling, the importance of a detailed tree of the cerebral arteries on wave reflections was first recognized by Avolio[149] and later recognized by Reymond et al.,[108] who showed that the predicted waveforms in the carotid artery are strongly affected by the presence of a detailed model of the cerebral circulation. The effects of lumped cerebral representation on the pressure and flow waveforms in the aorta were less affected by whether or not an arterial tree representation was present, implying that while a detailed description of the cerebral circulation may not be necessary when the scope of the model is confined to the larger systemic circulation, it becomes important to incorporate a sufficient representation of the cerebral vasculature when the focus is on the regional cerebral haemodynamics.

While compartmental models have agreed reasonably well in some respects with experimental data, there have been some discrepancies noted by authors. For instance, Zheng[150] highlighted some disagreements between simplified compartment models and experimental data acquired at high temporal resolution with invasive optical measurements of haemoglobin and blood flow changes. While increasing the number of compartments statistically improved the fit to experimental data and provided more reliable estimates of the haemodynamic response[150],[151], the compartmental models were still not capable of describing spatial characteristics of the haemodynamic response[103], such as the surround negativity response[138],[139]

and the negative BOLD signals[78],[140], observed in the cortex with optical imaging.

Indeed, in some cases, adding extra elements and compartments to the lumped representation can provide a better fit with microcirculation dynamics.[152] However, the addition of extra components makes the identification of the model parameters from the limited measurements more difficult and less robust. As more elements are included, the regression analysis that is normally conducted for parameter identification becomes non-trivial,[153] starts producing poor results, and is often replaced by a trial and error procedure that seeks to obtain an acceptable combination of parameters from an initially identified reasonable range.[111] In such cases, more than one set of parameters can satisfy the limited data supplied, and indeed the values adopted by different researchers show enormous differences and inconsistencies.[111] There is no way to tell which set of parameters is correct, because their values are only supposed to capture the aggregate properties of the different vessel generations, and hence they lack any physical interpretation or quantitative connection to the actual network physiology, such as measured lengths, diameters and mechanical properties of the constituent vessels. The percentage changes in the values of the lumped parameters are often calibrated based on experimental data[154],[155] that measure the response of individual vessels to changes in pressure and flow.[105],[118],[156] Accordingly, the compartmental models presume that the haemodynamic changes caused by the collective response of a particular segment in the vasculature can directly translate into changes in the effective parameter of the representative compartment. The relationship between the lumped parameters and the characteristics of the haemodynamic response, however, is unknown, and thus the accuracy of any estimates obtained from these models is uncertain.[103]

The percentage changes in vessel diameters in response to changes in flow or pressure, their time constants, and the relative contributions of the various dCA mechanisms are highly heterogeneous, depending on the vessel size, generation, and brain region.[141],[154],[157]–[162] For instance, experimental data[154],[161],[162] indicate that there is a hierarchy of responsiveness by arterioles that is dependent on both the size and type of the microvessel as well as the systemic arterial pressure. On the other hand, a single compartment in a lumped model can often contain many vessel generations.[55] What is needed are network models of the microvasculature that assign realistic vessel geometry and properties to the individual vessels; these, in turn, can be useful in the parameter setting of the lumped models.

Networks models of CBF have been constructed before; see[42],[62],[79],[103],[148],[163] for examples. Such models incorporating information about the geometries and connectivities of the vessels provide a much better characterisation of the flow and pressure distributions within the microvasculature networks, and how these distributions dynamically change in response to various stimuli. Indeed, a comparison of purely topological characteristics of the cerebral microvasculature with flow-based ones shows that a combined interpretation of flow and topology is indispensable.[45] For instance, the influence of localized changes on surrounding vessels was demonstrated in the simple network model by Boas et al.,[103] in which the dilation in one vessel causes a local increase in flow but a decrease in flow in other vessels. However, none of the previous network models explicitly models the active dynamic processes that govern the haemodynamic response. While models of dCA within an individual vessel have been constructed (see[116],[124] for examples), these single-vessel models do not account for the network effects.[67]

We thus construct a simple framework for modelling a vessel-driven network model of dCA, assembled from the actual connectivity and anatomy of the microvasculature under consideration. The different mechanisms of dCA adjust CBF by controlling the level of VSM tone, changing the stiffness (or compliance) of the vessel wall, and thereby adjusting the pressure-radius relationship of the vessel.[2],[79] At this stage, we include the myogenic and endothelial responses, and reserve the calibration of the two feedback pathways with experimental data, as well as incorporating other mechanisms, to Chapters 5 and 6.

Since the small cerebral arteries and arterioles have the largest fraction of VSM cells among the blood vessels, they are the primary vessels that control CBF[2],[164] (although the role of the capillary pericytes is becoming increasingly recognised; see[5],[76]–[78],[165]). Arterioles respond to changes in both shear stress and intraluminal pressure.[155] The shear stress response is caused by the viscous friction between the flowing blood and the endothelial wall,[2],[155],[166] and leads to VSM relaxation, inducing vasodilation. Meanwhile, the myogenic response is caused by increased transmural pressure and has a constrictive effect[155],[167] which interacts competitively with the endothelial response. Essentially, it is the balance between vasoconstricting and vasodilating factors that controls the wall stiffness by controlling the degree of VSM phosphorylation in the arteriolar walls.[2],[82]

We first describe how the fundamental haemodynamic principles are used to derive the equations for the dynamic pressure and flow fields throughout a network model of the microvasculature. Next, we describe the compliance feedback model through which the dCA mechanisms are incorporated, thereby allowing the vessels to respond to perturbations in pressure. We briefly describe the 1-D network model used as a benchmark test case to assess the accuracy of the proposed model. We then show how our model can be applied to a simple bifurcating network in response to a drop in inlet pressure, and examine the associated errors and differences in computational cost when comparing the results to those obtained from the 1-D model. This validation is important in ensuring that the computational cost of a network-based model of autoregulation is not prohibitive, which would be the case when using a 1-D model. We then conduct a global sensitivity analysis to quantify the relative importance of the compliance input parameters on the model output variables. Finally, we discuss the results, assumptions and limitations of the proposed model, and how the network model paves the way for developing the multiscale model in Chapter 4.

3.2 Materials and Methods

In this section, we first derive an approximate analytical solution for the dynamic pressure and flow fields within a single compliant vessel, and obtain a relationship between the vessel inlet and outlet pressures and flows that is similar to the one presented in the previous work of Payne and El-Bouri.[79] However, to account for the effects of the dCA mechanisms on the pressure and flow fields within the vessel, the new derivation proposed in this chapter accommodates the additional degree of freedom of a dynamically changing vessel compliance that changes in response to the feedback mechanisms, giving rise to an additional term in the final expressions for the vessel inlet and outlet flows when compared to the similar derivation which has assumed a static vessel compliance.[79] We also propose a simple feedback formulation to reproduce the effects of the myogenic and endothelial mechanisms, which, in response to changes in transmural pressure and wall shear stress, respectively, alter the wall stiffness, and hence compliance, of the autoregulatory vessels. By changing the compliance, the relationship between the vessel diameter and transmural pressure is altered, allowing the vasculature to establish a new equilibrium state in response to changes in ABP.[82] The ensuing changes in the vessel resistance and compliance in response to perturbations in blood

pressure then act to restore flow within the vessel.

3.2.1 The Governing Haemodynamic Equations

The cross-sectional (CS) area-averaged equation for mass conservation within a compliant vessel is given by[168]:

$$\frac{\partial Q}{\partial x} + \frac{\partial A}{\partial t} = 0 \tag{3.1}$$

where the flow rate (Q) is the integral of the axial velocity over the CS area (A). Similarly, the momentum conservation equation can also be written in its CS area-averaged form.[168] Since the advection term can be effectively ignored throughout the cerebral vasculature,[4],[79] the momentum equation can be reduced to a linear form and transferred into the frequency domain (see[169]), which, under the relevant assumptions (see Appendix D) simplifies to the generalised Darcy's law[169]:

$$\hat{Q}(x,\omega) = -\frac{\overline{A}\mu}{i\omega\rho}\Big[1 - \frac{2J_1(i^{3/2}\alpha)}{i^{3/2}J_0(i^{3/2}\alpha)}\Big]\frac{\partial \hat{P}(x,\omega)}{\partial x} \tag{3.2}$$

where P is the uniform pressure over the CS, μ is the dynamic viscosity of blood, $\rho = 1040$ kgm^{-3} is the blood density, and the hat denotes that the variables are transformed into the frequency domain. We will assume hereon that ρ and the gravity vector $(\mathbf{g})$ are constant within the cerebral microcirculation, as is customary in cerebral haemodynamic modelling studies,[81],[133] such that the pressure in all equations is defined as the fluid pressures minus the hydrostatic pressures. J_0 and J_1 are Bessel functions of the first kind of order zero and one, respectively. The Womersley number is denoted by $\alpha = R\sqrt{\frac{\omega}{\nu}}$ (where ν is the kinematic blood viscosity), and is a dimensionless ratio of the oscillatory forces to the viscous forces. In practice, a common approximation when applying the Womersley model for blood flow in a compliant vessel is to use a time (and occasionally also space) averaged CS area ([62],[147],[169],[170]), denoted here as $\overline{A}$, to maintain linearity in the frequency domain. $\overline{A}$ is usually obtained after running 1-D flow simulations in the time domain under the same initial and BCs and network properties and averaging the CS area profile for each vessel or using the CS area of the vessel at the mean arterial pressure (MAP).

We use the *in-vivo* empirical model[100] in Equation (2.4) to approximate the effective viscosity relative to plasma (μ_{rel}) based on the vessel diameter in μm (D) and the discharge haematocrit (H_D). For simplicity, H_D is assumed here to have a uniform value of 0.42, an assumption that is discussed in Section 3.5. To close the loop, we need a relationship that relates the changes in the transmural pressure ($P_t = P - P_{ext}$) to those in the CS area, which is commonly known as the tube law. Many different formulations for this tube law have been used in previous studies; see[171] for a general summary. In this study, we will consider the relations which are derived from linear elastic theory (see Appendix A.1). One pressure-area relationship that has been extensively used[107],[170],[172]–[175] is given by Equation (3.3):

$$P_t = \beta \left(\sqrt{A} - \sqrt{A_{ref}} \right) \tag{3.3}$$

where A_{ref} is the reference CS area at zero transmural pressure. The parameter β characterises the material properties of the vessel, and is given by:

$$\beta = \frac{4\sqrt{\pi} E h}{3 A_{ref}} \tag{3.4}$$

where h is the vessel thickness and E is the Young's modulus of the vessel wall.

Another tube law that has been used is the compliance law (see[62],[108],[123],[145],[147],[148],[169],[176]). By definition, the vessel compliance (C) in the passive (non-autoregulating) case is given by:

$$C = \frac{dV}{dP_t} \tag{3.5}$$

which is often written in the more convenient form:

$$\frac{dV}{dt} = C \frac{dP_t}{dt} \tag{3.6}$$

where V is the vessel volume, the integration of the CS area over the vessel length (L). Similar to the assumptions made in deriving Equation (3.3), the expression for baseline compliance

(C_0) around the baseline radius (R_0) can be derived from combining Laplace's law for cylindrical vessels with the constitutive relation for linear elastic and incompressible wall material behaviour (see Appendix A.1), giving rise to the independent ring model[169],[177]:

$$C_0 = \frac{3\pi R_0^3 L}{2Eh} \tag{3.7}$$

We can obtain an expression for C in terms of β around the baseline radius R_0 (assuming uniform CS area such that $V \approx LA$) by applying the definition of compliance in Equation (3.5) to the non-linear formulation in Equation (3.3) to get:

$$C = \frac{\partial V_{|_{V_0}}}{\partial P} = \frac{2\sqrt{LV_{|_{V_0}}}}{\beta} \tag{3.8}$$

Note that we can obtain this relation between C and β via linearization of the pressure-area relationship in Equation (3.3) around the baseline CS area and then applying the definition of compliance in Equation (3.5) to the linearized approximation.

The compliance tube law can be adapted to accommodate the active case where the vessel stiffness can change due to the action of the dCA mechanisms. We use the equation proposed by Ursino et al., which successfully reproduced the qualitative effects of the regulatory mechanisms in their lumped compartmental model.[123] The equation can be applied locally at each CS area to account for the pressure variation across the vessel length to give:

$$\frac{\partial A(x,t)}{\partial t} = \frac{1}{L}\left(C(t)\frac{\partial P_t(x,t)}{\partial t} + \frac{dC(t)}{dt}P_t(x,t)\right) \tag{3.9}$$

Based on Equation (3.9), we distinguish between two vessel types. Non-regulating vessels have a constant C, and hence only react passively to changes in P_t. On the other hand, in regulating vessels, C is dynamically modified by the actions of the cerebral control mechanisms. Hence, the change in the CS area can be ascribed to both the passive response to P_t changes and the action of control mechanisms on C. To maintain linearity when working in the frequency domain, we assume that the perturbations in P and C for each vessel occur about their baseline conditions:

$$P_t(x,t) \approx \overline{P_t} + \tilde{P}_t(x,t) \tag{3.10}$$

$$C(t) \approx \overline{C} + \tilde{C}(t) \tag{3.11}$$

where $\overline{P_t} = \overline{P}_v - \overline{P}_{ext}$ and $\overline{P}_v$ denotes the average baseline intraluminal pressure inside the vessel. The three governing haemodynamic principles in Equations (3.1), (3.2), and (3.9) can then be combined together (see Appendix A.2) to obtain the second order harmonic oscillator partial differential equation (PDE) for P_t:

$$-\left(\frac{i^{3/2}\alpha J_0(i^{3/2}\alpha)}{i^{3/2}\alpha J_0(i^{3/2}\alpha) - 2J_1(i^{3/2}\alpha)}\right)\left(\frac{\omega^2\rho}{\pi R^2 L}\right)\left(\overline{C}P_t + \overline{P_t}C\right) = \frac{\partial^2 P_t}{\partial x^2} \tag{3.12}$$

We conduct perturbation analysis to obtain an approximate solution for the PDE in Equation (3.12). The analysis is similar to the one presented in the previous work of Payne and El-Bouri,[79] with the difference being that the tube law used here accommodates dynamic compliance. The first step in the perturbation analysis is to assign a non-dimensional perturbation parameter ϵ, defined as:

$$\epsilon = i^{3/2}\alpha \tag{3.13}$$

This parameter should be sufficiently small ($\epsilon << 1$), meaning the analysis is only valid for vessels with a sufficiently small diameter ($D \lesssim 1mm$).[79] The next step is to perform an asymptotic series expansion of the pressure variable (dropping the t subscript for now), such that the solution can be broken into a solvable, or zeroth order part and perturbative parts of successively higher orders of ϵ.

$$P = P_0 + \epsilon P_1 + \epsilon^2 P_2 + ... \tag{3.14}$$

Successive terms in the series at higher powers of ϵ become smaller when ϵ is sufficiently small, and thus an approximate perturbation solution is obtained by truncating the series, usually

after the second-order solution. Hence, Equation (3.12) can be written as:

$$\epsilon^5 J_0(\epsilon)\left(\frac{\nu\mu}{\pi R^6 L}\right)\left(\overline{C}(P_0+\epsilon P_1+\epsilon^2 P_2+...)+\overline{P}C\right)$$
$$=\big(\epsilon J_0(\epsilon)-2J_1(\epsilon)\big)(\frac{\partial^2 P_0}{\partial x^2}+\epsilon\frac{\partial^2 P_1}{\partial x^2}+\epsilon^2\frac{\partial^2 P_2}{\partial x^2}+...) \qquad x\in[0,L] \tag{3.15}$$

where we used the fact that ($\epsilon^4=-R^4(\frac{\omega}{\nu})^2$), according to Equation (3.13). We next use the series expansion of the Bessel functions:

$$J_0(\epsilon)=\Sigma_{k=0}^{\infty}\frac{(-1)^k}{2^{2k}(k!)^2}\epsilon^{2k}=1-\frac{\epsilon^2}{4}+\frac{\epsilon^4}{64}-... \tag{3.16}$$
$$J_1(\epsilon)=\Sigma_{k=0}^{\infty}\frac{(-1)^k}{2^{2k+1}(k!)(k+1)!}\epsilon^{2k+1}=\frac{\epsilon}{2}-\frac{\epsilon^3}{16}+\frac{\epsilon^5}{384}-... \tag{3.17}$$

to arrive at the following expression:

$$\epsilon J0(\epsilon)-2J_1(\epsilon)=\Sigma_{k=0}^{\infty}\frac{(-1)^k}{2^{2k}(k!)^2}\epsilon^{2k+1}\frac{k}{k+1}=\epsilon^3\left(-\frac{1}{8}+\frac{\epsilon^2}{96}-\frac{\epsilon^4}{3072}+...\right) \tag{3.18}$$

Non-dimensionalizing the length variable in Equation (3.15) and inserting the series expansion for the Bessel functions, we obtain:

$$\frac{\nu\mu L}{\pi R^6}\epsilon^2\left(1-\frac{\epsilon^2}{4}+...\right)\left(\overline{C}(P+\epsilon P_1+\epsilon^2 P_2+...)+\overline{P}C\right)$$
$$=\left(-\frac{1}{8}+\frac{\epsilon^2}{96}-...\right)(\frac{\partial^2 P_0}{\partial x^2}+\epsilon\frac{\partial^2 P_1}{\partial x^2}+\epsilon^2\frac{\partial^2 P_2}{\partial x^2}+...) \qquad x\in[0,1] \tag{3.19}$$

Equation (3.19) is a nested sequence of problems corresponding to different powers of ϵ. We make the usual assumption that the BCs, which are the values for pressure at the inlet ($P_{in}=P(x=0)$) and the outlet ($P_{out}=P(x=1)$) of the vessel, are contained within the zeroth order solution, hence the BCs for all the higher order solutions are zero. Balancing the

coefficients of ϵ in terms of ascending powers of ϵ, we solve for the zeroth, first, and second order solutions for the pressure field in Equation (3.14) to obtain:

$$\hat{P}_0 = \hat{P}_{in} + (\hat{P}_{out} - \hat{P}_{in})x \tag{3.20}$$

$$\hat{P}_1 = 0 \tag{3.21}$$

$$\hat{P}_2 = -\frac{4\nu\mu L\overline{C}}{3\pi R^6}(P_{out} - P_{in})x^3 - \frac{4\nu\mu L}{\pi R^6}(\overline{C}P_{in} + \overline{P}C)x^2 + \frac{4\nu\mu L}{3\pi R^6}\big(\overline{C}(P_{out} + 2P_{in}) + 3\overline{P}C\big)x \tag{3.22}$$

The pressure solution can be reconstructed by summing the perturbation series given in Equation (3.14). Similarly, the flow field can then be calculated, using a power series expansion for the flow:

$$\hat{Q} = \hat{Q}_0 + \epsilon\hat{Q}_1 + \epsilon^2\hat{Q}_2 + ... \tag{3.23}$$

Substituting the solution for the pressure field into Equation (3.2), non-dimensionalizing the length variable, and balancing in terms of powers of ϵ, an expression for the flow field inside the vessel is obtained, just as we have done for the pressure field. The zeroth, first, and second order solutions for flow can then be given by:

$$\hat{Q}_0 = \frac{1}{\mathcal{R}}\hat{P}_0 \tag{3.24}$$

$$\hat{Q}_1 = 0 \tag{3.25}$$

$$\hat{Q}_2 = \frac{-1}{\mathcal{R}}\left(\frac{\hat{P}_0'}{6} + \hat{P}_2'\right) \tag{3.26}$$

where ($\mathcal{R} = \frac{8\mu L}{\pi R^4}$) is the Poiseuille resistance. We note from Equations (3.20-3.22) that the pressure profile at the vessel boundaries is sufficient to fully characterise the pressure and flow fields. Hence, we can more usefully simplify the 1-D flow solution into the 0-D solution by solving for the flow in Equations (3.24-3.26) at the vessel boundaries, and inserting the

solution back into Equation (3.23) to obtain:

$$\begin{pmatrix} \hat{Q}_{in} \\ \hat{Q}_{out} \end{pmatrix} = \frac{1}{\mathcal{R}} \begin{pmatrix} 1 & -1 \\ 1 & -1 \end{pmatrix} \begin{pmatrix} \hat{P}_{in} \\ \hat{P}_{out} \end{pmatrix} - \left[\frac{R^2}{6\nu\mathcal{R}} \begin{pmatrix} 1 & -1 \\ 1 & -1 \end{pmatrix} + \frac{\overline{C}}{6} \begin{pmatrix} -2 & -1 \\ 1 & 2 \end{pmatrix} \right] i\omega \begin{pmatrix} \hat{P}_{in} \\ \hat{P}_{out} \end{pmatrix} + \frac{\overline{P}}{2} i\omega C \begin{pmatrix} 1 \\ -1 \end{pmatrix} \tag{3.27}$$

To obtain an expression for the flow in the time domain, we take the inverse Fourier transform of Equation (3.27). Next, we rewrite the pressure terms in terms of intraluminal and external pressure $P_t = P - P_{ext}$. The end result is the final approximate analytical solution for the vessel inlet (Q_{in}) and outlet (Q_{out}) flows in terms of the inlet (P_{in}) and outlet (P_{out}) pressure profiles and the vessel properties:

$$\begin{pmatrix} Q_{in} \\ Q_{out} \end{pmatrix} = \frac{1}{\mathcal{R}} \begin{pmatrix} 1 & -1 \\ 1 & -1 \end{pmatrix} \begin{pmatrix} P_{in} \\ P_{out} \end{pmatrix} - \left[\frac{R^2}{6\nu\mathcal{R}} \begin{pmatrix} 1 & -1 \\ 1 & -1 \end{pmatrix} + \frac{\overline{C}}{6} \begin{pmatrix} -2 & -1 \\ 1 & 2 \end{pmatrix} \right] \frac{d}{dt} \begin{pmatrix} P_{in} - P_{ext} \\ P_{out} - P_{ext} \end{pmatrix} + \left(\frac{\overline{P}_v - \overline{P}_{ext}}{2} \right) \frac{dC}{dt} \begin{pmatrix} 1 \\ -1 \end{pmatrix} \tag{3.28}$$

Note that the steady-state term in Equation (3.28) exactly matches the Poiseuille flow solution, while the remaining terms, which depend on both the fluid and vessel properties, correspond to the dynamic flow behaviour due to the fluid-wall interaction. Note that in the passive case when C is constant, Equation (3.28) matches the one that has been derived previously[79]; the additional term arising from the current analysis accounts for the contributions of the dCA mechanisms on flow via the dynamically changing C. Also, note that the inlet and outlet flows can be swapped around and the formulation will remain the same, as would be expected. Finally, defining the vessel volume rate of change according to principles of volume conservation ($\frac{dV}{dt} = Q_{in} - Q_{out}$), and using the formulae for Q_{in} and Q_{out} from Equation (3.28), we get:

$$\frac{dV}{dt} = \overline{C}\left(\frac{P_{in} + P_{out}}{2} - P_{ext}\right) + \frac{dC}{dt}\left(\overline{P} - P_{ext}\right) \tag{3.29}$$

which is consistent with the tube law approximation in Equation (A11) that we used to derive the approximate analytical pressure and flow field solutions since integrating the zeroth order pressure from the perturbation analysis in Equation (3.20) along the vessel length gives the average of the inlet and the outlet pressures.

3.2.2 Compliance Feedback Model

To model the interaction between the myogenic and the endothelial responses, we assume a linear feedback model for the vessel relative stiffness k, with first-order low-pass dynamics:

$$T_k \frac{dk}{dt} = -(k-1) + S_\sigma \left(\frac{\sigma}{\bar{\sigma}} - 1\right) - S_\tau \left(\frac{\tau}{\bar{\tau}} - 1\right) \tag{3.30}$$

where S is the sensitivity, or gain factor, for the perturbations of each of the direct (σ) and shear (τ) stress from their baseline values, and T_k is the time constant, which for simplicity is assumed to be the same for both mechanisms (although this assumption is relaxed in Chapters 5 and 6). We approximate the intraluminal pressure as the average of the inlet and outlet pressures, as a result of integrating the zeroth order pressure solution from the perturbation analysis along the vessel length. The shear stress can be derived from force balance analysis in the quasi-steady state,[84] and thus can be given as a fraction of the baseline shear stress:

$$\frac{\tau}{\bar{\tau}} = \frac{R|P_{in} - P_{out}|}{\bar{R}|\bar{P}_{in} - \bar{P}_{out}|} \tag{3.31}$$

We then map the vessel stiffness into vessel compliance through a non-linear sigmoidal function, as proposed by Ursino et al.,[121] since compliance can only vary within set limits:

$$C = C_0 \left[1 + \frac{\Delta C^{\pm}}{C_0} tanh\left(\frac{1}{G}\frac{C_0}{\Delta C^{\pm}}\left(\frac{1}{k} - 1\right)\right)\right] \tag{3.32}$$

The maximum positive and negative changes in compliance, given by $\frac{\Delta C^{\pm}}{C_0}$, are different to account for the fact that compliance is not symmetrical about its baseline value.[105] The parameter G sets the central slope steepness of the sigmoidal dependence of compliance on stiffness. Figure 3.1 depicts a block diagram summarising the action of cerebrovascular reg-

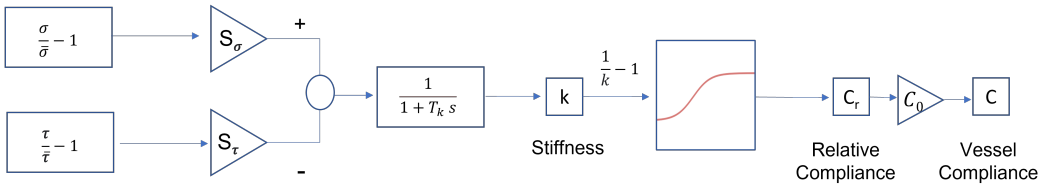

Figure 3.1: Block diagram describing the action of cerebrovascular regulation mechanisms in the present model. The upper branch describes the myogenic response, while the lower branch indicates the endothelial response. The input quantity for the myogenic and endothelial responses are the perturbations of the direct (σ) and shear (τ) stresses from their baseline values, respectively. The dynamics are simulated by means of a gain factor (S) for each mechanism and a first-order low-pass filter with time constant T_k. The wall stiffness is then non-linearly related to the compliance via a sigmoidal static relationship that sets the compliance relative to the baseline vessel compliance (C_0).

ulation mechanisms according to the present model.

3.2.3 Connecting the Network

We represent the cerebral microvasculature as a graph, comprising a collection of edges denoting the vessels, each of which connects a pair of nodes representing the locations where vessels bifurcate, converge, or end. To solve for the pressure and flow fields throughout the network, an appropriate choice of BCs relating to flow and pressure at the internal nodes where vessels meet is required. We assume conservation of flow at the nodes such that the inlet and outlet CBF into any internal node, according to Equation (3.28), from all vessels connected to the node, must balance at all times:

$$\sum_{j \in N} q_j = 0 \tag{3.33}$$

where the index j refers to any vessel connected to node N. We match the static pressures at the nodes where vessels meet since the difference between matching the static pressure and the total pressure in the microvasculature is minuscule and can effectively be ignored (see[79],[110] and Section 3.4). Hence, each node is associated with a pressure value, giving rise to a linear system of equations:

$$\boldsymbol{B}_{int}\frac{d\boldsymbol{p}_{int}}{dt} + \boldsymbol{A}_{int}\boldsymbol{p}_{int} = -\boldsymbol{B}_b\frac{d\boldsymbol{p}_b}{dt} - \boldsymbol{A}_b\boldsymbol{p}_b - \boldsymbol{C} \tag{3.34}$$

where the subscript b refers to the boundary (inlet and outlet) entries. We impose pressure

BCs ($\boldsymbol{p}_b$ and $\frac{d\boldsymbol{p}_b}{dt}$) at the external nodes where arterioles and venules enter and exit the network, and solve for the pressures at the internal nodes ($\boldsymbol{p}_{int}$). Each row in Equation (4.30) is a restatement of the zero net flow condition given in Equation (3.33) for each internal node. The $\boldsymbol{A}$, $\boldsymbol{B}$ and $\boldsymbol{C}$ matrix entries are populated according to the connectivity of the nodes and the dynamic vessel properties as per Equation (3.28).

3.2.4 Parameter Values

Given the heterogeneous composition and the anisotropic properties of the vessel walls,[95],[178] and the presence of structural support surrounding the vessels,[178]–[181] we use the experimentally derived values for the effective Young's modulus (Table 1) that capture the overall radial stretch of the microvessel walls in response to applied stresses. When used in 1-D flow simulations,[182] these values have generated wave propagation characteristics in complex microvascular networks that are in very good agreement with experimental data.[183]

Table 1: Values of the effective Young's modulus (E) in the microvasculature.

Vessel	E ($\times 10^5$ Pa)	Source
Capillary	3.70	[181]
Venule	3.88	[181]
Arteriole (Diameter $\geq 20\mu m$)	6.3	[184]
Arteriole ($15\mu m \leq$ Diameter $< 20\mu m$)	2.6	[184]
Arteriole (Diameter$< 15\mu m$)	1.6	[184]

Since Kontos et al.[154] reported a time constant of about 5-20 seconds for the arteriolar dilation in response to acute hypotension, and in line with Ursino's choice of a time constant for pressure-dependent autoregulatory mechanisms,[121] we use a value of T_k=10 seconds. The maximum changes in compliance are taken directly from Ursino's model.[105]

There is, however, no clear validation from experimental data for the other values in the compliance feedback model (S_σ,S_τ, G), due to limited data on the cerebral microvasculature networks. For now, we make an initial estimate of these values based on our understanding of

how the overall response behaves. We choose S_σ to be higher than S_τ since myogenic contributions have previously been found to dominate over endothelial ones.[86] The values for the feedback parameters used here are given in Table 2. We conduct a global parameter sensitivity analysis (Section 3.4) to quantify the strengths of the different feedback mechanisms and assess their relative importance on CBF recovery.

Table 2: Compliance feedback parameter values

Parameter	Value
S_σ	4
S_τ	0.5
T_k	10 seconds
$\Delta C^+/C_0$	10
$\Delta C^-/C_0$	0.8
G	0.1

3.3 1-D Model used for Benchmark Assessment

We assess the accuracy of the derived model and the assumptions on which it is predicated in a benchmark test case in which we compare the simulation results of the model derived from perturbation theory with those of more elaborate models, namely a full 1-D flow model when run using the same network properties and pressure BCs, and examine the associated errors and differences in computational cost. This is done to quantify whether our proposed model can be easily scaled over larger networks in the future, enabling our approach to be adopted more widely. Table D.1 in Appendix D summarises the differences in the assumptions and formulations between the derived perturbation model and the 1-D model. 1-D models have been extensively assessed and found to agree favourably with 3-D models,[29],[104],[106],[185] as well as benchmarked against physical measurements.[107]–[109] The 1-D governing CS area averaged momentum conservation equation can be given by[49],[110],[168]:

$$\frac{\partial Q}{\partial t} + \frac{\partial}{\partial x}(\alpha_m \frac{Q^2}{A}) + \frac{A}{\rho}\frac{\partial P}{\partial x} = -2\pi\nu(\lambda+2)\frac{Q}{A} \tag{3.35}$$

where λ is the polynomial order of the CS velocity power law profile that satisfies the relevant BCs (*i.e.* zero velocity at the wall and zero velocity gradient at the centre) and is assigned a value of 2 for the microvasculature to account for the parabolic velocity profile (as a function of radial distance from the centerline) resulting from Newtonian flow.[186] The coefficient α_m is the momentum correction (Coriolis) factor and is related to λ via Equation (3.36):

$$\alpha_m = \frac{\lambda+2}{\lambda+1} \tag{3.36}$$

Equations (3.1), (3.3), and (3.35) can be combined to form a PDE system in terms of the two variables A and Q, which can be expressed in the conservative form in terms of the conservative variable ($\boldsymbol{U}$), the flux ($\boldsymbol{F}$), and the source ($\boldsymbol{S}$) vectors:

$$\frac{\partial \boldsymbol{U}}{\partial t} + \frac{\partial \boldsymbol{F}(\boldsymbol{U})}{\partial x} = \boldsymbol{S}(\boldsymbol{U}) \tag{3.37}$$

where

$$\boldsymbol{U} = \begin{pmatrix} A \\ Q \end{pmatrix} \qquad \boldsymbol{F} = \begin{pmatrix} Q \\ \alpha_m \frac{Q^2}{A} + \frac{\beta}{3\rho}A^{3/2} \end{pmatrix} \qquad \boldsymbol{S} = \begin{pmatrix} 0 \\ -2\pi\nu(\lambda+2)\frac{Q}{A} + \frac{A}{\rho}\frac{dB}{dx}(\sqrt{A_{ref}} - \frac{2}{3}\sqrt{A}) \end{pmatrix}$$

The analytical steady-state solution of Equation (3.37) can be given by:

$$\frac{\beta}{5\rho}\left[A^{5/2} - A_1^{5/2}\right] - \alpha_m Q_0^2 ln(\frac{A}{A_1}) = -2\pi\nu(\lambda+2)Q_0 x \tag{3.38}$$

where Q_0 is the steady-state flow through the vessel, A_1 is the CS area at the vessel inlet, and x is the axial position from the vessel inlet. When the network initial BCs are imposed, the initial Q and P profiles throughout the network are obtained by coupling the steady-state formulation for each vessel in Equation (3.38) to the conditions of mass conservation and

(a) (b)

Figure 3.2: Illustration of a compliant vessel segment. The uni-axial flow rate is Q, the internal pressure is P, and the internal CS area is A (a). Configuration of a bifurcating node, with six unknowns at the conjunction point: A_1, Q_1, A_2, Q_2, A_3, Q_3 (b).

total pressure continuity (Bernoulli's equations) at the internal nodal junctions, which for the sample bifurcation shown in Figure 3.2(b) can be given by:

$$Q_1 - \sum_i Q_i = 0 \qquad i = 2, 3 \tag{3.39}$$

$$P(A_1) + \frac{1}{2}\rho\left(\frac{Q_1}{A_1}\right)^2 - P(A_i) - \frac{1}{2}\rho\left(\frac{Q_i}{A_i}\right)^2 = 0 \qquad i = 2, 3 \tag{3.40}$$

where $P(A)$ is provided by Equation (3.3). Of course, all other (e.g. converging) junction points can be treated with the same method. In response to perturbations in the inlet pressure, the dynamic system can then be numerically solved using the explicit second-order MacCormack FD method,[187] with a slight modification based on source term averaging[188] which has been shown to improve the scheme's stability. To ensure the proper allocation of the BCs at the vessel ends, one must carry out a local characteristic analysis of the hyperbolic PDE system in Equation (3.37).

3.3.1 Characteristic Analysis of the 1-D Model Hyperbolic System

For PDEs with two independent variables, one important mathematical property is the existence or non-existence of the so-called characteristic curves of the system, which in turn dictates the types of BCs that are appropriate.[189] In this section we analyse the characteristic system of the governing PDEs, which provides a framework to discuss the proper allocation

of the BCs. We can rewrite the conservative of our PDE system in Equation (3.37) in its quasi-linear (non-conservative) form:

$$\frac{\partial \boldsymbol{U}}{\partial t} + \mathbf{A}(\mathbf{U})\frac{\partial \mathbf{U}}{\partial x} = \mathbf{B}(U) \tag{3.41}$$

where $\mathbf{A}(\mathbf{U})$ is the Jacobian matrix of the flux vector:

$$\mathbf{A} = \frac{\partial \mathbf{F}}{\partial \mathbf{U}} = \begin{pmatrix} 0 & 1 \\ \\ \frac{\beta}{2\rho}\sqrt{A} - \alpha_m \left(\frac{Q}{A}\right)^2 & 2\alpha_m \frac{Q}{A} \end{pmatrix} \tag{3.42}$$

and, in the case of uniform properties of the vessel wall (such that $\frac{\partial \beta}{\partial x} = \frac{\partial A_{ref}}{\partial x} = 0$), then $B(\mathbf{U}) = S(\mathbf{U})$, although this assumption could be easily relaxed. It has been shown[49] that, as long as $A > 0$, which is indeed the case if we want to have a physically relevant solution, then the Jacobian matrix $\mathbf{J}(\mathbf{U})$ has two unique eigenvalues:

$$\lambda_{1,2} = \alpha_m \frac{Q}{A} \pm \sqrt{c^2 + \left(\frac{Q}{A}\right)^2 \alpha_m \left(\alpha_m - 1\right)} \tag{3.43}$$

where c denotes the system pulse wave speed, which depends on the local area-pressure relationship within the vessel:

$$c = \sqrt{\frac{A}{\rho}\frac{\partial P}{\partial A}} \tag{3.44}$$

In the case of the tube law given in Equation (3.3), the pulse wave velocity can be expressed as:

$$c = \sqrt{\frac{\beta}{2\rho}\sqrt{A}} \tag{3.45}$$

The existence of real and distinct eigenvalues (since $\alpha_m \geq 1$) means that the PDE quasilinear

system is strictly hyperbolic.[190] Hyperbolic PDEs are used to model a large and extremely important collection of phenomena, which include dynamic flows of fluid through porous media and atmospheric flows, among many others.[60] The phenomena modelled by hyperbolic equations, and hence the solutions to those equations, tend to be more complex and interesting compared to their parabolic and elliptic PDE counterparts.[191]

One of the main distinguishing features of hyperbolic initial boundary value problem (IBVP) PDE systems is that boundary treatment is not as simple as for elliptic or parabolic PDEs.[192] As discussed in Section 3.3.2, one of the crucial issues regarding boundary treatment is the determination of the correct number and kind of boundary conditions that can be imposed to yield a well-posed problem.[193] Another characteristic of hyperbolic PDEs is that perturbations in the spatial domain propagate at a finite speed,[192] such that perturbations at one point in space do not instantly affect the whole spatial domain. The finite speed of propagation has interesting implications on the stability and convergence and hence on the limits of the spatial and temporal discretisations of the numerical schemes used to solve the PDE system, as discussed in Section 3.3.3.

Given the uniqueness of the eigenvalues, the Jacobian matrix $\mathbf{A}$ has two right eigenvectors $(\mathbf{r}_{1,2})$, each of which satisfies:

$$\mathbf{A}\mathbf{r}_k = \lambda_k \mathbf{r}_k \qquad k = 1, 2 \tag{3.46}$$

Since the eigenvalues are distinct, the two eigenvectors form a basis set. Similarly, each of the two left eigenvectors $(\mathbf{l}_{1,2})$ of the Jacobian matrix satisfies:

$$\mathbf{l}_k^T \mathbf{A} = \mathbf{l}_k^T \lambda_k \qquad k = 1, 2 \tag{3.47}$$

The expression for the left eigenvectors is given by[49]:

$$\mathbf{l}_1 = \zeta \begin{pmatrix} \frac{\beta}{2\rho}\sqrt{A} + \left(\frac{Q}{A}\right)^2 \alpha_m \left(\alpha_m - 1\right) - \alpha_m \frac{Q}{A} \\ \\ 1 \end{pmatrix} \qquad \mathbf{l}_2 = \zeta \begin{pmatrix} -\frac{\beta}{2\rho}\sqrt{A} + \left(\frac{Q}{A}\right)^2 \alpha_m \left(\alpha_m - 1\right) - \alpha_m \frac{Q}{A} \\ \\ 1 \end{pmatrix} \tag{3.48}$$

where $\zeta(A, Q)$ is an arbitrary smooth function, which in our case is simply considered to be a scaling constant. The two couples of the left and right eigenvectors are mutually orthogonal,[49],[194] such that:

$$\mathbf{l}_j^T \mathbf{r}_k = \mathbf{l}_j \cdot \mathbf{r}_k = 0 \qquad j \neq k \tag{3.49}$$

Therefore, and without loss of generality, we can normalise the left eigenvectors such that:

$$\mathbf{l}_j^T \mathbf{r}_k = \delta_{jk} \tag{3.50}$$

where δ_{jk} is the Kronecker delta function. Accordingly, we can define two matrices $\mathbf{R}$ and $\mathbf{L}$, where $\mathbf{R}$ is the matrix with columns $\mathbf{r}_1$ and $\mathbf{r}_2$ and $\mathbf{L}$ is the matrix with rows $\mathbf{l}_1^T$ and $\mathbf{l}_2^T$:

$$\mathbf{R} = \begin{pmatrix} & \\ \mathbf{r}_1 & \mathbf{r}_2 \end{pmatrix} \qquad \mathbf{L} = \begin{pmatrix} \mathbf{l}_1^T \\ \\ \mathbf{l}_2^T \end{pmatrix} \tag{3.51}$$

such that ($\mathbf{RL} = \mathbf{I}$). This means that the Jacobian matrix $\mathbf{A}$ can be decomposed into the diagonal form:

$$\mathbf{A} = \mathbf{R}\Lambda\mathbf{L} \tag{3.52}$$

where Λ is the diagonal matrix of the eigenvalues. Inserting Equation (3.52) into Equation

(3.41), we multiply both sides by **L**, to obtain:

$$\mathbf{L}\frac{\partial \mathbf{U}}{\partial t} + \Lambda \mathbf{L}\frac{\partial \mathbf{U}}{\partial x} = \mathbf{LB} \tag{3.53}$$

Next, we introduce the characteristic variables of our hyperbolic system, $\mathbf{W} = [W_1, W_2]^T$, also known as the Riemann invariants, which satisfy:

$$\frac{\partial \mathbf{W}}{\partial \mathbf{U}} = \mathbf{L} \tag{3.54}$$

Component-wise, this reads:

$$\frac{\partial W_1}{\partial \mathbf{U}} = \mathbf{l}_1 \tag{3.55}$$

$$\frac{\partial W_2}{\partial \mathbf{U}} = \mathbf{l}_2 \tag{3.56}$$

Inserting Equation (3.54) into Equation (3.53), we obtain:

$$\frac{\partial \mathbf{W}}{\partial t} + \Lambda \frac{\partial \mathbf{W}}{\partial x} = \mathbf{LB} \tag{3.57}$$

The two Reimann invariants determine the pulse wave dynamics of the system.[111] For the physiological vessel elastic properties and flow conditions, the pulse wave velocity (c) is much greater than the convective average velocity $U = \frac{Q}{A}$ (*i.e.* the flow is subcritical), which means that $\lambda_1 > 0 > \lambda_2$. As a result, one characteristic W_1, to be called the forward characteristic, propagates changes in pressure and flow downstream the vessel from the proximal to the distal parts, while the backward characteristic W_2 carries the information upstream from the distal to the proximal parts. In Section 3.3.2 we examine the practicality behind the working in terms of the characteristic variables for purposes of properly prescribing the network and vessel ends BCs, where boundary treatment must undergo a local characteristic analysis.

3.3.2 Boundary Conditions for the 1-D Model Hyperbolic System

The discussion about the admissibility and proper treatment of BCs for hyperbolic equations is classical and can be found in many textbooks dealing with general hyperbolic systems and ones about the applications in fluid dynamics,[60],[190],[192],[194]–[197] and also in the particular context of 1-D modelling of blood flow in a compliant vessel.[49] The BCs for the hyperbolic system cannot be arbitrarily assigned, since care must be taken to ensure the analytic hyperbolic IBVP problem is well-posed[1]. For a subcritical hyperbolic system where $c > 0$, one should prescribe as many BCs at $x = 0$ as the number of negative eigenvalues of the Jacobian matrix $\mathbf{A}$, and as many BCs at $x = L$ as the number of positive eigenvalues,[60],[190] which in our case translates to one BC at each end of the vessel.

If an explicit formulation of the characteristic variables is available, BCs may be directly expressed in terms of the relevant characteristic variable.[110] Hence, at each boundary, one would prescribe the BC corresponding to the characteristic entering the domain (W_1 at the inlet, W_2 at the outlet), while ensuring that the outgoing characteristic, which carries information from within the interior of the domain, satisfies Equation (3.57), which, when expanded component-wise at each boundary, provides the so-called 'compatibility relations'[49],[110]:

$$\frac{\partial W_2}{\partial t} + \lambda_2 \frac{\partial W_2}{\partial x} = \mathbf{l}_2 \mathbf{B} \qquad x = 0 \tag{3.58}$$

$$\frac{\partial W_1}{\partial t} + \lambda_1 \frac{\partial W_1}{\partial x} = \mathbf{l}_1 \mathbf{B} \qquad x = L \tag{3.59}$$

Note that while the outgoing characteristic must be computed from the differential equation or the values of the primitive variables (A, Q) within the interior domain of the vessel (either via extrapolation or via FD discretisation as described below), the incoming characteristic must be prescribed, meaning it cannot be extracted solely from the differential equations in the interior of the domain as can be done for the outgoing characteristic, or else instability occurs.[190]

[1] A problem is well-posed if it has a solution, the solution is unique, and it depends continuously on the data given in the problem, primarily the initial conditions and BCs.[60],[190],[192],[194]

In the most general case, the inlet characteristics prescribed at the boundaries can take the following form[194]:

$$\begin{aligned} W_1(t,0) &= S_0(t)W_2(t,0) + g_0(t) \qquad && x = 0 \\ W_2(t,L) &= S_1(t)W_1(t,L) + g_1(t) && x = L \end{aligned} \tag{3.60}$$

where $g_0(t)$ and $g_1(t)$ are smooth vector functions and S_0 and S_1 are the rectangular reflection matrices (in our case of only 2 eigenvalues of different signs they are of size 1×1). In the simplest non-reflecting case, $S_{0,1} = 0$ and the incoming characteristics are explicitly prescribed by the vector functions $g_{0,1}(t)$. However, seldom does one have an explicit formulation of the incoming characteristics (or the vector functions $g_{0,1}(t)$) at one's disposal, and in practice it is more intuitive and convenient to work in terms of the primitive physical variables (A, Q) that come from measurements or other models.

Here we need to distinguish between the given analytical treatment of BCs that follow from the brief description earlier on the one hand, where only one BC at each end of the vessel is admissible, and the numerical BCs on the other hand, which involve the allocation of both A, Q at each boundary as required by the chosen numerical solver (the MacCormack scheme in our case). In the context of 1-D blood flow modelling in a compliant vessel, it has been shown that the prescription of either the area or the flow at each boundary is permitted.[49] The other BC as required for the numerical scheme cannot be arbitrarily assigned, but must rather be chosen carefully in accordance with the compatibility relations in Equations (3.58) and (3.59) to ensure the well-posedness of the hyperbolic IVBP.

If we want to work in terms of the primitive variables, the correct way to ascribe the BCs then is to work in terms of the characteristic variables, which we know would make the problem stable and well-posed, and then transform the characteristic variables into the primitive variables, so that the BCs in terms of the primitive variables are also stable and well-posed.[191],[192]

We first briefly describe the simplifications, assumptions, and ensuing interpretations that have conventionally been made by authors when conducting a local characteristic analysis to assign BCs in 1-D models of blood flow in a compliant vessel, discuss the limitations and

contrarieties behind such assumptions, and describe alternate methods for properly handling BCs.

The existence of the characteristic curves means that the PDE system can be reduced to a system of ODEs in terms of the Reimann invariants.[189] This characteristic analysis of the hyperbolic system of the 1-D model of blood flow in a compliant vessel has been previously described.[49],[174] If we define $\hat{x}(t)$ as the parametric function in the (x,t) space, then we can write the variation of the characteristic variables with time along the parametric path $\hat{x}(t)$ as:

$$\frac{d\mathbf{W}\left(\hat{x}(t),t\right)}{dt} = \frac{\partial \mathbf{W}}{\partial t} + \frac{d\hat{x}(t)}{dt}\mathbf{I}\frac{\partial \mathbf{W}}{\partial x} \tag{3.61}$$

Comparison of Equations (3.57) and (3.61) shows that if

$$\frac{d\hat{x}}{dt}\mathbf{I} = \mathbf{\Lambda} \tag{3.62}$$

then:

$$\frac{d\mathbf{W}}{dt} = \mathbf{LB} \tag{3.63}$$

Hence, the continuity and momentum PDEs, which are expressed in terms of the primitive variables (A, Q), are transferred into a system of ODEs in terms of the hyperbolic system characteristic variables (W_1, W_2), the solution for which can be integrated along the parameterised characteristic curves from some initial data on those curves.[62],[174],[189]) We can see from Equation (3.63) that in the special case where $\mathbf{B} = 0$ (source term neglected), then the characteristic variables W_1 and W_2 are decoupled, and are constant along the two characteristic curves in the (x,t) plane defined by expressing Equation (3.62) in its component-wise form:

$$\begin{aligned} \frac{d\hat{x}}{dt} &= \lambda_1 \qquad for \quad W_1 \\ \frac{d\hat{x}}{dt} &= \lambda_2 \qquad for \quad W_2 \end{aligned} \tag{3.64}$$

Many authors[31],[49],[109],[110],[174] utilise the implications of ignoring the source term in the neighbourhood of any boundary points to decouple the two characteristic variables. For instance, solving the decoupled ODE equations in (3.64) would provide the solution for the characteristic variables at any point in time and space in terms of their initial value at the appropriate point within the vessel's interior domain:

$$W_k(x,t) = W_k(x - \lambda_k t, 0) \quad k = 1, 2 \tag{3.65}$$

Or more appropriately, since the Jacobian matrix **A** and hence the eigenvalues are not constant or uniform, the value for the outgoing characteristic at the boundary for the time step $(n+1)$ can be extrapolated from the previous time step n using the value of the characteristic variable propagating in the same direction at an appropriate location within the vessel's interior domain:

$$\begin{aligned} W_2^{n+1}(x=0) &= W_2^n(-\lambda_2^n(x=0)\Delta t) \\ W_1^{n+1}(x=L) &= W_1^n(L - \lambda_1^n(x=L)\Delta t) \end{aligned} \tag{3.66}$$

Note that for a discrete representation of the spatial domain (such as the one obtained from an FD scheme), the characteristic value within the interior domain would also need to be interpolated from those at the neighbouring grid points. This method of characteristic extrapolation has been readily proposed and implemented,[49],[109] along with other extrapolation propositions that similarly rely on the assumption of local inviscid fluid in the neighbourhood of the boundaries points.[31],[174]

The second assumption that has been repeatedly made by authors is that the value of the

Coriolis correction coefficient α_m is equal to 1 at the boundaries. This assumption is made to considerably simplify the expressions for the left eigenvectors $(\mathbf{l}_1, \mathbf{l}_2)$ in Equation (3.48), thereby enabling the integration of Equation (3.54) to obtain an explicit formulation of the characteristic variables in terms of the primitive physical variables:

$$W_{1,2} = \frac{Q}{A} \pm 4(c - c_0) \tag{3.67}$$

The values of the outgoing characteristics $(W_2(0)^{n+1}, W_1(L)^{n+1})$ obtained from the characteristic extrapolation, along with the imposed BCs in terms of one of the primitive variables, and the explicit expression of the characteristics in terms of the primitive variables as in Equation (3.67), effectively complete the system and enable a direct calculation of the second primitive numerical BC, while also ensuring that the overall problem is well-posed. Such simplifications have also been applied at the bifurcation nodes where vessels meet, in which the compatibility conditions for the outgoing characteristics at the bifurcating interface are expressed in terms of the primitive variables and supplemented with conditions of flux continuity and total (or static) pressure matching.

We discuss the limitations and inconsistencies behind these two assumptions. First of all, ignoring the term $\mathbf{B}(\mathbf{U})$, which accounts for the dissipation of the momentum due to friction loss, would erroneously dismiss the natural decay in the pressure P (and hence A) due to the source term at the boundaries. Given the large number of bifurcations in the cerebral microcirculatory network, ignoring the effect of friction loss at both endpoints of each arterial vessel in the whole cerebral arterial network when solving for the primitive variables at the bifurcation interface could potentially accumulate significant errors. Furthermore, the presence of the source term (due to friction loss) means that the characteristic variables are no longer constant along the characteristic curves in the (x, t) space, and hence they can no longer be decoupled. Often when dealing with systems of PDEs, it often not necessarily desirable or even possible to uncouple a system, and any uncoupling as a result of simplifications or assumptions is usually more of a theoretical tool rather than a practical tool.[60]

Second, the assumption of $\alpha_m = 1$ essentially means that the velocity profile is flat at the boundaries. While the blood velocity profile tends to be close to plug flow in the larger ves-

sels with a Stokes layer near the wall, a completely blunt velocity profile would violate the imposed no-slip BC at the vessel walls that characterises the power law velocity profile, which is required to derive the expressions for the friction loss and the convective acceleration terms in Equation (3.35). For instance, by rearranging Equation (3.36), the polynomial order of the velocity profile can be expressed in terms of the correction coefficient (α_m):

$$\lambda = \frac{2 - \alpha_m}{\alpha_m - 1} \tag{3.68}$$

A value of $\alpha_m = 1$ results in an unbounded value of λ and therefore an unbounded value of the fiction loss term according to Equation (3.35), which is physiologically unrealistic, and is also in stark contrast to the prior assumption of inviscid flow at the boundaries. If implemented incorrectly, the numerical realisation of BCs can often be a potential source of instabilities in the numerical solver,[192], and indeed we have found that when these assumptions were applied at the vessel boundaries of the 13-generation network[198] representing to cerebral microvasculature in order to simplify the treatment of BCs, the numerical scheme became unstable. Thus, it is preferable to refrain from resorting to any assumptions that would give rise to such mathematical inconsistencies, especially if such simplifications are unwarranted.

The relation between the imposed BC in terms of one of the primitive variables, and the numerical BC in terms of the other primitive variable required to solve the numerical problem, is indeed provided by enforcing the mass and momentum conservation differential equations themselves, yet projected along the direction of the outgoing characteristic. Multiplying the compatibility relations for each of the outgoing characteristics in Equations (3.58) and (3.59), by their respective left eigenvector, and using the definition of the characteristic variables in Equations (3.55) and (3.56) to transform the characteristic variables back in terms of the primitive variables, we end up with a single relation at each boundary:

$$\mathbf{l}_2^T \left(\frac{\partial \mathbf{U}}{\partial t} + \mathbf{J} \frac{\partial \mathbf{U}}{\partial x} - \mathbf{B} \right) = 0 \qquad x = 0 \qquad t > 0 \tag{3.69}$$

$$\mathbf{l}_1^T \left(\frac{\partial \mathbf{U}}{\partial t} + \mathbf{J} \frac{\partial \mathbf{U}}{\partial x} - \mathbf{B} \right) = 0 \qquad x = L \qquad t > 0 \tag{3.70}$$

This boundary treatment for hyperbolic systems was proposed by Gottlieb et al.[199] and later generalised by Canuto and Quarteroni[200] and Quarteroni,[192] where it was referred to as the 'spectral collocation approximation' (since it entails satisfying the differential equations at the collocation nodes, or grid points). The same idea has been used[201] for the numerical treatment of reflecting BC in the context of gas dynamics. For further analysis of the method the reader is referred to Canuto et al.[202]

Transforming the quasi-linear expressions in Equations (3.69) and (3.70) back to their conservative form (since $\mathbf{B}(\mathbf{U}) = \mathbf{S}(\mathbf{U})$) and expanding the dot product to a scalar expression we get:

$$\left[\pm\sqrt{\frac{\beta}{2\rho}\sqrt{A}+\left(\frac{Q}{A}\right)^2\alpha_m(\alpha_m-1)}-\alpha_m\frac{Q}{A}\right]\left[\frac{\partial A}{\partial t}+\frac{\partial Q}{\partial x}\right]$$
$$+\left[\frac{\partial Q}{\partial t}+\frac{\partial}{\partial x}\left[\alpha_m\frac{Q^2}{A}+\frac{\beta}{3\rho}A^{\frac{3}{2}}\right]+2\pi\nu(\lambda+2)\frac{Q}{A}\right]=0 \tag{3.71}$$

where for inlet boundaries, the first term is negative, while for outlet boundaries the first term is positive. We see from Equation (3.71) that projecting the differential equation along the outgoing characteristics at the boundaries is equivalent to imposing a linear combination of the mass and momentum conservation equations. The compatibility relation in Equation (3.71) is discretised in time and space to convert it from the non-linear differential form to the non-linear algebraic form before solving for the numerical BC at each time step. The spatial derivative terms may be evaluated from values of the interior[194] using a one-sided FD formulation, which makes sense since the outgoing characteristic captures the propagation of information from the vessel's interior domain.

Care must be taken when the equation corresponding to the BC is discretised, such that the numerical solver at the boundary is at least of the same order of accuracy and stability as the original (Mackormack) scheme to ensure that the order of accuracy and stability of the overall numerical scheme is not compromised.[60] Hence, the time derivative in Equation (3.71) is discretised using a second-order implicit trapezoidal scheme, and the spatial derivative is discretised using a higher ($\geq 2^{nd}$) one-sided FD scheme.

We do realise that, to obtain the second numerical boundary condition at each timestep, the proposed method entails solving a non-linear equation for each boundary, as opposed to its direction evaluation from the imposed boundary condition and the values of the primitive variables within the vessel's interior domain at that timestep, as would be carried out if the assumptions of inviscid flow at the boundaries and that of $\alpha_m = 1$ were allowed. However, we do note that solving for the vessel terminal values of (A, Q) at each nodal junction also requires solving a non-linear system of equations at each time step, and hence the added computational cost of solving the non-linear Equation in (3.71) at the network boundaries is very nominal.

To solve for the variables at the junctions, the compatibility equations in Equation (3.71) accounting for the transfer of mass and momentum across each branching point are supplemented with conditions of flux continuity and total pressure matching as given in Equations (3.39) and (3.40) (for the bifurcating node example in Figure 3.2(b)). The six equations give rise to a non-linear square system of unknowns that is solved at each time step using an iterative Levenberg–Marquardt algorithm implemented in the MATLAB Optimization Toolbox function lsqnonlin.

3.3.3 Numerical Stability of the 1-D Solver

As a result of the finite speed of propagation, the solution for hyperbolic equations has a finite analytical domain of dependence.[60],[203] For a linear hyperbolic equation with a propagation speed c, the information at any given ϵ on the x-axis at any given time t influences the solution at another time $t + \Delta t$ only in the interval $[\epsilon - c\Delta t, \epsilon + c\Delta t]$.[203] Equivalently, perturbations at any point ϵ influence the solution at another point $x = x^*$ only after $\Delta t^* = \frac{|x^* - \epsilon|}{c}$ has elapsed.

Accordingly, a requirement for the stability (and hence the convergence) of a numerical scheme is that the analytical domain of dependence in space and time is constrained within the numerical domain of dependence,[60],[203] which is in turn determined by the spatial and temporal discretisation parameters of the numerical scheme. In other words, the time step Δt used in the approximation scheme must be less than the time required for the wave to travel to adjacent grid points, in order to ensure that the numerical scheme could access information needed to form the solution. The numerical domain of dependence encompasses the analytic

domain of dependence when the Courant–Friedrichs–Lewy (CFL) convergence condition is met:

$$C = \frac{|U + c|\Delta t}{\Delta x} \leq C_{max} \tag{3.72}$$

where $C_{max} = 1$ for the second-order accurate MacCormack scheme when used for a linear PDE. Assuming a uniform spatial discretisation of $\Delta x = \frac{L}{N-1}$, where N is the number of grid points in a vessel, and inserting the expression for c in Equation (3.45) into Equation (3.72) and rearranging, we obtain an expression for the upper bound value of Δt:

$$\Delta t \leq \frac{L}{(N-1) \cdot \left| \frac{Q}{A} + \sqrt{\frac{\beta}{2\rho}\sqrt{A}} \right|} C_{max} \tag{3.73}$$

It is crucial to note, however, that for systems of PDEs, and especially non-linear ones, it becomes difficult to pinpoint an exact criterion for stability. In fact, for non-linear hyperbolic systems, the CFL condition becomes a necessary but not sufficient condition for stability,[60],[203] and the exact stability limit can only be determined via numerical experimentation. Nonetheless, the CFL condition remains a useful (albeit abused[60]) metric to provide a coarse measure, or upper bound on the timestep Δt, because it is easy to compute. For the microcirculation network used in this chapter, C_{max} was approximated from the simulations to be around 0.37, which is within the 0.35-0.99 range for the CFL number reported when implementing the Mackormack scheme in large arteries and arterial networks of the human systemic circulation.[106]

We can also see from Equation (3.73) that as we start incorporating the shorter vessels on the distal end within the network under study, the stability limit entails the imposition of smaller simulation time-steps (Δt). By the point at which we start incorporating cortical and subcortical arteries and arterioles, the timestep becomes too small, rendering any computational simulations unfeasible.

3.4 Results

3.4.1 Numerical Simulation in a Simple Bifurcating Network

We test the behaviour of our proposed network regulation model using the simple 13-generation symmetrical network proposed by Payne and Lucas,[198] shown in Figure 3.3, as this has been validated against experimental data in steady-state conditions. The vessel wall thickness in Equations (3.3) and (3.7) is set to $h = 0.2R$. As only the arteriolar vessels exhibit this form of autoregulation, we only allow vessels in generations A1-A6 to regulate with the remaining vessels remaining passive in behaviour. Due to the low Womersley numbers ($\alpha < 0.1$), the pulsatile nature of cortical blood micro-flow can be ignored.[4] We consider the response of the network to a 15% drop, 15% increase, and 10% drop in the starting inlet pressure (P_0) according to the smooth functions in Equations (3.74), (3.75), and (3.76), respectively, while maintaining a constant outlet pressure (P_{out}) and a zero external pressure P_{ext}.

$$P_{inlet} = P_0 \left(1 - \left(0.075 \left(1 + tanh\left(\frac{t-0}{0.3}\right)\right)\right)\right) \tag{3.74}$$

$$P_{inlet} = P_0 \left(1 + \left(0.075 \left(1 + tanh\left(\frac{t-0}{0.3}\right)\right)\right)\right) \tag{3.75}$$

$$P_{inlet} = P_0 \left(1 - \left(0.05 \left(1 + tanh\left(\frac{t-0}{0.3}\right)\right)\right)\right) \tag{3.76}$$

The functions are selected purely to test the model, and are not necessarily intended to simulate a real physiological stimulus; rather they provide a convenient method for examining the system response to a stimulus. For the simple network, $P_0 = 60$ mmHg and P_{out} = 25 mmHg according to the network steady-state conditions. The network CBF for both the active and passive (*i.e.* impaired autoregulation) cases is shown in Figures 3.4(a), 3.5(a), and 3.6(a) when solved for using our perturbation model and in Figures 3.4(b), 3.5(b), and 3.4(b) when solved for using the 1-D model under the same network properties and pressure BCs. In the active case, the arteriolar compliance is quasi-statically updated according to the feedback model described in Section 3.2.2, after which the vessel stiffness parameter β is updated according to Equation (3.8). The maximum errors in the pressure, flow, and radius profiles

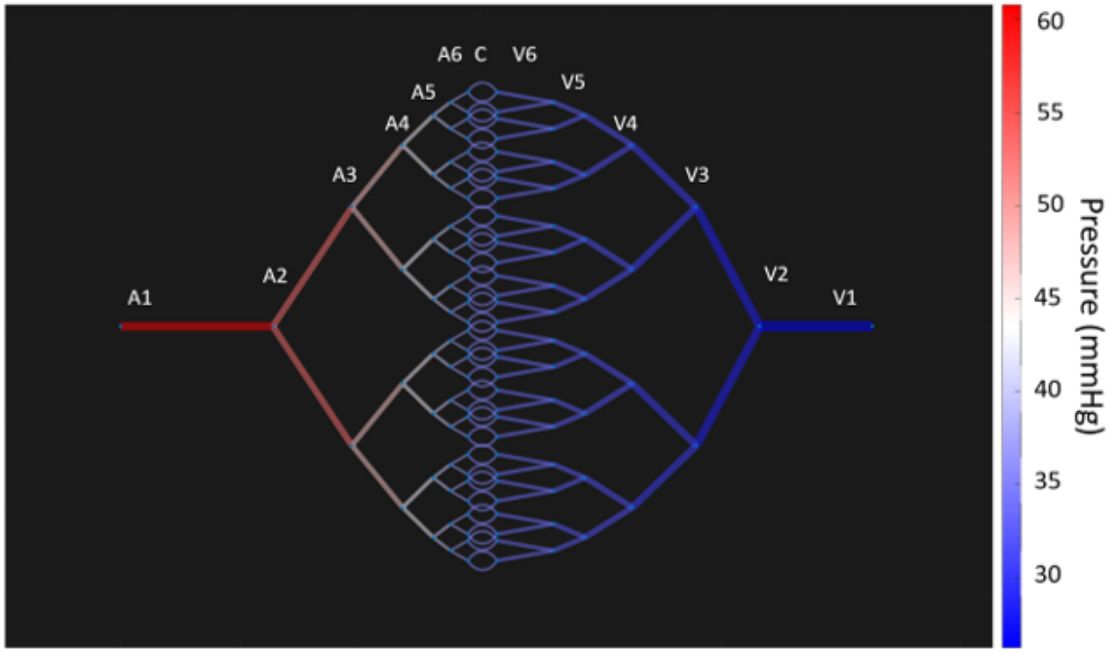

Figure 3.3: The 13 generation network under steady-state conditions, with the inlet and outlet pressures defined at the left node of the A1 vessel, and the right node of the V1 vessel, respectively.

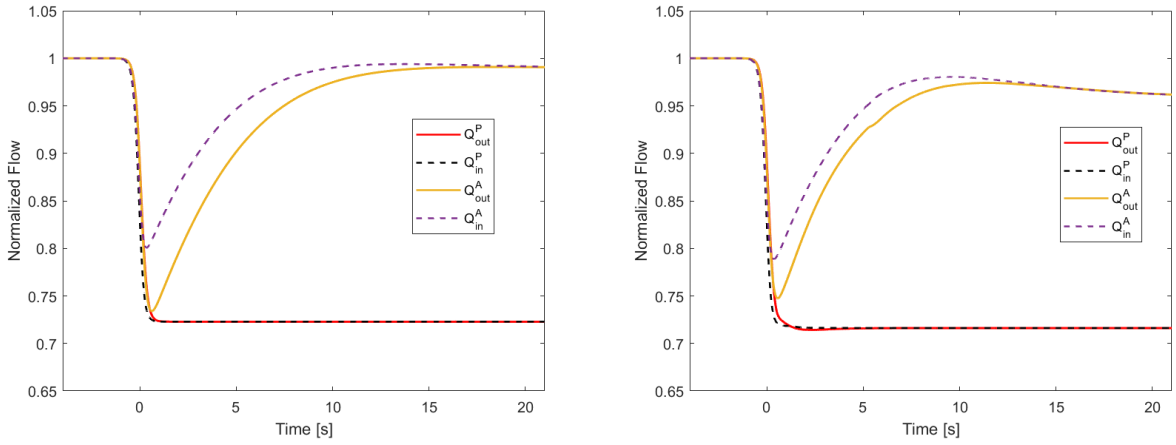

(**a**) (**b**)

Figure 3.4: Flow (relative to baseline) through the 13-generation bifurcating network using our perturbation model (a), and using the 1-D model (b), in response to a 15% inlet pressure drop, featuring both the active (A) and passive (P) cases representing functional and impaired CA, respectively.

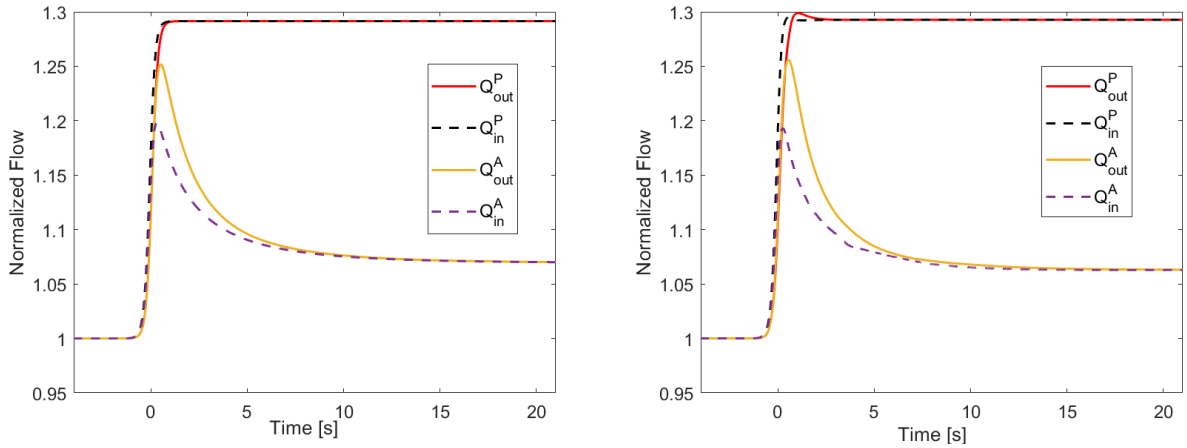

(a) (b)

Figure 3.5: Flow (relative to baseline) through the 13-generation bifurcating network using our perturbation model (a), and using the 1-D model (b), in response to a 15% inlet pressure increase, featuring both the active (A) and passive (P) cases representing functional and impaired CA, respectively.

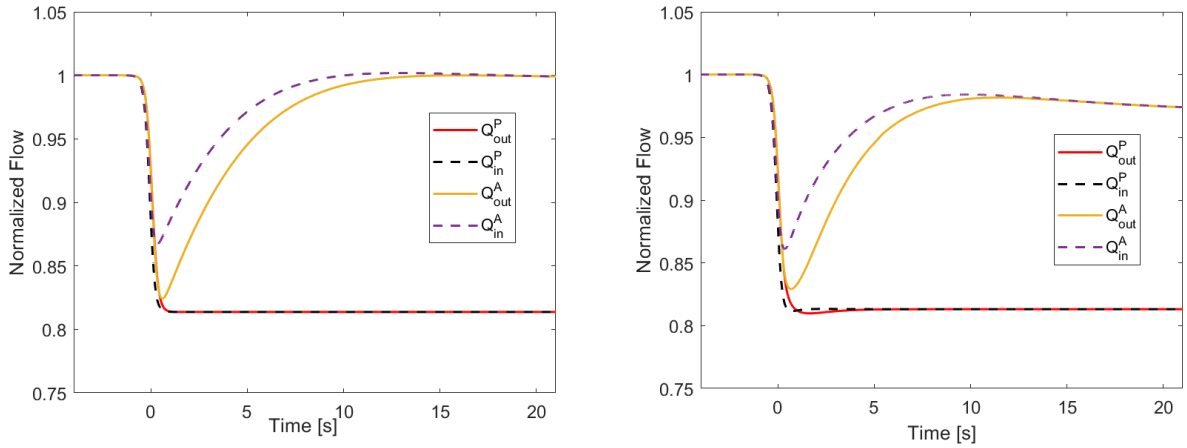

(a) (b)

Figure 3.6: Flow (relative to baseline) through the 13-generation bifurcating network using our perturbation model (a), and using the 1-D model (b), in response to a 10% inlet pressure drop, featuring both the active (A) and passive (P) cases representing functional and impaired CA, respectively.

Table 3: Maximum Errors in Q, P and R between the perturbation and 1-D models for both the active case and the passive case in response to a 15% drop, 15% increase, and 10% drop in the microvasculature inlet pressure.

ΔP_{inlet}	Condition	Flow	Pressure	Radius
-15%	Active	2.9%	0.9%	2.4%
	Passive	0.4%	0.2%	0.3%
$+15\%$	Active	1.5%	0.7%	1.2%
	Passive	1.5%	0.7%	0.1%
-10%	Active	2.5%	0.7%	2.7%
	Passive	0.6%	0.3%	0.1%

between the perturbation model and the 1-D model simulations, as calculated from Equations (3.77-3.79), are given in Table 3.

$$E^Q_{max} = \max_{vessel}\left\{\frac{|Q_{network}(t) - Q_{1D}(t)|}{0.5(Q_{network}(t) + Q_{1D}(t))}\right\}\times 100 \tag{3.77}$$

$$E^P_{max} = \max_{node}\left\{\frac{|P_{network}(t) - P_{1D}(t)|}{0.5(P_{network}(t) + P_{1D}(t))}\right\}\times 100 \tag{3.78}$$

$$E^R_{max} = \max_{vessel}\left\{\frac{|R_{network}(t) - \overline{R}_{1D}(t)|}{0.5(P_{network}(t) + \overline{R}_{1D}(t))}\right\}\times 100 \tag{3.79}$$

where Q_{1D} is computed for the inlet and outlet of each vessel, and $\overline{R}$ is the average CS radial profile across the vessel grid points in the 1-D model. The 1-D model simulations for the response in the 20s following the pressure drop took 12 days to complete on the cluster (the job was using 12 cores of one Intel Xeon Platinum CPU 8268 CPU @ 2.90GHz, and 96GB of memory, on a server running Linux (CentOS 8.1)), even when utilising the network symmetry, due to the CFL stability condition dictating the upper bound for the time-step in Equation (3.73). Conversely, when solved semi-implicitly, our perturbation model simulation took around 1 minute to complete.

To quantify how the model can be used to investigate the relative contributions of the different dCA mechanisms across the different vessel generations, Figure 3.7 shows the relative changes in the intraluminal pressure and shear stress for each arteriole vessel generation in the simple

network, along with the corresponding changes in vessel radius, flow, and wall stiffness, in response to a $15\$$ drop in the inlet pressure, when both mechanisms are intact, and when only the myogenic response is functioning. Figure 3.8 shows the changes in the intraluminal pressure (Figure 3.8(a)) and vessel radius (Figure 3.8(b)) in the third generation arteriole in response to the 15% inlet pressure drop, under different combinations of control mechanisms: endothelial and myogenic (E+M), endothelial only (E), myogenic only (M), and no control mechanisms (None). Figure 3.9 shows the changes in the capillary perfusion in response to the 15% inlet pressure drop, under the different aforementioned combinations of control mechanisms.

3.4.2 Global Parameter Sensitivity Analysis

Global parameter sensitivity analysis is the process of apportioning the uncertainty in outputs to the uncertainty in each input variable over the entire range of interest when all input factors are varied simultaneously. For the input parameters, we chose the four compliance feedback parameters in Table 2, which are the myogenic sensitivity S_α, the endothelial sensitivity S_τ, the stiffness-compliance slope G, and the maximum fractional change in compliance $\frac{\Delta C^+}{C_0}$, since compliance increases in response to pressure drop. We investigate the effects of these input parameters on the model output variables, which are listed in Figure 3.10.

We use the Sobol sequence to generate quasi-random sample sizes of the input space, which is assumed to have a uniform distribution at $\pm 50\%$ of the baseline values in Table 2. Using the framework developed by Saltelli,[204],[205] the input space is fed into an MC simulation (N=2000) to produce variance-based estimates of the first-order sensitivity indices of the input parameters on the model output variables, the results of which are summarised in Figure 3.10. Input-output scatterplots are constructed and are provided (see Appendix A.3) to help visualise the total effects of the model inputs on the outputs.

3.5 Discussion

We developed a simple framework for modelling dCA, using a network representation of the cerebral microvasculature. As shown in Figure 3.4(a), in response to the upstream pressure

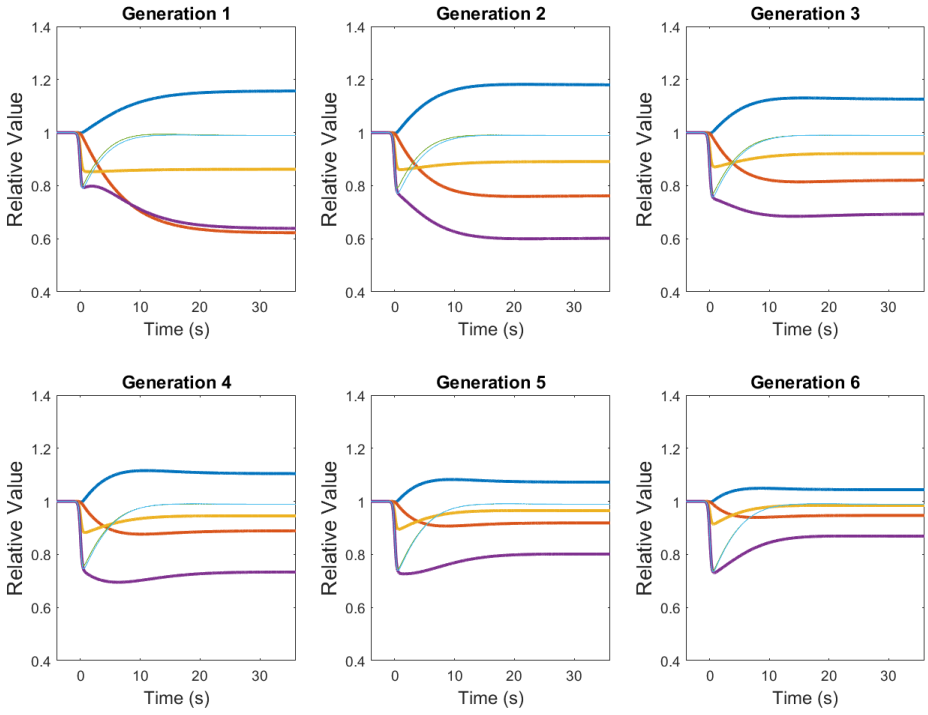

(a)

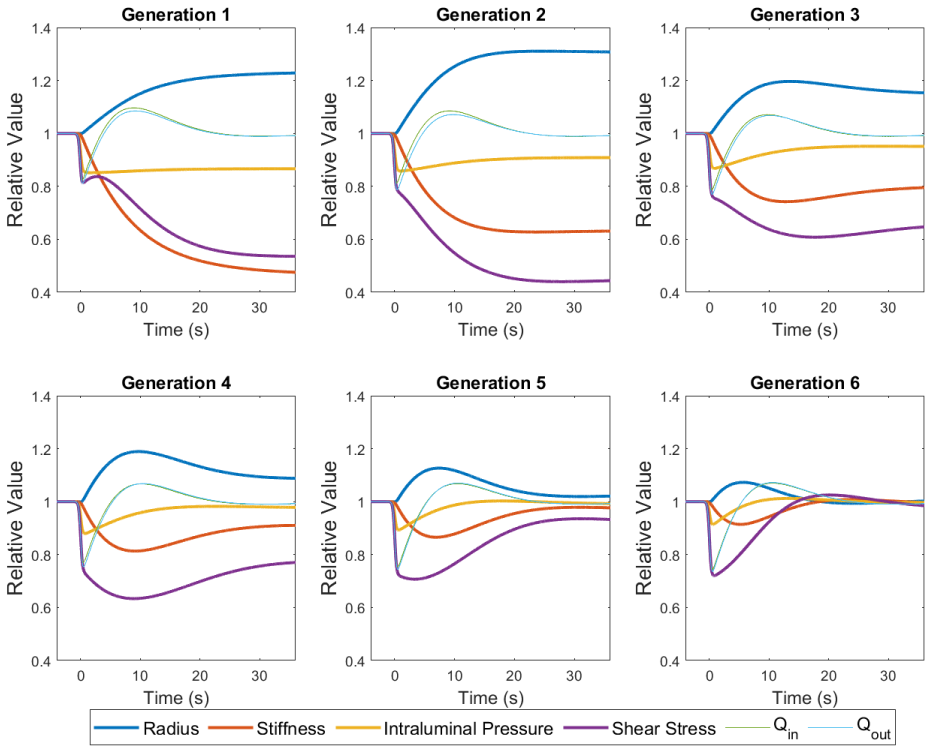

(b)

Figure 3.7: The changes in the radius, stiffness, intraluminal pressure, shear stress, and flow, relative to their baseline values, across the arteriole vessel generations in the 13-generation network, under the actions of both the myogenic and endothelial responses (a) and the myogenic response only (b).

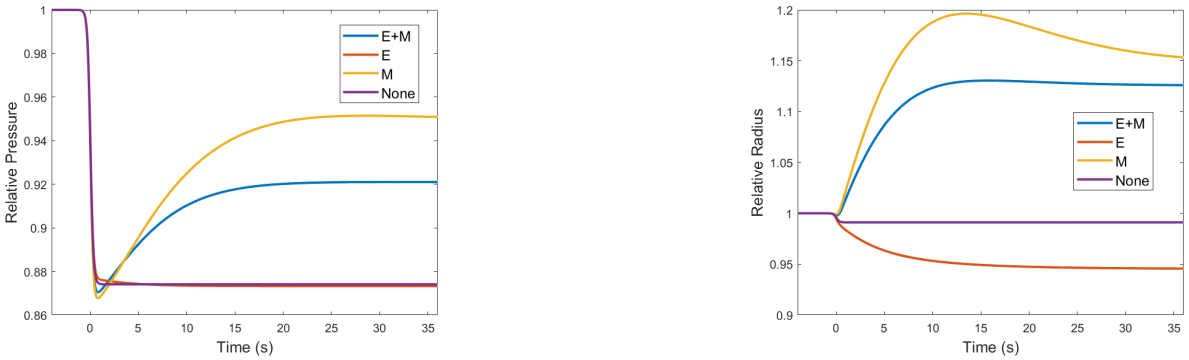

(a) (b)

Figure 3.8: Change in the intraluminal pressure (a), and the corresponding change in the vessel calibre (b), relative to their baseline values, in a third generation arteriole vessel in the 13-generation bifurcating network, under different combinations of control mechanisms: endothelial and myogenic (E+M), endothelial only (E), myogenic only (M), and no control mechanisms (None).

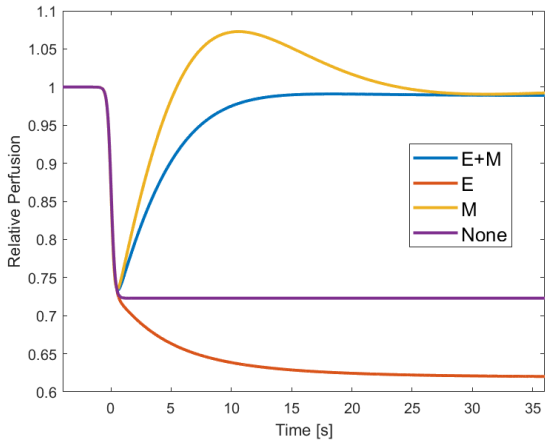

Figure 3.9: Perfusion of the capillary bed (relative to baseline) in the 13-generation network under different combinations of control mechanisms: endothelial and myogenic (E+M), endothelial only (E), myogenic only (M), and no control mechanisms (None).

drop, the network recovers perfusion while exhibiting the physiologically occurring characteristic autoregulatory behaviour in terms of the biphasic flow response observed experimentally.[80] The dynamic differences between the network inlet and the outlet flows are clearly shown, with the net differences marking a net increase in the arteriolar volume as indicated by the increase in the arteriolar radii in Figure 3.7(a). These dynamic differences are primarily due to the vessel compliance, and demonstrate that changes in pressure and flow throughout a network are not instantaneous as one would get from assuming a steady-state solution, but rather exhibit some delay as changes in pressure propagate downstream from the inlet to the outlet. Such dynamic differences could have implications in terms of determining the speed of the dCA response, as well as in terms of linking model simulations to actual physical measurements and imaging modalities, for instance, to those obtained from dynamic susceptibility contrast (DSC) brain MRI studies, where a bolus injection of a paramagnetic

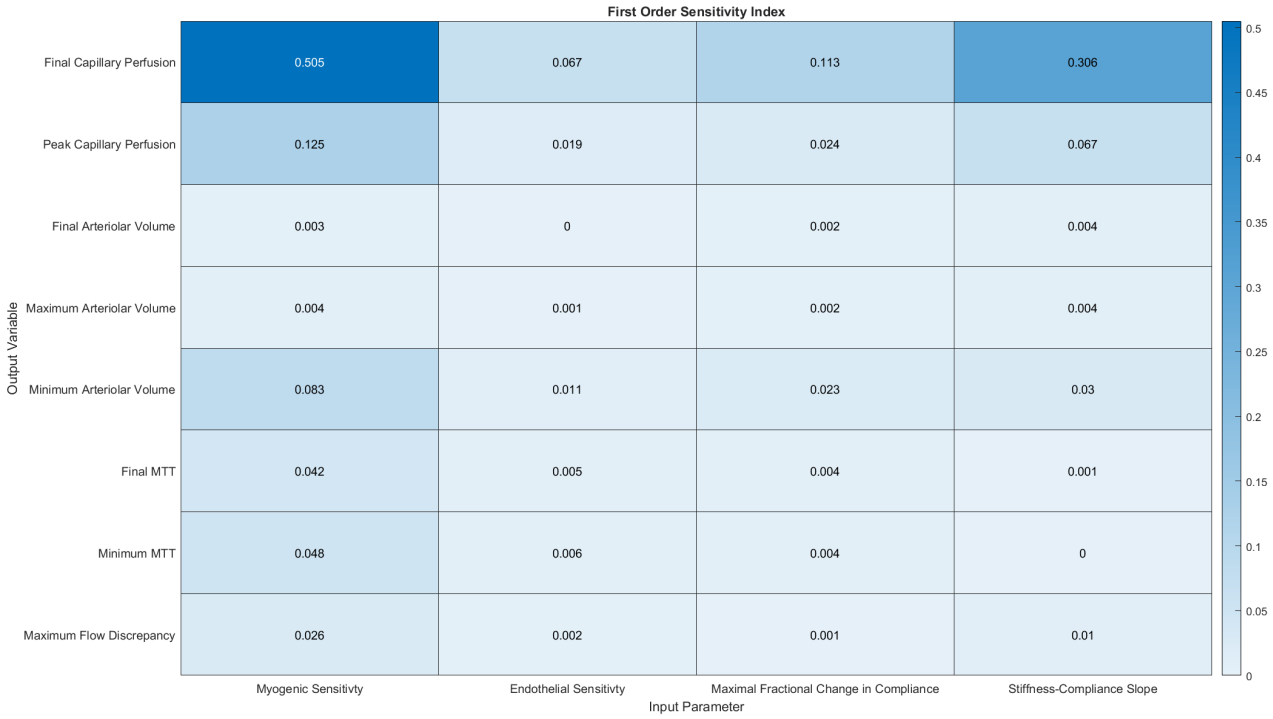

Figure 3.10: First order sensitivity indices for the compliance feedback parameters on the model output variables. Darker values indicate higher sensitivity of the input parameter to the output parameter. The output variables are: the final and peak capillary perfusion, the final, peak and nadir of the arteriolar volume, the final and nadir of the mean transit time (MTT), defined as the network CBV/CBF, and the maximum discrepancy between the network inlet and outlet flows, defined as $Q_{in}(t) - Q_{out}(t)$.

contrast agent is administered, and its passage through the vasculature is monitored by serial measurement of the MRI signal loss in the surrounding tissue. Ignoring the delay effects that take place from the site of measurement (of the arterial input function) to the tissue can cause significant errors in the quantification of CBF, and thus can lead to inaccurate information on stroke since DSC MRI is commonly used in clinical studies of cerebral ischaemia.[206]–[208]

Figure 3.7(a) demonstrates the variations in the autoregulatory response across the arteriole generations in the simple network. Generally, the greater the deviation of the vessel wall stiffness from its baseline value, the stronger the autoregulatory response found in that vessel. In the first-generation vessel, the inlet pressure is decreased and maintained at 85% of its baseline value according to Equation (3.74). Hence, the intraluminal pressure in the vessel can only exhibit a limited recovery. The dCA mechanisms in the first two vessel generations respond to the relatively high perturbation in intraluminal pressure from its baseline value by decreasing the vessel wall stiffness, which results in the vessel being maintained at a relatively highly distended state. As we move downstream, the vessels become more distant from

the source of the pressure drop (which could correspond to a decreased MAP in the larger circulation), and the upstream resistance decreases. Hence, the intraluminal pressure sustains a more marked recovery towards its baseline value in the later generation vessels, and the changes in the wall stiffness, and hence in the calibre of the vessels, become progressively less pronounced in the subsequent generations. It is worth noting that such response variation across the vessel generations is present even when using the same compliance feedback parameters values for the vessels; *i.e.* without accounting for response heterogeneity across the vessels. For now, we used the same feedback values, though this assumption could be easily relaxed in the future to account for response heterogeneity.

When considering each of the myogenic and endothelial mechanisms in isolation, the contrasting effects of the two responses are evident. The endothelial response further constricts the arteriolar vessels (Figure 3.8(b)) in response to the pressure drop, thereby increasing arteriolar resistance and decreasing capillary perfusion (Figure 3.9). In contrast, the myogenic response results in arteriolar dilation (Figure 3.8(b)), thereby increasing capillary perfusion (Figure 3.9). It is clear from Figure 3.9 that when both mechanisms are present, the myogenic response is the dominant one, and that this is modulated by the endothelial response, as has been previously proposed.[86] Interestingly, while the myogenic response produces a slight temporary overshoot in the radial profile of the downstream arteriolar vessels (Figure 3.7(b)) with a subsequent temporary overshoot in the capillary perfusion as shown in Figure 3.9, the end-steady-state perfusion is the same as when the competing endothelial mechanism is also present (Figure 3.9), indicating that the different mechanisms impact the steady-state and dynamic components of the response in different ways.

We hypothesise that this may be the case because the endothelial response attenuates the recovery of the intraluminal pressure towards its baseline value in the downstream arterioles. For instance, when the endothelial response is impaired in Figure 3.7(b), the intraluminal pressure in the downstream arterioles drops in response to the pressure drop, then recovers due to the myogenic mechanisms, resulting in a concomitant increase then decrease in the vessel radius, before they both reach their steady-state value. In contrast, the intraluminal pressure in the downstream arterioles never makes the same recovery when the endothelial response is intact (Figure 3.7(a)). Since $S_\sigma > S_\tau$ in the stiffness feedback model (Table 2), the vessel radius is more directly affected by the intraluminal pressure than by the shear

stress. Hence, due to the endothelial response, the perturbation of the intraluminal pressure from its baseline value is maintained, which preserves the myogenic response and the vessel distension.

Of course, the feedback parameter values, which determine the dynamic interaction between the two mechanisms, are not unequivocally established and may differ between subjects, in particular, due to pathological conditions or clinical manoeuvres. The purpose of these observations is to demonstrate how the current model could be used to better understand such interplay. To help better assess the relative contributions of the feedback parameters on the model output, we performed a global sensitivity analysis for the compliance input parameters as shown in Figure 3.10. We employ a global, variance-based sensitivity analysis as opposed to a local, derivative-based one since derivatives are only informative at the base point where they are computed and do not provide an exploration for the rest of the space of input factors, which would matter greatly for non-linear models with high uncertainty in the model inputs. Examining the first-order sensitivity indices in Figure 8, it appears that the myogenic sensitivity (S_α) and the stiffness-compliance slope (G) are the most important parameters influencing perfusion. Examining the total effects of the input variables from the slope of input/output scatterplots (in Appendix A.3), the myogenic sensitivity input factor appears to be the dominant factor affecting perfusion. This finding supports the earlier conclusion of myogenic dominance from Figure 3.9, which is also in agreement with earlier modelling studies.[82] Hence, this model parameter can be chosen to be the focus of further studies.

Next, we discuss some of the limitations and assumptions in the current framework. With only three feedback parameters (S_σ, S_τ, and G), we have restricted ourselves to a high-level treatment of the processes that drive dCA through changes in the vessel stiffness, as summarised in Figure 3.1. To maintain the simplicity of our model, we do not explicitly include the exact biochemical pathways that set the level of phosphorylation of the myosin heads, nor do we rely on a mechanical interpretation, such as Laplace's law, to describe how changes in the wall tension affect the P-A relationship, as has been done by some authors, both in single vessel models[209] and compartmental models.[116],[121]

However, such detailed models contain a large number of parameters, which would undermine the model's utility in clinical problems due to excessive mathematical intricacy.[105] In

their compartmental model, Ursino et al.[123] attempted to verify the possibility of characterising intracranial dynamics through a limited number of parameters, and found that the capacity of their simplified model employing the compliance tube law in Equation (3.9) to reproduce the velocity and intracranial pressure (ICP) tracings was equivalent to that of a previous, more complex model[121] that characterises changes in the compartmental wall tension, but with a much shorter computational time when both models were used aposteriori after a best-fitting procedure to assign some parameter values. Purely law-driven models without any simplifications are customarily overparameterized, as they may include more relevant laws than the amount of available data would support.[204] This work aims to describe and validate a simplified model that can incorporate the main mechanisms involved in dCA and permit their quantitative assessment, with a drastic reduction in computational cost and mathematical complexity, which can in turn improve the clinical meaning of the results obtained and facilitate parameter assignment.[121]

For the tube law in Equations (3.3) and (3.9), the vessel wall behaviour was assumed to be that of an elastic one, and the viscoelastic behaviour was ignored. While opinions on the importance of the viscoelastic effects are mixed, these effects seem to be small within the physiological range of pressure and flow,[110],[210] and have thus been disregarded in many studies. It is also well known that the vessel wall exhibits a non-linear stress-strain curve[95],[178] due to the heterogeneous composition of the vessel wall, with the arteries and arterioles becoming markedly stiffer as they are stretched. Therefore, the value of E used in Equation (3.4) is an effective Young's modulus that captures the cumulative contributions of the vessel wall layers (and potential support from external structures; see Section 3.2.4), and depends on at which point along the stress-strain curve the wall material is operating.

However, since the diameter changes in the microvasculature are relatively small, the vessel wall material tends to operate in a relatively linear region of the stress-strain curve in the pressure range exhibited over the cardiac cycle and during physiological perturbations,[111] such that the assumption of a linear elastic behaviour is a reasonable one in this context.

Comparing the tube law non-linear formulation in Equation (3.3) with the linear one in Equation (3.6), it becomes evident that C is a function of P (or equivalently R), even in the absence of the dCA mechanisms, and indeed the dependence of C on P in models utilising

the compliance tube law has been included by some authors,[108],[145] while neglected by others.[62],[123],[147],[169],[170],[176] The computational differences between the linear and non-linear representations of the vessel wall behaviour have been previously investigated. There appear to be no significant differences in the results obtained from the linear vs non-linear formulations of the tube law, both in compartmental models (see[123],[211]) and in 1-D network models (see[107],[172],[212]). Comparably, the linear frequency-based formulation in Flores et al.[169] derived from locally applying the linear compliance tube law in Equation (3.6) at each CS produces nominal maximum errors in pressure (<2.1%) and flow (<2.3%) in their studies when used for the macrovasculature when comparing the results to those obtained from 1-D and 3-D models in the time domain. In their review, Shi et al.[111] commented that while it might be deemed necessary to consider the pressure-dependent vascular properties in the coronary vessels and collapsible veins, the argument for their usage in the other vessels is less compelling.

On that account, we have used the linear compliance tube law in the derivation of our model. This is because of the practicality procured when working with linear terms in the frequency domain as part of the model derivation, and because usage of the compliance tube law could facilitate the direct correspondence and comparison with compartmental models that employ similar compliance feedback models for the autoregulation mechanisms, for instance, for future parameter setting. Benchmark corroboration of our network model with the results of more elaborate 1-D models employing the non-linear tube law in Equation (3.3) (Section 3.4) also demonstrate the validity of working with the linear tube law representation. In addition, in Chapter 5 we demonstrate how the compliance feedback model achieves very good agreement with experimental data upon parameter calibration.

Absi[171] remarked that the different linear and non-linear tube laws commonly used are practically indistinguishable if $\left(P_t \frac{Eh}{R_{ref}} < 0.05\right)$, and simple linear relationships can be used 'with an acceptable gap' until $\left(P_t \frac{Eh}{R_{ref}} = 0.1\right)$, after which the divergence becomes non-negligible. We have found that under baseline conditions, for the microvasculature network used in the simulations of the study (Figure 3.3), $\left(P_t \frac{Eh}{R_{ref}} < 0.05\right)$ for all microvessels except for the capillaries where $\left(P_t \frac{Eh}{R_{ref}} = 0.14\right)$. Similarly, we find (see Appendix A.1) that the non-linear dependence of C on P is minor for all microvessels except for the capillaries. On that account, we deduce that the compliance tube law is a valid representation of the linear elastic

vessel behaviour for the cerebral cortical vessels except for the capillaries, which in any case could be more appropriately represented as a homogenised porous medium within a hybrid multiscale framework, as described in Chapter 4.

As mentioned, in line with the approach that has been conventionally adopted in the frequency domain,[62],[147],[169],[170] the radial profile R is replaced with a time and spatially averaged radius $\overline{R}$ to maintain linearity. However, obtaining this averaged value strictly requires prior simulations of the network of interest in the time domain under the same conditions using higher dimensional models. As an alternative approximation, we have retained the use of the averaged radius as required to maintain the linearity in the frequency domain, and proceeded with the perturbation analysis to derive the approximate analytical solution for the vessel inlet and outlet flows, and only after inverse transforming the solution back into the time domain in Equation (3.28), do we substitute the time-averaged radius parameter with its dynamic counterpart that is updated quasi-statically at each time-step according to Equation (3.9). By invoking the quasi-steady state approximation for R, our model is thus relatively simple, requiring only two dynamic (P, Q) variables to be perturbed.

When compared to 1-D simulations, the maximum errors as defined by the metrics in Equations $(3.77\text{-}3.79)$ were less than $3\%, 1\%$ and 2.7% for the vessel flow, nodal pressure and vessel radial profiles, respectively. Potential sources of discrepancy between the perturbation and 1-D network models include the use of different tube laws for the vessel wall behaviour, neglecting the advection term, and assuming a uniform CS area in our perturbation model. Other sources of error could arise due to the use of a time and spatially averaged CS area in the frequency domain which is then substituted by its dynamic counterpart in the time domain when deriving the model, neglecting the higher-order terms in the asymptotic expansion of the pressure and flow variables as normally required in the perturbation analysis, and matching the static pressure at the junction nodes in the perturbation model compared to matching the total pressure in the 1-D model. However, these errors are relatively minor and are well within the acceptable range, and are likely thus to be irrelevant in clinical applications. This is because they are well below the range of errors that normally arise when comparing experimental and numerical (1-D or 3-D) results, which are in the range of $4 - 6\%$ for P and $19 - 26\%$ for Q waveforms,[106]–[108],[153] which normally arise due to measurement uncertainties, modelling limitations, and lack of patient-specific adaptations. Hence, the network

model developed provides a very accurate representation of the microvasculature haemodynamics when used within an active regulation model.

We also note the significant computational advantage our approach bears over the 1-D approach when used for modelling the microvasculature. We can see from Equation (3.73) that as we start incorporating the shorter vessels on the distal end, the stability requirement of the numerical scheme, as provided by the CFL condition, will entail the imposition of smaller simulation time-steps (Δt), such that the simulation becomes too computationally demanding by the point we start incorporating cortical and subcortical vessels. Simulations using the 1-D approach to model the network response in the 20s following the pressure drop took 12 days to complete on the cluster (the job was using 12 cores of one Intel Xeon Platinum CPU 8268 CPU @ 2.90GHz, and 96GB of memory, on a server running Linux (CentOS 8.1)) even when utilising the network symmetric geometry, while the simulation time using our model was finished in 1 minute when the equations were solved implicitly. Thus, our proposed model offers a considerable advantage over more detailed models of CBF and regulation.

It should be noted that our model has incorporated only the myogenic mechanism, which has been previously mathematically proposed to dominate the autoregulatory response,[82],[86] and the endothelial mechanism, and did not account for other effects and control modalities such as the metabolic response, the vascular reactivity in response to the partial pressure of CO_2, the neurovascular coupling which requires a detailed model of local changes in metabolism, or the role of the sympathetic response, which remains poorly understood. We have also assumed that each vessel responds to local changes, with no coordination of the response or information transfer between the vessels arising, for instance, from the upstream conducted response. Furthermore, we note that the current model does not yet incorporate the intracranial pressure dynamics, which have been shown to have an important role in cerebral haemodynamics[105],[121],[213]; because the overall intracranial volume must remain constant, changes in the vessel volumes must be accompanied by an opposite change in the remaining intracranial volumes with a concomitant variation in the intracranial pressure.

However, our model could provide a highly suitable framework for examining such effects to varying degrees of complexities in the future, considering the modular manner by which it has been set up, as shall be demonstrated in Chapter 6. We also note that the endothelial

and myogenic response dynamics are combined into the same linear feedback equation in (3.30), thereby assuming the same time constant for both processes. In Chapters 5 and 6, and as more autoregulatory mechanisms are incorporated, the dynamics of each mechanism can be modelled separately to account for the heterogeneity in the time response across the mechanisms, before they are non-linearly imposed to effect changes on the vessel compliance.

In our simulations, we used a uniform haematocrit value of 0.42 throughout the network when calculating μ in Equation (2.4), and hence do not account for the phase separation effect. Compared to the *in-vitro* empirical models, the viscosity from the *in-vivo* laws used here is more sensitive to the haematocrit levels in the diameter ranges investigated. However, previous studies have found that phase separation models have very little influence on the pressure distribution, and only a minor effect on the blood flux and that the haematocrit variations inside the cortex are quite modest ($< 15\%$).[214] The distribution of haematocrit in the network and the phase separation effect could, in theory, be accounted for using an empirical law that links haematocrit and flow rate ratios at bifurcations[215]; this however, would render the problem non-linear and would thus necessitate an iterative solver. Hence, we maintain the constant haematocrit in our framework, significantly reducing the computation time.

In addition to performing a sensitivity analysis for the compliance input parameters, it is crucial in the future to extract the parameter values from *in-vivo* measurements and compare the simulation results to such measurements. However, CBF and blood pressure measurements in the cerebral microvasculature are very scarce and are challenging to acquire.[216] In Chapter 5, we show how the compliance feedback model parameters can be calibrated based on a set of experimental data examining the response of individual arteriolar vessels to changes in pressure and flow. Furthermore, if CBF measurements were to be validated against clinical data, the model needs to be upscaled to the size of a realistically sized MRI voxel, and potentially linked to the larger cerebral circulation, for which there are more available data on how dCA is challenged by blood pressure variations; see[86]for example. Thus, as we move towards more realistic network geometries, our approach can be extended to develop a dynamic hybrid network-continuum model, in which a spatially informed network structure of the cortical penetrating vessels is constructed and modelled via the approach developed in this chapter, and is then coupled to the capillary bed, which is, in turn, homogenised and treated as a porous medium (see[41],[133],[217]), as illustrated in Chapter 4.

3.6 Conclusion

Overall, the proposed model shows how the network can recover CBF close to basal levels, while successfully reproducing the characteristic physiological autoregulatory behaviour in terms of changes in the vessel calibre and the biphasic flow response that arise from the dCA mechanisms. To the best of our knowledge, this is the first network model of cerebral vasculature that incorporates the dCA mechanisms at the level of the individual vessel, within a network of both active and passive vessels. This model can be used to investigate the spatial specificity and heterogeneity of the various control mechanisms and help to disentangle their contributions, which is hard to do experimentally.[2] The network model can also be used for investigating some of the recent (and occasionally controversial) premises regarding the increasingly recognised role of the capillaries and pericytes in controlling CBF (see[5],[76],[77]). For instance, the role of the pericytes could relatively easily be incorporated from a recent model[165] that is derived from experimental data on capillary diameter variation due to the activity of pericytes. A network model can also help better understand how various pathologies and vascular alterations affect the network CBF under both normal and impaired autoregulatory responses, by imposing subtle changes in the *in-silico* model input or the microvasculature geometry. The model can also be used for preliminary testing of hypotheses which are challenging or dangerous to conduct in real life, such as whether or not blood pressure should be lowered in hypotensive or stroke patients. Network models can also be useful for validating assumptions in the compartmental models, which remain valuable tools in modelling the haemodynamic responses due to their simplicity and low computational cost.

Chapter 4

A Multiscale Model of Blood Flow and Control in the Cerebral Cortex

Abstract

For the results of the haemodynamic model to be validated against clinical MRI data, the model simulations need to be computationally feasible when used on networks on the scale of an MRI voxel. This requires some form of an upscaling approach that bypasses the need for an explicit architectural representation of the whole network while maintaining the relevant anatomical connections. To this end, we developed a hybrid multiscale model of blood flow and autoregulation that traces the dynamic changes in blood flow, volume, and pressure in the cortical microvasculature, in which the discrete topology of the penetrating vessels is preserved, and these are then appropriately coupled to the homogenised capillary bed by a spatially distributing support function in the terminal endings. In contrast to the other multiscale models, the model developed here accounts for the dynamic physiological phenomena of the blood flow and the autoregulation processes in the microvessels. We show how the adaptive meshing scheme for the capillary bed developed in this study can be employed to ensure a scale-invariant coupling formulation and numerically accurate simulations, all without compromising the computational feasibility of the model. A statistically accurate cortical network on the scale of an MRI voxel is generated, and the model parameter values are calibrated using a Monte Carlo Filtering analysis to ensure that the model results are physiologically informed. The model is found to be able to capture the steep pressure gradients that have been reported to occur at coupling interfaces. Furthermore, in response to an upstream pressure drop, the network is found to be able to recover cerebral blood flow while exhibiting the characteristic autoregulatory behaviour in terms of changes in vessel calibre and the biphasic flow response. Overall, the model developed here offers a high-quality characterisation of dynamic flow and autoregulation in the microvasculature at improved computational efficiency and lays the ground for whole-brain dynamic simulations.

4.1 Introduction

Models of CBF in the microvasculature can be used to investigate the complex interplay between the flow control mechanisms across the vessel generations and examine the flow and pressure patterns in the microvasculature, alterations in which have been theorised and shown to be implicated in disease conditions.[141]–[144],[218] To be able to achieve such functionality, the model must account for the network's spatial heterogeneity[78],[138]–[140] and its complex interconnectivity. The model discussed in the previous chapter provided an accurate and computationally feasible framework to be used in the microvasculature networks for the dynamic modelling of CBF and dCA. However, the model relies on a classical network representation of the vasculature and thus requires information about the vessels' connectivity and vascular geometry, the extraction and reconstruction of which for the capillary bed is a non-trivial task, for which the available quantitative anatomical data specifically focused on the spatial organisation of cerebral capillary networks in humans are very scarce.[131] Furthermore, with a capillary vessel density of approximately 8000 $vessels/mm^3$,[55] a network simulation on the scale of the whole brain region, using the classical network approach, would simply be computationally infeasible.

What is needed is some form of an upscaling approach. One natural approach for representing the structure and function of the capillary bed while bypassing its innate micro-scale complexity is the use of the homogenisation technique, described in Section 2.6. However, the homogenisation method might not be the most suitable representation to describe CBF through the sub-cortical penetrating arteriole and venule trees feeding into and draining from the capillary bed, respectively, since it cannot capture their fractal-like branching patterns, which are non-homogeneous at the network scale.[37],[130],[133] This becomes particularly relevant when attempting to model the cerebral autoregulation mechanisms, which predominantly induce changes at the level of the individual arteriolar vessel.[2],[164] For example, Reichold et al.[42] observed that the dilation of the penetrating arterioles leads to increased flow in the capillary bed but this increase is limited to a cortical depth that coincides with the depth of the terminal arterioles of the tree, indicating a strong dependence of flow on the topological features of the penetrating arterioles. Alternatively, one way to proceed is to use some form of a multiscale approach, in which models of different resolution scales are combined to offer an accurate

and computationally feasible characterisation of the overall system across its range of scales.

Multiscale modelling is an emerging modelling paradigm that has shown a lot of promise and utility in models across various disciplines,[219] and has been recently extended to include cerebral haemodynamics (see[127],[133],[217]). For such an approach, a hybrid network-continuum model of the microvasculature is generated, in which the network structure of the cortical penetrating vessels is preserved and is coupled to the capillary bed, which is, in turn, homogenised and treated as a porous medium. The flow through the terminal penetrating vessels becomes the source (or sink) flow in the porous capillary bed, thereby mediating the flow between the discrete and continuum representations.

However, a challenging topic within multiscale flow models is the designation of the precise mathematical formulation at the coupling interface.[133],[217],[220] Peyrounette et al.[133] demonstrated that, under steady-state conditions, assuming a simple condition of pressure continuity at the transition between the Hagen–Poiseuille 0-D modelled penetrating vessels of the cerebral cortex and the FV discretised capillary porous medium leads to a significant underestimation of the strong local pressure gradients at these transitional regions and thereby results in a loss in the local shape of the solution. By imposing a simple condition of pressure continuity, the local errors in pressure and flow in their model significantly increased with the ratio h/l_{cap}, where h is the side length of the control volume (CV) cube arising from the geometrical FV discretisation (*i.e.* meshing), and l_{cap} is the characteristic capillary length. In particular, for $h/l_{cap} = 4$, the local errors at the coupling points reach up to 29% for the pressure and up to 150 % for the flow and continue to rise for higher ratios of h/l_{cap}.[133]

This problem at the transition region arises in part because there is a modelling gap between the explicit, macro-scale representation of blood flow in the penetrating trees, and the microcirculation in the porous 3-D domain.[133],[217] While the blood pressure in the conventional 0-D and 1-D network models describes the cross-sectional area-averaged pressure within each tube at the vessel ends, the pressure in the continuum representation represents a spatially averaged field over the mesoscopic scale. In the case of a cell-centred second-order FV approach, the error is a result of the assumed linear variation of the pressure field solution within the CV,[221] since the pressure that is defined at the centroid of the CV is the local averaging of the pressure field within the whole CV. Although it does not change the nature of the orig-

inal differential equation being solved, an incorrect scheme can provide a locally incorrect picture of the solution[221] at the network-continuum interface and by extension can alter the overall picture of the pressure field in the multiscale model as errors propagate through the whole system. With larger CVs, the discrepancies in the physical interpretation of the pressure between the coupled FV cells and the cortical terminal vessels become more prominent, explaining the aforementioned increase in error as the ratio of h/l_{cap} increases.

Another concern with multiscale modelling is the possibility of scale variance and the emergence of physical and numerical singularities in the model. The use of a Dirac formulation to represent the highly localized forcing function of flow at the coupling interface confines the source flow at the terminal endings at a single point, which is not physically sound, compromises the numerical accuracy of the governing equation,[217] and can lead to numeric scale variance in which the pressure gradient at the coupling point becomes dependent on the choice of size of the CV discretisation (in case of a FV approach) at the transitional interface, with very small CVs leading to singularities in the solution. Hence, an appropriate mathematical formulation at the coupling interface is also required. Hodneland et al.[217] proposed using a mass-conserving and smooth spatially distributing support function, in which the source/sink flow is distributed across a finite support radius in the continuum domain around the terminal endings to maintain the well-posedness and stability at the interface and circumvent the emergence of any singularities and scale variance in the numerical solution.[217]

Still, and to the best of our knowledge, none of the multiscale models constructed so far account for the dynamic behaviour of CBF arising, for instance, due to the fluid oscillation and the interaction between the unsteady fluid motion and an elastic wall,[79] as modelled in Chapter 3. In addition, none of the previous models accounts for the dCA mechanisms that act to regulate CBF. This is because to maintain computational feasibility, the constituent sub-models are typically chosen to be linear, which would in turn ensure that the final multiscale model assembled from the sub-models is also linear. Characterising the dynamic behaviour, especially that of the strongly time-dependent and usually non-linear dCA mechanisms,[129] would typically require non-linear formulations, as opposed to the resistive part of the microcirculation. However, as shown in Chapter 3, the resistive and dynamic behaviour of CBF in a vessel network, as well as the effects of the dCA mechanisms, can all be feasibly accounted for using a 0-D CBF model comprised of a linear system of ODEs used in tandem with a

quasi-steady-state compliance feedback model of the dCA mechanisms.

To this end, we develop a comprehensive multiscale system in this study that can be used to examine the dynamic CBF and dCA mechanisms in the human cerebral cortical microcirculation. The model is assembled from the following parts: (i) the 0-D network-based model of CBF and dCA developed in Chapter 3 to model the flow in the cortical penetrating vessels; (ii) the 3-D Darcy flow within the homogenised capillary continuum, that is, in turn, discretised using an adaptive non-uniform meshing scheme developed here to ensure mass balance and numerical accuracy without compromising the model's computational feasibility; and (iii) the spatially distributed support function to model the transition between the two domains at the coupling interface, as proposed by Hodneland et al.,[217] which in the proposed model is adapted to a dynamic context. We also propose the employment of a simple, methodological analysis that utilises an MCF scheme to obtain physiologically informed estimates for some of the model parameter values and their interactions even before any data fitting (which is conducted in Chapter 5). We use our model to analyse the changes in CBF and CBV in the microcirculation in response to pressure perturbations, and show how the model proposed is physiologically grounded, mathematically robust, and computationally feasible, all of which are important characteristics of the model as we move towards the goal of developing accurate, spatially informed and computational feasible simulations of whole brain perfusion and its control.

The chapter is divided as follows: Section 4.2.1 outlines how we can generate a data-informed statistical model of a hybrid network of the size of an MRI voxel. Section 4.2.2 describes the novel meshing algorithm used to carry out the local mesh refinement of the capillary bed. Section 4.2.3 describes the FV equation discretisation procedure following from the geometrical domain discretisation procedure in Section 4.2.2, the sources of errors arising from local mesh non-orthogonality and skewness, and how the meshing scheme helps to ensure such errors are mitigated. Section 4.2.4 outlines how the distributed support function can be used in a dynamic context to address the modelling gap at the interface between the discrete and continuous representations, which would in turn allow us to combine the equations governing the flow in the two domains into a single linear dynamic system, as described in Section 4.2.5. Section 4.2.6 outlines how the model parameter values are assigned and analysed, including a description of the MCF analysis and the Elementary Effects (EE) global parameter

sensitivity analysis conducted in this study. Next, in Section 4.3, we present the results of the MCF analysis, the dynamic changes in CBF, CBV and the pressure field in the hybrid network in response to a pressure drop, the effect of the meshing scheme on the overall flow, as well as those of the parameter sensitivity analysis. Finally, in Section 4.4, we discuss the simulation results of the study, compare our model results and formulation with those of other models, discuss some of the limitations of multiscale approaches in haemodynamic modelling, and offer concluding remarks in Section 4.5.

4.2 Materials and Methods

4.2.1 Generating a Statistical Hybrid Network of the Size of an MRI Voxel

We generate a large-scale model of a clinically sized MRI voxel ($1\times1\times2.4\,mm^3$). Assuming the porous capillary bed covers the entire voxel volume, we discretise the voxel domain into CV cells, with the cell centroids representing the capillary internal nodes. We chose a cubic shape for the CV to ensure an ideal meshing aspect ratio[222] and to simplify the non-uniform mesh and equation discretisation procedures (see Sections 4.2.2 and 4.2.3). The depth of the voxel runs from the pial surface down to around the grey matter/white matter interface.[69] The penetrating vessels can then be embedded into the discretised voxel in 3-D space to construct the multiscale model network. The penetrating trees start at the cortical pial surface and then transverse the grey matter cortical layers where they bifurcate into gradually narrowing trees, whose terminal vessels feed into or drain from the capillary bed.[37]

Each penetrating tree is normally found to transverse the cortex, with conspicuous large columns orthogonal to the pial surface.[68] Hence, each tree can be individually embedded into the cortex, starting from the pial surface.[39] The brain pial system acts as a reservoir that delivers blood at a near-uniform pressure over the entire cortical surface[223]; hence, we impose Dirichlet BCs by prescribing the same inlet (and outlet) pressure values at the arteriole (and venule) nodes on the cortical surface, respectively. We use the statistically generated arteriole and venule penetrating vessels[39] of average pial surface diameters of 40 and 110 μm, respectively which have been morphometrically validated against experimental data,[26] thus bypassing the labour-intensive, time-consuming and error-prone method of experimen-

tally extracting and reconstructing the microvasculature structure.[41],[42] One example of a penetrating arteriole is shown in Figure 4.1(a).

We assume that the capillary bed is periodic, as required by the homogenisation procedure, which is reasonable due to the randomness of the network at this length scale.[224],[225] It has been previously shown[133] that a multiscale scheme becomes less accurate when the coupling point occurs less than one cell from the boundary point. Therefore, given the assumption of periodic BCs, and to mitigate the errors induced by the proximity of the coupling points to the domain boundaries, we allocate periodic BCs to the four sides of the voxel perpendicular to the pial surface, where FV cells at the boundary are connected to the cells at the opposite boundary. The capillary bed at the pial surface of the voxel is given a Neumann no-flow BC, as is the grey/white matter interface at the bottom, as has been assumed in previous multiscale models,[127],[133] since the penetrating cortical vessels transverse the six layers of the cortex, and the white matter is much less vascularized than the grey matter.[37]

The homogenisation of the capillary bed, as well as the assumption of periodic BCs at the surfaces of the capillary voxel, mitigate the strong effect of the BCs on the haemodynamic predictions.[126],[127] Nonetheless, the current mathematical model could still suffer from boundary effects at sides perpendicular to the cortical surface due to insufficient characterisation of the vascular topology at these borders.[43],[67] In our case, such effects could for instance arise due to the necessary pruning of vessels that terminate outside the domain, or failure to include branches terminating in the voxel domain whose upstream connections originate from outside the chosen pial surface. Therefore, we can further suppress the boundary effects by simulating flow through a larger voxel of size $(1.5 \times 1.5 \times 2.4mm^3)$, and restricting our analysis to a central region of interest (ROI) that is of the same size as the clinically sized MRI voxel.

The surface area density of the penetrating vessels is chosen to be 9 vessels$/mm^2$ in line with experimental data.[26],[226] Earlier studies in humans[125],[227] have indicated that the arterioles make up approximately two-thirds of the total penetrating vessels connected to the pial surface, the remaining one third being venous vessels. As the precise spacing of these vessels is uncertain, and this model is statistical, we split the $1.5 \times 1.5mm^2$ pial surface area into 9 equally sized squares, each containing 1 arteriole, and also split it into 4 squares, each con-

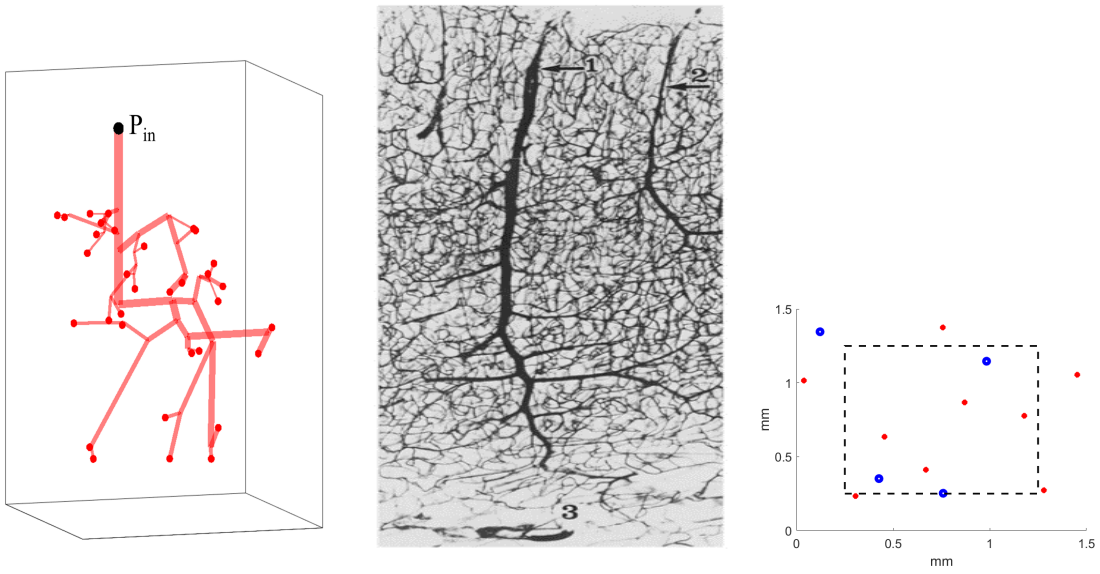

(a) (b) (c)

Figure 4.1: (a) Example of one statistically generated arteriole with an inlet node (black circle) at the pial surface and terminal nodes (red) embedding the cortex. (b) Example of a real penetrating arteriole tree extracted from imaging (reproduced with permission from[37]). (c) The penetrating arterioles (red) and venules (blue) are randomly positioned on the pial surface and a $1 \times 1mm^2$ ROI is then selected.

taining 1 venule. We then randomly place the trees inside each square on the pial surface, an example of which is shown in Figure 4.1(c).

4.2.2 Finite Volume Method Mesh Refinement Algorithm

The geometrical discretisation step involves the transformation of the physical domain into a mesh that forms the computational domain, resulting in a set of non-overlapping elements whose centres or vertices represent the points at which the solution is sought.[221],[228] Previous studies[133] have shown that using a more refined mesh for the capillary bed could result in a better approximation of the local pressure gradient around the coupling points. The local mesh refinement near the terminal endings also prevents the clustering of multiple coupling points inside a single CV; errors by up to 7% for flow and 2.5% for pressure were observed for configurations involving more than coupling inside one CV cell, suggesting that the accuracy of reconstructing the pressure field is limited by the density of couplings per cell.[133] Intuitively, a finer mesh would help to mitigate this issue, and we have found that CV cubes of at most $50\mu m$ side length generally appear to prevent multiple couplings in one CV in most voxel reconstructions.

Furthermore, we have observed that insufficient mesh resolution around the coupling points

compromises the numerical accuracy of the distributed source flow integral between the discrete vessels and the homogenised capillary continuum, and in some cases can lead to non-conservative flow (see Section 4.2.4). All these points support the use of locally refined meshes around the coupling points. In the first iteration of the model, we attempted to employ two levels of mesh refinement: one tight mesh that ensures no local clustering of more than one coupling point inside a single CV around the coupling points, and a coarser mesh for the remaining voxel domain. The resulting number of capillary nodes significantly decreased compared to when using a uniform tight mesh but was still too large if the model were to be up-scaled or if we were to conduct repeated dynamic simulations, such as for parameter sensitivity analysis (see Section 4.2.6).

To overcome the aforementioned challenges, we have created a new meshing algorithm that employs three levels of refinement (an octree mesh), as illustrated in Figure 4.2. To the best of our knowledge, none of the previous multiscale models of blood flow has previously implemented an adaptive localized mesh refinement process. In this automated algorithm, the voxel domain is discretised using an initial coarse mesh (of cubes of side length $L_1 = 75\mu m$), with the nodes representing the CV centroids. The penetrating network vessels are then embedded into the domain, and CVs that contain at least one coupling point are labelled and further discretised (using cubes of side length $L_2 = L_1/2$). The penetrating vessel network is re-embedded into the non-uniform mesh, and the CVs that still contain multiple terminal nodes, where the first level of refinement was insufficient, are marked for successive refinement and are further discretised (using cubes of side length $L_3 = L_1/4$). Cells of side length L_1 neighbouring cells of side length L_3 are also further discretised to cells of side length L_2 to ensure a smooth transition in size between contiguous cells. Finally, the penetrating vessel network is then re-embedded into the non-uniform mesh, and the final element-to-element relations for the structured mesh are stored.

Note that in Figure 4.2, using too small of an initial coarse cube length (L_1) will increase the computational cost due to many unnecessarily small CV cells in the voxel domain that are not within proximity to the terminal endings. On the other hand, using too large of a coarse cube length will, in addition to comprising the accuracy of the model, also increase the computational cost due to a greater number of smaller FV cells upon further discretisation around the coupling points. In the last discretisation step in Figure 4.2, we only further discretised

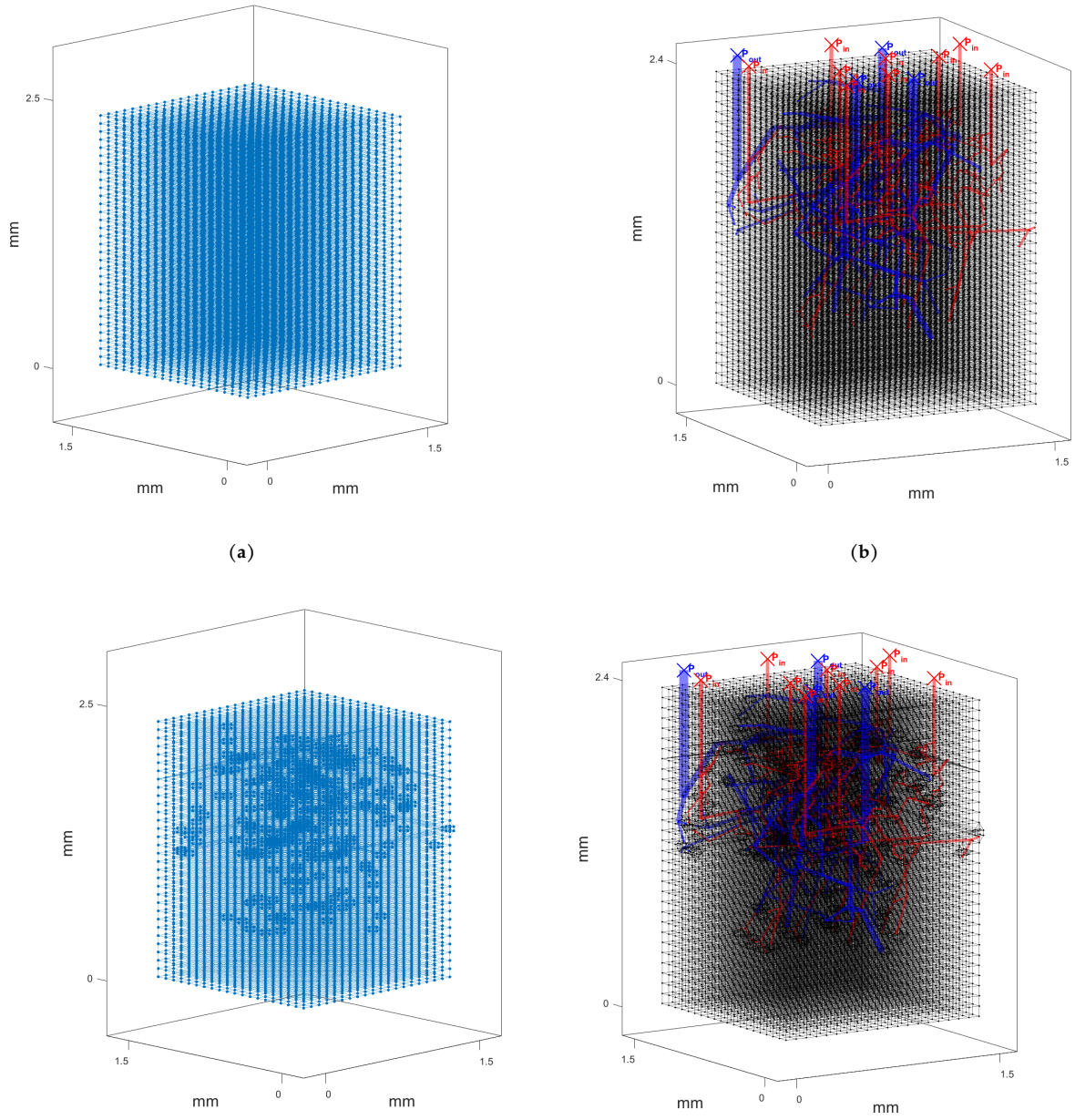

Figure 4.2: a) The voxel domain is discretised using an initial coarse mesh of cubes of side length $L_1 = 75\mu m$, with the markers representing the CV centroids. b) The penetrating network vessels are embedded into the domain. CVs with at least one coupling point are labelled and further discretised using cubes of side length $L_2 = L_1/2$. c) The penetrating vessel network is re-embedded into the non-uniform mesh, and the CVs that still contain multiple coupling points, where the first level of refinement was insufficient, are marked for successive refinement and are further discretised using cubes of side length $L_3 = L_1/4$. Cells of side length L_1 neighbouring cells of side length L_3 are also further discretised to cells of side length L_2 to ensure a smooth transition in size between contiguous cells. d) The penetrating vessel network is then re-embedded into the non-uniform mesh, and the final element-to-element relations for the structured mesh are stored.

the cells with multiple coupling points down to CV of $L_3 = L_2/2$, for which the finer mesh using cubes of side length L_2 was found to be insufficient to prevent coupling point overlap. To ensure mesh quality, it is desirable to create a mesh with a smooth transition between the coarse and fine regions. Hence, after step (c) in Figure 4.2, any remaining cells of side length L_1 neighbouring cells of side length L_3 are also further discretised to cells of side length L_2 to ensure a smooth expansion rate. This, in turn, will also minimise the mesh non-orthogonality angle and skewness effects, which are discussed in Section 4.2.3. Finally, the connectivity of the continuum nodes is modified according to Figure 4.3, and the corresponding element-to-element relations in the structured grid are stored.

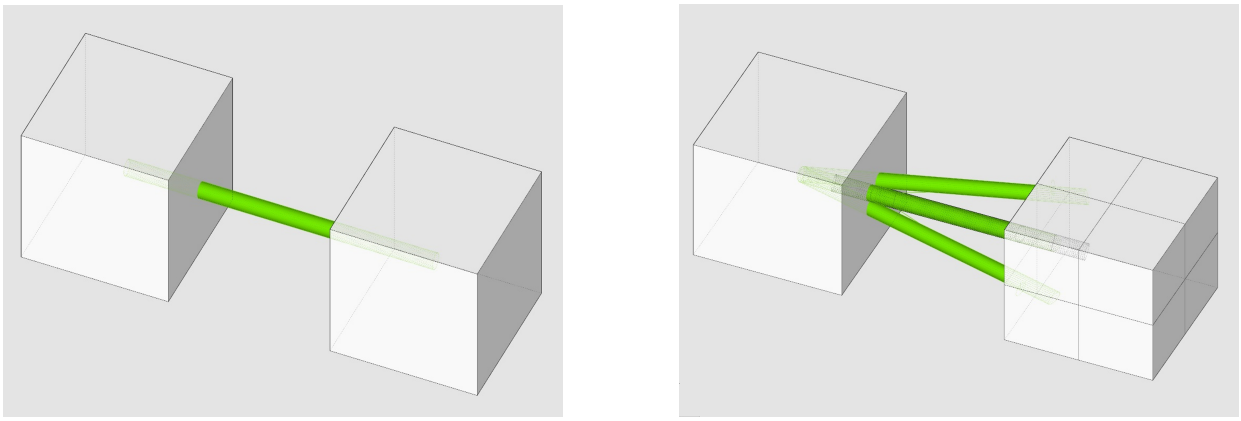

Figure 4.3: (a) When two neighbouring CV cubes are of the same size, connect the centre nodes. (b) When a larger CV cube of side length L_1 or L_2 is adjacent to a smaller CV cube of side length L_2 or L_3, respectively connect the centroid node of the larger CV cube to the four centroid nodes of the smaller CV cubes.

4.2.3 Modelling Blood Flow in the Capillary Bed

As discussed in Section 2.6, when modelling the capillary bed as a porous medium, the macro-scale flow through the capillary bed can be described by the volume-averaged form of Darcy's law in Equation (2.7). We combine Equation (2.7) with the principle of mass conservation in Equation (4.1):

$$\nabla \cdot \mathbf{u}_c = S \tag{4.1}$$

where S represents any source or sink flow (per unit volume) into or out of the porous media, giving rise to Poisson's Equation in 3-D:

$$-\nabla \cdot (\mathbf{K}\nabla P) = S \tag{4.2}$$

Poisson's equation in Equation (4.2) is characteristic of a second-order continuum mechanics problem, and thus we use a second-order accurate FV discretisation scheme to solve for the pressure field. The equation discretisation procedure is divided into two steps. In the first step, the conservation PDE in Equation (4.2) is integrated and transformed into balance algebraic equations over each element. Integrating Equation (4.2) over an arbitrary CV element C and applying the divergence theorem to the volume integral we get:

$$-\int_{V_C} \nabla \cdot (\mathbf{K}\nabla P)\, dV = -K \oint_{S_C} d\overrightarrow{S} \cdot (\nabla P) \tag{4.3}$$

where, given the isotropic, diagonally dominant structure of the permeability tensor,[41] we have used the approximation that $\mathbf{K}\nabla P \approx K\nabla P$ (where $\mathbf{K}_{11} = \mathbf{K}_{22} = \mathbf{K}_{33} = K$). The surface integral can then be replaced by summation over the CV faces through the use of simple mean value integration, in which the pressure gradient is evaluated at the centroid (f_i) of the surface:

$$-K \oint_{S_C} d\overrightarrow{S} \cdot (\nabla P) = -K \sum_{f \in faces(C)} \int_f d\overrightarrow{S} \cdot (\nabla P) \approx K \sum_f -\overrightarrow{S}_{f_i} \cdot (\nabla P)_{f_i} \tag{4.4}$$

The major focus in discretisation here will be on the second step, which involves the linearization of the surface flux in Equation (4.4) in a non-uniform mesh setting. The pressure gradient in Equation (4.4) needs to be evaluated at the face centroid to maintain the second-order accuracy of the scheme.[221],[228],[229] When the two neighbouring cube CV are of the same size, the surface normal vector $\overrightarrow{S}_{f_i}$ and the line vector $\overrightarrow{CN_i}$ connecting the two cell centroids straddling the surface S_{f_i} are in parallel, as shown in Figure 4.4(a). This is known as an orthogonal neighbouring arrangement, and in such a case the term $(\nabla P)_{fi} \cdot \overrightarrow{S}_{fi}$ can be easily computed using a central differencing scheme:

$$(\nabla P)_{fi} \cdot \overrightarrow{S}_{fi} \approx S_{f_i} \frac{P_{N_i} - P_C}{|\overrightarrow{CN_i}|} \tag{4.5}$$

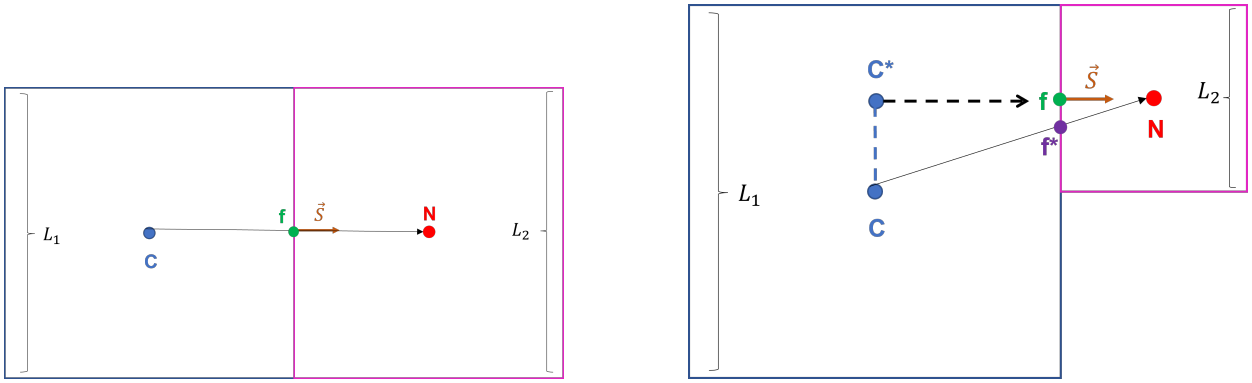

Figure 4.4: 2D projection of an orthogonal (a) and non-orthogonal (b) neighbouring arrangement between two adjacent cube CVs. The DGEM method in (b) is applied to construct a virtual grid point for the larger cube of side length L_1. The virtual grid point for the smaller cube is maintained at its centroid.

When the neighbouring orientation is non-orthogonal, which means that there exists a non-zero angle between $\overrightarrow{S}_{f_i}$ and $\overrightarrow{CN_i}$ as in Figure 4.4(b), then $(\nabla P)_{fi} \cdot \overrightarrow{S}_{fi}$ can no longer be explicitly expressed solely in terms of the pressure values of the two centroids straddling the surface. In such cases, the diffusive flux between two CVs can be divided into two parts: a principal (or orthogonal) flux that can be expressed in terms of the values at the nodes straddling the surface, and a non-orthogonal correction or cross-diffusion term, the computational molecule or stencil of which would include 'second neighbours', or non-conjunctional CVs not directly neighbouring cell C.[221],[228]

This non-orthogonality can be quantified by the angle between $\overrightarrow{S}_{f_i}$ and $\overrightarrow{CN_i}$, which can range from $0°$ (best) to $90°$ (worse):[221],[228],[230]

$$\theta = \arccos\left(\frac{\overrightarrow{S}_{f_i} \cdot \overrightarrow{CN_i}}{|\overrightarrow{S}_{f_i}||\overrightarrow{CN_i}|}\right) \tag{4.6}$$

The larger the angle θ, the larger the explicit (non-orthogonal) flux contribution term, and the less robust the discretisation method becomes.[228] Higher degrees of non-orthogonality should generally be avoided since they could cause numerical instability.[221],[228] The non-orthogonality angle throughout most of the voxel domain is $0°$ (since it is mostly occupied by CVs with an orthogonal neighbouring arrangement). By bounding the smoothness expansion rate between neighbouring CVs of different sizes to 2 as explained in Section 4.2.2, the non-orthogonality angle for the geometric neighbouring arrangement shown in Figure 4.4 is set to $\approx 25°$, which is well within the acceptable limit that has been proposed of below

$60°$.[221],[230]

Here we also introduce the concept of mesh skewness. Skewness between two centroids C and N_i is characterised by the non-coincidence between the face centroid (f_i) and the intersection point (f_i^*) between the line $\overrightarrow{CN_i}$ and the interface, as shown in Figure 4.4(b). To maintain the second-order accuracy of the scheme, all pressure gradients at the interface surfaces need to be calculated at or interpolated to the point f_i.[228] If f_i^* is instead used as the integration point in Equation (4.4), the accuracy of face integrals is effectively reduced to first order,[221],[231] thereby introducing a numeric-diffusion type of error called the skewness error, the influence of which in highly distorted meshes could be significant.[221] As is the case with non-orthogonality, it is desirable to keep mesh skewness to a minimum. Mesh skewness can be quantified by a skew factor[221]:

$$\text{skew factor} = \frac{|\overrightarrow{f_i f_i^*}|}{|\overrightarrow{CN_i}|} \tag{4.7}$$

Again, as with the non-orthogonality angle, we can calculate the skewness factor from the geometrical arrangement in Figure 4.4(b), and find that it has maximum value of 0.14, which is within the acceptable range for meshes of reasonable quality, reported to have a skew factor of less than one.[221]

To proceed, we simplify the nomenclature and rewrite Equation (4.2) in its more rudimentary and intuitive form:

$$\sum_{N_i \in \mathcal{N}(C)} \phi_{C \to N_i} = S_c \tag{4.8}$$

where S_c represents the absolute source or sink flow (in $m^3 s^{-1}$) into or out of the CV, $\mathcal{N}(C)$ represents the set of CVs directly adjacent to cell C and $\phi_{C \to N_i}$ represents the flow flux from the 'owner' CV cell C to the 'neighbour' CV cell N_i through the mutual surface S_{f_i} with centroid f_i and the unit normal vector $\hat{n}_{C \to N_i}$ that points outwards from the 'owner' CV cell C:

$$\phi_{C\to N_i} = -KS_{f_i}(\nabla P)_{f_i} \cdot \hat{n}_{C\to N_i} \tag{4.9}$$

We employ the direct gradient evaluation method (DGEM) to decompose $\phi_{C\to N_i}$ for the particular non-orthogonal neighbouring arrangement demonstrated in Figure 4.4(b) into its orthogonal and non-orthogonal parts. The core idea of the DGEM scheme is to construct two virtual points, one for each CV involved in a non-orthogonal neighbouring arrangement, on the mid-perpendicular line of the interface that passes through the surface centroid f_i.[229],[231]

Different choices for the location of the virtual points are possible (see[231]–[233]). In this study, the virtual point for the larger cell in a non-orthogonal neighbouring arrangement is obtained from the orthogonal projection of the CV cell centroid onto the mid-perpendicular line, while the virtual point for the smaller cube is maintained at the CV centroid, as outlined in Figure 4.4(b). Assuming that cell C in Equation (4.9) is the larger cube with side length L_C and cell N_i is the smaller cube with side length L_{N_i}, then the mutual face surface area is $L_{N_i}^2$ and the orthogonal distance is $L_C + L_{N_i}$. Hence, using Equation (4.9), we can express the diffusive flux from centroid C to N_i as:

$$\phi_{C\to N_i} = \frac{2KL_{N_i}^2}{L_c + L_{N_i}} (P_{C^*} - P_{N_i}) \tag{4.10}$$

where P_C^* is the interpolated pressure at the virtual point of the larger cube, and L_C and L_{N_i} are the side lengths of the FV cells. P_{C^*} can be approximated using the following second-order expression from the Taylor series expansion:

$$P_{C^*} = P_C + (\nabla P)_C \cdot \overrightarrow{CC^*} \tag{4.11}$$

Inserting Equation (4.11) into Equation (4.10), we obtain the decomposition of the diffusive flux term into its orthogonal and non-orthogonal parts:

$$\phi_{C\to N_i} = \frac{2KL_{N_i}^2}{L_c + L_{N_i}} (P_C - P_{N_i}) + \frac{2KL_{N_i}^2}{L_c + L_{N_i}} (\nabla P)_C \cdot \overrightarrow{CC'_{N_i}} \tag{4.12}$$

Note that the orthogonal contribution to the flux, which is the first part of the RHS in Equation (4.12), explicitly depends only on the pressure values of the centroids straddling the interface surface. In the orthogonal arrangement where FV cells C and N_i are of the same size, the skewness and hence the non-orthogonal flux contribution (the second part of the RHS in Equation (4.12)) is zero, and the orthogonal contribution is the same as that in Equation (4.5). For non-orthogonal neighbouring arrangements, the evaluation of the gradient term (∇P_C) in the interpolation of Equation (4.11) is normally the main source of error in the DGEM method.[231]

In models of fluid dynamics, the boundedness of the solution may not be guaranteed when evaluating the gradient term in Equation (4.12).[221],[231] Indeed, when attempting to account for the non-orthogonal flux contributions by using the Green-Gauss theorem to evaluate the pressure gradients, the capillary CV pressures were no longer bound by the boundary pressures of the system that are prescribed at the cortical surface. Often, if boundedness is essential (as is in our case), it is permissible and even sometimes necessary to relax the order of accuracy and disregard the non-orthogonal contribution in certain regions of the discretisation domain,[221],[231] which is the approach that is followed in this study.

To examine if the non-orthogonal contributions can be ignored without significant loss of accuracy, we compared the steady-state pressure and flow fields in a voxel network with a non-uniform capillary bed mesh obtained from applying the proposed meshing scheme, to those from a voxel network with a more refined, uniform mesh in which there are no regions of mesh non-orthogonality and skewness (see Section 4.3). Hence, accounting only for orthogonal contributions, we can simplify the flux between two adjacent centroids in Equation (4.12) and express it in terms of the pressures at the two centroids:

$$\phi_{C \to N_i} = G^{eff}_{C,N_i} \left(P_C - P_{N_i} \right) \tag{4.13}$$

where G^{eff}_{C,N_i} is the effective conductance between the two centroids that can be given in terms of K and the side lengths (L_c and L_{N_i}) of the FV cubes:

$$G^{eff}_{C,N_i} = \frac{2K L^2_{N_i}}{L_c + L_{N_i}} \tag{4.14}$$

4.2.4 The Distributed Source Term

We evaluate the dynamic flow through the penetrating vessels using the model developed in Chapter 3. The source term in Equation (4.2) forms the link between the 0-D penetrating cortical network and the homogenised capillary continuum representations. A suitable coupling model for the transmittance of flow between the two mediums should ensure scale invariance, in which, as long as the size of the CV discretisation is within the convergence range, the source/sink flow between the 1-D tubular network terminals and the 3-D capillary continuum should be independent of the discretisation level of the capillary bed. Hence, we employ the local support function, as proposed by Hodneland et al.,[217] which entails the distribution of the volumetric source flow Q^{ϵ} $[s^{-1}]$ from the network terminal endings over the region of the capillary domain that is enclosed within a specified (prescribed) support radius (ϵ) around the terminal endings. Similarly, for terminal venules, which function as sink vessels, the opposite process takes place with fluid uptake instead of distribution.

In the limit of a localised source flow, in which all the source flow within the capillary bed were to be restricted to the terminal node of the penetrating vessel, the support radius would be $\epsilon = 0$, giving rise to what is essentially the Dirac measure, a mathematical artifice for representing an extremely localized function within a finite total area[189]:

$$Q^0(\mathbf{x}) = \int_{\Omega} Q(\mathbf{y})\delta(\mathbf{x}-\mathbf{y})\, d\mathbf{y} \tag{4.15}$$

where Ω represents the capillary domain. The choice of the Dirac measure, however, might not be physically sound,[217] since it implies the collection of fluid flow from a terminal vessel with a finite radius into a singular, infinitesimally small point in space. The numerical accuracy of elliptic PDEs with Dirac source terms can also be below order estimates given that the solution is not in $H^1(\Omega)$.[65],[217],[234] The problem of numerical stability can be mitigated by using smoothing kernels for the source term itself, by using locally refined meshes, or quasi-uniform meshes.[65],[235] And yet, in a multiscale setting, where different mathematical formulations for the different sub-systems are combined into a single system of equations, the use of the Dirac measure to represent the source flow can give rise to scale variant, non-convergent solutions, in which the pressure drop at the multiscale system transitional

interface keeps increasing with smaller local FV sizes (see Figure 4.10 and Section 4.4).

The idea proposed by Hodneland et al.[217] is to replace the Dirac measure with a more realistic model of the source region with some prescribed characteristic radius ϵ, representing the unresolved fine scale network within the capillary continuum around the terminal endings through which blood from the terminal vessel is distributed. In such a manner, the span of the source or sink flow becomes approximately independent of the mesh discretisation choice, so long as sufficient mesh refinement is locally introduced. In what follows, we describe how the distributed flow source model can be incorporated into our dynamic multiscale setting. We first define the support function η^ϵ:

$$\eta^\epsilon(x) := \frac{1}{\epsilon^3}\eta\left(\frac{x}{\epsilon}\right) \tag{4.16}$$

where η is a positive and continuously differentiable shape function and x is the distance from the terminal ending. In principle, η should reflect the sub-resolution structure of the surrounding capillary microcirculation, but due to the lack of such data the authors of the distributed source model have adopted the generic, monotonically decreasing function choice[217]:

$$\eta(x) = \begin{cases} Cexp\left(\frac{1}{|x|^2-1}\right) & x < 1 \\ 0 & x \geq 1 \end{cases} \tag{4.17}$$

The expression for the volumetric source term then becomes:

$$Q^\epsilon(\mathbf{x}) = \int_\Omega Q(\mathbf{y})\eta^\epsilon(|\mathbf{x}-\mathbf{y}|)\, d\mathbf{y} \tag{4.18}$$

To ensure global mass balance from the terminals (such that Equation (4.18) converges to (4.15) in the limit as $\epsilon \to 0$), the source distribution function in Equation (4.16) must integrate to unity over the spatial domain. Representing the integral in spherical coordinates, we can hence use this fact to find the analytical value for the constant C in Equation (4.17):

$$\int_{\Omega} \eta^{\epsilon}(|\mathbf{x}|)\, d\mathbf{x} = 1 = C \int_{\phi=0}^{\pi} \int_{\theta=0}^{2\pi} \int_{r=0}^{\epsilon} \frac{1}{\epsilon^3} exp\left(\frac{1}{\left(\frac{r}{\epsilon}\right)^2 - 1}\right) r^2 sin(\phi)\, dr d\, d\theta\, d\phi \tag{4.19}$$

Hence the constant C can be computed as:

$$C = \frac{1}{4\pi \int_0^1 exp\left(\frac{1}{u^2-1}\right) u^2\, du} \tag{4.20}$$

where we have used the change in variables $u = \frac{r}{\epsilon}$. We numerically evaluated the integral in Equation (4.20) and found it has a value of 0.0351. Using the $(\sim)$ notation to refer to variables from the cortical penetrating tree networks, the volumetric source term can be related to the absolute flow $\tilde{q}_k$ (in m^3/s) from/into the terminal node by:

$$Q^{\epsilon}(\mathbf{x}) = \tilde{q}_k \eta^{\epsilon}(|\mathbf{x} - \mathbf{x}_k|) \tag{4.21}$$

In the flow-distribution region around each terminal $(|x - x_k|) \leq \epsilon)$, we require that the pressure drop between the terminal node N_k and the surrounding capillary bed scales with the terminal flow up to a user-provided constant γ $[m^4 s/kg]$[217] representing the conductance in the unresolved network at the arteriole-capillary (γ_a) and capillary-venule (γ_v) interfaces, extending from the terminal node N_k:

$$\tilde{q}_k = \gamma \left(\tilde{P}_k - \int_{\Omega} \eta^{\epsilon}(|\mathbf{x} - \mathbf{x}_k|) P_c(\mathbf{x})\, d\mathbf{x} \right) \tag{4.22}$$

where $\tilde{P}_k$ and $P_c(\mathbf{x})$ are the pressure values at the terminal node and in the capillary continuum, respectively. Let $\mathcal{N}(N_k)$ be the set of all capillary nodes (j) receiving a non-zero fluid distribution $(\eta^{\epsilon}(|\mathbf{x} - \mathbf{x}_k|) > 0)$ from terminal node N_k: *i.e.* $\mathcal{N}(N_k) := \{j : |\mathbf{x}_j - \mathbf{x}_k| < \epsilon\}$. The condition in Equation (4.22) can then be approximated as:

$$\tilde{q}_k = \gamma \left(\tilde{P}_k - \sum_{j \in \mathcal{N}(N_k)} \eta^{\epsilon}(|\mathbf{x}_j - \mathbf{x}_k|) P_j |\Omega_j| \right) \tag{4.23}$$

where P_j is the CV centroid pressure, and $|\Omega_j|$ is the CV volume. In moving from the analytical representation in Equation (4.22) to the discrete one in Equation (4.23), we have assumed that the values of the pressure (P_j) and the support function ($\eta^\epsilon(|\mathbf{x}_j - \mathbf{x}_k|)$) at each CV centroid can be used to represent the values throughout the whole CV:

$$\int_{CV_j} \eta^\epsilon(|\mathbf{x} - \mathbf{x}_k|) P_c(\mathbf{x})\, d\mathbf{x} \approx \eta^\epsilon(|\mathbf{x}_j - \mathbf{x}_k|) P_j |\Omega_j| \tag{4.24}$$

Following the spatial discretisation of the capillary continuum, there will be CVs whose centroids are within the radius of influence (*i.e.* part of $\mathcal{N}(N_k)$) and are thus included in the summation in Equation (4.23), but which contain segments that are outside the radius of influence (grey CVs in Figure 4.5). Comparably, there are CVs with regions inside the radius of influence but whose centroids lie outside the peripheries of the region of influence and are thus excluded from the summation in Equation (4.23) (blue CVs in Figure 4.5). Such partial volume effects, along with the approximation made in Equation (4.24), undermine the numerical evaluation of the integral in Equation (4.22) as we move from the integral to the discrete representation, and has resulted in non-conservative flow between the discrete vessels and the capillary continuum in our simulations. Intuitively, a finer mesh around the coupling points, as per the proposed meshing scheme, decreases the ratio $\frac{\epsilon}{L}$, thereby reducing these sources of errors and ensuring numerical flow conservation.

Due to slight discrepancies between the numerical and analytical integration of the support function in Equation (4.16), and to guarantee the conservation of flow at the interface, the final value of C in Equation (4.20) for each terminal ending is adjusted such that:

$$\sum_{j \in \mathcal{N}(N_k)} \eta^\epsilon(|\mathbf{x}_j - \mathbf{x}_k|) |\Omega_j| = 1 \tag{4.25}$$

4.2.5 Numerical Implementation of Flow

We connect the different segments of the multiscale model described in Sections 4.2.3, 4.2.4 and Chapter 3 using the fundamental premises of mass conservation, such that the sum of

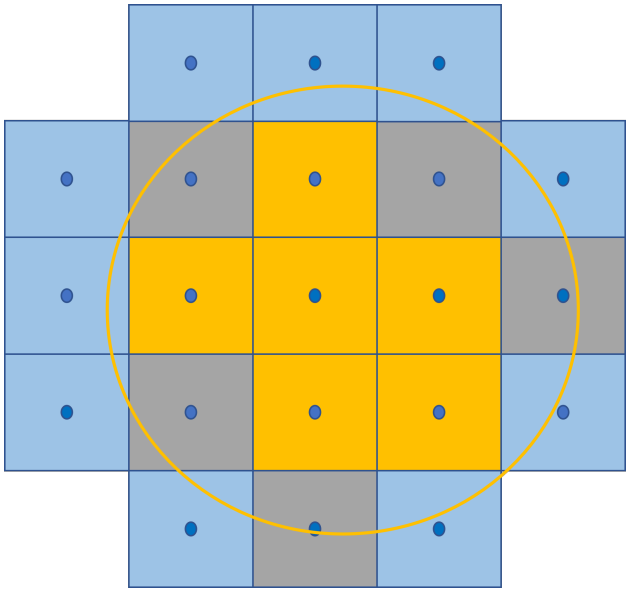

Figure 4.5: Capillary CVs surrounding the terminal ending with a prescribed radius or influence ϵ (orange circle). Orange CVs are those that are fully within the radius of influence. Grey CVs are those whose centroids are within the radius of influence but which contain segments outside the radius of influence. Blue CVs are those whose centroids are outside the radius of influence but which contain segments within the radius of influence.

flow out of any internal node is zero. For a node C that is part of the capillary bed continuum, the flow conservation condition in Equation (4.8) becomes:

$$\sum_{N_i \in \mathcal{N}(C)} G^{eff}_{C,N_i} \left(P_C - P_{N_i}\right) - \sum_{k \in \mathcal{T}_a(C)} Q^{a,k}_{out} \eta^{\epsilon}(|\mathbf{x}_C - \mathbf{x}_k|)|\Omega_C| + \sum_{k \in \mathcal{T}_v(C)} Q^{v,k}_{in} \eta^{\epsilon}(|\mathbf{x}_C - \mathbf{x}_k|)|\Omega_C| = 0 \tag{4.26}$$

where the first term results from the FV discretisation, k refers to the terminal arteriole (a) or venule (v) network node, and $\mathcal{T}_a(C)$ and $\mathcal{T}_v(C)$ correspond, respectively, the terminal arteriole and venule nodes with a non-zero source flow to the capillary node C. Inserting the expressions for the network inlet and outlet flows in Equation (3.28) into Equation (4.26), we obtain:

$$\begin{aligned} &\sum_{N_i \in \mathcal{N}(C)} G^{eff}_{C,N_i} \left(P_C - P_{N_i}\right) + |\Omega_C| \sum_{k \in \mathcal{T}(C)} \eta^{\epsilon}(|\mathbf{x}_C - \mathbf{x}_k|) \Big[\frac{1}{\mathcal{R}} \left(P_k - P_j\right) \\ &- \frac{R^2}{6\nu\mathcal{R}} \left(\frac{dP_k}{dt} - \frac{dP_j}{dt} \right) + \frac{\overline{C}}{6} \left(2\frac{dP_k}{dt} + \frac{dP_j}{dt} \right) + \frac{\overline{P}_v}{2} \frac{dC}{dt} \Big] = 0 \end{aligned} \tag{4.27}$$

where j refers to the preceding network node connected to the terminal node k. The final ex-

pression for the computational stencil of the distributed source flow from a terminal node is the same whether the terminal node belongs to the arteriole or venule network, as expected, even though the expressions for Q_{in} and Q_{out} are different (in Equation (3.28)), since what determines if a terminal vessel functions as a source or a sink vessel is the prescribed pressure BC at the cortical node of its penetrating tree. For a terminal arteriole or venule node k, connected to the network node j, and for which the source flow into or out of the capillary bed is given by Equation (4.23), the flow conservation condition becomes:

$$\frac{1}{\mathcal{R}}\left(P_k - P_j\right) - \frac{R^2}{6\nu\mathcal{R}}\left(\frac{dP_k}{dt} - \frac{dP_j}{dt}\right) + \frac{\overline{C}}{6}\left(2\frac{dP_k}{dt} + \frac{dP_j}{dt}\right) + \frac{\overline{P}_v}{2}\frac{dC}{dt} + \gamma\left(P_k - \sum_{j\in\mathcal{N}(N_k)} \eta^{\epsilon}(|\mathbf{x}_j - \mathbf{x}_k|)P_j|\Omega_j|\right) = 0 \tag{4.28}$$

For the interior network nodes of the penetrating arterioles and venules, the mass conservation condition is coupled with that of static pressure matching at the nodes where the vessels intersect. The zero-sum flow condition then becomes:

$$\sum_{\beta\in\mathcal{N}(k)} Q^v_{in}(k,\beta) = 0 \tag{4.29}$$

where $\mathcal{N}(k)$ is the set of network nodes connected to node k, and $Q^v_{in}(k,\beta)$ is the inlet flow in Equation (3.28) of the vessel with k and β as the inlet and outlet nodes, respectively. Equations (4.27), (4.28), and (4.29) are first-order linear ODEs describing the flow conservation condition for each type of internal node. In all three cases, the flow into any internal node is expressed in terms of the pressure at the node and the surrounding nodes, and the relevant vessel, fluid, FV geometry, and/or capillary permeability properties. We can combine these equations to create a linear system of the form in Equation (4.30), the solution of which characterises the pressure at the internal nodes ($\mathbf{p}_{int}$) containing both the penetrating vessel trees nodes and the FV-discretised homogenised capillary bed nodes, once the pressure profile at the external nodes on the pial surface ($\mathbf{p}_b$) is specified:

$$\mathbf{B}_{int}\frac{d\mathbf{p}_{int}}{dt} + \mathbf{A}_{int}\mathbf{p}_{int} = -\mathbf{B}_b\frac{d\mathbf{p}_b}{dt} - \mathbf{A}_b\mathbf{p}_b - \mathbf{C} \tag{4.30}$$

$$\mathbf{A} = \left(\begin{array}{c|c} K\begin{bmatrix} FV_{c\to c} \end{bmatrix} & S^{steady}_{a,v\to C} \\ \hline S^{steady}_{C\to a,v} & \begin{array}{c} N^{steady}_{a,v\to a,v} \\ \\ S^{steady}_{a,v\to a,v} \end{array} \end{array}\right) \quad \mathbf{B} = \left(\begin{array}{c|c} \mathbf{0} & S^{dynamic}_{a,v\to C} \\ \hline \mathbf{0} & N^{dynamic}_{a,v\to a,v} \end{array}\right) \quad \mathbf{P}_{int} = \begin{pmatrix} P_{C,1} \\ \vdots \\ P_{C,end} \\ P_{N_{int},1} \\ \vdots \\ P_{N_{int},end} \end{pmatrix} \quad \mathbf{C} = \begin{pmatrix} C_{a,v\to C} \\ \vdots \\ C_{a,v\to a,v} \\ \vdots \end{pmatrix} \tag{4.31}$$

Each equation (row) in the linear system of 4.30 is thus a restatement of the zero-sum flow conditions for the internal nodes. Matrices **A** and **B** represent the steady-state and dynamic portions of Equations (4.27), (4.23), and (4.29), respectively. The sub-matrix $FV_{c\to c}$ in **A** denotes the interactions among the nodes of the capillary bed, based on the connectivity of the capillary centroids and the values of G^{eff}_{C,N_i} in Equation (4.14), and only needs to be constructed once for the dynamic simulation, during the meshing procedure. Any potential dynamic modulations happening within the capillary bed can be incorporated by changes in the value of the permeability constant K, either globally or locally.

The other entries of the **A** and **B** matrices are updated quasi-statically following the changes in vessel compliance, and the ensuing changes in vessel radius and resistance, as described in the model in Chapter 3. $S_{a,v\to C}$ denotes the contribution of the terminal nodes to the zero sum flow conditions in the capillary bed according to Equation (4.27), and $S_{C\to a,v}$ denotes the contributions of the capillary bed to the zero sum flow condition of the terminal nodes in

Equation (4.28). $N_{a,v\rightarrow a,v}$ corresponds to the interaction among the nodes of the penetrating arteriole and venule trees according to Equation (4.29). The entries of the vector **C** correspond to the dynamic compliance term in Equation (3.28). We use an implicit Euler solver for Equation (4.30) due to the stiffness of the system to ensure numerical stability.

4.2.6 Parameter Assignment

In the original steady-state model by Hodneland et al.,[217] there was no physiological basis behind the choice of the input parameters ($X_i = K$, γ_a, and γ_v), which encapsulate the sub-imaging resolution connective and geometrical properties of the capillary bed. Hence, in this study, we establish the parameter values by determining the ranges that provide physiologically meaningful pressure and flow distributions throughout the hybrid network. We first conduct an MCF analysis (see[204]) for the steady-state case to ensure the physiologically relevant parameter value assignments of the parameters ($X_i = K$, γ_a, and γ_v). We sample each of the three input parameters independently over the range of parameter values shown in Figure 4.6(a), for a total set of $N = 8 \times 10^4$ MC runs. We compute the steady-state pressure and flow profiles for each MC run, and partition the MC realisations into complementary behavioural (B), or acceptable, and non-behavioural ($\overline{B}$) subsets based on whether or not the steady-state model outputs complied with the predetermined physiological target ranges, defined as follows:

1. The steady-state internal nodes pressure profile is bounded by the prescribed inlet and outlet cortical pressures.
2. The steady-state whole network perfusion should ensure global flow conservation (*i.e.*, $Q_{in}^{network} = Q_{out}^{network}$).
3. The flow through all the arteriole and venule penetrating vessels obeys the expected directionality; *i.e.* from the cortical surface to the capillary bed for the arterioles and vice versa for the venules.
4. The distribution of the pressure within the capillary bed has a range of at least 10mmHg.
5. The regional cerebral blood flow (rCBF) per 100g of tissue, or perfusion, within the

central ROI, falls within the $45 - 65ml/100g/min$ range. The relationship between flow and perfusion in this context can be defined in Equation (4.32):

$$rCBF = \frac{100Q}{V\rho\,(1-\lambda)} \tag{4.32}$$

in which V is the flow domain volume, ρ is the parenchymal tissue density, taken to be $1.04g/cm^3$,[236] and λ is the vascular volume fraction, taken to be 3.19%.[226] For the MCF analysis, Q (in mL/min) is defined as the sum of flow leaving the terminal arterioles confined within the central ROI and into the capillary bed, and V is the volume of the central ROI. We examine the reasons behind choosing the target ranges mentioned above in Section 4.4. We map the $(B - \overline{B})$ partitioning of the output for each run back onto the input parameters, each of which is also partitioned into behavioural and non-behavioural subsets. We then use the two-sample Kolmogorov-Smirnov test to determine if each parameter's behavioural and non-behavioural subset distributions are different, and plot a three-dimensional projection of the behavioural sub-samples to determine the range of permissible values.

To examine the dynamic behaviour of the network, we consider its response to a 7.5% drop in the arterial inlet pressure (P_0) according to the smooth function in Equation (4.33), while maintaining a constant outlet pressure (P_{out}) and a zero external pressure P_{ext}.

$$P_{inlet} = P_0\left(1 - \left(0.05\left(1 + tanh\left(\frac{t}{2}\right)\right)\right)\right) \tag{4.33}$$

The function is selected to test the model and is not necessarily intended to simulate a real physiological stimulus. The baseline values of the inlet (P_0) and outlet (P_{out}) are set to be 52 and 20 mmHg, respectively, as explained in Section 4.4.

The dynamic parameter values were primarily taken to be the same as those used for the network model in Chapter 3 (Table 2, except that S_σ was set to 6 instead of 4), in which the parameter values chosen from analysing the model output based on an overall understanding of the behaviour of the network physiological response. As previously explained, the values for the time constant and the (maximum and minimum) fractional changes in compliance were based on experimental data and previous modelling studies. However, there is no clear

validation from experimental data for the other values of the compliance feedback model (S_σ,S_τ, G, $\frac{\Delta C^{\pm}}{C_0}$), due to limited data on the dynamic behaviour of the cerebral microvasculature vessels. Hence, given the uncertainty in these parameter values, we conduct a sensitivity analysis of the model to examine how changes in the input values affect the multiscale model output and to explore which input factors influence the model output the most. The ranges for the dynamic input parameters are taken here to be $\pm 25\%$ of their baseline values, while the model outputs are chosen to be the final perfusion inside the central ROI and the final blood volume inside the penetrating vessels.

To conduct the sensitivity analysis, we use the Elementary Effects (EE) method as proposed initially by Morris[237] which produces two measures of sensitivity: the mean (μ_{EE}) and standard deviation (σ_{EE}) of the EEs. As proposed by Campolongo et al,[238] a revised sampling strategy is implemented to facilitate better sampling through the hypercube in the input parameter space, and a third metric ($\mu_{|EE|}$), which takes the absolute values of the elementary effects before averaging, is estimated from the EEs analysis, both of which are carried out at no extra computational cost (same number of model executions). We then analyse the three metrics in tandem to extract the maximum amount of sensitivity information. For a fuller discussion of the meaning of these metrics and the techniques used to calculate them, the reader is referred to the text by Saltelli et al.[204] The use of the EE method is convenient here because it offers the advantage of examining each factor individually (to prevent cancellation effects) across the input space and provides a well-defined strategy to assess the importance of each factor,[204] without the significant cost of sophisticated variance-based techniques.[204],[238] In this study, using 10 trajectories to analyse the effects of the 4 dynamic input parameters required only a total of $N = 50$ model executions when using the EE method. In contrast, with four input factors, variance-based techniques would require a much larger number of model executions ($N > 1000$) to achieve convergence, which, when given the execution time per each MC realisation, would render the computational cost of variance-based techniques excessive for the sole purpose of conducting a parameter sensitivity analyses of the compliance feedback parameter values in Table 2.

Table 4: Results of the MCF analysis showing the permissible range of values for the parameters K, γ_a, γ_v, as well as the p-value obtained from the two-sample Kolmogorov-Smirnov test when comparing the distributions between the behavioural and non-behavioural subsets.

MCF Parameter	K $(\times 10^{-12} m^3 s/kg)$	γ_a $(\times 10^{-16} m^4 s/kg)$	γ_v $(\times 10^{-16} m^4 s/kg)$
Behavioural Range	$1.2 - 7.6$	$0.01 - 7.6 \times 10^5$	$1.6 - 26$
p-value	< 0.001	0.432	< 0.001

4.3 Network Simulation Results

Figure 4.6(a) demonstrates the 3-D projection of the behavioural and non-behavioural sub-samples when conducting the MCF analysis on the model steady-state output for the network generated in Figure 4.2, from which the ranges for the permissible values of the steady-state input parameters are then extracted. For the input ranges shown in Figure 4.6(a), the two-sample Kolmogorov-Smirnov test revealed significant differences between the distributions of the behavioural and non-behavioural sub-samples for the parameters K and γ_v but a non-significant difference between the distributions for γ_a, as indicated by the p-values in Table 4. Figure 4.6(b) presents the two-dimensional projection of the behavioural subsets for K and γ_v ($(K|B)$ vs $(\gamma_v|B)$) over the range of the behavioural values, which are summarised in Table 4, demonstrating a clear inverse relationship between the two parameter values.

Figure 4.7 shows the steady-state (initial) 3-D pressure profile of the capillary bed within the central ROI for the network constructed in Figure 4.2 when a behavioural realisation of the steady-state input factors is randomly chosen. The resulting steady-state capillary perfusion inside the central ROI of the voxel is calculated to be $56.5ml/100g/min$. Assuming a capillary bed volume fraction of 2.22% in grey matter,[239] the steady-state distribution of the CBV within the microvessels can be approximated to be distributed as follows: 13.4% in the arterioles, 37.5% in the venules, and 49.1% within the homogenised capillary bed, for a total baseline CBV of $4.25ml/100g$ of tissue, which is in agreement with the experimentally obtained range of values of $4.6 \pm 1ml/100g$.[240]

Next, and in response to the 7.5% drop in inlet pressure, the dynamic changes in perfusion for both the active and passive (*i.e.* impaired autoregulation) cases are shown in both the whole network (Figure 4.8(a)) and within the capillary bed inside the central ROI domain (Figure

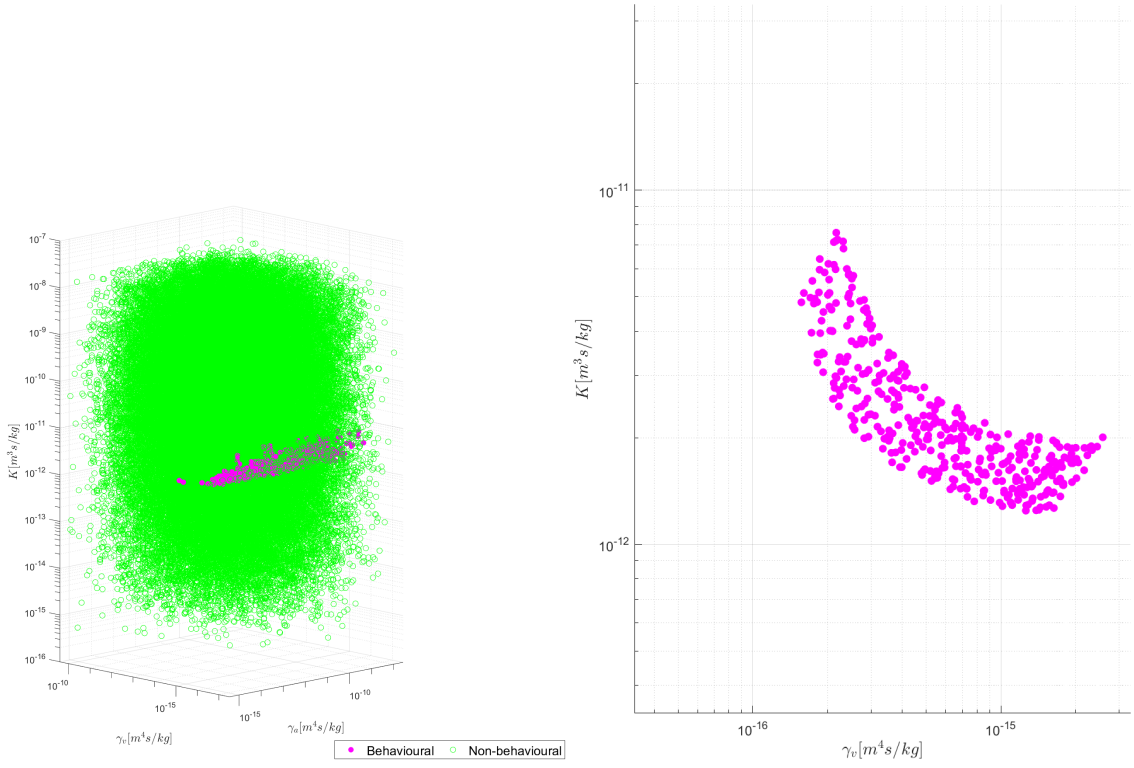

(**a**) (**b**)

Figure 4.6: Three-dimensional projection of the behavioural (magenta) and non-behavioural (green) sub-samples obtained from the MCF analysis ($N = 8 \times 10^4$) of the model steady-state output. The model inputs used in the MCF analysis are the three steady-state input parameters characterising the sub-resolution capillary properties: K, γ_a, and γ_v (a). Two-dimensional projection of the behavioural subset along the K and γ_v parameters (b).

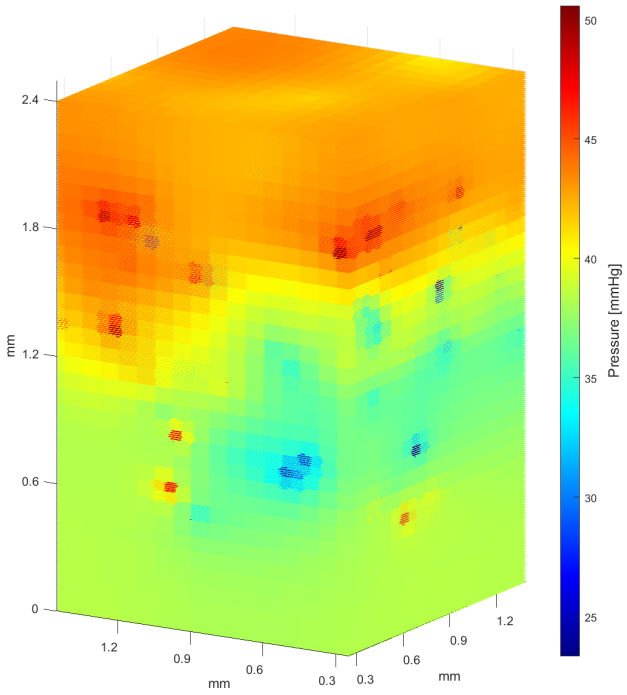

Figure 4.7: The steady-state pressure profile of the capillary bed inside the central ROI, for the network constructed in Figure 4.2, when setting $K = 1.71 \times 10^{-12} m^3 s/kg$, $\gamma_v = 8.20 \times 10^{-16} m^4 s/kg$, and $\gamma_a = 1.17 \times 10^{-10} m^4 s/kg$. The values for the pressure were interpolated from the calculated capillary centroid pressure values using the nearest neighbour interpolation scheme in MATLAB.

4.8(b)). Figures 4.8(c) and 4.8(d) show the dynamic changes in the blood volume inside the penetrating vessels for both the active and passive cases. The job was run using 1 core of one Intel Xeon Platinum CPU 8268 @ 2.90GHz, and 96GB of memory, on a server running Linux (CentOS 8.1), for a total duration of 110 minutes.

W calculate the three metrics of the EE sensitivity analysis from the network's response to the drop in inlet pressure to characterise the relative influences of the compliance feedback parameters on the model outputs, defined in this case to be the final ROI perfusion and the final CBV in the penetrating vessels, and are plotted in Figures 4.9(a) and 4.9(b). The meaning behind the EE sensitivity results is examined in Section 4.4. We also construct input-output scatter plots (see Appendix B.1) to help visualise the total effects of two of the model inputs (S_σ and G) on the model outputs and determine the extent to which the final perfusion and blood volume are affected by changes in those input parameters.

Finally, we examine the impact of the mesh refinement level and the mesh non-orthogonality and skewness, on the steady-state solution. We have found that (ϵ/L_1) needs to be in the

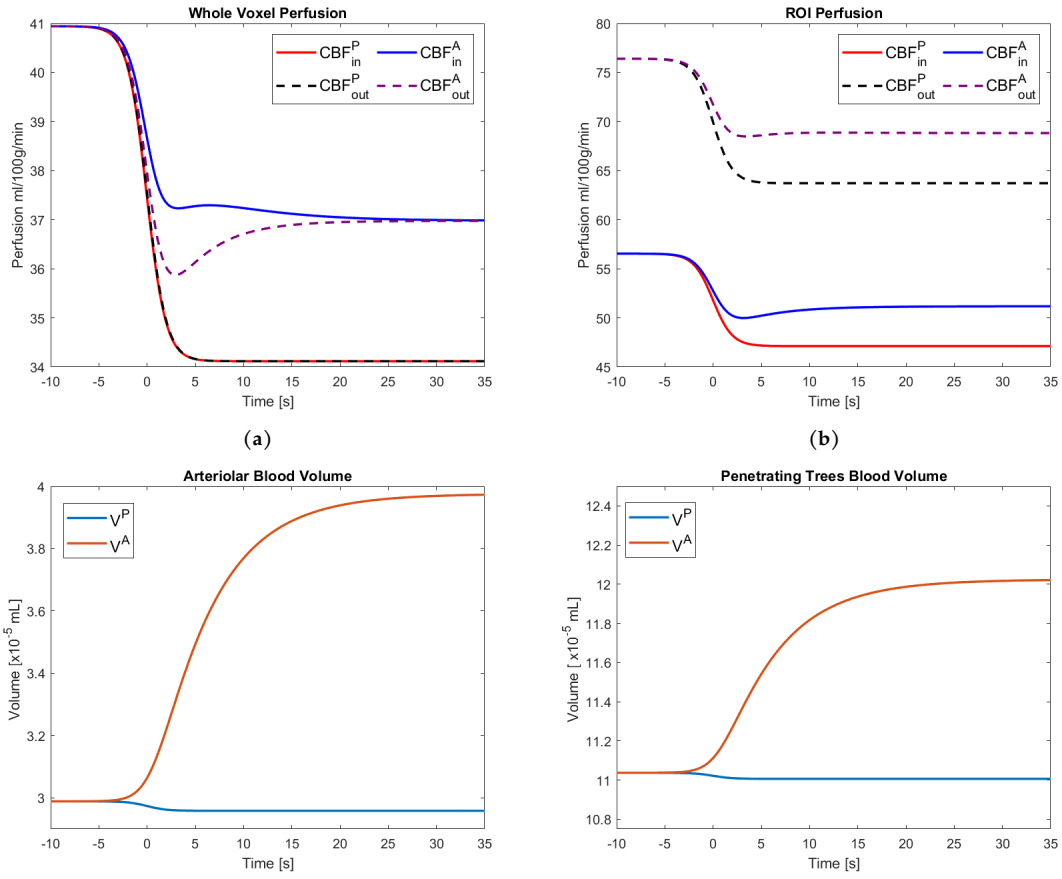

Figure 4.8: The dynamic perfusion through the inlet arterioles and outlet venules of the whole network (a), and through the terminal arterioles and venules inside the central ROI domain (b), and the dynamic changes in the total volume of the arteriole penetrating vessels (c), and the total volume in the arteriole and venule vessels (d), for the network constructed in Figure 4.2, in response to a 7.5% drop in inlet pressure, under both the active (A) and passive (P) cases.

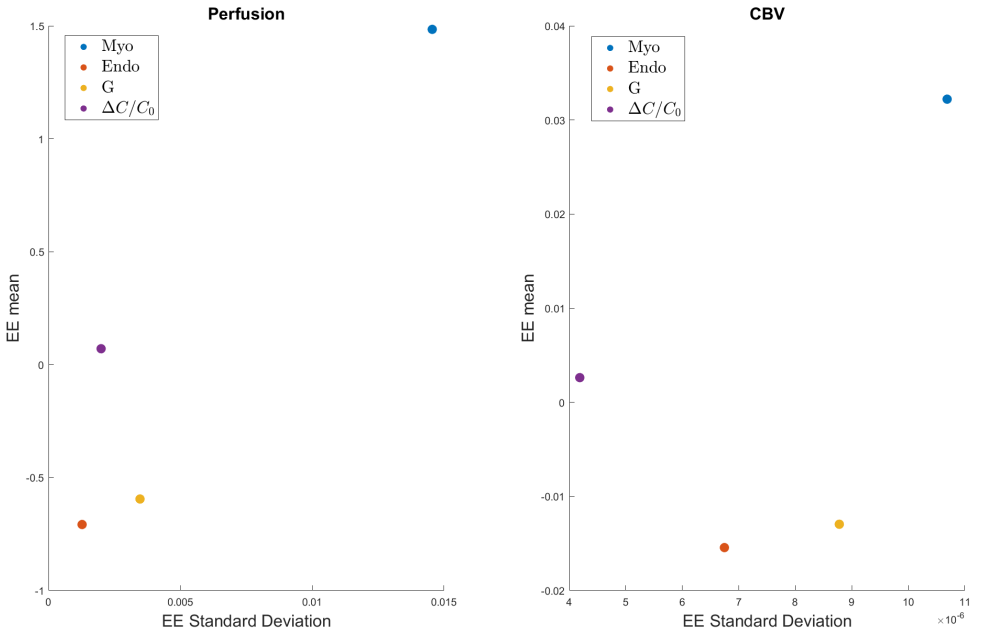

(a)

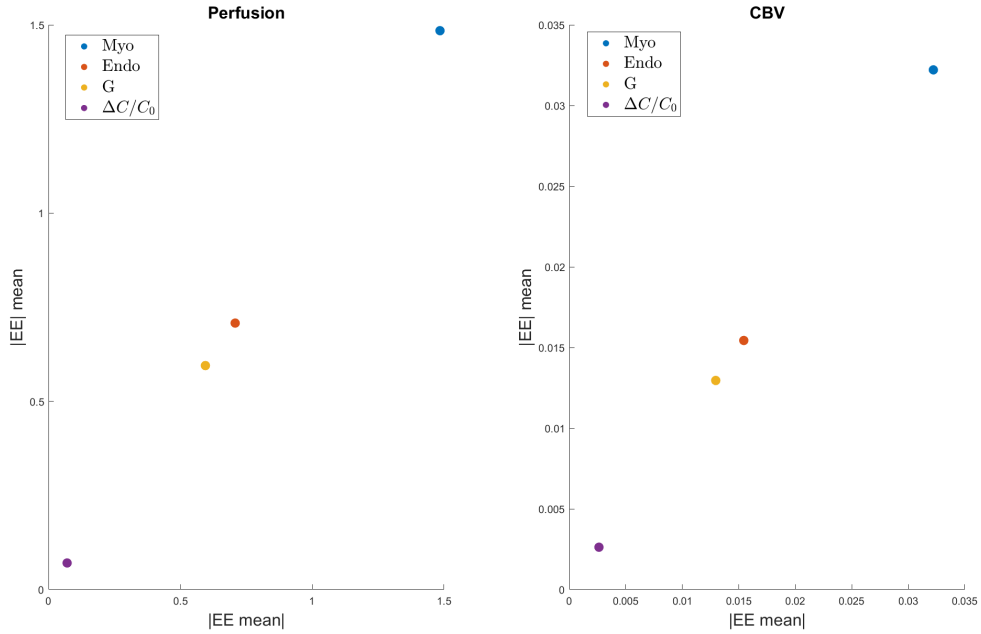

(b)

Figure 4.9: The mean vs the standard deviation of the EEs (a) and the mean of the absolute values of the EEs vs the absolute value of the mean EE (b) based on the effects of fractional changes in each of the dynamic compliance parameters on the final perfusion (left) and CBV (right).

approximate range of $0.35 \leq \epsilon/L_1 \leq 0.45$, to ensure numerical stability. Hence, and to examine solely the influence of the mesh refinement level, the value of ϵ is fixed (to $30\mu m$ as used for the voxel domain with $L_1 = 75\mu m$ in Figure 4.7), and the steady-state flow through the network is compared across the different values for L_1 $(67 - 86\mu m)$. We also compare the results of our model over this range to that in which no coupling scheme is used, where the terminal coupling nodes are simply shifted and superposed to the centroids of the enclosing FVs, as shown in Figure 4.10(c), and a simple condition of pressure continuity is assumed. For validation, we compare the flow throughout the network for both meshing arrangements to that when using a refined uniform meshing scheme of $L_2 = L_1/2 = 37.5\mu m$ which features no mesh non-orthogonality or skewness. Because the computation of the steady-state pressure field inside the $1.5 \times 1.5 \times 2.4mm^3$ voxel requires significant computational resources and memory allocation when using the refined mesh throughout the whole voxel domain, the simulations conducted for validation are carried over a smaller reconstructed voxel domain of $0.75 \times 0.75 \times 2.4mm^3$, with no two coupling points sharing the same FV (hence there is no need for the further discretisation using $L_3 = L_2/2$). The results are shown in Figure 4.10(a). In addition, for the original network shown in Figure 4.2(d), we examine the impact of changing the value of ϵ, the radius of support, within the permissible range described above, on the steady-state flow and pressure profiles, while fixing the values of K, γ_a, and γ_v. The impact of the ϵ value on the network's global flow, the pressure profile within the capillary bed ROI, and the probability density function (PDF) for the pressure distribution throughout the capillary bed, are demonstrated in Figures B3, B4, and B5, respectively.

4.4 Discussion

Several multiscale frameworks employing a porous representation of the capillary bed have been constructed.[129],[133],[217] However, to the best of our knowledge, all these models solely capture the steady-state perfusion by accounting only for the resistive part of the microcirculation, and do not account for the dynamic behaviour of CBF. As a consequence, none of the previous models is suited for modelling the strongly time-dependent and non-linear processes that characterise the dCA mechanisms.[129] Our main contribution here is the development of a comprehensive model that integrates three sub-models at different length scales into a single multiscale model to describe the dynamic haemodynamics of the cerebral grey

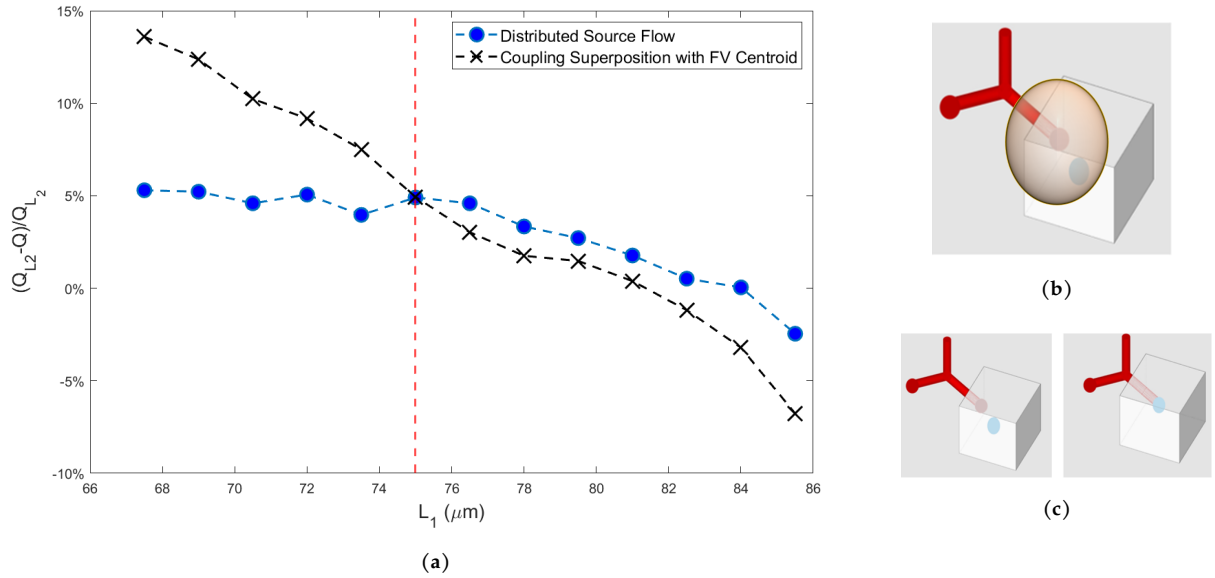

Figure 4.10: (a) The relationship between the value of L_1, the side length of the largest FV, and the network flow (Q) of the reconstructed voxel of size $0.75 \times 0.75 \times 2.4mm^3$, when utilising the distributed flow coupling scheme with $\epsilon = 30\mu m$ (blue line) as depicted in (b) or when assuming a simple condition of pressure continuity between the network and continuum domains (black line) as depicted in (c). The network flows are compared to the flow (Q_{L2}) obtained when using a uniform FV side length of $L_2 = L_1^*/2$ and $\epsilon = 30\mu m$, where $L_1^* = 75\mu m$ (red line) is the largest side length used for the discretisation of the voxel in Figure 4.7.

matter cortex, including the effects of the CBF control mechanisms. The underlying system of equations characterising the spatiotemporal pressure and flow profiles in Equation (4.30) is a linear one, constructed from the integration of linear sub-models, thereby preserving the computational feasibility of the simulations. Furthermore, with only 3 microscale and 4 dynamic feedback parameters, our model remains a compact, albeit physiologically informed representation of the system, avoiding the sometimes highly complex and over-parameterised approach of other authors.

The first sub-model, proposed in Chapter 3, is a 0-D model that describes the dynamics of CBF and CBV in the tubular vessels of the cortical penetrating trees, and this is used in tandem with a compliance feedback model to account for the dCA mechanisms. The second sub-model employs an FV formulation to discretise the homogenised capillary bed and model it as a continuum, relying on a newly devised meshing algorithm that selectively refines the capillary domain to capture the important physiological features occurring at the transition interface and to ensure the numerical accuracy of the overall hybrid scheme without compromising its computational feasibility. Finally, the third sub-model adapts the support function proposed by Hodneland et al.[217] to the dynamic context to ensure a smooth, physically plausible, and numerically stable transition between the discrete vessel representation of the

penetrating trees and the continuum representation of the homogenised capillary bed.

A suitable coupling scheme for linking the 0-D flow in the discrete vessel network to the 3-D Darcy flow in the continuum must generally obey the following five criteria: it must not give rise to any singularities in the model output, it must achieve scale-invariance, it must be physically sound, it should ideally not rely on any prior knowledge of the precise microscopic properties of the sub-resolution transitional network, and it must ensure the computational feasibility of the overall model. We have shown that our multiscale model precludes the emergence of singularities and achieves scale invariance, and thus meets the first two criteria. When examining the steady-state solution at different levels of mesh refinement in Figure 4.10(a) when no coupling scheme is applied, the resulting pressure gradients around the coupling points, and hence the pressure profile throughout the hybrid network, were found to be dependent on the choice of the CV size, which would ultimately give rise to singularities in the solution for smaller CVs. The smaller the FV cell size around the coupling point, the greater the resistance and pressure drop at the coupling point, the lower the flow throughout the whole network, and the lower the pressure drops across the resistance arteriole vessels. The network flow continues to exhibit scale variance for smaller values of L_1. Meanwhile, the use of the support function with a prescribed radius of influence in our model means that at the slight cost of non-locality of the source term[217] in Equation (4.2), the spatial range of the source flow distribution becomes independent of the size of the chosen FV cell. Indeed, after a local mesh refinement threshold around the coupling points (around $77\mu m$), the pressure and flow profiles become approximately independent of the degree of discretisation, with the flow error converging to around 5%, as shown in Figure 4.10(a).

The proposed support function in Equation (4.17) is also compliant with what is physiologically expected from the distribution of the microflow from the terminal vessels into the sub-imaging resolution network: it assumes that the majority of the fluid is distributed close to the terminals rather than far away and allocates no fluid flow beyond a strict threshold radius of ϵ. Furthermore, provided sufficient local mesh resolution, the distributed flow ensures a local, and thus global conservation of flow as a result of the volumetric normalisation of the source term in Equation (4.25). This mass balance can indeed also be demonstrated in the dynamic flow results for the whole hybrid network in Figure 4.8(a), in which the inlet and outlet network flows converge at the beginning and the end of the simulation as the network

reaches steady-state, as is indeed required when prescribing periodic BCs. Furthermore, the proposed coupling model can capture the steep pressure gradients that occur at the penetrating tree-capillary continuum interface,[133] as demonstrated by the red and blue spherical clusters in the steady-state pressure profile in Figure 4.7, simply by calibrating the ranges of the model inputs in such a way that the model output achieves the prescribed physiological pressure and perfusion profiles (see MCF analysis in Section 4.2.6). The choice of the support function is not constrained to the one in Equation (4.17), and other formulations adhering to the requirements above are in theory also permissible.

Of particular relevance for comparison is the work by Peyrounette et al.[133] in which local analytical coupling formulations are derived and used around the terminal nodes. Comparing the two coupling formulations to one another, the one proposed by Peyrounette et al. requires a pointwise consistency of the pressure drop across the adjacent FV cells and does not explicitly allocate the distributed flow across the adjacent FV cells, while the one proposed by Hodneland et al.[217] and used in this study requires consistency only in the average pressure drop as in Equation (4.22) while specifying the allocation of the distributed flow into the adjacent FV cells based on the distance of the FV centroids from the coupling point according to Equation (4.17). The piecewise analytical formulation by Peyrounette et al. is comprised of a linear variation in pressure in the region closest to the coupling point up to a distance l_τ, derived from solving for the network structure at the scale of the capillary vessel, which is then pointwise matched to the spherical pressure approximation derived from an analytical approximation of the solution for Darcy's law in Equation (2.7). The coupling condition is completed by assuming the existence of a domain where both the spherical approximation and the FV formulation are valid, such that the pressure from the FV formulation at two cells away matches the pressure of the pointwise spherical solution. Similar to the work by Hodneland et al.,[217] the governing equations for flow across the three scales can then be appropriately integrated into a single system of algebraic linear equations.

The coupling scheme proposed by Peyrounette et al. was also successful at capturing the strong pressure gradients around the coupling points and was found to significantly reduce the errors in flow and pressure that arise from assuming a simple condition of pressure continuity.[133] In their model, however, the linear variation in pressure in the vicinity of the coupling point follows from adopting the Hagen-Poiseuille flow description in the pre-capillary

and post-capillary transitional vessels. Given that the red blood cells (RBCs) percolate 'single-file' in the dense capillary network,[24] the use of the Hagen-Poiseuille flow model, which is aimed at capturing the Newtonian flow dynamics in the capillary vessels, might not be the most accurate representation of the flux dynamics of the RBCs in the narrow capillary vessels, where only a single RBC can go through at one time.[45],[62],[67] Furthermore, prior knowledge of the architecture and connectivity of the capillary bed around the coupling points was required to determine the values for the coupling parameters (for example, l_τ) of the analytical formulation. This prerequisite posed no problem in their work since the capillary connectivity was pre-established and was assumed to comprise a regular lattice topology since the goal of the study was to evaluate the accuracy of the proposed coupling model in the hybrid coupling approach, and the use of synthetic capillaries precludes the generation of uncertainties in the effective parameters (*i.e.* $\mathbf{K}$), which would otherwise be indiscernible from errors induced in the coupling model.

However, in a realistic setting, the capillary bed, albeit isotropic and homogeneous at network-scale[41],[131] is highly asymmetrical and locally randomised,[131],[224],[225] and its precise morphological nature around the different coupling points cannot be assumed to be known a priori.[217] Smith et al.[131] demonstrated that the simple approach of constructing grid-like networks, particularly the cubic lattice network with 6 connectivities per node, was not sufficient to replicate the geometrical or functional properties of cerebral capillary networks, and highlighted the need for introducing a sufficient level of randomness in the capillary generation schemes. A hybrid framework that requires information about the exact capillary connectivity would not meet the fourth criteria for a suitable coupling scheme mentioned above, and would also defeat the purpose of homogenisation; *i.e.*, to eliminate the need for precise knowledge of the capillary network topology. In theory, the transitional network segments at the mesoscale below the imaging resolution could be reconstructed from a set of growth rules, but ultimately the generation of such networks is mathematically redundant to achieving the goal of a smooth distribution of flow,[217] as we have demonstrated in our study that a simple, smooth support function can achieve the same goal even in a dynamic context.

The use of the MCF analysis to assign physiologically realistic values of the coupling parameters (γ_a and γ_v) reduces the need for knowledge about the pre-capillary and post-capillary transitional network structures. Of course, in principle, a similar MCF analysis could be car-

ried out when implementing the coupling formulation proposed by Peyrounette et al. to gain general insight into the range of permissible values for the parameter l_τ, without needing to reconstruct the sub-resolution network, and it would indeed be interesting in the future to make a comparison between the results of the MCF analysis and the dynamic simulations when adopting both coupling schemes, under both the steady-state and dynamic contexts.

Note that in our model, as well as that of Peyrounette et al.,[133] the penetrating arteriole and venule trees are embedded into the same compartment (the $1.5 \times 1.5 \times 2.4mm^3$ voxel), while the model by Hodneland et al.[217] separates the capillary domain into two identical compartments, one for each of the two vessel networks. The flow between two capillary domains is then computed from the pressure difference between each CV pair, multiplied by a perfusion parameter. This is done to explicitly express perfusion as a clinical parameter in line with its proposed definition; *i.e.* the transmittance of blood from the arteriole 'side' to the venous 'side' in a two-compartment model.[241]–[244] In both our and their compartmental representations, perfusion refers to the flow through the capillary domain and thus both can be viewed as valid characterisations of clinical perfusion.

The two-compartmental model, however, introduces an additional sub-resolution parameter that needs to be evaluated, thereby adding to the challenge of correctly selecting the sub-resolution parameter settings in cerebral haemodynamic models, which typically have a high parameter dimensional space and limited experimental data available.[82],[129] In addition, anatomically speaking, there is no obvious segregation between the arteriolar and venous territories of the capillary bed.[126] Most importantly, however, is that a two-compartmental model requires twice the number of capillary bed CVs, thereby significantly increasing the computational cost of any multiscale simulation, which is an important barrier for extending the dynamic model and achieving whole region or organ dynamic simulations.

Finally, it is worth comparing the model proposed in this paper to the porous Finite Element framework proposed by Jozsa et al.[129] In their study, the microcirculation is segmented into coexisting arteriole, venule, and capillary compartments. However, instead of using a discrete topological representation of the cortical trees, their model also extends the porous representation to the arteriole and venule compartments; *i.e.* by using the volume-averaged Darcy's law with anisotropic permeability tensors. The remaining pre-capillary and post-capillary

vessels that are not part of any compartments are effectively lumped into arteriole-capillary and capillary-venule coupling coefficients that link the compartments, similar to the γ_a and γ_v parameters in our model. The values for the coupling coefficients are selected based on a combination of inferences made from experimental pressure values from rodents, estimates of cerebral perfusion pressure, selection for the value of grey matter perfusion, and minimisation of a constructed cost function.

However, since the branching patterns of the descending arterioles and the ascending venules dictate the location of the terminal coupling nodes where this pressure drop occurs, a porous representation of the arteriole and venule compartments would be unable to account for the key influence that the patterns of anatomical branching exert on the spatial pressure and perfusion profiles throughout the cortical domain. In contrast, the network model of dynamic CBF and dCA developed in Chapter 3 and used here accounts for the penetrating vessels' spatial heterogeneity and incorporates the morphological details that account for the attributes and responses of individual microvessels and is suitable for investigating the impact of the vessels' individual dCA responses to perturbations in pressure or flow.

It is important to use physiologically informed values for the model parameter space to ensure that the model outputs reflect the physiological reality of the microvasculature. Hence, another important novelty of this work is utilising the MCF framework, combined with a global parameter sensitivity analysis, to gain valuable insights into the parameter influence, the range of permissible parameter values, and the interaction among the parameters prior to parameter value extraction. These, in turn, could aid in the model simplification and parameter research prioritization[204] and thus prepare grounds for more efficient and insightful extraction and uncertainty quantification of the physiological parameters, which are burdened by very high uncertainties and limited experimental data.[82],[129]

The pressure drop and distribution across the capillary bed, as well as the CBF through the voxel, are determined in part by the values of K, γ_a, and γ_v characterising the sub-resolution structure of the capillary bed and the pre/post-capillary vessels, respectively. This means that the degree to which the pre-capillary arterioles have to dilate to restore CBF is also affected by the value of these parameters. However, the relative contribution of the cerebral capillary bed to the total resistance is not unequivocally established due to the diffi-

Table 5: Comparison of the effective isotropic capillary permeability values (K_{eff}) between the different multiscale models employing a porous representation of the cortical grey matter capillary bed.

Model	K_{eff} ($\times 10^{-12} m^3 s/kg$)	Approximation Method
Peyrounette et al.[133]	1.1-7.8	Simulations over capillary network micro-cells.[133]
El-Bouri et al.[127]	0.428	Simulations over capillary network micro-cells.[41]
Hodneland et al.[217]	4160-8320	Trial and error process.[217]
Smith et al.[131]	0.384 - 0.428	Simulations over capillary network micro-cells.[131]
Our Model	1.2-7.6	MC filtering analysis.

culty in measuring the *in-vivo* pressures in those vessels, with authors reporting anywhere between 15% to 70% of the cortical microvasculature pressure drop occurring in the capillaries.[2],[45],[67],[129],[132],[245]–[247] Different authors have resorted to different methods to determine the effective capillary permeability (see Table 5), with a noticeable variation in the values obtained between the models.

While the aim is not to settle the aforementioned controversy, we note that the MCF analysis presented here offers a very simple yet insightful approach for investigating the permissible values of K, its influence on the pressure and perfusion profiles, and its interaction with the other parameters, namely γ_v. Interestingly, the permeability values obtained here are very similar to the range of values obtained by Peyrounette et al.,[133] the latter of which was obtained by conducting flow simulations over a cubic domain of a capillary network comprised of a 3-connectivity (periodic) and 6-connectivity (cubic) regular network topology of vessels of uniform or Gaussian diameter distribution. This could imply that, even though simple lattice networks could fail to replicate the architectural (morphometric, topological and space-filling) properties of human cerebral capillary networks at the local scale,[131] they can potentially be used to match the fundamental functional (flow and transport) properties at the network-scale.

In our first iteration of the MCF analysis, before adding the fourth MCF criterion in Section 4.2.6, the capillary bed pressure profile exhibited narrow and non-physiological distributions. Hence, an extra filtering criterion of a steady-state pressure range of at least $10 mmHg$ was added to ensure an adequately spread pressure distribution throughout the capillary bed.

We have chosen the range of permissible perfusion values in the MCF analysis to be predominantly weighted towards those obtained from the Positron Emission Tomography imaging modalities, which traces flow through functional tissue that can exchange nutrients and waste products, rather than that of perfusion computerised tomography (CT) scans, which include signals from regions without functional exchange with the brain tissues.[248] Since our framework also accounts for the CBV inside the penetrating vessel trees, an MCF criterion for rCBF obtained from CT perfusion measurements can also be in theory introduced.

Examining Figure 4.6, there is an identifiable behavioural subset of values for each of γ_v and K, as is confirmed by the two-sample k-S test, indicating that both these input parameters are likely key factors driving the steady-state perfusion and pressure profiles. Interestingly, from Figure 4.6(a), any value of γ_a is likely to fall into either the behavioural or non-behavioural subsets, as is confirmed by the results of the KS-test ($\mathrm{p} = 0.4132$); the behavioural and non-behavioural subsets are statistically and visually indistinct, signifying that γ_a is unlikely to exert an important influence on the steady-state profile, and can potentially be factor-fixed in the future. These results make for an interesting contrast when compared to the sensitivity analysis results of the model by Jozsa et al.,[129] which revealed a weak impact of the capillary permeability, and a strong impact of the coupling coefficients, on perfusion. In the future, these microscale variables of the model can be included in the global parameter sensitivity analysis conducted for the dynamic compliance feedback model parameters, and their interaction with the dynamic parameters investigated.

Upon prescribing the pressure BCs and the permissible range of perfusion values, and given that the baseline network properties of the penetrating vessels are fixed, the remaining network resistance is then allocated between either at the venule-capillary interface or within the capillary continuum, which explains the inverse relationship between the permissible values for γ_v and K in Figure 4.6(b). The precise range of permissible values for K, γ_a, and γ_v estimated here should of course be taken with caution since the simulations are based on a single reconstruction of the voxel domain, and it would be of interest in the future to examine the range across a larger set of statistically generated networks.

In this study, the support radius ϵ for the distributed source flow was chosen to be equal to $0.45L_1^*$, where L_1^* is the side length of the largest cube in the capillary mesh in Figure 4.2(d).

In general, the choice of ϵ has been found to be tied to the choice of L_1: $0.35 \leq \epsilon/L_1 \leq 0.45$. Intuitively, the lower limit is needed to ensure that each terminal node is coupled to the capillary bed FV centroids. The upper limit has been found to be required to ensure boundedness, possibly by preventing excessive overlap in the support radii of the terminal nodes. Physiologically speaking, the penetrating vessels link to the capillary vessels at a small number of bifurcations at the transition regions.[24] Hence, the logic behind choosing a relatively small value for ϵ, as opposed to the large values used in the whole-brain perfusion model by Hodneland et al.,[217] is to achieve a scale-invariant transition at the coupling interface while also minimising the non-locality of the distributed source term so as not to disrupt the capillary flow dynamics which are modelled using the volume-averaged Darcy's law in Equation (2.7).

In Figure B3, we examine the influence of the value of ϵ on the steady-state flow profile for the network in Figure 4.2(d). The global network perfusion increases with a semi-linear trend as the value of ϵ increases. This could be explained by the increase in the number of pathways for blood to flow between the terminal arteriole and venule vessels, and the capillary bed, thereby decreasing the network's overall effective resistance to blood flow. Nonetheless, the overall change in perfusion between the maximum and minimum permissible values of ϵ is only $2.6mL/min/100g$, or 6% of the original value in Figure 4.8(a). We also examined the influence of the ϵ parameter value on the capillary bed pressure profile. As expected, smaller values of ϵ result in smaller spherical clusters around the terminal coupling points in Figure B4, though the permissible range of values for ϵ is not wide enough to lead to any significant changes in the overall pressure profile, as demonstrated by Figures B4 and B5.

In addition to the proper assignment of the model parameter values, prescribing the correct pressure BCs is crucial to obtain the correct perfusion and pressure profile throughout the network, given the strong influence of the imposed pressure BCs at the inlet/outlet of the penetrating vessels on the CBF.[214] There are no human studies reporting blood pressure in the distal arterioles. In most models (see[127],[198],[249]), a pressure of 65-75 mmHg is typically chosen for the penetrating arterioles of $40\mu m$ inlet diameter, and a pressure of 15-22 mmHg is chosen at the penetrating venules of $110\mu m$ outlet diameter. These models rely on the data from Zweifach and Lipowsky[250],[251] to set the pressure BCs. These data, however, rely on studies that examine the microvasculature in the cat mesentery and the omentum. The pressure distribution in the microvasculature in one organ is not necessarily the same

in another organ, due to differences between the organs in the relative contributions of the microvasculature to the total resistance across a network. Fukaswa showed that the large arterial branches are responsible for a much larger proportion of the total arterial length (and hence resistance) in the brain compared to arterial systems in other organs and that cerebral arterioles are relatively shorter.[252] While it is the small arteries and arterioles that are the major resistance vessels in peripheral organs,[2],[247] both large arteries and small arterioles contribute significantly to vascular resistance in the brain.[247][253] Measurements of blood pressure in the brains of anaesthetized cats[154],[254] have demonstrated that 40-45% of the total flow resistance is located upstream of cerebral pial arteries 30-40μm diameter, meaning that the pressure at the pial inlet is approximately 55% of the MAP. Interpolating data from similar experiments[46],[245] leads to similar conclusions. Hence, while recognising the limitations of extrapolating from animal studies, and assuming a MAP of 93 mmHg, we chose an inlet pressure of 52 mmHg and an outlet pressure of 20 mmHg.

Since the error that can be potentially caused by insufficient mesh resolution covers only a small portion of the computational domain (*i.e.* at the coupling points), one can use larger elements on areas where the mesh resolution changes slowly, and use local patches of refinement only in the vicinity of the coupling points where high resolution is needed.[221] In addition to capturing the pressure gradient, the local mesh refinement serves two other purposes. First, it prevents the occurrence of multiple coupling terminal nodes inside the same CV, which has been found to introduce local pressure and flow errors.[133] The second purpose is to ensure local mass balance and improve the accuracy of the numerical integration in Equation (4.18), as discussed in Section 4.2.4. The latter case is similar to that of local grid refinement in the model by Jozsa et al.[129] which was needed to mitigate the errors in volumetric blood flow estimation through cortical surface regions when using a non-conservative finite element formulation. Note that the selective mesh refinement, as needed to ensure mass balance, is only around the terminal endings, since the FV formulation for the capillary bed is inherently conservative,[228] as is the 0-D model for flow in the penetrating vessels, thus any sources of mass imbalance would stem from numerical inaccuracies from the distributed source flow. The conservative feature of the FV method used here makes it a particularly appropriate choice for domain discretisation that would help ensure global flow conservation throughout the entire multiscale network, as opposed to other non-conservative discretisation

schemes that have been used in multiscale blood flow modelling,[129] in which mass balance could not be guaranteed.

Having said that, a non-uniform domain discretisation, as a result of employing local patches of mesh refinement, does introduce local regions of mesh non-orthogonality and skewness, that could potentially undermine the accuracy of simple FV formulations, like the two-point flux approximation method, that is widely applied in simple schemes to estimate the face gradients.[221],[228],[229],[255] There are ongoing efforts to improve the diffusion schemes and to incorporate the best available ones for various types of non-uniform and unstructured meshes.[231],[256]–[260] However, these scheme implementations are generally designed for conventional CFD settings and contexts as they generally require iterative solution procedures that potentially preclude them from being utilisable in a coupled multiscale setting where the source term in the capillary continuum sub-matrix assembled from the FV discretisation needs to be implicitly treated and appropriately incorporated into the final global matrix as in Equation (4.30).

Remedies to decrease the errors induced by the non-orthogonality (θ) and skewness ($\mathbf{x}(f_i) - \mathbf{x}(f_i^*)$) errors would normally entail the use of higher interpolation schemes and applying local mesh refinement to areas where they occur in the spatial grid.[221] The meshing scheme proposed here (see Figure 4.2) by default overlaps the areas of non-orthogonality and skewness in the regions surrounding the coupling points with areas of greater local mesh refinement, with the rest of the voxel domain having a uniform mesh. Hence, the scheme automatically helps to ensure that such errors are kept to a minimum. As seen in Figure 4.10(a), after achieving sufficient local mesh resolution, the error introduced as a result of local mesh non-orthogonality and skewness oscillates around 5% for the global flow (and $< 2\%$ for coupling pressure), which the authors perceive to be well within the acceptable limit.

We have also demonstrated how the model can be used to quantify the dynamic alterations in rCBF and CBV in the microcirculation following a drop in CPP, as well as the role of the dCA mechanisms in restoring the flow, as shown in Figure 4.8. In the passive simulations when no dCA mechanisms are accounted for, the rCBF dropped by 16.6%, which is slightly greater than the drop in CPP ($\approx 12\%$) due to the decrease in the transmural pressure of the compliant arteriole vessels that leads to their constriction, as shown in Figures 4.8(c) and 4.8(d), leading

to an increase in the arteriolar resistance and a further drop in flow. Meanwhile, in the active case, the final fractional decrease in rCBF (9.4%) was smaller than that in CPP, with the rCBF recovery exhibiting a biphasic behaviour, as shown in Figures 4.8(a) and 4.8(b) that is characteristic of the autoregulatory response observed experimentally,[8],[80] and which occurs a result of the dCA mechanisms altering the vessel tone and hence the calibre of the arteriolar vessels, as demonstrated in Figure 4.8(c).

This transient increase in the arteriolar blood volume as a result of changes in the compliance of the vessels gives rise to the transient discrepancies between the inlet and the outlet flows shown in Figure 4.8(a). Such dynamic differences underscore the fact that changes in pressure and flow throughout a network are not instantaneous as one would obtain from assuming a steady-state solution, but rather exhibit some delay as the changes propagate downstream from the inlet to the outlet. The potential to model and quantitatively trace such small dynamic changes in rCBF and CBV $(4.2\%$ change in total CBV in our simulations$)$ can have important implications in terms of interpreting the results of the transient, small, and oftentimes noisy[261] changes in the signal acquired from perfusion images that occur as the contrast agent passes through the vasculature, especially when used in conjunction with kinematic models of the administered contrast agent. For instance, it is known that the reduction in CPP that is associated with pathological conditions results in delayed bolus arrival time and prolonged vascular transit time, two conditions that are not appropriately addressed in current singular value decomposition and deconvolution image post-processing algorithms, thereby potentially leading to a gross underestimation of the rCBF and CBV from the perfusion images.[261] In addition, by running the acquired measurements against various *in-silico* simulation settings, the dynamic model can be used to help provide an elementary assessment of the microvascular architecture and the autoregulatory response under both healthy and pathological states.

Note that the perfusion (in $mL/min/100g$) for the whole voxel in Figure 4.8(a) is less than that in the central ROI in Figure 4.8(b), as expected, due to the lower vascular density in the whole voxel as a result of voxel reconstruction artefacts discussed earlier in Section 4.2.1, and which are collectively referred to here as the boundary effects, thereby highlighting the importance of restricting our analysis to a central ROI at a distance from the boundaries. When the capillary bed was assumed to comprise 2.22% of the total volume in the grey matter cortex

(and hence encompass 50% of the total CBV), the baseline CBV throughout the whole voxel domain was found to be $4.25ml/100g$, which is in good agreement with the experimentally obtained range of values of $4.6 \pm 1ml/100g$.[240] This measurement is a rough estimate, since the blood volume in the capillary bed, which constitutes about half of the total CBV, was estimated from the capillary fraction in the grey matter cortex[239]; nonetheless, it serves as a valuable measurement for tracing the changes in the total CBV, the quantifiable CBV metric from the perfusion maps.

Lastly, we look at the results of the global parameter sensitivity analysis. Traditionally, there have been few attempts to quantify the most important parameters in haemodynamic models; these considerations, however, are becoming increasingly important for "preventing models from becoming unvalidated black boxes with too many/few parameters."[81] The μ_{EE} metric in Figures 4.9(a) and 4.9(b) assesses the overall influence of the factor on the output. Meanwhile, the σ_{EE} metric estimates the ensemble of factor's effects, whether nonlinear and/or due to interaction with other factors; a high value indicates that the effect of the parameter on the output is closely tied to the choice of its and other parameters' values.[204] However, factors with non-monotonic effects can produce both positive and negative elements in the elementary distribution, thus producing a low μ_{EE} even for an important factor, which is why it is important for the value of μ_{EE} for each parameter to be considered against the values of both σ_{EE} and $\mu_{|EE|}$ of that parameter, as has been done in this study.

All the points of the $\mu_{|EE|}$ vs μ_{EE} plot in Figure 4.9(b) lie on or very close to the $\mu_{|EE|} = \mu_{EE}$ line, indicating a high degree of monotonicity for all the model parameters. This is supported by the input-output scatterplots (see Appendix B.1) examining the influence of the two variables S_α and G on the final perfusion and CBV, in which there are clearly identifiable and monotonic input-output trends. The points for the maximal fractional change in compliance parameter, $\Delta C^+/C_0$, lie close to the origin in all the EE plots and indicate that the parameter can be regarded as non-influential and thus it can be potentially factor-fixed in the future to reduce the model's dimensional parameter space. This is understandable, given that for the small perturbations in inlet blood pressure examined here ($< 15\%$), the vessel compliance is far from its saturation limits and is still operating in the relatively linear regime of the stiffness-compliance curve in Figure 3.1.

The sensitivity analysis results indicate that the myogenic sensitivity (S_α) is the most influential factor affecting perfusion and CBV since it has the greatest values across all σ_{EE}, $\mu_{|EE|}$ and σ_{EE} metrics. Examining the total effects in the input-output scatterplots (in Appendix B.1), the myogenic sensitivity input factor appears to be the more dominant factor affecting capillary perfusion and CBV changes, as indicated by the greater slope between S_α and the outputs. While one has to be careful from making any direct conclusions from a sensitivity analysis, this result supports the conclusion of the myogenic dominance in the earlier modelling studies[82],[86] and in Chapter 3, although ultimately a direct comparison with the previous models cannot be made due to different methods and network representations used. It is interesting to note that this result resembles what happens in the case of autoregulation mechanisms in retinal microcirculation.[262],[263] The retinal and cerebral microcirculation share many physiological and morphological properties, with recent interest in utilising non-invasive clinical assessment and measurements of the state of autoregulation and vascular reactivity in the retinal microvasculature as a marker for the cerebral autoregulation state.[264],[265] Hence, while the exact network geometry used in this study is specific to the cortical cerebral microvasculature, the mathematical model can be extended to other regions of the body.

Examining Figure 4.9(a), the endothelial sensitivity (S_τ) has a greater μ_{EE} compared to the stiffness-compliance central slope parameter (G) for both perfusion and penetrating vessel CBV output parameters, leading one to think that S_τ could be the more important factor. However, variations in G produce greater σ_{EE}, possibly indicating a greater interaction of the parameter with the other input parameters. This is understandable, given that in the stiffness-compliance formulation used in this model, as summarised in Figure 3.1, the effects of both the myogenic and endothelial mechanisms are mapped onto the compliance via the factor G. Hence, both factors can be flagged as important factors influencing the output.

The MC analysis conducted to generate the scatterplots (in Appendix B.1) could also be used to give further insight into the autoregulation response. With up to $\pm 25\%$ variation in S_α and G from their baseline values, the recovery of perfusion and changes in penetrating tree CBV do not exceed 2% and 4.5%, respectively, from their initial values, despite the monotonic effects of the variables. It should be noted that the parameter baseline values are not unequivocally established at this stage, and hence the results are by no means conclusive. Nonetheless, these

results could indicate that while the myogenic response plays a significant role in attenuating the rCBF drop in response to the CPP drop, it might be insufficient in itself to restore the perfusion close to the baseline values, and other mechanisms must also play a role.

Given that our model employs a dynamic network representation of the arteriolar vessels, it is very much well-suited for the purposes of examining the other mechanisms responsible for dCA and their interplay, as well as the associated pathological conditions, such as vessel occlusion or remodelling of mural cell coverage, or the myogenic response impairment implicated in acute ischaemic stroke, all of which predominantly occur at the level of the individual vessel.[2],[17],[27],[266] For instance, some of the mechanisms that could be investigated with our model include the conducted vascular response that relies on the propagation of the vasomotor signal, as demonstrated in Chapter 6, the modelling of which would require the ability to account for the vessel connectivity and geometry, and the neurovascular response, an intrinsically local response that requires consideration of the local changes in flow, all the requirements of which are provided by our model.

In this study, we did not account for the role of the capillaries and pericytes in regulating flow, which is becoming increasingly recognised.[5],[76]–[78] This is due to the much slower response dynamics of the capillary vessels, which are relatively stable over time, at least over the timescale explored in this study.[24],[27] Nonetheless, in the future, and for simulations over a longer period, the model can be used to account for the contribution of the capillaries and pericytes to the regulation of the flow at the network scale, for instance, via a varying value for the capillary bed permeability, whose dynamics can be obtained from conducting simulations over a periodic micro-cell of the capillary network.

Regarding the limitations of the model, the homogenisation approach is not capable of capturing the discrete paths of blood flow through the capillary bed.[43] Furthermore, as discussed in Section 2.3, the cerebral microvasculature exists as a continuum of morphologies; hence, the transition boundary between the branching penetrating arterioles, modelled here as discrete vessels, and the mesh-like capillary bed, which is homogenised and treated as a porous continuum, is not as straightforwardly delineated. Nonetheless, when examining the diameter and the vessel generation number (from the pial surface) of the statistically generated[39] arteriole vessel trees used in constructing the MRI voxel-sized networks, we find that they mostly

agree with the proposed nomenclature and categorisation distilled by Hartman et al.,[27] described in Section 2.3. The terminal vessels have been found to approximately correspond to the ACT region that is covered by the ensheathing pericytes, while the vessels upstream correspond to the penetrating arterioles, covered by VSM cells. This means that the vessels downstream of the terminal arterioles, which in our multiscale network would be part of the homogenised capillary bed, are indeed likely to belong to the net-like vessels of the capillary bed that are covered with mesh pericytes. Additional attributes of the cortical microvasculature, such as the precapillary sphincters and the distension of the lumen that often occurs right after (denoted as the bulb),[71] can be integrated in the future into the multiscale network model, for instance, by incorporating such features into the density-filling algorithms used to generate the penetrating vessels based on statistical morphological data.[39]

4.5 Conclusion

The framework developed here lays down the foundation for enabling dynamic simulations of CBF and control over sizeable portions of the cerebral cortex, as well as for further validation and uncertainty quantification of the model output and its parameters. These, in turn, can shift the role of microvasculature modelling from merely providing the BCs for the larger vessels to being actively studied in normal and diseased conditions, whether when examined in isolation, or as part of dynamic multiscale whole-brain perfusion models where the microvasculature model developed here is coupled to 1-D models of blood flow in the larger arteries. Hence, the model in this study constitutes an important step towards gaining a better understanding of the disruptions in flow that occur in the cerebral microvasculature, their role in the initiation and progression of brain pathologies, as well as the interaction of the microvasculature with the rest of the circulation, enabling a better representation of cerebral haemodynamics across the vast scale range of the brain vasculature, from the carotid artery with a diameter close to $6mm$ down to the capillaries with a diameter of approximately $6\mu m$.

Chapter 5

Using Approximate Bayesian Computation Schemes to Calibrate the Compliance Feedback Model

Abstract

This chapter aims to utilise available experimental data on the vessels' elastic and autoregulatory behaviour, primarily the myogenic and endothelial responses, to calibrate the parameters and functional form of the compliance feedback model. We devise and employ a two-stage sequential MC approximate Bayesian computation (ABC) scheme to obtain a posterior distribution for the model parameter space. The final parameter space distribution is informed by the prior distributions and knowledge of the parameters, the model dynamics, and the available experimental data. The experimental data used in this chapter traces the changes in vessel calibre of individual arteriolar vessels in response to changes in intraluminal pressure and/or the pressure gradient, which correspond to the myogenic and endothelial mechanisms, respectively. Furthermore, we demonstrate how the adoption of a suitable parameter calibration scheme can help provide insights into the mechanistic features of the dynamical system. Namely, the ABC scheme reveals that there is a marked difference in the time constants between the myogenic-induced dilation and constriction. Overall, upon parameter calibration, the compliance feedback model achieves very good agreement with the experimental measurements, despite the limited data availability. This indicates that the compliance feedback model utilised is a simple, compact, and physiologically grounded characterisation of the autoregulatory response, and could enhance the model's potential clinical utility in the future.

5.1 Introduction

In models of CA and CBF control, there have been very few attempts to estimate the model parameter values in a rigorous manner or to quantify which ones are the most influential. This is partly because models describing the elastic and autoregulatory behaviour of the arteriolar vessels tend to be overparameterized (see[124],[209] for example) and often include more relevant laws than the limited amount of available data would support.[204] For this reason, in Chapters 3 and 4, we have relied on a simple representation, the compliance feedback model, to characterise the elastic and autoregulatory behaviour of the individual vessels; this, in turn, would facilitate parameter assignment from the limited data available.

The experiments by Kuo et al.[155],[267] are, to the best of our knowledge, the only experiments that trace the change in the diameters of the individual arteriole vessels when activating the myogenic and endothelial mechanisms, both in isolation as well as when interacting, in response to changes in the transmural pressure and the pressure gradient. In these experiments, the arteriole vessels are first identified and isolated, and the ends of each arteriole vessel are cannulated and secured with glass micro-pipettes. Each of the two tips is connected to an independent reservoir system. The cannulated arteriole can be pressurized without flow by setting the reservoirs at the two ends to the same hydrostatic level, which can be achieved by simultaneously moving both reservoirs in the same direction, thereby initiating the myogenic response without the endothelial response. Conversely, flow can be initiated by simultaneously moving the reservoirs in opposite directions by the same magnitude thereby generating a pressure difference (ΔP) and initiating the endothelial response without altering the midpoint intraluminal pressure (P_I). The two mechanisms are examined both under isolation and when interacting with one another by changing the P_I, ΔP, or both, and the corresponding changes in the internal diameter of the cannulated vessel are measured continuously throughout the experiment using video-microscopic techniques.

We utilise ABC techniques to calibrate the compliance feedback model parameters. ABC constitutes a class of computational methods rooted in Bayesian statistics that can be used to estimate the posterior distributions of model parameters. Let θ be a parameter vector to be estimated. Given some prior distribution $\pi(\theta)$, the goal is to approximate the posterior distribution, $\pi(\theta|x) \propto f(x|\theta)\pi(\theta)$, where $f(x|\theta)$ is the likelihood of obtaining the data x given

θ.[268] ABC methods have been conceived to infer posterior distributions without having to calculate the likelihood functions, which in many cases can be computationally intractable or too costly to evaluate.[268] Instead, they exploit the computational efficiency of modern simulation techniques by replacing the calculation of the likelihood with a comparison between the measured and simulated data, via some form of MC simulations, which in our case would correspond to the output of the dynamic compliance feedback model. We have used the compliance feedback model in Chapters 3 and 4 for model development, verification, and parameter sensitivity analysis, as well as to provide general insight into the interactions between the myogenic and endothelial responses prior to parameter extraction. Hereon, we introduce a few modifications to the compliance feedback model to achieve better parameter calibration while still maintaining its mathematical simplicity and numerical feasibility.

To this end, we first describe the experimental data by Kuo et al. used to calibrate the compliance feedback model. We then describe the modifications applied to the compliance feedback model used in Chapters 3 and 4, and the reasons behind introducing these modifications. We then describe the two-stage ABC iterative schemes devised and utilised in this study and present the results for each stage, which correspond to the parameter posterior distributions, as well as the comparison between the simulated and the measured diameter traces. Finally, we discuss the results and insights from the parameter calibration approach adopted in this chapter and offer concluding remarks.

5.2 Experimental Data used for Model Calibration

Figure 5.1 demonstrates the continuous measurements in internal diameters of the six isolated vessels from the two studies in response to the changes in P_I and ΔP. The isolated arterioles from the two studies have *in-vivo* diameters in the range of $40-80\mu m$, and lengths in the range of $0.7 - 1.1mm$.[155],[267] Since the model is not suitable for large perturbations in pressure and compliance, the experimental data by kuo et al.[155],[267] have been effectively truncated so as not to include any time series points in which the perturbations in P_I and ΔP from the baseline value are greater than 40 cm H_2O (30 $mmHg$) and 10 cm H_2O (7.3 $mmHg$), respectively. Also, any step changes in P_I and ΔP input functions were slightly smoothed out to circumvent any singularities in the numerical simulation output. It should be noted

that these experimental data are for porcine coronary autoregulating arterioles; while the use of animal models to try and understand the behaviour of human physiology is not without flaws,[81] it does provide a useful starting point from which this can be attempted, especially since obtaining in vivo human data is naturally very difficult.

5.3 Model Mathematical Formulation

Equation (3.9) characterises the dynamic relationship between the vessel pressure and diameter, and how the relationship is altered due to the effect of the autoregulatory mechanisms on vessel compliance. The initial diameters of the vessels can be determined from the individual experimental measurements. The exact lengths of the vessels, however, which are needed to calculate the baseline compliance and the vessel volume rate of change according to Equations (3.7) and (3.9), have not been specified for each experiment. Hence, we use the definition of compliance per unit length ($C^* = C/L$) and rewrite Equation (3.9) as:

$$2\pi R\frac{dR}{dt} = C_b^* P_I + \overline{P}_v \frac{dC^*}{dt} \tag{5.1}$$

where C_b^* is the baseline compliance per unit length and is now equal to:

$$C_b^* = \frac{3\pi R_0^3}{2Eh} \tag{5.2}$$

We first assume a linear feedback model emulating first-order low-pass filter dynamics for each of the myogenic (x_m) and endothelial (x_e) activation factors, which are then combined into a single activation factor. This is in contrast to assuming a single equation for the vessel stiffness (k) for both the endothelial and myogenic responses in Chapters 3 and 4. The separation is carried out to account for the potentially different time constants between the two mechanisms; indeed, at least in non-cerebral vascular beds, shear stress-based regulation is a slow process, characterised by a time constant on the order of 60s.[269],[270] Furthermore, the separation would facilitate the incorporation of additional autoregulatory feedback mechanisms, which we carry out in Chapter 6.

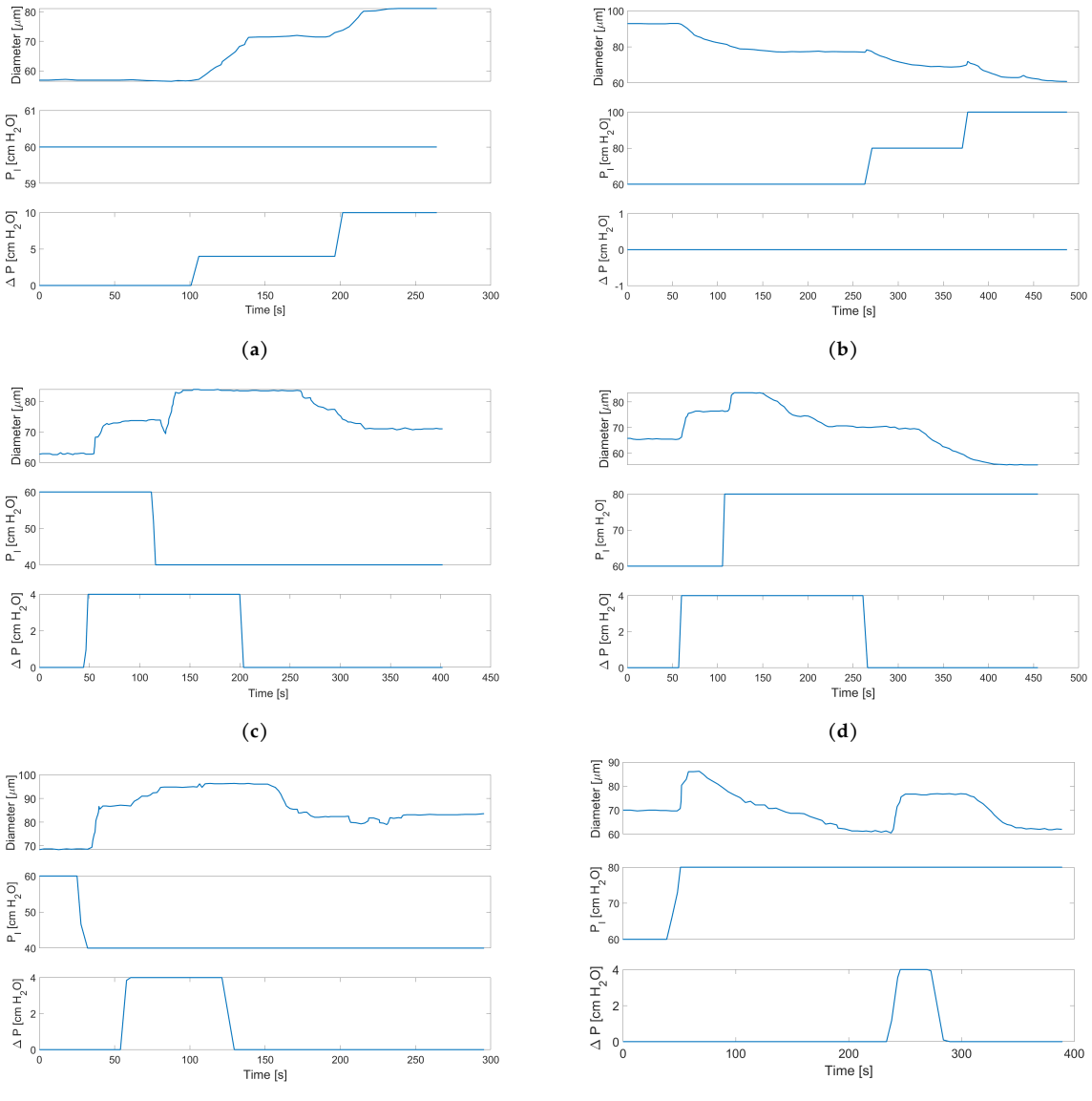

Figure 5.1: The experimental data, reproduced from the traces by Kuo et al.[155],[267] which includes continuous recordings of the internal diameters of six arteriolar vessels when changing the intraluminal pressure (P_I) and the pressure difference (ΔP). The data has been deliberately truncated so as not to include any time series points in which the perturbations in P_I and ΔP from baseline are greater than 40 cm H_2O (30 $mmHg$) and 10 cm H_2O (7.3 $mmHg$), respectively. The subfigures (a-f) correspond to experiments (1-6).

Secondly, we note that, conventionally, the myogenic response initiation has been modelled to be driven by changes in the transmural pressure (P_I).[121],[156] However, physiologically speaking, the vessel VSM wall cannot directly detect changes in the transmural pressure but rather responds to alterations in the tension in the VSM wall,[84],[85] as described in Section 2.4, the latter of which is modified via changes in the transmural pressure according to Laplace's law: $T = P_I R$ (note here that intramural and transmural pressure are used interchangeably since P_{ext} is assumed to be negligible). Accordingly, in the modified feedback model, the perturbation signal initiating the myogenic response is a change in the VSM tension and not P_I.

In the previous compliance feedback model, the gain factor S for each of the myogenic and endothelial responses amplified the perturbations in each of the transmural pressure and shear stress from their baseline values. At the time, such a choice for a model was satisfactory when the goal was to get an 'activation' of these two mechanisms following decreases in the transmural and shear stresses. However, physiologically speaking, the myogenic and endothelial responses are present and set the vessel tone during, or even below baseline tension and shear stress values,[2],[271] and the dCA is affected by the basal VSM tone.[80] Hence, in this new model, the activation term for each of the two responses depends on the perturbation from a reference value of tension T_0 and shear value τ_0 (equal to shear stress divided by $2L$), respectively, at which the myogenic or endothelial gain factor would be zero. Furthermore, to ensure that no activation (or deactivation) happens below such reference values, we also borrow from the field of neural networks the rectifier or $ReLU$ activation function:

$$ReLU(x) = max(0, x) \tag{5.3}$$

such that the perturbation signal for each of the two responses first goes through the $ReLU$ function before being amplified by the gain factor. Finally, as seen in Figures 5.1(b), 5.1(c), 5.1(d), 5.1(e), and 5.1(f), we notice that when endothelial-induced constriction takes place as a result of a drop in ΔP, there is a delay before the constriction takes place (for Figure 5.1(b), the endothelial constriction is postulated to occur as a result of removing the vessel from an environment where shear stress was present, to the experimental setup where $\Delta P = 0$). This delay can be hypothesized (though in no way confirmed) to occur as a result of the

presence of lingering nitric oxide endothelial factor that takes time to degrade[271] or wash away through advection and diffusion when the shear stress acting on the endothelial layer decreases. Regardless of the underlying physiological basis, this delay in activation (d) can be simply mathematically described as:

$$d = \begin{cases} \zeta & \frac{d\tau}{dt} < 0 \\ 0 & \text{otherwise} \end{cases} \tag{5.4}$$

Incorporating all these changes into the previous compliance feedback model, we obtain the two first-order low-pass filter dynamic equations for the myogenic and endothelial activation factors:

$$\frac{dx_m}{dt} = \frac{1}{\tau_m}\left(-x_m + S_m\left(ReLU\left(\frac{RP_I - T_0}{T_0}\right)\right)\right) \tag{5.5}$$

$$\frac{dx_e}{dt} = \frac{1}{\tau_e}\left(-x_e + S_e\left(ReLU\left(\frac{R(t-d)\Delta P(t-d) - \tau_0}{\tau_0}\right)\right)\right) \tag{5.6}$$

where τ_m and τ_e are the time constants of the myogenic and endothelial mechanisms, respectively. S is the sensitivity, or gain factor, for the perturbations of each of the wall tension or shear stress from their reference values. The sum of the myogenic and endothelial activation factors is then non-linearly mapped into the vessel compliance via a non-symmetrical sigmoidal function, similar to the stiffness-compliance feedback model in Chapters 3 and 4:

$$C^* = C_b^*\left[1 + \frac{\Delta C^{\pm}}{C^b tanh\left(\frac{1}{G}\frac{C_0}{\Delta C^{\pm}}\left(x_e - x_m\right)\right)}\right] \tag{5.7}$$

We differentiate Equation (5.7) with respect to time to obtain an expression for $\frac{dC}{dt}$ in terms of x_e and x_m, as well as their rates of change, $\frac{dx_m}{dt}$ and $\frac{dx_e}{dt}$, the expressions for which can be derived from Equations (5.5) and (5.6). The expression for $\frac{dC}{dt}$ can then be inserted into Equation (5.1), to obtain the first-order differential equation for the rate of change of the internal radius:

$$\frac{dR}{dt} = \frac{1}{2\pi R}\left[C_b^* P_I + \overline{P}_v \frac{C_b^*}{G} sech^2\left(\frac{C_b^*}{G}\left(x_e - x_m\right)\right) \cdot \left(\frac{x_m}{\tau_m} - \frac{S_m}{\tau_m}\left(ReLU\left(\frac{RP_{int} - T_0}{T_0}\right)\right) - \frac{x_e}{\tau_e} + \frac{S_e}{\tau_e}\left(ReLU\left(\frac{R(t-d)\Delta P(t-d) - \tau_0}{\tau_0}\right)\right)\right)\right] \tag{5.8}$$

Equations (5.5), (5.6), and (5.8) form a system of three first-order non-linear ODEs in terms of the system variables **U**:

$$\frac{d\mathbf{U}}{dt} = f(\mathbf{U}, \theta, \mathbf{X}) \tag{5.9}$$

where $\mathbf{U} = [R, x_m, x_e]^T$ are the system variables, $\theta = [S_m, S_e, G, T_0, \tau_0, \tau_m, \tau_e, d]^T$ are the eight model parameters, and $\mathbf{X} = [I_P, \Delta P]^T$ is the input vector for the experimental setup. Note that from the state variables **U**, only R is directly measured. Furthermore, to account for errors in the radial measurements and uncertainties in the state variables, the initial conditions $\mathbf{U}_i = [R_i, x_{mi}, x_{ei}]^T$ are also assumed to be unknown and are concatenated with the parameter vector θ to obtain the vector of variables **V** to be calibrated.

5.4 First-Stage Approximate Bayesian Computation

The simplest ABC algorithm is the ABC rejection sampler,[272] which is summarised below:

1. Sample candidate parameter vector θ^* from some proposal (prior) distribution $\pi(\theta)$.
2. Simulate a dataset x^* from the dynamic model, described by a conditional probability distribution $f(x|\theta^*)$.
3. Compare the simulated dataset, x^*, with the experimental data, x_0, using a distance function, d and tolerance ϵ. If $d(x_0, x^*) \leq \epsilon$, accept θ^*, otherwise reject.
4. Return to step (1) and repeat.

The ABC rejection sampler is very easy to implement, and relies on the generation of independent realisations and thus can be very easily parallelised. However, the acceptance rate is low when the prior distribution is very different from the posterior distribution.[268],[273] In our model, while some form of a prior distribution can be constructed for some parameters based on physiological grounds (e.g. the time constants), the prior distribution for other parameters cannot be approximated a priori, as discussed in Section 5.4. To mitigate this problem, Marjoram et al.[273] introduced a Markov Chain Monte Carlo (MCMC) scheme for generating observations from a posterior distribution without the use of likelihoods. However, when we tried implementing the MCMC AMC algorithm, we ended up with very long chains, and the chains often got stuck in regions of low probability for a long time. This has indeed been identified as a potential disadvantage of ABC MCMC algorithms as a result of the correlated nature of samples coupled with the potentially low acceptance probability.[268] Furthermore, since MCMC algorithms rely on some form of a perturbation kernel to obtain the parameter space for the next iteration from the previous iteration, the process cannot be straightforwardly parallelised.

The disadvantages above can, at least in part, be mitigated in ABC algorithms based on SMC methods, which were first developed by Sisson[274] and later adapted by Toni et al.[268] One of the key features of SMC methods is that the acceptance tolerances gradually tighten from one iteration to another, such that the distributions gradually evolve or converge towards the target distribution. The two proposed ABC SMC algorithms, however, are too mathematically involved, especially when there are multiple parameters to be calibrated.

As an alternative, we have devised our own iterative SMC algorithm for parameter calibration, which utilises the notion of sequential narrowing of the tolerances and convergence of the parameter distributions, while bypassing the mathematical intricacy of the two developed SMC methods mentioned earlier. As shall be demonstrated, the iterative algorithm devised here is not entirely streamlined but rather requires systematic input and analysis by the user between each iteration to fit and convert the posterior distribution from one iteration into the prior distribution of the next iteration, and to decide on the tolerances of the next iteration. Nonetheless, given that we only have one dynamic model to verify and for which to extract the parameters, and given that for each iteration the realisations can be run independently thereby permitting the parallelisation of the computation, the semi-automated nature of the

algorithm did not pose any major challenges. The first-stage algorithm is summarised below:

```
for i=1:r  %number of iterations
    V = sample(pi_V, MC) %Initialize the vector space V = [theta,U_i] by ...
        sampling from the prior distribution for a total of MC number of ...
        realisations.
    accepted_V = []
    for j=1:MC  %for each realisation j  in the MC realizations generated:
        D_j = obtain_diameter_trace(V, P_I, dP) %Simulate the diameter ...
            dataset using the dynamic model, subject to the experimental ...
            inputs of P_I(t) and Delta P(t) of the experiment.
        if i=1  %for first iteration only use two-error norm
            if L2(D_j,D_0) ≤ epsilon_2  %if the two-error norm is within ...
                prescribed tolerance
                accepted_V[end+1,:] = theta %accept realization
        else if i ≠ 1
            if L2(D_j,D_0) ≤ epsilon_2 & L4(D_j,D_0)≤ epsilon_4 & ...
                L_inf(D_j,D_0)≤epsilon_inf %if all error norms are within ...
                prescribed error tolerances
                accepted_V[end+1,:] = theta %accept realization
    pi_V_new = distribution_fit(accepted_V) %Use the space of accepted ...
        realisations to generate a posterior  probability distribution that ...
        is within all the prescribed error tolerances
    pi_V = pi_v_new %Set the obtained posterior probability distribution ...
        from the previous iteration to be the prior distribution for the ...
        next iteration.
    Decrease the error tolerance(s) epsilon_2 (and epsilon_4 and ...
        epsilon_inf for i>1).
```

In the algorithm above, r is the number of iterations (set here to 5). For $i = 1$, The starting prior distribution for the variable space $\mathbf{V}$ was assumed to be a Gaussian (normal) distribution, as described in Section 5.4. For the sake of simplicity, we assume that the experimental inputs $P_I(t)$ and $\Delta P(t)$ have no associated errors. For the first iteration ($i = 1$), the L_2 (Euclidean) norm is calculated between the simulated dataset D_j^* and the measured dataset D_0, and it must be below the error tolerance ϵ_2 for the realisation to be accepted. For the remaining iterations, the L_4 and L_∞ norms are also calculated and must also be below certain thresholds

to accept the realisation, which we have found to result in better filtering of the realisations overall since the two norms prevent larger discrepancies for a particular time point.

After the realisations are accepted or rejected, and the space of accepted realisations $\mathbf{V}_k$ is compiled, MATLAB's DistributionFitter application from the Statistics and Machine Learning toolbox is used to fit a univariate distribution to $\mathbf{V}_k$. The choice of the univariate distribution is selected via visual inspection of the one that provides the best fit. The most commonly used distributions fitted were the normal, beta, gamma, Nakagami, and Weibull distributions, but other distributions used included the logistic, exponential, half-normal, extreme value, generalised extreme value, Burr, and Birnbaum Saunders distributions. In some cases, other non-univariate distributions, such as a uniform distribution, were used. In rare cases, when no univariate distribution was deemed fit, a kernel distribution, defined by a smoothing function and a bandwidth value that controls the smoothness of the fitting curve, was used to fit the data. The parameters characterising the posterior fitted distribution are then used to generate the variables space $\mathbf{V}$ for the next iteration from which the realisations are sampled. The error tolerances are appropriately decreased for the next iteration, the exact value by which depends on the calculated L-norms of the accepted realisations $\mathbf{V}_k$. The algorithm is first applied independently for each of the six experiments involving six different vessels, such that for each experiment, final posterior distributions for the parameters and initial conditions are obtained.

The ABC algorithm described above requires an initial prior distribution of the parameters. As mentioned, the initial distribution of all parameters (except x_{ei}) is assumed to be Gaussian, which requires two parameters to be specified, the mean (μ) and the standard deviation (σ). The mean for the initial diameters is set to $\mu = D_0(0)$ (*i.e.* the experimentally measured initial diameter) and the standard deviation is set to $\sigma = 5\mu m$. Since the myogenic response has been reported to occur faster than the endothelial response, the initial distributions of the time constants are set to $\tau_m \sim N(18, 10)s$ and $\tau_e \sim N(40, 20)s$ in line with the range of values from the literature.[105],[156],[267] The distributions for the gain factors of the myogenic and endothelial responses are initialized to $S_m \sim N(4, 2)$ and $S_e \sim N(1, 0.75)$, which are approximately the values used in Chapters 3 and 4. In these previous models, the parameter values were chosen after analysing the model output based on an overall understanding of the behaviour of the network physiological response, with S_m chosen to be greater than S_e

due to the myogenic dominance reported in other studies.[82],[86] Similarly, the mean value for G was chosen from the previous model simulations, to give a distribution of $G \sim N(0.1, 0.03)$.

The mean values for reference values of tension (T_0) and normalised shear stress (τ_0) at which no activation occurs were chosen to be equal to half of the baseline values of the vessel wall tension and shear stress, respectively for each vessel. The baseline values for tension and shear stress were extracted as follows: in the experiments by Kuo et al.,[155],[267] the baseline value for P_I reflecting *in-situ* conditions for vessels of such diameter and length range was reported by the authors of the study to be $60cmH_2O = 44.13mmHg$ (which is also the value for $\overline{P}_v$ in Equation (5.8)). The baseline (*in-situ*) value for the ΔP was set to $5mmHg$ by extrapolating the data by Payne and Lucas,[198] which has listed the pressure drop across the arteriolar microvessels based on their lengths and internal diameter. The distribution mean for the constrictive endothelial response delay (ζ) was determined by calculating the delay across the experiments between the time points at which ΔP is decreased, and the time points when endothelial-induced constriction starts, which was then averaged across the different experiments involving endothelial-based constriction, resulting in a distribution of $\zeta \sim N(33, 10)s$.

The initial values for x_m and x_e for each experiment were determined by approximating the values that give rise to the steady-state value of $D_0(0)$ using the dynamic model when the vessel is subject to $P_I(0)$ and $\Delta P(0)$. The initial values were used as the mean, with standard deviations of 1 and 0.75 for x_m and x_e respectively. For all experiments with $\Delta P(0) = 0$, $\mu(x_{ei})$ was set to zero and the distribution was modelled using a half-normal distribution (*i.e.* ignoring the negative values). Finally, only for the second experiment in Figure 5.1(b), an additional parameter $\tau_{0,\text{hist}}$, also calculated from the initial steady-state baseline conditions, was initialized and added to the variable space as a parameter to be calibrated. This parameter corresponds to the value of the normalized shear stress before starting the measurement recording ($\tau(t < 0)$), since at $t = 0$, ΔP drops, giving rise to a delayed endothelial-induced constriction, which, according to Equation (5.8) requires prior knowledge of $\tau(t < 0)$. The distributions were chosen such that it is highly unlikely for a random variable to have a value < 0; nonetheless, a filtering criterion was added to prevent negative value realizations.

5.5 Results of the First-Stage Approximate Bayesian Computation

Figure 5.2 demonstrates a comparison between the measured internal diameter and the values obtained from the dynamic model simulation for each experiment when using a parameter realisation obtained from the final posterior distribution. We can see that there is a very good agreement between the simulated and measured diameter traces, except for Figure 5.2(f) corresponding to experiment 6. Given the low agreement between the experimental data and model output in Figure 5.2(f), experiment 6 is excluded from the second-stage analysis in Section 5.6, and the potential reasons for such discrepancies are discussed in Section 5.8. Figure 5.3 demonstrates an example of the evolution of the PDF for one of the parameters as it converges towards its final posterior distribution across the first-stage ABC scheme iterations. We can see that the range (and hence the uncertainty) in the parameter values narrows, and the distribution changes from a normal to a slightly left-side skewed (Weibull) distribution as it converges across the iterations.

Figures 5.4(a) and 5.4(b) demonstrate the final posterior distribution for τ_m for experiments involving myogenic-induced dilation (due to a decrease in wall tension), while Figures 5.4(c) and 5.4(d) demonstrate the distribution of τ_m obtained from experiments involving myogenic-induced constriction (due to an increase in wall tension). While there is a general agreement in the final distributions of τ_m within each group, we can see that τ_m in the case of a constriction response converges to a final distribution encompassing greater values compared to that of myogenic-induced dilation. We can approximate the time constants for myogenic dilation and constriction directly from the experiments, by calculating the time it takes from the initiation of the myogenic response for the vessel diameter to drop to $1 - 1/e$ of its value. Indeed, the interquartile values of τ_m for myogenic-induced constriction of (48-61) seconds are greater than those calculated for myogenic-induced dilation of (21-34) seconds. A similar trend can be noticed for the extracted variable distribution of S_m (results not shown), in which the distribution tends to be the same within the experiments involving myogenic-induced constriction or those involving myogenic-induced dilation, but the distribution in the case of dilation encompass values that are higher ($\approx 3 - 5$ interquartile values) compared to the distribution in the case of constriction ($\approx 1 - 3$ interquartile values).

This effectively demonstrates how sequential ABC schemes can not only be used for model

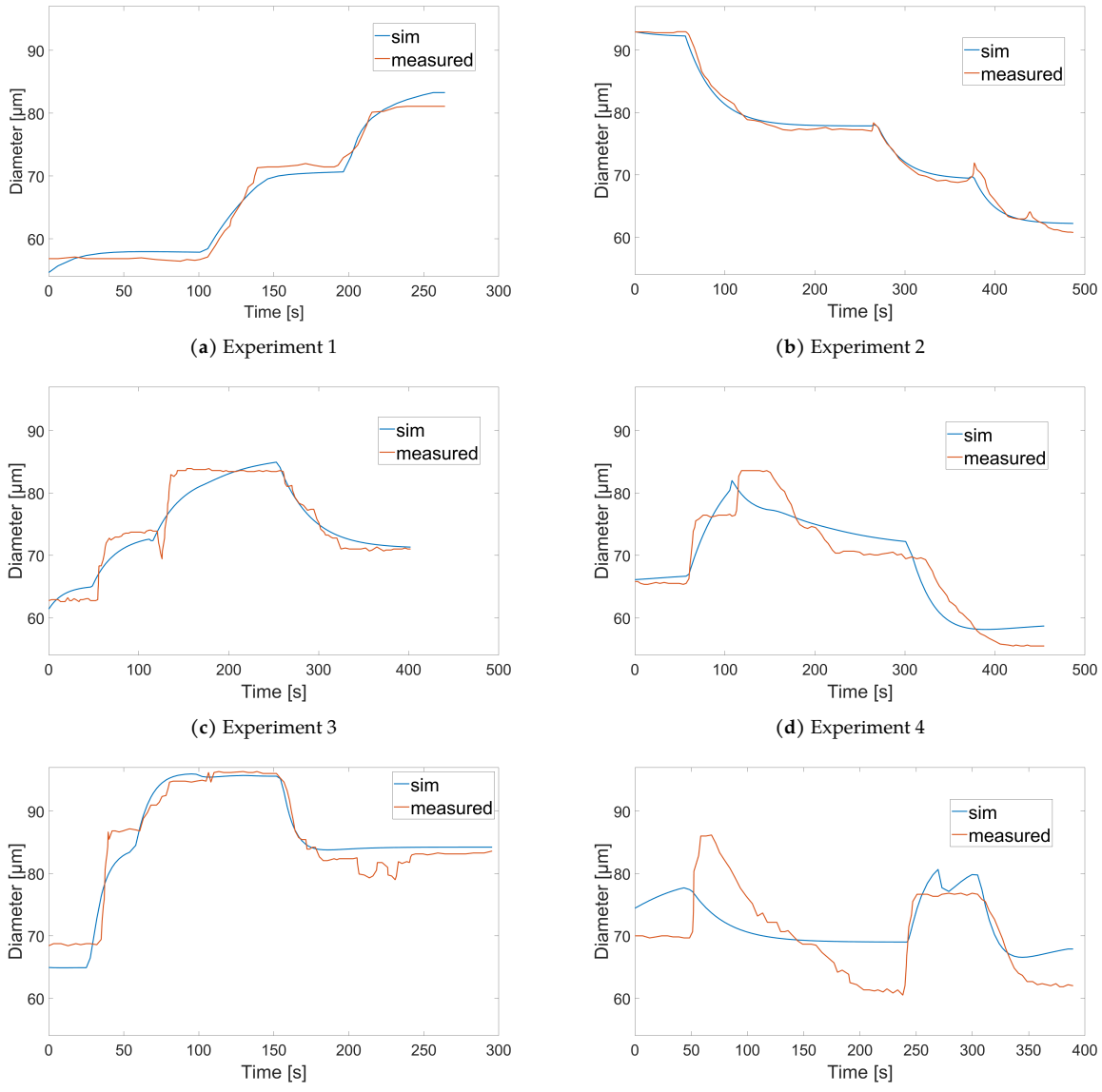

(**a**) Experiment 1

(**b**) Experiment 2

(**c**) Experiment 3

(**d**) Experiment 4

(**e**) Experiment 5

(**f**) Experiment 6

Figure 5.2: The first-stage ABC results of the dynamic model simulations when choosing a realisation from the final posterior variable space distribution for each experiment (sim), compared to the experimental measurements obtained by kuo et al.[155],[267] (measured). The model achieves good agreement for all vessels/experiments except for experiment/vessel 6, the data for which are hence not used for the second-stage ABC scheme.

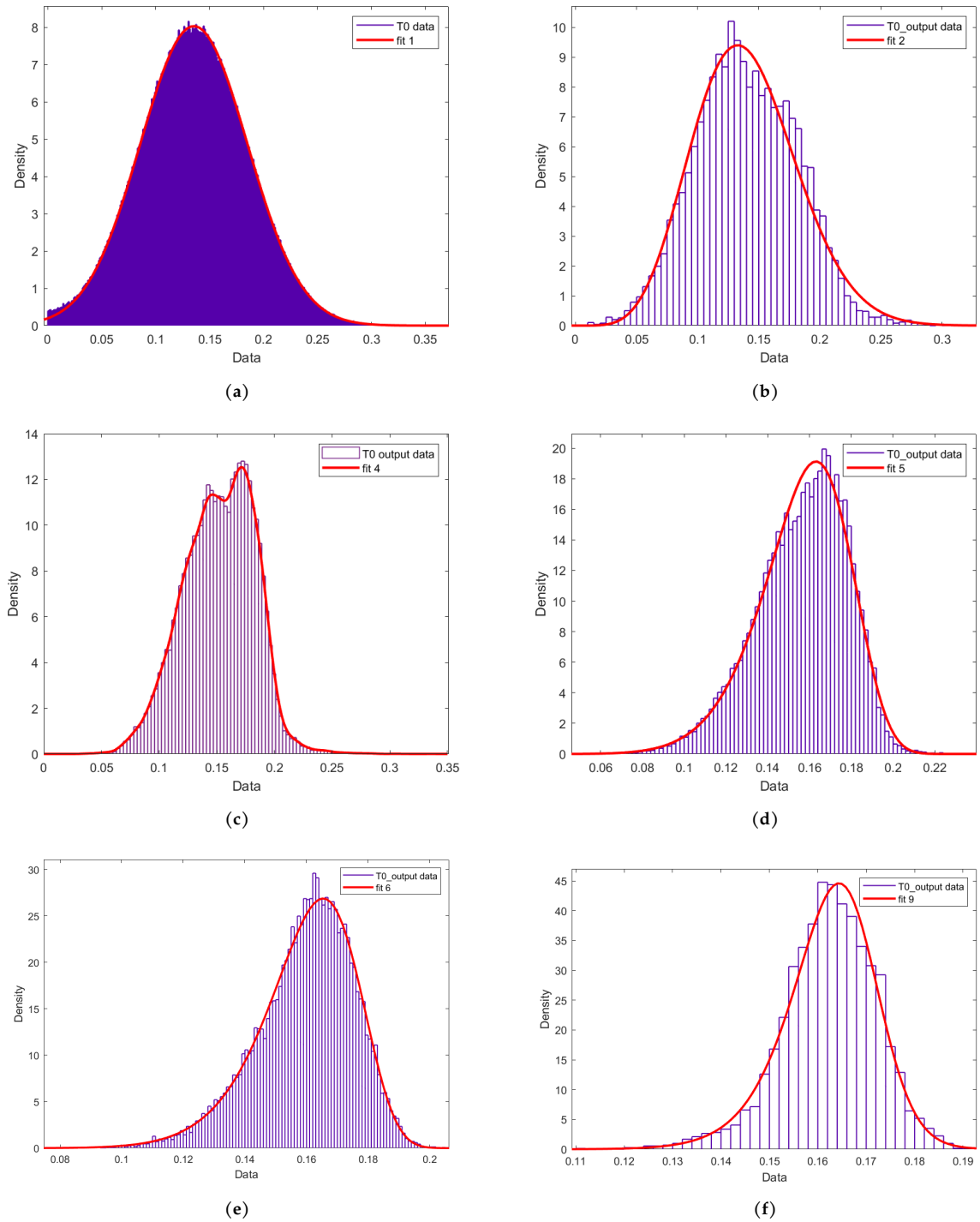

Figure 5.3: The evolution of the probability distribution function across the five iterations of the first-stage ABC scheme for the tension reference parameter T_0 $(Pa.m)$ for experiment 3. The red lines correspond to the univariate distributions (or kernel functions) that are fitted to the posterior data after each iteration. The distributions fitted to the posterior data across the iterations are as follows: (a) normal (r=0), (b) Nakagami (r=1), (c) normal kernel smoothing function (r=2), (d) Weibull (r=3), (e) Weibull (r=4), and (f) Burr (r=5).

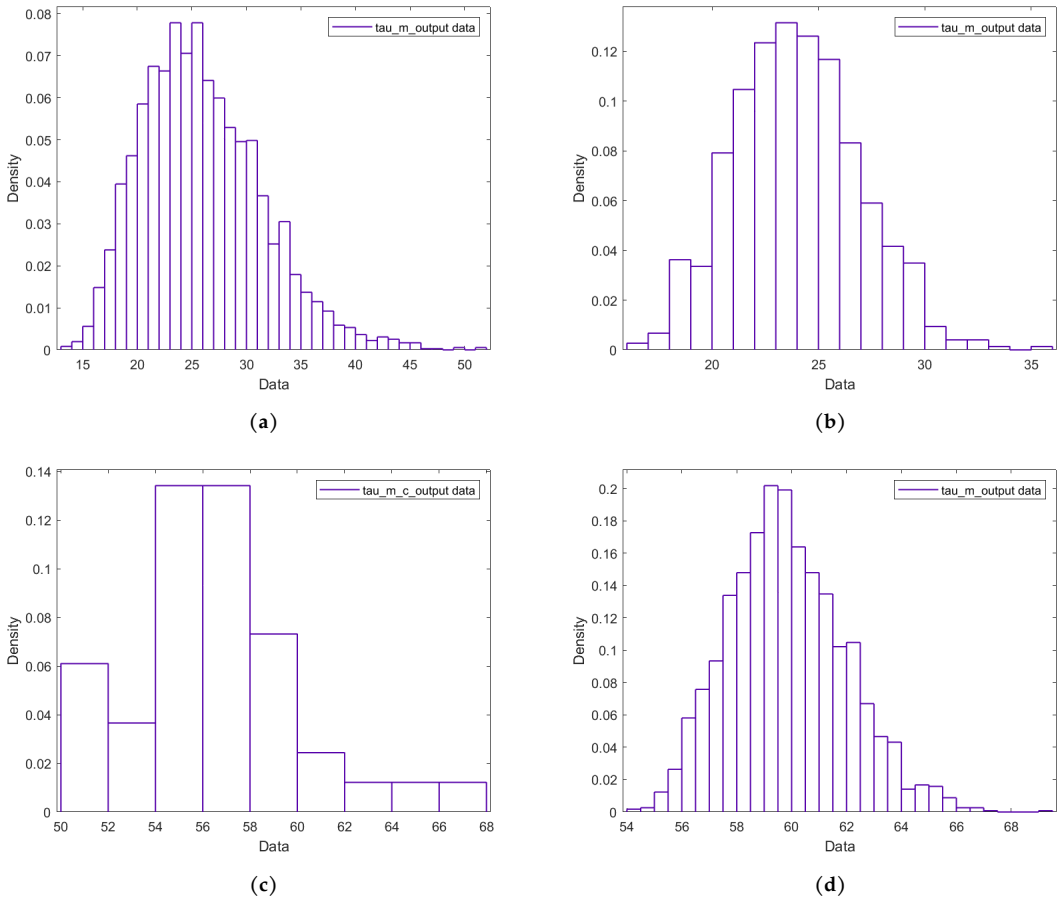

Figure 5.4: The final first-stage posterior distributions of τ_m (in seconds) from experiments (3 and 5) involving myogenic-induced dilation due to a decrease in wall tension (top figures (a) and (b)), and from experiments (4 and 6) involving myogenic-induced constriction due to an increase in wall tension (bottom figures (c) and (d)).

parameter calibration and validation but can also give insight into the mechanistic features of the dynamical system that the model is trying to simulate; in this case, it elucidates the differences in the myogenic time response and sensitivity between vessel dilation and vessel constriction. Accordingly, for the second-state ABC in which we seek a unified parameter distribution based on all experiments simultaneously, we differentiate between the two cases of myogenic-induced constriction and dilation, as described in Section 5.6.

5.6 Second-Stage Approximate Bayesian Computation

The ABC scheme aims to obtain a single final probability distribution of the model parameters. The final distributions obtained from the first stage relate to each experiment (*i.e.* vessel) individually. Due to the interaction and non-linear effects between the model parameters illustrated in Chapters 3 and 4, the final distributions for the model parameters cannot be sim-

ply combined across the different experiments to obtain a single distribution representative of all experiments. The final distribution for the model parameters must fit all relevant experiments, meaning that a single realisation of the parameter space must simultaneously lie within the prescribed error tolerance across all the relevant experiments for it to be accepted. To this end, we carry out a second round of an iterative ABC scheme as described below.

First, we divide the experiments, the results for which are demonstrated in Figure 5.1, into two groups: group A encompassing experiments (1, 3, and 5), where the myogenic response is dilation-based, and group B encompassing experiments (1, 2, and 4) in which the myogenic response results in constriction. Note that both groups include experiment 1, which does not feature any significant myogenic response (P_I is kept constant), but is rather used to help calibrate the parameters of the endothelial response along with the other experiments in the group.

Within each group, variables that are specific to the individual experimental setup (the initial conditions D_i, x_{mi}, x_{ei}) are treated independently and are sampled from the final posterior distribution of the first-stage ABC in Section 5.4. Meanwhile, variables that are shared (all the parameter space θ) are sampled from a single distribution. The prior distribution for the shared parameters is initially constructed by sampling from the fitted final posterior distributions from section 5.4 with an equal probability across the three experiments within each group. Note that for the first iteration, the final posterior distributions of the parameters from the first-stage ABC of the myogenic response (T_0, τ_m and S_m) for experiment 1 are not used in constructing the prior distribution in second-stage ABC, since the myogenic response is not directly induced in that experiment.

Next, we devise an iterative ABC algorithm, where, just as in the first-stage in Section 5.4, a variable space realisation is accepted only if the L_2, L_4, and L_∞ norms across all three experimental measurements and simulation outputs are within the prescribed error tolerances; these, in turn, being gradually narrowed across the iterations. Again, just as for the first-stage ABC, the fitted posterior distributions for a particular iteration become the prior distribution for the next iteration from which the variable space is sampled. Note that after the first iteration, before the parameter space starts to converge, the posterior parameter distributions can (and tend to be) be multimodal (mostly bimodal), and hence cannot be fit by the univariate

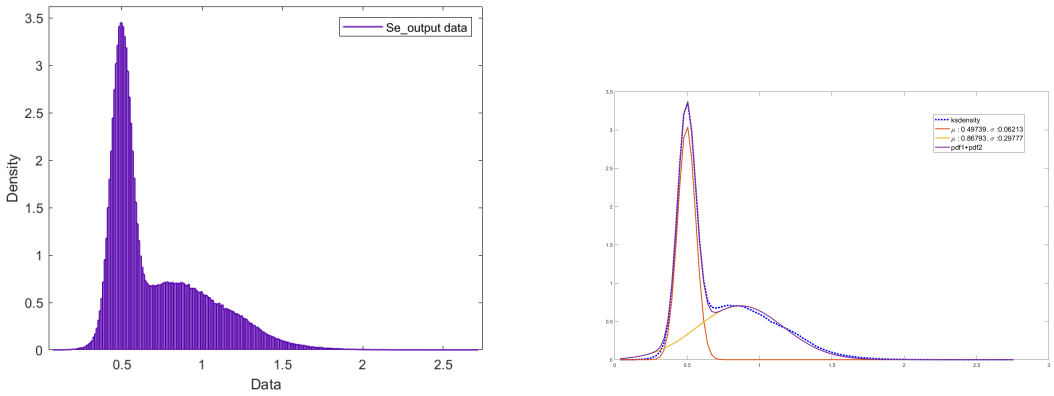

(a) (b)

Figure 5.5: (a) The posterior bimodal distribution for the parameter S_e, obtained after the first iteration of the second-stage ABC scheme for group B experiments (experiments 1,2, and 4). (b) The prior bimodal distribution (purple), constructed from the weighted mixture of two normal distributions (orange and red) to fit the posterior data (blue).

distribution options offered by the DistributionFitter application. In that case, if upon visual inspection the distribution is found to be bimodal, then a separate algorithm, developed to fit a bimodal distribution to the data through the weighted mixture of two normal distributions, is used. Figure 5.5(a) shows the initial bimodal distribution for the S_e parameter after the first iteration of the second-stage ABC algorithm for experiments group B, and Figure 5.5(b) demonstrates how the distribution can be approximated from the weighted mixture of two normal distributions. The multimodal parameter distribution would then gradually converge into a more pronounced univariate distribution across the iterations, as shown for the final distribution in Figure 5.7(b). The algorithm for the second-stage iterative SMC ABC scheme is described below.

```
1 for i=1:r  %number of iterations
2     V = sample(pi_V, MC) %Initialize the vector space V = [theta,U_i] by ...
          sampling from the prior distribution for a total of MC number of ...
          realisations.
3     accepted_V = []
4     for j=1:MC  %for each realisation j  in the MC realizations generated:
5         D_j_1 = obtain_diameter_trace(V, P_I_1, dP_1) %Simulate the first ...
              diameter dataset from the first experiment using the dynamic ...
              model, subject to the experimental inputs of P_I_1(t) and ...
              Delta_P_1(t) of the experiment.
6             if L2(D_j_1,D_1) ≤ epsilon_2 & L4(D_j_1,D_1)≤ epsilon_4 & ...
                  L_inf(D_j_1,D_1)≤epsilon_inf %if all error norms are within ...
```

```
                prescribed error tolerances for first experiment
7               D_j_2 = obtain_diameter_trace(V, P_I_2, dP_2) %Simulate the ...
                    second diameter dataset  from the second experiment ...
                    using the dynamic model, subject to the experimental ...
                    inputs of P_I_2(t) and Delta_P_2(t)
8               if L2(D_j_2,D_2) ≤ epsilon_2 & L4(D_j_2,D_2)≤ epsilon_4 & ...
                    L_inf(D_j_2,D_2)≤epsilon_inf %if all error norms are ...
                    within prescribed error tolerances for second experiment
9                   D_j_3 = obtain_diameter_trace(V, P_I_3, dP_3) %Simulate ...
                        the third diameter dataset  from the third ...
                        experiment using the dynamic model, subject to the ...
                        experimental inputs of P_I_3(t) and Delta_P_3(t)
10                  if L2(D_j_3,D_3) ≤ epsilon_2 & L4(D_j_3,D_3)≤ epsilon_4 ...
                        & L_inf(D_j_3,D_3)≤epsilon_inf %if all error norms ...
                        are within prescribed error tolerances for third ...
                        experiment
11                      accepted_V[end+1,:] = theta %accept realization
12      pi_V_new = distribution_fit(accepted_V) %Use the space of accepted ...
            realisations to generate a posterior  probability distribution that ...
            is within all the prescribed error tolerances for all experiments ...
            simultaneously
13      pi_V = pi_v_new %Set the obtained posterior probability distribution ...
            from the previous iteration to be the prior distribution for the ...
            next iteration.
14      Decrease the error tolerance(s) epsilon_2, epsilon_4, and epsilon_inf
```

5.7 Results of the second-stage ABC scheme

Figures 5.6 and 5.7 show the final unified model parameter distributions for group A (experiments 1, 3, and 5 where the myogenic response elicits dilation) and group B (1, 2 and 4, where the myogenic response is constriction-based), after 5 iterations (r=5) of the second-stage ABC algorithm. Figures 5.8 and 5.9 illustrate comparisons between the measured internal diameter and the values obtained from the dynamic model simulation for each experiment when using a parameter realisation obtained from the final posterior distribution.

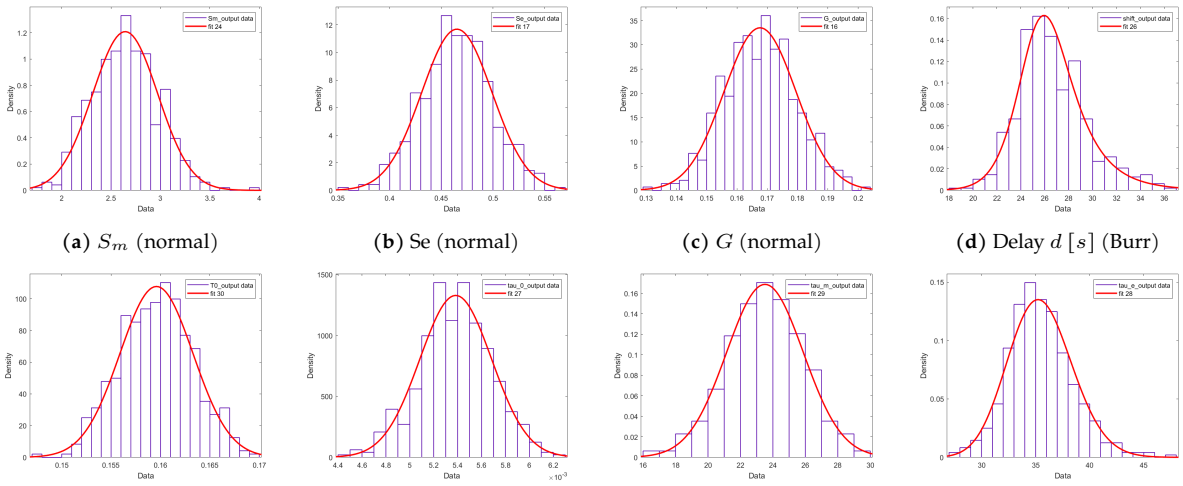

(**a**) S_m (normal) (**b**) Se (normal) (**c**) G (normal) (**d**) Delay $d\,[s]$ (Burr)

(**e**) $T_0\,[Pa.m]$ (normal) (**f**) $\tau_0\,[Pa.m]$ (normal) (**g**) $\tau_m\,[s]$ (normal) (**h**) $\tau_e\,[s]$ (gamma)

Figure 5.6: The final posterior distribution of the eight model parameters obtained from the second-stage ABC scheme (5 iterations) for group A experiments (1, 3 and 5), in which the myogenic response (if any) results in dilation. The best-fit univariate distribution (red curves) family type is indicated below each figure.

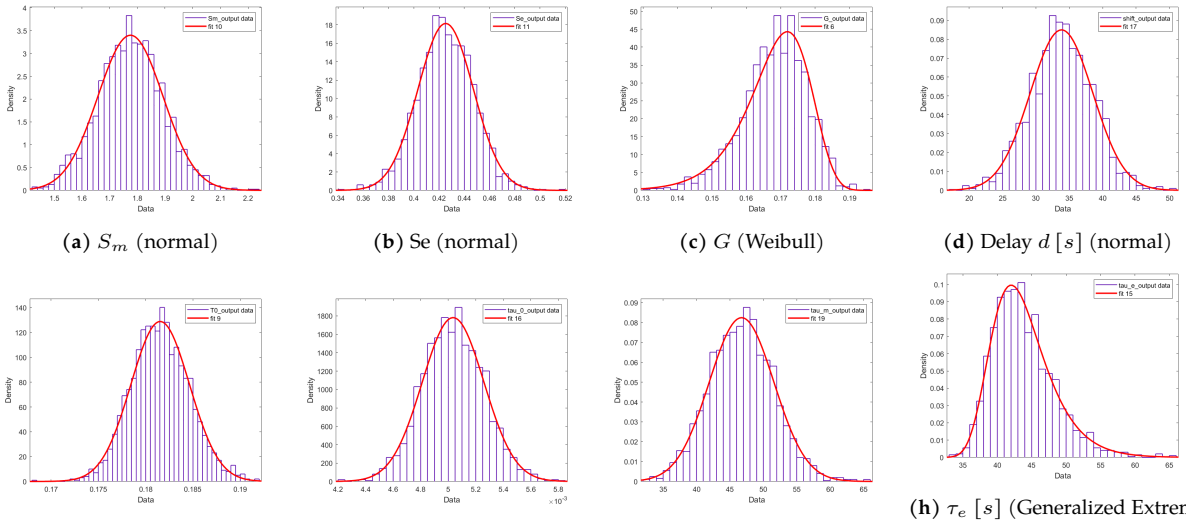

(**a**) S_m (normal) (**b**) Se (normal) (**c**) G (Weibull) (**d**) Delay $d\,[s]$ (normal)

(**e**) $T_0\,[Pa.m]$ (normal) (**f**) $\tau_0\,[Pa.m]$ (normal) (**g**) $\tau_m\,[s]$ (normal) (**h**) $\tau_e\,[s]$ (Generalized Extreme Value)

Figure 5.7: The final posterior distribution of the eight model parameters obtained from the second-stage ABC scheme (5 iterations) for group B experiments (1, 2 and 4), in which the myogenic response (if any) results in constriction. The best-fit univariate distribution (red curves) family type is indicated below each figure.

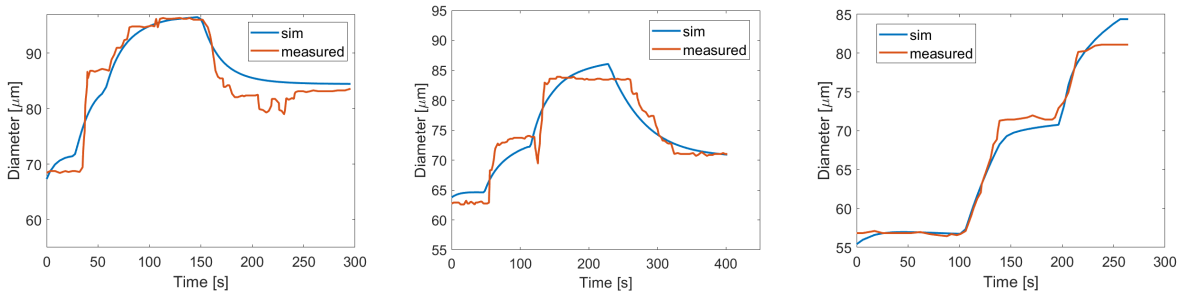

(**a**) Experiment 5 (**b**) Experiment 3 (**c**) Experiment 1

Figure 5.8: Examples comparing the traces of the simulated datasets to those of experimental measurements for each of the experiments in Group A, after sampling from the unified parameter distribution in Figure 5.6 obtained from the second-stage ABC scheme.

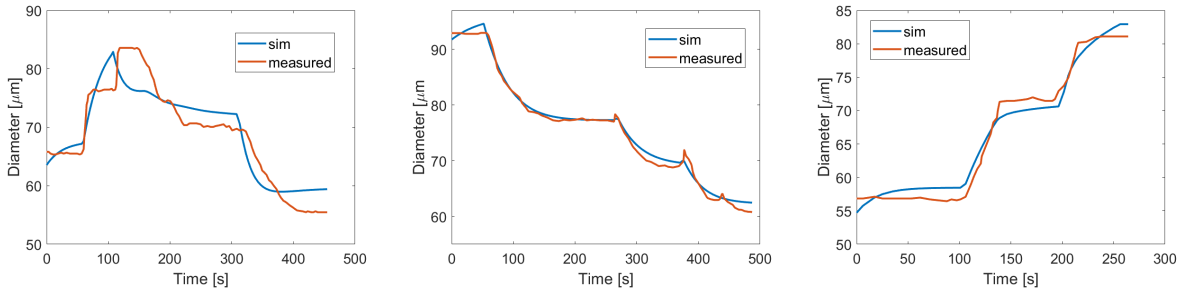

(**a**) Experiment 4 (**b**) Experiment 2 (**c**) Experiment 1

Figure 5.9: Examples comparing the traces of the simulated datasets to those of experimental measurements for each of the experiments in Group B, after sampling from the unified parameter distribution in Figure 5.7 obtained from the second-stage ABC scheme.

5.8 Discussion

In this chapter, we have presented a two-stage semi-automated parameter calibration algorithm and used it to calibrate parameter values for the vessel compliance model, which incorporates the myogenic and endothelial responses. The experimental data used for calibration consists of diameter traces of individual arteriolar vessels in response to the stimulation of the myogenic or endothelial mechanisms, as well as their interactions. Five out of the six experiments available across the two studies by the same research group,[155],[267] were ultimately used for parameter calibration. In the second-stage ABC scheme, and based on the results of the first-stage scheme, the experiments were divided into two groups (with one experiment present in both groups), to distinguish between myogenic-induced dilation and constriction. The distributions of the parameters characterising the myogenic response (S_m, τ_m, and T_0) are different between the two groups, with the constriction-based myogenic response exhibiting lower values of S_m, higher values of τ_m, and slightly higher values of T_0. Hence, it appears that the vessel responds faster and stronger to a drop in blood pressure via myogenic-induced dilation than to an increase in blood pressure eliciting myogenic-induced constriction. The mechanisms underlying this greater reactivity to hypotension than to hypertension may be related to a greater influence of vasodilator than vasoconstriction mediators on intracranial vascular tone.[92],[275] In other words, ensuring proper oxygenation might be more important than exerting protective influences elicited by hypertension. The differences in the parameter distributions characterising the myogenic response illustrate how adopting a suitable parameter calibration scheme to analyse experimental data could potentially provide valuable insights into the mechanisms and pathways of dynamical biological systems under study.

Meanwhile, there is a very good overall agreement and overlap in the remaining model parameter values between groups A and B, demonstrating general consistency and reliability of the compliance feedback model to reproduce the vessel response dynamics.

For the second-stage ABC scheme, the final parameter space distribution within each group was collectively calibrated based on data from all three experiments in that group; thus, it is understood as somewhat of a compromise between the optimal distributions of the three experiments within each group. This explains why the agreement between the simulated and measured traces in Figures 5.6 and 5.7 is slightly less pronounced than in Figures 5.2(a), 5.2(b), 5.2(c), 5.2(d) and 5.2(e) from the first-stage ABC scheme, in which the parameter distributions were independently calibrated for each experiment. Nonetheless, sampling from the final unified distribution has resulted in an overall very good agreement among all five experiments in groups A and B, meaning that the compliance feedback dynamic model can achieve great accuracy following parameter calibration, all while maintaining a very low computational cost: the simulation duration per realization for a single vessel was $< 2s$ when run on a Desktop computer for a $300s$ simulation time. Furthermore, while the final distributions in Figures 5.6 and 5.7 are meant to accommodate data from all three experimental setups within each group, the distributions are sufficiently narrow that a meaningful range of the parameter values can be obtained and used in future simulations (see Chapter 6).

Next, we discuss some of the reasons for the discrepancy between the simulated and measured diameter traces for experiment 6 in Figure 5.1(f), which was excluded from the second-stage ABC scheme. First, we note that there is a delay of about 10s between the increase in P_I and the myogenic-induced vessel constriction (and a delay of about 4.5s between the increase in ΔP and the following endothelial-induced dilation). In the compartmental model by Lanzarone et al.,[276] a pure delay of 2.5s was introduced to simulate the time interval between the reading of the arteriolar pressure and the myogenic response of the smooth muscle, potentially as a result of the viscoelastic behaviour of the vessel wall.[95],[277],[278] However, these viscoelastic effects seem to be small within the physiological range of pressure and flow,[171],[210] which is why many models using tube laws derived from linear elastic theory disregard the viscoelastic behaviour.[171] Considering that the myogenic time delay is negligible in the remaining experiments exhibiting increases in P_I, the 10s delay seems unlikely to be due to the viscoelastic effects. Second, we note that there is an increase in the vessel diameter occurring

simultaneously with the increase in P_I, and this could be attributed to the 'passive' component of the vessel compliance behaviour in our model; *i.e.*, before the myogenic-induced constriction takes place. However, this increase of $17\mu m$ seems to be quite significant, especially when compared to the passive changes observed in the other experiments conducted under similar conditions. Experimental data can be affected by confounding factors and corrupted by artefacts and noise, such that an accurate calibration can sometimes be difficult to achieve. Data thus have always to be treated with caution. Furthermore, we recognize that the compliance feedback model, while physiologically grounded, is a simplified representation of the VSM cell dynamics. Ultimately, given the significant discrepancies between the simulation results and measurements, we decided to exclude experiment 6 from further analysis so as not to erroneously affect the parameter calibration process.

Note that we have treated the maximal and minimal fractional change in compliance parameters ($\frac{\Delta C^{\pm}}{C_b}$)) as constants, with values of 10 and 0.8, respectively, based on the values from a previous compliance feedback model.[105] Incorporating those additional parameters into the variable space could have resulted in a better fit between the simulated data set and the experimental measurements, but we opted not to include them to maintain a reasonable parameter space dimensionality, with eight model parameters. In addition, potentially better fits between the simulated datasets and the measurements, as well as narrower final posterior distributions, could have been obtained by increasing the number of iterations in the second-stage ABC scheme, but we have generally found that after conducting five iterations the decrease in the error norms is insignificant, especially when contrasted against the increased computational cost. We note that in the future, the semi-automated algorithm could be potentially streamlined so that it is entirely automated, by exclusively using smoothing kernels, as opposed to relying on known univariate (or bivariate) distributions, to fit the posterior distributions. However, the designation of the error tolerances, which get gradually reduced in the SMC scheme across the iterations, did require some trial and error process that necessitated intervention in between the ABC iterations.

5.9 Conclusion

Overall, we have demonstrated that the chosen compliance model functional form provides a succinct but suitable description of the vessel behaviour mechanics. While haemodynamic models and mathematical formulations, especially ones characterising the vessel compliance and autoregulatory responses, traditionally tend to be either law-driven or data-driven, the calibration of the parameter space and the functional form of the compliance feedback model means that the model combines both approaches. The mathematical simplicity, computational feasibility, physiological relevance, and favourable agreement with the experimental data render the compliance feedback model a suitable candidate to be integrated into haemodynamic simulations and future clinical studies.

Chapter 6

The Conducted Vascular Response as a Mediator of Hypercapnic Reactivity: A Modelling Study

Abstract

It is well established that CBF shows exquisite sensitivity to changes in the arterial blood partial pressure of CO_2 (P_{a,CO_2}), which is reflected by an index termed cerebrovascular reactivity. In response to elevations in P_{a,CO_2} (hypercapnia), the vessels of the cerebral microvasculature dilate, thereby decreasing the vascular resistance and increasing CBF. Due to the challenges of access, scale and complexity encountered when studying the microvasculature, however, the mechanisms behind cerebrovascular reactivity are not fully understood. Experiments have previously established that the cholinergic release of the Acetylcholine (ACh) neurotransmitter in the cortex is a prerequisite for the hypercapnic response. It is also known that ACh functions as an endothelial-dependent agonist, in which the local administration of ACh elicits local hyperpolarization in the vascular wall; this hyperpolarization signal is then propagated upstream the vascular network through the endothelial layer and is coupled to a vasodilatory response in the VSM layer in what is known as the conducted vascular response (CVR). Finally, experimental data indicate that the hypercapnic response is more strongly correlated with the CO_2 levels in the tissue than in the arterioles. Accordingly, we hypothesize that the CVR, evoked by increases in local tissue CO_2 levels and a subsequent local release of ACh, is responsible for the CBF increase observed in response to elevations in P_{a,CO_2}. By constructing physiologically grounded dynamic models of CBF and control in the cerebral vasculature, ones that integrate the available knowledge and experimental data, we build a new model of the series of signalling events and pathways underpinning the hypercapnic response and use the model to provide compelling evidence that corroborates the aforementioned hypothesis. If the CVR indeed acts as a mediator of the hypercapnic response, the proposed mechanism would provide an important addition to our understanding of the repertoire of metabolic signalling pathways possessed by the brain and would motivate further *in-vivo* investigation. We also model the interaction of the hypercapnic response with the mechanisms of dCA and show how the dCA mechanisms, which otherwise tend to be overlooked when analysing experimental results of cerebrovascular reactivity, could play a significant role in shaping the CBF response to elevations in P_{a,CO_2}. Such *in-silico* models

can be used in tandem with *in-vivo* experiments to expand our understanding of cerebrovascular diseases, which continue to be among the leading causes of morbidity and mortality in humans.

6.1 Introduction

6.1.1 Cerebrovascular Reactivity

It is well established that the cerebral vasculature is profoundly affected by the blood CO_2 gas levels.[279] Elevations in the arterial partial pressure of CO_2 (P_{a,CO_2}), known as hypercapnia, lead to vascular dilation and a corresponding increase in CBF, whereas reductions in P_{a,CO_2} (hypocapnia) lead to vasoconstriction and a subsequent decrease in CBF.[280] This ability of the cerebrovascular bed to constrict or dilate with changes in P_{a,CO_2} is reflected by an index called cerebrovascular reactivity.[92] The highly sensitive CBF response to blood CO_2 levels serves as a vital homeostatic regulator that helps regulate and maintain the central pH in the environment surrounding the brain parenchyma.[92] Impairments in the cerebrovascular reactivity response have been implicated with numerous cerebrovascular pathologies including ischaemia,[281] small vessel disease,[282] cognitive impairment[283] and Alzheimer's,[284] as well as with peripheral pathologies, such as breathing instability in patients with obstructive sleep apnea[285] via interactions with the chemoreflex control of breathing.[92]

The mechanism behind cerebrovascular reactivity has not, however, yet been fully elucidated.[92],[286]–[288] Experimental evidence indicates the vasodilatory response involves the activation of K^+ channels on the VSM and ECs, resulting in hyperpolarization and a decrease in the activity of voltage-dependent Ca^{2+} channels; the reduced intracellular Ca^{2+} then lead to VSM relaxation and dilation.[288]–[292] This theory is supported by the fact that the ECs express four different types of K^+ channels,[292],[293] and that the endothelial and smooth muscle layers are connected via connexin myoendothelial gap junctions that relay the membrane potential changes from the endothelial layer to the VSM layer.[288],[294],[295] Another complementary pathway proposed involves the activation of nitric oxide synthase in ECs in response to increased CO_2 levels and/or pH[296]–[298]; nitric oxide, which functions as a vasoactive factor, is then released and diffuses into the VSM cells resulting in relaxation.[92],[288]

The precise mechanism through which changes in blood CO_2 levels evoke endothelial and VSM hyperpolarization remains to be understood. Some authors[299],[300] have proposed that the influence of CO_2 in the cerebral circulation involves the direct effects of extracellular pH on pial vessels. This theory, however, does not account for the different response dynamics between hypercapnic-induced dilation and hypocapnia-induced constriction. It has become increasingly clear that the cerebrovascular response to changes in CO_2 levels, is not symmetric, with the hypocapnic and hypercapnic responses exhibiting considerable differences in the speed and sensitivity of the response, location of signal initiation, and correlations with the blood gas levels in the different arteriole, venule and tissue compartments.

While the cerebrovascular reactivity is generally reported to be around $2-4\%$ around the baseline conditions,[286],[301],[302] a closer examination reveals a higher sensitivity in the hypercapnic range compared to the hypocapnic range.[303]–[307] Ainslee and Duffin[92] have speculated that, from a functional perspective, the higher reactivity in the hypercapnic range might serve as a protective mechanism to prevent compromised CBF during transient drops in arterial CO_2 levels, which could occur in a range of physiological (eg., exercise or postural changes) or pathological (e.g. congestive heart failure, anxiety attacks, asthma) situations. In other words, preserving sufficient oxygenation of cerebral tissue might be more important than mitigating pH disturbances. Furthermore, experimental data on cerebrovascular reactivity have reported that there was a threshold in P_{a,CO_2} (as low as $\approx 44.4mmHg$), above which increases in CO_2 tension can also result in increases in blood pressure.[92],[286] Such hypercapnia-induced increases in blood pressure would contribute to increases in CBF irrespective of changes in vascular resistance, and would thus mask the true interpretation of cerebrovascular reactivity,[92] which is conventionally ascribed to the changes in CBF that arise as a result of adaptive changes in vessel calibre.[92]

Interestingly, the cerebrovascular reactivity in the hypercapnic range has been reported to be significantly higher (by 97%) when presented against jugular venous partial pressure instead of that in the arterioles, compared to a relatively modest increase (by only 24%) in the hypocapnic case.[92] Experimental observations demonstrate that during hypocapnic conditions, P_{a,CO_2} may have a more important role in dictating the CBF response than the partial pressure in the jugular vein.[308] However, under conditions of CO_2 elevation, changes in the jugular venous CO_2 partial pressure provided a better correlation to the CBF response com-

pared to changes in P_{a,CO_2}.[309] Furthermore, while the hypocapnic-induced vasoconstriction is unaffected by vessel size, it is primarily the smallest blood vessels that are most responsive to elevations in CO_2 levels.[310] For instance, in cats, when P_{a,CO_2} was increased from $35-43.5mmHg$ to $47-117mmHg$ the average percentage increase in the diameter of arteriole vessels of $\leq 30\mu m$ resting diameter was 92%, nearly threefold that of vessels of resting diameter of $\geq 30\mu m$ (34%). Meanwhile, when P_{a,CO_2} was lowered from $35-45$ to $17-33mmHg$, the average percentage decreases in diameters were 16.9% and 13.9% across the two vessel groups.[307] Finally, we note the earlier works of Kontos et al.,[299] which demonstrated that, while vasodilation as a result of an increase in P_{a,CO_2} was completely inhibited by a reduction in CSF CO_2 (which is likely reflective of tissue CO_2 levels, P_{t,CO_2}), an equivalent reduction in P_{t,CO_2} but under normal P_{a,CO_2} resulted in no vasoconstriction. Given that the jugular venous CO_2 partial pressure is likely to be a closer index of P_{t,CO_2} than P_{a,CO_2} is to P_{t,CO_2},[305],[311]–[314] these experimental findings seem to reflect a differential control of CBF, that is primarily instigated by changes in the CO_2 levels on the arterial side during hypocapnia,[315] and brain tissue CO_2 levels during hypercapnia; the latter would, in theory, permit a response that is more specific and reflective of the tissue environment and metabolic demands, thereby circumventing the risk of hypoperfusion.

Different values have been reported in the literature regarding the speed and latency of the cerebrovascular response to CO_2,[307] and in many cases, the data do not allow for a calculation of an exact time constant.[316] For example, Poulin et al.[287] reported a time constant of 45s for a hypercapnic stimulus, while a value of 80s can be approximated from the data by Shapiro et al.[309] In one study measuring the hypercapnic response, a time constant of up to 339.2s was reported for the hypercapnic response (and 40.9s for the hypocapnic response).[317] Meanwhile, for the CBF response to a step hypocanic response, Severinghaus and Lassen[308] found a time constant of about 18s. These differences in timescale can be attributed, in part, to different studies relying on different measurement techniques and measuring different quantities; for instance, it has been proposed that the delay between the input and output reported in some studies is a result of measuring end-tidal P_{CO_2} as opposed to directly measuring P_{a,CO_2} and that delay differences seem to derive from different speeds for CO_2 uptake and different transit time it takes for blood to pass from blood to the brain.[122],[307] Furthermore, it is worth noting that different experimental protocols for changing CO_2 gas

blood levels could give rise to different response dynamics. For instance, the steady-state and rebreathing techniques, the two methods employed to elicit changes in blood CO_2 levels, can result in different incremental changes in P_{t,CO_2},[312],[313] and can have different effects on the CO_2 gradients between the arterial, venous and brain tissue compartments, which could explain the differences in the reported cerebrovascular reactivity between the two methods.[92] Clearly, this is a case in which a better understanding of the physiological changes induced by changes in blood CO_2 levels can help better interpret experimental data, which, at times, can appear contradictory, and assist researchers in making a more informed decision regarding the choice of breathing intervention, depending on the objectives of the experiment.

Finally, while previous compartmental models have used the same value (20s) for the cerebrovascular reactivity time constant under both hypocanpic and hypercapnic responses,[86],[122] results from the same experimental protocol suggest that the two responses operate on different time scales. For instance, the fitted time constant for the hypercapnic response was more than seven times larger than that for the hypocapnic response, with the cerebrovascular response reaching its peak by around 6 seconds and 2 minutes following hypocapnic and hypercapnic step protocols, respectively.[287] Similarly, the time constant for the hypocapnic response in anaesthetized cats when measuring the end-tidal P_{CO_2} was 8.3 times smaller on average than that for the hypercapnic response.[317] While such experiments provide important and valuable insights, it is difficult to rely on such limited data, most of which provide information on only the arterial-venous CO_2 partial pressure gradients with no information on the CO_2 flux across the brain, to obtain accurate interpretation and representation of the mechanisms behind the cerebrovascular reactivity response.[92]

Discerning the physiological dynamics behind cerebrovascular reactivity is also crucial for understanding the pathophysiology behind impaired reactivity, and its implications on the brain and the body. For instance, an emerging field of interest is the interaction between cerebrovascular reactivity and the ventilatory response.[92] An impaired CBF reactivity response affects the control of central pH, which would in turn alter the gain of the chemoreflex control of breathing and may thus be a critical cause behind breathing instability that occurs in central sleep apnoea in patients with cognitive heart failure,[92] a notion that indeed has been supported by experimental studies.[306],[318] In such a scenario, understanding the physiological mechanisms behind cerebrovascular reactivity can help better elucidate the close relationship

between CBF and chemoreflex control of breathing, and help provide a more integrative and holistic understanding and treatment of the pathologies underpinning breathing instability.

However, given that the hypercapnic response occurs predominantly in the cerebral microvasculature,[307],[310] our capacity to investigate the response's physiological dynamics and origins in vivo becomes limited due to the challenges of access, insufficient spatial and temporal resolutions, and complexity of the cerebral microcirculation.[319] The authors of a previous study[287] have remarked that a first-order model consisting of a single delay, gain term, time constant and offset may be an oversimplified representation of the CBF dynamics recorded during a hypercapnic protocol. Consistent with this notion, another study demonstrated that the initial CBF response to a step change in the P_{a,CO_2} is a highly complex process with marked intrasubject variability,[92] and that no stable relation is observable between vessel diameter and P_{a,CO_2}.[307]Furthermore, experimental data examining the reactivity response (see[287] for example) lack the time resolution required to capture the nuances of the complex hypercapnic response. Finally, experiments assessing the cerebrovascular reactivity examine either the overall response of CBF in response to blood CO_2 level changes or the response of individual vessels to changes in pH. Hence, they are unable to capture the spatial and regional variations in the vascular response, as well as the possible interactions between the vessels within the interconnected network, the characterisation of which is crucial, given the strong coupling between the haemodynamics of blood flow, and the precise vascular architecture.[26],[125]

Increasingly, mathematical modelling is being utilised to provide an alternative, precisely controlled tool for investigating biophysical phenomena,[320] especially when accompanied by corroborating *in-vivo data*. Unhampered by the limitations of the *in-vivo* experiments, *in-silico* models can play a vital role in filling in the gap in our understanding of the in vivo function of the brain. In this study, we integrate established experimental data and knowledge concerning the structural, chemical and electrical properties of the microvasculature, and encode these pathways within a mathematical computational framework that is then used to enhance our understanding of the in vivo processes within the brain, and offer a viable explanation of the sequence of events underpinning the physiological origins and dynamics of the hypercapnic response. The *in-silico model* developed in this study offers a fast, easy, and safe environment for selectively altering the constituent signalling components of the hypercapnic response. By comparing the model output under the different simulation conditions with

experimental and clinical data, the model can provide researchers with insight into the signalling components that are affected in cases of a compromised hypercapnic response and can help guide clinicians towards the development and administration of better-targeted drugs and treatment plans.

To this end, we first review the evidence from experimental data that motivates the choice of signalling pathways used in this study. We then describe how such signalling pathways can be mathematically formulated and encoded into the computational simulations. We also demonstrate how the model parameter values of the constituent cellular pathways can be calibrated and verified from the experimental data available. Finally, we run dynamic simulations of CBF and control and compare the model output to available experimental data characterising the overall response of the vasculature to assess the validity of the hypothesis being tested regarding the mechanistic origins and dynamics of the hypercapnic response.

6.1.2 Experimental Background

Acetylcholine as a Mediator of the Cerebral Hypercapnic Response We first review the experimental evidence that supports the involvement of the ACh cholinergic system in mediating the effects of hypercapnia on cerebrovascular resistance. ACh released from the neurons or the supporting glial cells is known to affect cerebrovascular resistance and CBF.[321]–[325] The administration of atropine in animals, an agent that blocks the ACh muscarinic receptors, has been shown to completely block the hypercapnic-induced increase in CBF, though it did not affect the CBF under normocapnic conditions when the animals were breathing normal air.[326] Furthermore, the hypercapnic CBF response was considerably amplified upon the administration of esserine, an inhibitor of cholinesterases that breaks down ACh.[326] Other experiments have similarly reported that the increase in CBF normally accompanying hypercapnia is potentiated by the inhibition of acetylcholinesterase activity, and reduced or abolished by muscarinic cholinergic receptor blocking agents,[323],[327],[328] thereby corroborating the notion that the hypercapnic response is mediated via a cholinergic step.

The involvement of the cholinergic pathway in the hypercapnic response seems to occur through the release of the ACh neurotransmitter and its local effect on the blood vessels. Previous experiments have established the presence of cholinergic neurons in the cortex,[329]

as well as the presence of cholinergic dilatory receptors on the surface of cortical vessels.[330] The release of ACh in the cortex was shown to induce vasodilation and an increase in regional cortical CBF.[322] The dilatory effects of ACh were abolished in the cerebral arteries and arterioles of M5 muscarinic receptor knockout mice, but not the extra cerebral arteries outside the brain, implying that cholinergic dilation is uniquely mediated by M5 receptors situated on the cerebral blood vessels.[331] Furthermore, the fact that elevations in CO_2 levels did not trigger ACh release in *in-vitro preparations*[332] suggests that ACh efflux likely originates from the brain neuronal and glial cells.

Metz et al.[333] showed that hypercapnia evoked a significant increase in ACh release from the cerebral cortex above baseline levels. Interestingly, a combined stimulus of hypoxia and hypercapnia produced a similar ACh release comparable to the hypercapnia alone, while hypoxia alone did not affect ACh release,[333] indicating that the release of ACh is a direct result of elevated CO_2 (or decreased pH) levels. Along the same lines, other experimental observations reported that the effects of elevated CO_2 levels on ACh release were not correlated with metabolic activity.[323],[332] These experimental results seem to echo the more general notion put forward by Zhu et al.,[334] which is that the main signalling pathways involved in neurovascular coupling and metabolic feedback mechanism rely on the release of vasoactive molecules by neurons and astrocytes that would then act on the contractile cells of the vessel walls, rather than on direct metabolic feedback signals such as glucose levels.[335],[336]

We also discuss the relationship between ACh release and pathological conditions involving impaired CBF, notably cerebral ischaemia. Under transient ischaemic conditions, there is an increase in ACh release,[337]–[339] which was hypothesized to stabilize CBF in cerebral ischaemia.[323] Such an increase could be theorized to occur due to the decreased flow of blood and the reduced washout of accumulating CO_2 produced from metabolism. When the ischaemic state is prolonged, ACh output decreases, potentially due to decreased availability and synthesis of ACh precursors, notably Acetyl-CoA.[323],[337],[340],[341] This reduced availability of ACh was hypothesised to impair the survival of cells within the CNS and contribute to the pathology of dementia.[323] Conversely, ACh enhancers significantly improved perfusion in experimental models of cerebral ischaemia and brain traumatic injury.[323] Clearly, understanding the dynamic relationship between CBF control and ACh release can open new avenues for understanding both the disease conditions and potential treatments of cerebrovas-

cular diseases.

The Conducted Vascular Response Endothelial-dependent agonists administered in preparations and animal models elicit remarkably robust conducted vasodilations whose magnitudes are positively correlated with hyperpolarization.[294] The electrical responses always preceded the local changes in diameter, and both decayed with distance in an electronic manner.[294],[342] Perhaps the most notable of those agonists administered is ACh, which has routinely and characteristically evoked a conducted response that spread several mm along the arterial connection and cross-branching points.[343],[344] Experimental data have confirmed that ECs acted as both the local source of charge production in response to ACh administration, as well as the primary pathway for conducting the hyperpolarization current lengthwise along the arterial wall.[295],[342],[343],[345],[346]

The arterial wall is optimally designed to facilitate the upstream 'ascension' of the CVR from the penetrating arterioles to the cortical surface.[295] In arterioles, ACh hyperpolarizes the ECs by activating Ca^{2+}-activated K^{+} channels.[343] Direct cell-cell contact, as well as homocellular junctions between the ECs, were deemed as the two pathways for the longitudinal electrical conduction,[295] since interventions that diminished the gap junctional conductance or introduced a focal disruption in the endothelium impaired or eliminated the longitudinal hyperpolarization spread and the corresponding vasomotor responses along the arterioles,[295],[342],[347],[348] while reciprocal experiments introducing focal disruption to the VSM connectivity did not attenuate the spread of the hyperpolarization signal.[342],[345]

As the hyperpolarization signal travels along the endothelium, it is transmitted into the surrounding VSMs via connexin myoendothelial gap junctions, promoting vessel wall relaxation by decreasing intracellular levels of Ca^{2+} which decreases the levels of myosin-light phosphorylation required for VSM contraction.[295],[346],[349]–[353] Constrictor responses on the other hand, which are often but not exclusively initiated in VSM cells, spread with a marked degree of variability,[294] and generally decay steeply with distance.[353]

Summary and Hypothesis Summing up the principal points in Section 6.1.2, we note that: 1) the hypercapnic response is mediated in some means by the cholinergic release of ACh, 2)

ACh plays a prominent role as an endothelial agonist evoking local hyperpolarization that is then robustly conducted upstream via the endothelial layer, and 3) the hyperpolarizing current in the endothelial layer is transmitted to the VSM layer via myoendothelial gap junctions, thereby eliciting a vasodilatory response by changing the vessel wall tone. Given the previous data and information in Section 6.1.2, we hypothesise that the ACh and CVR signalling pathways, which are utilised in neurovascular coupling, are also activated during the hypercapnic response to allow for sufficient and widespread coordinated vasodilation in response to elevations in tissue CO_2. The capillary bed and pericytes have already been shown to function as an extensive sensory web[5] to detect and transmit neuronal signals with ECs, astrocytes and other pericytes during NVCs,[294],[354]–[357] and in theory, the upstream conduction of the dilatory response from the regions exhibiting an increased CO_2 burden would allow for a finer, more precise, and more efficient delivery and redistribution of blood and oxygen to the regions experiencing a mismatch between blood supply and demand.

Nonetheless, the isolated and correlative nature of these observational, cause-and-effect *in-vivo* studies means they are insufficient to establish a reconciliatory explanation of signalling mechanisms behind the cerebral hypercapnic response. To test this hypothesis, we propose a computational model of the hypercapnic response, which comprises the following four components: 1) the chemical signal, in the form of ACh release, in response to the increase in tissue CO_2, 2) the electrical event responsible for the local current generation and changes in membrane potential in response to ACh release, 3) the charge spread along the endothelium responsible for conducting the dilatory response upstream, and finally 4) the mechanical events translating changes in membrane potential into tone development in the VSM. The different components of the hypercapnic response according to our model, along with their interaction with the rest of the components of the cerebrovasculature, are summarised in Figure 6.1.

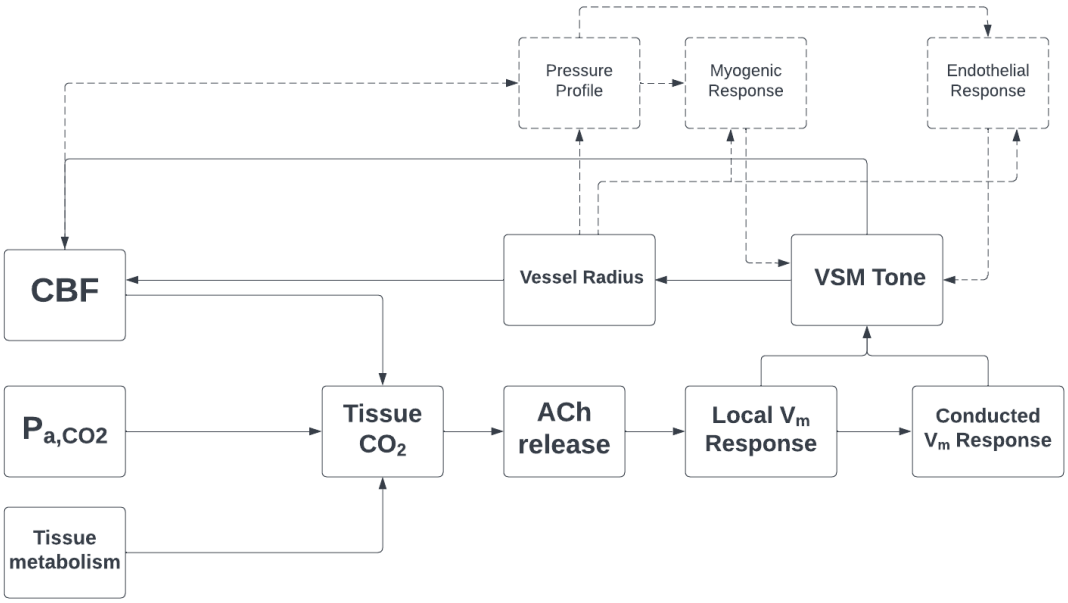

Figure 6.1: Summary of the components of the hypercapnic response in the model (indicated by bold and solid arrows and borders), and their interactions with the rest of the CBF control mechanisms (indicated by the dashed lines). The hypercapnic response is evoked by changes in tissue CO_2 levels, which could happen as a result of changes in any of the P_{a,CO_2}, capillary CBF or tissue metabolism. Increases in tissue CO_2 concentrations above their baseline values result in the local release of ACh, an endothelial agonist that elicits a local hyperpolarization response in the ECs. This hyperpolarization response is conducted upstream of the arteriolar network through the endothelial layer. The hyperpolarizing currents are conducted from the ECs to the adjacent circumferential VSM cells via myoendothelial gap junctions, causing the VSM cells to relax and the vessels to dilate, decreasing vascular resistance and thus increasing CBF. The hypercapnic response interacts with the myogenic and endothelial responses, which, in response to perturbations in the vessel wall tension and the shear stress, respectively, also alter the vessel tone.

6.2 Mathematical Model Formulation

6.2.1 The Metabolic Response: Signal Initiation

In our model, the metabolic response is initiated as a result of an increase in CO_2 levels, similar to the approach adopted by[86],[358] in their lumped compartmental models, given the role of CO_2 as a potent vasodilator,[299] as is in line with experimental findings like that by Auerr[307] who, in light of the lag between P_{a,CO_2} and diameter changes, suggested there is a metabolic event between changes in P_{a,CO_2} and its effect, vessel dilation. In this model, the hypercapnic response is mediated by changes in brain tissue CO_2 concentration, C_{t,CO_2}, rather than the CO_2 concentration in the arterioles, C_{a,CO_2}, as the C_{t,CO_2} provides a better correlate of the physiological stimulus during hypercapnia,[305],[311]–[314] as discussed in Section 6.1. However, it is the P_{a,CO_2} that has been customarily correlated in experimental measurements to changes in CBF in experiments quantifying the cerebral vasoreactivity (see for exam-

ple[286],[301],[302]). Furthermore, in such experiments, a hypercapnic state is achieved through voluntary modulations of the breathing pattern, including hyperventilation, breath-holding, and paced breathing[288],[359],[360] or by inhalation of CO_2-enriched gas.[288],[361],[362] Hence, it is the CO_2 level on the arterial side which is directly influenced by such manoeuvres. To allow for comparison and validation of the model output with experimental data, it is important to formulate the initial stimulus in our model, C_{t,CO_2}, in terms of P_{a,CO_2}, which can be achieved by considering the molar balance between CO_2 production and disposal in a volume of tissue perfused by a capillary segment[86]:

$$\frac{dC_{t,CO_2}}{dt} = m_{CO_2} - \frac{Q_c}{V_t}\left(C_{v,CO_2} - C_{a,CO_2}\right) \tag{6.1}$$

where m_{CO_2} corresponds to the rate of CO_2 production in the brain tissue (in $mol/(m^3.s)$), Q_c is the flow through the capillary bed perfusing a particular volume of brain tissue V_t, and C_{v,CO_2} is the CO_2 concentration (in mol/m^3) on the venule side of the capillary bed. Note that, since Equation (6.1) refers to the molar balance of CO_2 as blood passes through the capillary bed, C_{a,CO_2} refers to the total content per unit volume of CO_2 in the arterioles, including that which is bound to haemoglobin, rather than solely to that which is dissolved in blood plasma (C_{p,CO_2}). Given that the CO_2 dissolved in the arteriolar plasma constitutes around 6% of C_{a,CO_2},[363] and CO_2 has a solubility of 0.07 $mL\,CO_2/(100\,mL.mmHg)$ in arterial blood at body temperature,[364] a relationship between P_{a,CO_2} and C_{a,CO_2} which includes the total CO_2 content (dissolved and haemoglobin bound) can accordingly be derived:

$$C_{a,CO_2} = \left(\frac{0.5208mol}{m^3 mmHg}\right) P_{a,CO_2} \tag{6.2}$$

Due to its significantly higher solubility in water, CO_2 can diffuse about 20 times as rapidly as O_2,[365] such that the pressure difference required to cause CO_2 diffusion is far less than the pressure difference required for O_2 diffusion.[299],[365] Hence, with a partial pressure difference between intracellular, interstitial, and venous CO_2 of less than $1mmHg$,[365] we assume that the tissue CO_2 is in equilibrium with venous CO_2, as has been previously assumed in other modelling studies.[86] Note that for two dissolved gases to be in equilibrium, their partial pressures (not their concentrations) should be equal.[86],[366]

The relationship between venous CO_2 concentration and partial pressure can be described by Equation (6.3), which has been empirically derived from reduced blood samples having $14.7g\%$ Hb in a sample of healthy exercising individuals[367]:

$$C_{v,CO_2} = C_{v,CO_2,0} \left(\frac{P_{v,CO_2}}{P_{v,CO_2,0}} \right)^{0.34} \tag{6.3}$$

with $C_{v,CO_2,0} = 21mol/m^3$ and $P_{v,CO_2,0} = 40mmHg$. By combining Equation (6.3) with measurements of brain tissue CO_2 concentrations and partial pressures measured in dog brains,[368] and using the aforementioned assumption of equal partial pressures between the two compartments, Spronck et al.[86] empirically derived a linear relationship between C_{t,CO_2} and C_{v,CO_2}:

$$C_{v,CO_2} = \alpha_{t,v} C_{t,CO_2} + \beta_{t,v} \tag{6.4}$$

where $\alpha_{t,v} = 0.96$ and $\beta_{t,v} = 8.9mol/m^3$. Inserting Equation (6.4) into Equation (6.1), we can obtain an equation relating C_{t,CO_2} to C_{a,CO_2}, m_{CO_2}, and Q_c:

$$\frac{dC_{t,CO_2}}{dt} + \frac{Q_c}{V_t} \alpha_{t,v} C_{t,CO_2} = m_{CO_2} + \frac{Q_c}{V_t} \left(C_{a,CO_2} - \beta_{t,v} \right) \tag{6.5}$$

When applying Equation (6.5) to the 13-generation network proposed by Payne and Lucas[198] that is used in Chapter 3, if we were to assume a simple Krogh-cylinder arrangement, in which tissue is treated as a continuum of cells and represented as an array of uniformly distributed cylinders, then each capillary vessel independently perfuses a separate concentric tissue volume, $V_{t,i}$,[369] such that $Q_{c,i}$ refers to the flow through each capillary vessel. When applying the model to a multiscale network like the one constructed in Chapter 4, we assume that terminal arterioles feeding into the capillary bed are in sufficient proximity to the cholinergic site of ACh release, with a representative tissue volume surrounding each terminal arteriole, such that $Q_{c,i}$ would refer to the flow out of each terminal arteriole into the capillary continuum, also perusing a particular tissue segment of volume $V_{t,i}$. The use of the venous-arteriole CO_2 concentration gradient in Equation (6.1) in the multiscale network as a proxy of the CO_2

disposal is then justified by the fact that there are large overlapping regions of tissue fed and drained by the arterioles and venules,[126] and that set of arterioles feeding the capillary bed is in close proximity to the venous return,[86],[370] which can be indeed observed in the statistically generated multiscale network in Chapter 4, as demonstrated by the proximity of the red and blue clusters representing the locations of the terminal arterioles and venules, respectively, in Figure 4.2(d).

Finally, as discussed in Section 6.1.2, changes in C_{t,CO_2} at each representative tissue volume $V_{t,i}$, which could arise as a result of changes in any combination of C_{a,CO_2}, m_{CO_2}, or $Q_{c,i}$, would lead to the release of ACh, which then initiates the hyperpolarization response. As discussed, the blockage of the ACh cholinergic pathway has been shown to abolish the hypercapnic increase in CBF completely, yet it did not affect the basal CBF levels when breathing normal air.[326] On a similar note, while vasodilation as a result of increases in P_{a,CO_2} in arterioles has been completely inhibited by a reduction in CSF CO_2 levels (which are reflective of tissue CO_2 levels), no vasoconstriction was observed with an equivalent reduction in tissue CO_2 levels when P_{a,CO_2} was maintained under normal levels.[299] These experimental insights indicate that the signal triggering ACh release in response to hypercapnia is the increase in C_{t,CO_2} from its baseline level. To this end, we model the dynamics for such release via a first-order low-pass filter equation:

$$\tau_{ACh}\frac{dACh}{dt} = -ACh + S_{ACh}\left(\frac{C_{t,CO_2} - \overline{C}_{t,CO_2}}{\overline{C}_{t,CO_2}}\right) \tag{6.6}$$

where τ_{ACh} corresponds to the time constant characterising the ACh release in response to increases in C_{t,CO_2} from its baseline value, $\overline{C}_{t,CO_2}$, and S_{ACh} is the gain factor. The amount of ACh released is in arbitrary units (see Section 6.2.2). According to Equations (6.5) and (6.6), both a decrease in CBF or an increase in P_{a,CO_2} would result in an increase in ACh released from the cortex, which is in line with experimental data.[323]

Assuming CO_2 metabolism occurs due to aerobic respiration, the molar metabolic rate of CO_2 production, m_{CO_2}, is then equal to that of O_2 consumption, due to the identical stoichiometric coefficients of O_2 and CO_2 during cellular respiration. The O_2 cortical consumption rate in normal, conscious humans is $3.2 - 3.8ml/100g/min$,[371] which, assuming tissue density of

$1.04 g/cm^3$,[372] corresponds to a metabolic rate of $\approx 0.023 - 0.027 mol/(m^3 s)$. This is in agreement with the CO_2 metabolic rate of $0.58\, mL\, CO_2/(kgs)$ used in other studies,[86],[373] (the conversion can be done using the ideal gas law). Hence, m_{CO_2} in our model is chosen to be $0.025\, mol/(m^3 s)$. Previous studies have shown that cerebral O_2 consumption was unchanged with alterations in P_{a,CO_2}, at least in the range comparable with those measured during cerebrovascular reactivity testing,[3],[7],[374] meaning that, as long as the hypoxic threshold is not reached, m_{CO_2} can be approximately independent of the blood oxygen content and hence of Q_c. Note that metabolism can be linked to the levels of neuronal simulation (for example see[86]), but for simplicity, we assume here there are no changes in neuronal sensory input.

We can calculate the representative tissue volume $V_{t,i}$ perfused by each capillary region ($Q_{c,i}$) from the steady-state conditions (denoted by an overbar) of Equation (6.1):

$$V_{t,i} = \frac{\overline{Q}_{c,i}}{\overline{m}_{CO_2}} \left(\overline{C}_{v,CO_2} - \overline{C}_{a,CO_2} \right) \tag{6.7}$$

where $\overline{Q}_{c,i}$ refers to the calculated baseline flow through the capillary segment, and for the steady-state conditions, we assume CO_2 partial pressures of $40 mmHg$ and $45 mmHg$ on the arteriole and venule-sides, respectively. Note that, for the 13-generation network case, if the Krogh cylindrical arrangement is assumed, then we obtain a Krogh radius of $\approx 36 \mu m$, which is below the $100 \mu m$ upper limit that characterises the maximum distance between the blood vessel and cells required to ensure adequate oxygen diffusion to all tissue cells.[81] We also obtain a ratio of ≈ 9 for the tissue to capillary cylindrical radii, which is within the $7 - 11$ ratio used in modelling studies of O_2 transport.[369],[375]

There are no available experimental data from which one can directly deduce the values of τ_{ACh} and S_{ACh} in Equation (6.6) relating changes in tissue CO_2 levels to the amount of ACh released. To calibrate the S_{ACh} parameter, we examine the overall response of the network to elevations in P_{a,CO_2}, and compare the final, steady-state increase in CBF in the simulations as a result of the electrophysiological and CVR responses (as described in Sections 6.2.2, 6.2.3, and 6.2.4) to those recorded from experimental measurements. Experiments measuring cerebrovascular reactivity have generally derived a linear relationship between P_{a,CO_2} and CBF around baseline conditions, with a reported sensitivity in the range of $2 - 4\%/mmHg$ de-

pending on the study (see[286],[301],[302]). We first conduct simulations using the 13-generation network,[198] to determine the range of values for S_{ACh} that produce a $2-4\%$ percentage increase in CBF in response to a $1mmHg$ increase in P_{a,CO_2}, because they are significantly less computationally involved than those on the multiscale network. The obtained S_{ACh} values are then used to infer a value for S_{ACh} in the multiscale network, which is more representative of the microvasculature structure. The simulations are then conducted on the multiscale network using different levels of P_{a,CO_2} input, to assess whether or not the model can capture the experimentally derived linear relationship between CBF and P_{a,CO_2}, as well as compare the overall time dynamics of CBF changes to those reported from experiments.

To control for the confounding factor of blood pressure increases past the hypercapnic threshold, and to allow for appropriate comparison with the experimentally derived $CBF - P_{a,CO_2}$ relationship, we limit the P_{a,CO_2} used in calibration to a maximum of $44mmHg$. Also, for simplicity, and due to lack of available data otherwise, we assume $\tau_{ACh} = 1$, the choice for which is discussed in Section 6.4. Furthermore, while the reported increases in CBF as a result of changes in CO_2 levels are typically (and understandably) attributed to the cerebrovascular reactivity response, the measurements were likely recorded under fully functional myogenic and endothelial mechanisms that respond to the changes in the blood pressure and vessel calibre profile across the microvasculature network; these, in turn, would interact with the hypercapnic response. Hence, it is important to account for the presence of such mechanisms in the simulations, which are described in Section 6.2.4, when comparing the simulation results to experimental data for purposes of verification or parameter calibration.

6.2.2 Translating the Chemical Signal into an Electrical Signal

In arterioles, ACh hyperpolarizes ECs by activating Ca^{2+} activated K^+ channels; the hyperpolarizing current is then transmitted into the VSM layer via myoendothelial gap junctions. A model characterising the behaviour of the coupled endothelial-VSM cell behaviour to ACh and NE agonist administration has been previously constructed.[376],[377] The coupled model was formulated by combining the EC model of Silva et al.[378] which consisted of 10 differential equations, and the VSM model of Kapela et al.[379] which incorporated 25 ODEs, which were coupled through modelling the intercellular current and paracrine diffu-

sion of signalling molecules through the myoendothelial gap junctions.[376],[379] The equations thus characterise the electrophysiological behaviour of each respective cell type by tracing the flows of various ionic currents and signalling molecules.

The multiple ion channels and secondary messenger pathways through which neurotransmitters like ACh and NE elicit changes in the membrane potential render the mathematical modelling of the EC and VSM cell membrane potential dynamics a non-trivial task.[376] It has been subsequently demonstrated[376] that, in response to step increases in administered ACh, the membrane potential dynamics of each of the two cell types in the coupled endothelial-VSM cell model could be accurately and succinctly represented by the response of a second-order system, the solution for which takes the form of:

$$v(t) = ae^{-\frac{t-\delta}{\tau_1}} + ce^{-\frac{t-\delta}{\tau_2}} \tag{6.8}$$

where $v(t) = V(t) - V_m^\circ$ corresponds to incremental voltage changes from the cell's resting or quiescent membrane potential, and δ represents the delay in the EC response. This, in turn, allowed for the extraction of the transfer function in the Laplace domain, which, assuming system linearity, facilitates the interrogation of the membrane potential dynamics of the coupled system to other forms of ACh input, and not only a step response. To examine the appropriateness of the linear system approximation, the EC membrane potential dynamics in response to stimulation by concomitant ACh and NE, obtained from the Laplace transfer function approach, were compared to the membrane potential dynamics obtained from the original coupled cell model, with a very favourable agreement between the results obtained from the two methods,[376] thereby supporting the approximation of system linearity.

Here on, we describe how the transfer function can be used to derive an approximate relation in the time domain between ACh levels and the corresponding changes in membrane potential in response to any ACh input. For the subsequent analysis, we shall focus on the modelling of the EC membrane potential response to ACh simulation, since the EC layer represents the predominant pathway of conducting the hypercapnia-induced hyperpolarization signal, as discussed in Section 6.1.2, though the analysis is equally valid for the VSM layer.

Transforming Equation (6.8) into the Laplace domain, we obtain:

$$v_{step}(s) = \frac{a}{s-b}e^{-\delta s} + \frac{c}{s-d}e^{-\delta s} \tag{6.9}$$

where $b = -1/\tau_1$, and $d = -1/\tau_2$. Note the amount of ACh administered was initially formulated in terms of arbitrary units (a.u), in line with the other models,[376],[379] and a value of $ACh(t) = 1\,a.u$ was assigned to the simulation input condition of the coupled cell model from which the Laplace model variables (a, b, c, d) were extracted. 1 a.u corresponds to the ACh concentration in the original model by Kapela et al.[379] which yields an IP_3 release rate of $5.46 \times 10^{-8} M/s$. By comparing the ACh-induced response from the models to empirical data recorded from while-cell-patch-clampled ECs in situ in isolated vessels,[380] it was subsequently determined[376] that 1 a.u approximately corresponds to an ACh concentration of $360nM$. Working in terms of the a.u, the Laplace transform of the simulation input corresponding to a step increase in ACh to 1 a.u can be given by:

$$x_{step}(s) = \frac{1}{s} \tag{6.10}$$

and the resulting transfer function can be formulated as:

$$\begin{aligned} H(s) = \frac{v_{step}(s)}{x_{step}(s)} &= s\left(\frac{a}{s-b} + \frac{c}{s-d}\right)e^{-\delta s} \\ &= \left((a+c) + ab\left(\frac{1}{s-b}\right) + cd\left(\frac{1}{s-d}\right)\right)e^{-\delta s} \end{aligned} \tag{6.11}$$

The membrane potential output to any ACh administration input, $ACh(s)$, is then equal to $v(s) = H(s)ACh(s)$, and can be formulated as:

$$v(s) = (a+c)\,ACh(s)e^{-\delta s} + ab\frac{ACh(s)e^{-\delta s}}{s-b} + cd\frac{ACh(s)e^{-\delta s}}{s-d} \tag{6.12}$$

Equation (6.12) can then be inverse Laplace transformed to obtain a numerical expression in the time domain for the dynamics of the local incremental voltage of the endothelial layer in terms of any ACh concentration profile (in a.u): $v_{endo}(t) = v\big(t, ACh(t)\big)$. The inverse Laplace

transform of the first term on the RHS of equation 6.12 can be given as:

$$\mathcal{L}^{-1}\Bigg((a+c)\, ACh(s)e^{-\delta s} \Bigg) = (a+c)\, ACh(t-\delta) \tag{6.13}$$

The second term on the RHS of equation 6.12 can be written as the product of the Laplace transform of two functions in the time domain:

$$ab\frac{ACh(s)e^{-\delta s}}{s-b} = F(s)G(s) \tag{6.14}$$

where

$$F(s) = abACh(s)e^{-\delta s} \tag{6.15}$$

$$G(s) = \frac{1}{s-b} \tag{6.16}$$

Consequently, $f(t) = \mathcal{L}^{-1}\Big(F(s)\Big)$ and $g(t) = \mathcal{L}^{-1}\Big(G(s)\Big)$ can be obtained from the inverse Laplace transform of Equations (6.15) and (6.16):

$$f(t) = abACh(t-\delta) \tag{6.17}$$

$$g(t) = e^{bt} \tag{6.18}$$

Using the convolution theorem, the inverse Laplace transform of the second term in Equation (6.12) can be written as:

$$\begin{aligned}\mathcal{L}^{-1}\left(ab\frac{ACh(s)e^{-\delta s}}{s-b}\right) = (f \circledast g)(t) &= \int_0^t e^{b(t-t^*)} abACh(t^*-\delta)\, dt^* \\ &= abe^{bt}\int_0^t e^{-bt^*} ACh(t^*-\delta)\, dt^*\end{aligned} \tag{6.19}$$

Using the trapezoidal integration scheme with timestep Δt (where $n = t/\Delta t$) to approximate

the integral in Equation (6.19), and assuming steady-state conditions before any stimulus is introduced (*i.e.* $v(t<0)=0, ACh(t<0)=0$), then we can rewrite the expression in Equation (6.19) as:

$$abe^{bt}\int_0^t e^{-bt^*}ACh(t^*-\delta)\,dt^* \approx abe^{bt}\Delta t\left(\left(\sum_{n=1}^{\frac{t}{\Delta t}-1}ACh(n\Delta t-\delta)e^{-n\Delta tb}\right)+\frac{1}{2}ACh(t-\delta)e^{-bt}\right) \tag{6.20}$$

Similarly, we can obtain an expression for the inverse Laplace transform of the third term on the RHS of Equation (6.12):

$$\mathcal{L}^{-1}\left(cd\frac{ACh(s)e^{-\delta s}}{s-d}\right)\approx cde^{dt}\Delta t\left(\left(\sum_{n=1}^{\frac{t}{\Delta t}-1}ACh(n\Delta t-\delta)e^{-n\Delta td}\right)+\frac{1}{2}ACh(t-\delta)e^{-dt}\right) \tag{6.21}$$

Finally, the expressions in Equations (6.13), (6.20), and (6.21) can be added to obtain an expression for the local change in membrane potential in terms of any ACh concentration profile in the time domain: $v_{endo}(t)=v\big(t,ACh(t)\big)$.

Parameter Values of the Chemical-Electrical Coupling Emerson and Segal[345] reported that the onset of ACh stimulus preceded that of hyperpolarization by $0.8\pm0.1s$ in their experimental measurements. By comparing the ACh-induced response of the coupled EC-VSM cellular model to experimental data by Carter and Ogden,[380] Rego[376] calculated a value of 1.5s for the delay between ACh stimulus and initiation of local hyperpolarization. As a compromise, we choose a value of $\delta=1s$ for the delay in our model.

To obtain the values for the $a, b, c,$ and d parameters characterising the local $ACh-v_m$ relationship in Equations (6.13), (6.20) and (6.21), we fit the EC-VSM cellular coupled model output to a step increase in ACh,[376] to the characteristic second-order response solution in Equation (6.8), using the Curve Fitting Toolbox from MATLAB version 2023a (The MathWorks, Natick, MA, USA). Note that the Curve Fitting Toolbox does not accommodate the option of a response delay (δ in Equation (6.8)), and hence the v_m response of the EC to a

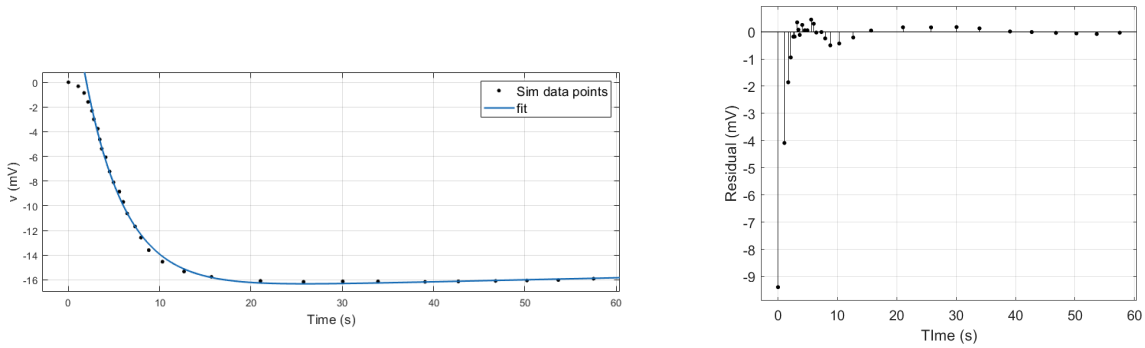

(a) (b)

Figure 6.2: Data points from the response of incremental change in membrane potential ($v_m = V_m - V_m^\circ$) in the EC-VSM cellular coupled model output to a step increase in ACh, along with the fitted second order exponential fit of the form $v(t) = ae^{-bt} + ce^{-dt}$ using MATLAB Curve Fitting toolbox ($R^2 = 0.99078$). Note that the data points were shifted by $1s$ to account for the delay in Equation (6.8). (a) Residual plot for the second-order exponential fit to the simulation data points. (b)

step ACh stimulus obtained from the model by Rego[376] was shifted in time by $\delta = 1s$ before fitting. Figure 6.2(a) shows how the best-fit curve compares against the model output data, while Table 6 summarises the range of values characterising the local EC V_m response to ACh stimulus.

Table 6: Values for the parameters characterising the relationship between local ACh release and the local change in membrane potential in Figure 6.2(a), obtained using the MATLAB Curve Fitting Toolbox.

Parameter	Optimal Value	Range
a	-16.84	[-17.99, -15.7]
b (s^{-1})	-1e-5	[-2.741, 0.682] e-3
c	26.24	[25, 27.48]
d (s^{-1})	-2.259e-1	[-2.482, -2.037] e-1

6.2.3 Relaying the Electrical Signal: Cable Model

The size of the ECs transmitting the electrical response is sufficiently small that a continuum approximation can be applied.[381] One option that can be used is the cable model. The use of the cable model implies that the endothelial and VSM layers are treated as a syncytium, which, intriguingly, despite the high myoendothelial coupling resistance,[294],[319] can be justified by the fact that the two layers are approximately isopotential around the physiological range

in response to endothelial-initiated agonists, with the endothelial layer eliciting near-parallel electrical responses in the VSMs as demonstrated both in experimental[124],[342],[382],[383] and in two cell-layered mathematical models,[376],[384],[385] producing an arterial wall V_m in the range of -35 to -55 mV under normal physiological conditions.[386],[387] Furthermore, VSMs lying circumferentially on a given ring around the arteriole have the same membrane potential, which justifies the treatment of the arteriolar tree conduction pathway as a branching network of 1-D vessels.[383]

The cable equation can be fundamentally derived by combining the core conductor model with a parallel conductance-capacitance circuit characterisation of the membrane electrical properties.[382] The core conductor equation can be given by:

$$\frac{\partial^2 V_m(x,t)}{\partial x^2} = (r_i + r_0) K_m(x,t) \tag{6.22}$$

where r_i and r_0 are the resistances per unit length (Ω/m) of the inner and outer conductors, respectively, with $r_i >> r_0$.[381],[382] Since longitudinal electrical conduction occurs predominantly through the endothelial layer,[346],[388] r_i represents the resistance within the EC cytoplasm and between the EC cells through the homocellular gap junctions, and is dominated by the latter.[381],[389] $K_m(x,t)$ is the membrane current per unit length (A/m) flowing from the inner conductor to the outer conductor.

To use the core conductor Equation in (6.22) to find the membrane current and voltage, another equation relating these variables via the electrical properties of the syncytium membrane must be utilised.[382] The electrical characteristics of the cell membrane could be represented by parallel conductance and capacitance,[382] such that (K_m) can be expressed as:

$$K_m(x,t) = g_m \left(V_m(x,t) - V_m^{\circ}\right) + c_m \frac{\partial V_m}{\partial t} \tag{6.23}$$

where c_m is the membrane capacitance per unit length (F/m) of the cylindrical syncytium, representing the insulation of the lipid bilayer, and g_m is the conductance per unit length (S/m) of the syncytium membrane, representing the conduction through the membrane ion channels. Combining Equations (6.22) and (6.23) we get the Equation for the cable model:

$$\frac{1}{r_i + r_0}\frac{\partial^2 V_m(x,t)}{\partial x^2} = c_m \frac{\partial V_m(x,t)}{\partial t} + g_m(V_m(x,t) - V_m^\circ) \tag{6.24}$$

Expressing the membrane potential as the incremental change from its resting value ($v_m(x,t) = V_m(x,t) - V_m^\circ(x)$), Equation (6.24) can be written in the incremental form:

$$\frac{1}{r_i + r_0}\frac{\partial^2 v_m(x,t)}{\partial x^2} = c_m \frac{\partial v_m(x,t)}{\partial t} + g_m v_m(x,t) \tag{6.25}$$

It is useful to define two constants; the time constant τ_M (s):

$$\tau_M = \frac{c_m}{g_m} \tag{6.26}$$

and the space constant λ_C (m):

$$\lambda_c = \frac{1}{\sqrt{(r_i + r_0)g_m}} \tag{6.27}$$

The time constant and space constant are characteristic values that indicate the speed and the discernible distance of signal propagation, respectively.[382] Hence, it is then useful to express the incremental form of the cable in terms of these two constants as follows:

$$\lambda_C^2 \frac{\partial^2 v_m(x,t)}{\partial x^2} = \tau_M \frac{\partial v_m(x,t)}{\partial t} + v_m(x,t) \tag{6.28}$$

We spatially discretise the vessels within a network into grid points with a spatial discretisation step of Δx_v within each vessel v. Using a step-size of Δt in the time domain, the solution at a point $(x,t) = (k\Delta x, n\Delta t)$ will be denoted as v_k^n. Equation (6.28) can then be appropriately spatio-temporally discretised to obtain a linear system of equations that can be used to solve for $\mathbf{v}^{n+1}$ in terms of $\mathbf{v}^n$ and $\mathbf{v}_t$, where $\mathbf{v}_t$ represents the incremental membrane potential at the terminal gridpoints where the electrical signal is initiated (*i.e.* where ACh acts). The discretisation stencil is then dependent on whether the relevant gridpoint is an interior, boundary, or junction gridpoint (see Figure 6.3(a) for an illustration of the gridpoint types).

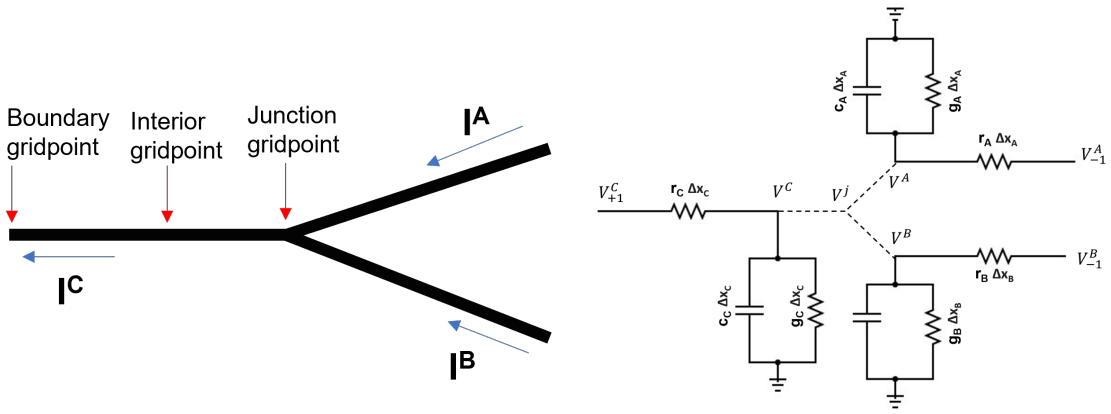

(a) (b)

Figure 6.3: The flow of the hyperpolarizing current (I) at a vessel junction from the downstream daughter vessels (A, B) to the upstream parent vessel (C) (a). A schematic of the cable model at the junction, composed of 3 vessels meeting at the converting node with incremental lengths of $\Delta x_1, \Delta x_2$, and Δx_3 (b).

For an interior gridpoint at location k surrounded by two gridpoints within the same vessel at locations $k-1$ and $k+1$, we can combine the second-order central spatial differencing scheme with the second-order Crank-Nicolson (CN) method, to obtain:

$$\begin{aligned}&\frac{\lambda^2}{2\Delta x^2}v_{k-1}^{n+1}+\left(-\frac{\lambda^2}{\Delta x^2}-\frac{\tau_M}{\Delta t}-\frac{1}{2}\right)v_k^{n+1}+\frac{\lambda^2}{2\Delta x^2}v_{k+1}^{n+1}\\&=-\frac{\lambda^2}{2\Delta x^2}v_{k-1}^{n}+\left(\frac{\lambda^2}{\Delta x^2}-\frac{\tau_M}{\Delta t}+\frac{1}{2}\right)v_k^{n}-\frac{\lambda^2}{2\Delta x^2}v_{k+1}^{n}\end{aligned}\tag{6.29}$$

Similarly, for boundary gridpoints, a second-order, one-sided differencing scheme can be combined with the CN method to obtain:

$$\begin{aligned}&\frac{\lambda^2}{2\Delta x^2}v_{k-2}^{n+1}+\frac{-\lambda^2}{\Delta x^2}v_{k-1}^{n+1}+\left(\frac{\lambda^2}{2\Delta x^2}-\frac{\tau_M}{\Delta t}-\frac{1}{2}\right)v_k^{n+1}\\&=\frac{-\lambda^2}{2\Delta x^2}v_{k-2}^{n}+\frac{\lambda^2}{\Delta x^2}v_{k-1}^{n}+\left(-\frac{\lambda^2}{2\Delta x^2}-\frac{\tau_M}{\Delta t}+\frac{1}{2}\right)v_k^{n}\end{aligned}\tag{6.30}$$

To obtain an expression for v_m at the junction gridpoint where vessels meet in Figure 6.3(a), we impose the fundamental law of charge conservation at the node:

$$I_A+I_B=I_C\tag{6.31}$$

and assume that the voltage drop across the junction is zero (*i.e.* the terminal gridpoints of the vessels meeting at the junction are equipotential). Figure 6.3(b) shows a schematic of the core conductor model for each of the 3 vessels meeting at the converting node with incremental lengths of ($\Delta x_1, \Delta x_2$, and Δx_3), combined with a parallel conductance-capacitance representation of the membrane used to derive the cable model. V_A, V_B and V_C are assumed to be equipotential (*i.e.* they all denote the same gridpoint), but for ease of visualisation they have been all connected via a zero-resistance pathway to the virtual gridpoint of membrane potential V_j in Figure 6.3(b). The variables in Equations (6.22), (6.23), and (6.25) have been intentionally expressed in their intrinsic form; i.e, they have no dependence on the length (or surface area) of the conductor or membrane under consideration (see Section 6.2.5). From the incremental representation of the cable model in Figure 6.3(b), an expression for the currents I_A, I_B, and I_C flowing into the terminal gridpoint can be obtained:

$$I_A = \frac{v_{A-} - v_A}{r_i \Delta x_A} - g_m \Delta x_A v_A - c_m \Delta x_A \frac{dv_A}{dt} \tag{6.32}$$

$$I_B = \frac{v_{B-} - v_B}{r_i \Delta x_B} - g_m \Delta x_B v_B - c_m \Delta x_B \frac{dv_B}{dt} \tag{6.33}$$

$$I_C = \frac{v_C - v_{C-}}{r_i \Delta x_C} + g_m \Delta x_C v_C + c_m \Delta x_C \frac{dv_C}{dt} \tag{6.34}$$

Substituting Equations (6.32), (6.33), and (6.34) into Equation (6.31), replacing v_A, v_B and v_C by v_j, and using a first-order implicit scheme for the temporal discretisation, we obtain:

$$\left(\lambda^2 \left(\sum_i \frac{1}{\Delta x_i}\right) + \left(\frac{\tau_M}{\Delta t} + 1\right) \sum_i \Delta x_i\right) v_j^{n+1} + \sum_i \left(v_{i-}^{n+1} \frac{-\lambda^2}{\Delta x_i}\right) = \frac{\tau_M}{\Delta t} \left(\sum_i (\Delta x_i)\right) v_j^n \tag{6.35}$$

where i denotes the vessel number and v_{i-}^{n+1} denotes the incremental voltage of vessel i at the gridpoint just preceding the junction. Since the signs of the voltage terms for the vessels meeting at the junction in Equation (6.35) are the same, the direction of the signal propagation across a converging junction does not depend on whether the vessel is a parent or child vessel. In other words, the propagation of the membrane potential is independent of the direction of CBF, as experimentally shown.[390] With Equations (6.29), (6.30) and (6.35) we have a linear

equation characterising the membrane potential for each gridpoint. The equations can be combined into a linear system of equations consisting of sparse matrices **A** and **B** accounting for the respective gridpoint adjacencies and gridpoint connections:

$$\mathbf{A}_{a\times b}\mathbf{v}_b^{n+1} = \mathbf{B}_{a\times b}\mathbf{v}_b^n \tag{6.36}$$

matrices **A** and **B** are of size $a \times b$, where a corresponds to the total number of interior, boundary and junction gridpoints, which from now on will be collectively referred to as internal (int) gridpoints, and b corresponds to the total number of gridpoints, including the terminal (term) gridpoints from which the signals are initiated. Rearranging the system of Equations in (6.37), we can finally solve for the membrane potential at the internal gridpoints ($\mathbf{v}^{\mathbf{int}n+1}_a$):

$$\mathbf{A}^{\mathbf{int}}{}_{a\times a}\mathbf{v}^{\mathbf{int}}{}^{n+1}_{a} = -\mathbf{A}^{\mathbf{term}}{}_{a\times(b-a)}\mathbf{v}^{\mathbf{term}}{}^{n+1}_{(b-a)} + \mathbf{B}_{a\times b}\mathbf{v}_b^n \tag{6.37}$$

Note that, while the numerical CN scheme is unconditionally stable and second-order accurate, it can under certain conditions give rise to oscillations that propagate as weakly damped and could get amplified in time, thereby compromising the accuracy of the solution.[391] This happens when there is a sudden jump in the initial or BCs, which occur, for instance, when simulating the hypercapnic response by a sudden increase in P_{a,CO_2} (see Section 6.3). In Appendix C.1, we describe how the numerical solver for modelling the propagation of the electrical component of the CVR is modified to circumvent the emergence of such oscillations.

6.2.4 Converting the Electrical Signal into a Vasodilatory Response

The final stage of the CVR is to convert the changes in membrane potential for each vessel into an appropriate autoregulatory response. As the hyperpolarizing currents longitudinally travel to neighbouring ECs by way of homocellular gap junctions, they may then be transmitted radially into the surrounding VSMs, via myoendothelial gap junctions,[346],[392] resulting in the closure of voltage-gated Ca^{2+} channels, and a subsequent reduction in intracellular Ca^{2+}.[3],[292],[393]

When examining the physiological characteristics and effects of the cerebrovascular CO_2 reactivity, it is important to take into account the dynamics of other physiologically occurring control feedback mechanisms at play, such as the myogenic and endothelial mechanisms. For instance, increases in the vessel calibre as a result of changes in arterial CO_2 levels, along with the corresponding changes in the upstream and downstream transmission of pressure, can lead to changes in the shear stress exerted on the endothelial layer, and changes in the VSM wall tension, thereby triggering the endothelial and myogenic mechanisms in tandem with the hypercapnia response. While the cerebrovascular reactivity measurements reported in experimental measurements can predominantly be attributed to changes in CO_2 levels, the measurements likely reflect the combined effects of different mechanisms on cerebrovascular resistance. Incorporating such mechanisms into the *in-silico* simulations of cerebrovascular reactivity can result in better model parameter calibration and interpretation of the available experimental data.[311]

Regardless of the vasodilatory stimulus and the corresponding pathway, whether it is changes in vessel wall tension that trigger the myogenic response, changes in the endothelial layer shear stress that trigger the release of vasodilatory metabolites like nitric oxide, or changes in the membrane potential that influence the open probability of Ca^{2+} channels, vasodilation is achieved via VSM relaxation as the various signalling pathways ultimately converge towards the common denominator of reducing the amount of intracellular Ca^{2+}, which is required to sustain the actin-myosin cross-bridge cycling and hence VSM contraction.[2],[349]–[351],[394]

To this end, we model the effect of each of the myogenic, endothelial and conducted vascular responses on the vessel VSM tone via an activation factor (x_m, x_e and x_C, respectively), that is altered via changes in the corresponding signal via a first-order equation emulating low-pass filter dynamics:

$$\tau_m \frac{dx_m}{dt} = -x_m + S_m \left(ReLU \left(\frac{RP_I - T_0}{T_0} \right) \right) \tag{6.38}$$

$$\tau_e \frac{dx_e}{dt} = -x_e + S_e \left(ReLU \left(\frac{R(t-d)\Delta P(t-d) - \tau_0}{\tau_0} \right) \right) \tag{6.39}$$

$$\tau_{CVR} \frac{dx_C}{dt} = -x_C + S_{CVR} \left(ReLU \left(\frac{v_m}{V_m^0} \right) \right) \tag{6.40}$$

where $P_I = (P_{in} + P_{out})/2 - P_{ext}$ is the vessel intraluminal pressure in terms of the vessel inlet, outlet and external pressures, $\Delta P = P_{in} - P_{out}$ is the pressure gradient across the vessel, and R is the vessel radius. T_0 and τ_0 correspond to the reference tension and shear stress values, respectively, at which the vessel exhibits no myogenic and endothelial activation, and d corresponds to the time delay during endothelial-induced constriction (see Section 6.2.5). Finally, τ and S denote the time constant and sensitivity, or gain, for each of the mechanisms. The use of a first-order model in Equation (6.40) to relay the changes in the membrane potential into the appropriate vasomotor response, is similar to the approach by Diep et al.,[351] and was necessary since the vessel diameters do not concomitantly change with alterations in membrane potential.[345],[351]

We note that the CVR model is used to account for only the hypercapnic case (*i.e.* $v \leq 0$), since, based on the discussion in Section 6.1, the hypocapnic and hypercapnic responses are unlikely to utilise the same constituent pathways and are likely to elicit different response dynamics. Furthermore, to ensure that no activation (or deactivation) happens for each feedback mechanism below the reference values at which no activation occurs, we borrow from the field of neural networks the rectifier or $ReLU$ activation function:

$$ReLU(x) = max(0, x) \tag{6.41}$$

such that the perturbation signal for each of the three responses first goes through the $ReLU$ function before being amplified by the gain factor. We then non-linearly map the summation of the control mechanism activation factors into the vessel wall compliance via an asymmetrical sigmoidal relationship, just as has been proposed in other compliance-based models of autoregulation[121] and in Chapters 3, 4, and 5:

$$C = C_0 \left(1 + \frac{\Delta C^{\pm}}{C_0} tanh \left(\frac{C_0 \left(x_C + x_e - x_m\right)}{G \Delta C^{\pm}}\right)\right) \tag{6.42}$$

where $\Delta C^{\pm}$ refer to the maximal and minimal changes in compliance, G is a parameter that dictates the central slope of the compliance sigmoidal curve, and C_0 is the baseline vessel compliance, which is obtained from the independent ring model[169],[177] for linear elastic and

incompressible wall material behaviour in Equation (3.7).

Changes in muscle tone thereby alter the pressure-radius relationship of the vessel,[2],[82] as required to elicit the appropriate changes in cerebrovascular resistance to maintain CBF, according to the tube law[62],[108],[123],[145],[147],[148],[169],[176] in Equation (3.9).

6.2.5 Conducted Vascular Response Model parameters

In our model, the CVR is assumed to be an intrinsic property of the arteriolar wall since it was shown to occur independently of any neural activity, intravascular pressure, and blood flow.[395] In contrast to applying the cable model to model electrical conduction in neuronal axons, the inner conductor in the CVR scenario is not the cytoplasm but rather the coupled endothelial-VSM syncytium. Hence, while the electrical properties of the inner conductor in the former case would depend on the vessel radius,[382] in the CVR case the conduction is more likely influenced by the vessel wall properties. Within the cerebral cortex, arteriole vessel walls generally share similar structural features across the generations, in which the vessels are encircled by a wall composed of circumferentially arranged VSMs forming a single VSM layer that is $5 - 8\mu m$ in thickness, and longitudinal ECs forming a single layer $3 - 5\mu m$ in thickness. Hence, we assume that the CVR parameters are uniform across the arteriolar vessels of the microvasculature network.

We use simple MC ABC schemes to obtain representative distributions of the CVR model parameters, one that is informed by the prior distribution, the model dynamics, and the available experimental data. In an experiment by Emerson and Segal,[345] a single hamster arteriole vessel was isolated, and ACh was administered to one end of the vessel (at $x = 0$), resulting in local hyperpolarization and vasodilatory responses at the stimulation site. The local simulation also resulted in electrical and vasomotor responses downstream, and the peak changes in membrane potential and diameter from their resting values were recorded at predefined distances ($x_i = 0, 500, 1000, 2000\,\mu m$) from the simulation site. These recorded measurements ($\Delta V_m^{meas}(x_i)$, $\Delta D^{meas}(x_i)$) constitute the observed data that are subsequently compared to the outputs of our dynamic model.

First, we construct an *in-silico* representation of the experimental setup described above. We

start with a single vessel of the same length $(4000\mu m)$, with the same initial conditions as those of the experiment, which are a resting diameter $(54-58\mu m)$ and resting membrane potential $(\approx -37mV)$, and assume an intravascular pressure of $P_I = 40mmHg$ that is typical in vivo for an arteriole of such diameter.[155] Then we numerically impose a local change in membrane potential at the location corresponding to the simulation site that is identical to the trace obtained under the experimental conditions.[345] Next, we employ the cable model in Equation (6.28) using different values of τ_M and λ sampled from a prior distribution, to obtain the peak changes in the membrane potential at the recording sites x_i. Resting values for the cable model parameters have been observed experimentally and have been reported to be in the range of $\approx 1-2.5$mm for λ,[348],[383],[396],[397] and $\approx 0.2-0.6$s for τ_M.[383] Accordingly, we start with a uniform prior distribution for each of the two parameters covering the ranges above. An MC realization is accepted if the membrane potential simulation output at all the recording sites $(\Delta V_m^{sim}(x_i))$ is within the recorded standard deviation range of $(\Delta V_m^{meas}(x_i))$.

The obtained posterior distribution for τ_M and λ are then used again as prior distributions for a second round of an MC ABC, this time integrating the vasomotor response and compliance feedback models in Equations (3.9),(6.40), and (6.42) into the dynamic simulations, and comparing the peak diameter outputs of the simulation to $\Delta D^{meas}(x_i)$ to obtain a representative distribution of the remaining parameters which characterise conveyance of the electrical signal into an appropriate vasodilatory response. In this case, an MC realization is accepted if both the membrane potential and diameter simulation outputs at all the recording sites ($\Delta V_m^{sim}(x_i)$ and $\Delta D^{sim}(x_i)$) are within the recorded standard deviation range of ($\Delta V_m^{meas}(x_i)$ and $\Delta D^{meas}(x_i)$).

Experimental data has shown that the vasodilatory response closely follows the hyperpolarization response with a time constant of $1334ms$;[342] hence the prior distribution for τ_{CVR} is chosen as $N(1334, 10)\, ms$. Since there is no prior information for the gain parameter S_{CVR}, we assume a normal prior distribution of $N(4, 2.5)$ with a truncation interval of $0-10$. Figure 6.4 shows how a realization from the posterior distribution parameter space compares with experimental data.

The distributions for the remaining parameters characterising the myogenic and endothelial responses, including the parameter G, are obtained from the results of Chapter 5. The final

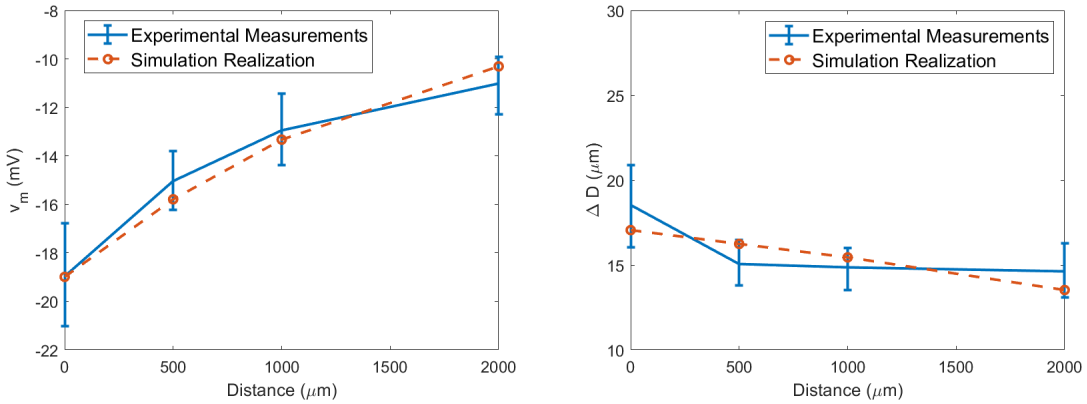

(a) (b)

Figure 6.4: The experimentally measured values for $\Delta V = V_m^{peak} - V_m^{\circ}$ (a) and $\Delta D = D^{peak} - D^0$ (b) along with their standard deviations recorded at $x = 0, 500, 1000$, and $2000\,\mu m$ from the site of Acetylcholine administration, are shown in blue. The outputs of one parameter space realization from the calculated posterior distribution of the CVR parameters are shown in orange.

distribution for the G parameter was then used as an initial distribution for the CVR model calibration process described above. The posterior distributions obtained for the model parameters are shown in Appendix C.2

6.3 Cerebrovascular Response Simulation Results

We examine the CBF response of the two networks to an increase in P_{a,CO_2} of the form:

$$P_{a,CO_2} = 40\left(1 + \left(0.0125\phi\left(1 + tanh\left(\frac{t}{2}\right)\right)\right)\right) \tag{6.43}$$

where ϕ corresponds to the amount of increase in P_{a,CO_2} (in $mmHg$) from the baseline conditions of $P^0_{a,CO_2} = 40mmHg$. Note that the function is selected purely to test the model and is not necessarily intended to simulate a real physiological stimulus; rather it provides a convenient method for examining the system response to a stimulus. We use the 0-D dynamic model developed in Chapter 3 to solve for dynamic flow and pressure profiles in the simple network[198] consisting of compliant vessels. The resulting change in C_{a,CO_2} in response to a $1mmHg$ increase in Pa, CO_2 (*i.e.* $\phi = 1$), as well as the ensuing changes in C_{t,CO_2} for the 13-generation network, are shown in Figure 6.5. The resulting changes in the CBF into the capillary vessels in response to a $1mmHg$ increase in P_{a,CO_2} are shown in Figure 6.6.

Next, we examine the dynamic CBF and vasomotor responses of the multiscale network to in-

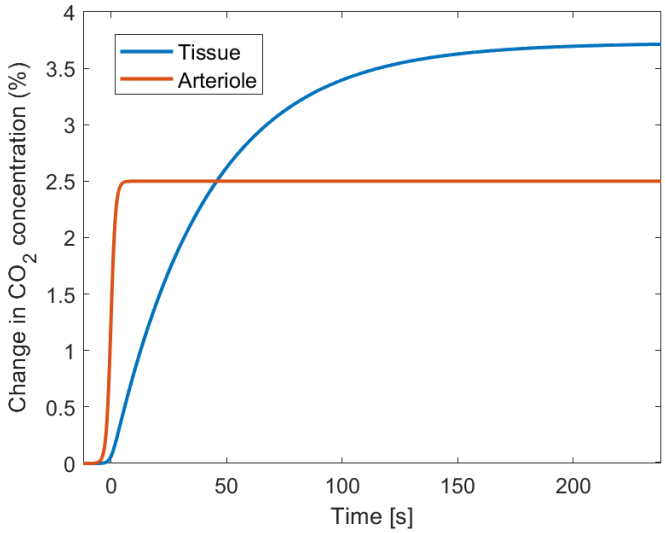

Figure 6.5: Percentage changes in the CO_2 concentrations in the arteriole vessels and the brain tissue for the 13-generation network, in response to a $1mmHg$ increase in P_{a,CO_2}. The following parameters are used for the CVR: $S_{ACh} = 0.75$, $\lambda = 2.5mm$, $\tau_M = 2.5s$, $\tau_{CVR} = 1.33s$.

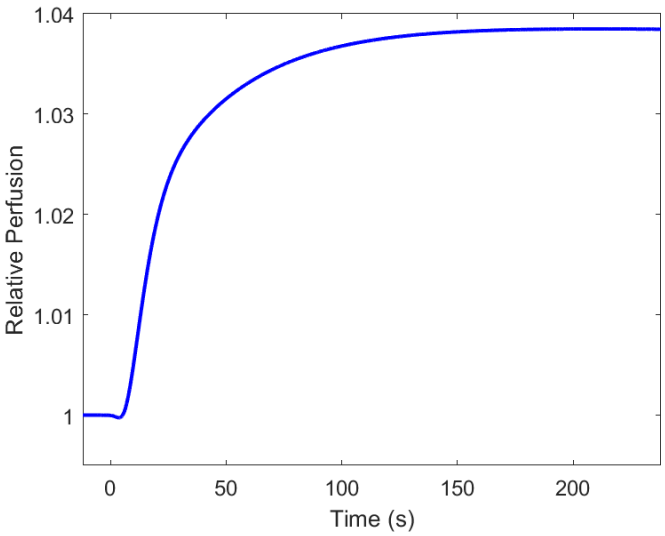

Figure 6.6: Changes in the capillary CBF (relative to baseline) in the 13-generation network in response to a $1mmHg$ increase in P_{a,CO_2} at $t = 0s$, using the following parameter values for the CVR: $S_{ACh} = 0.75$, $\lambda = 2.5mm$, $\tau_M = 2.5s$, $\tau_{CVR} = 1.33s$.

creases in P_{a,CO_2}, using the hybrid network model constructed in Chapter 4. The baseline values of CBF reported in experiments measuring the cerebrovascular reactivity response were in the range of $48-51mL/100g/min$.[286],[301],[302] In the multiscale model, calibration of the three parameters characterising the mesoscopic-scale properties of the homogenised capillary bed were done by ensuring that the steady-state flow and pressure profile throughout the network complies with physiologically reported values of CBF in the range of $45 - 65mL/100g/min$. Hence, for an appropriate comparison between the model and experimental data, a parameter space realization of the three parameters was chosen such that the steady-state CBF inside

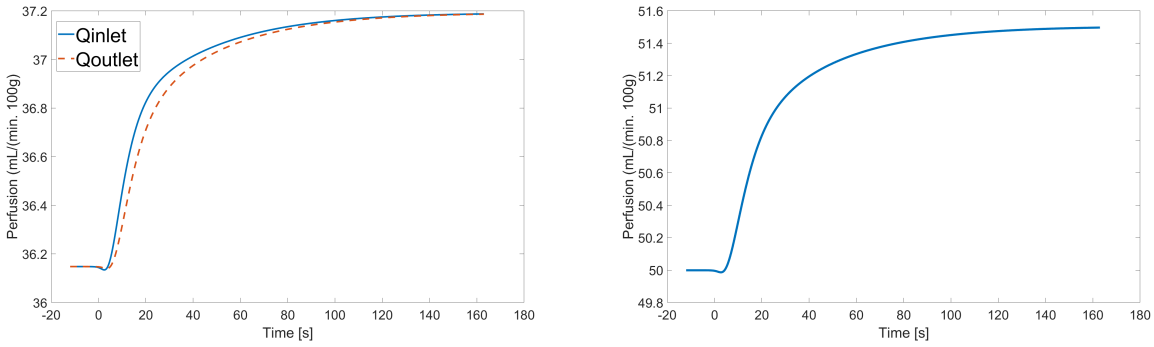

(a) (b)

Figure 6.7: Changes in the inlet and outlet perfusion for the whole network (a) and for the central ROI (b), in response to an increase in P_{a,CO_2} by $1mmHg$ at $t = 0$. The following parameters are used for the CVR: $S_{ACh} = 2.5$, $\lambda = 2.5mm$, $\tau_M = 2.5s$, $\tau_{CVR} = 1.33s$.

the ROI that is sufficiently distant from the network boundaries is $50ml100g/min$. In response to a $1mmHg$ increase in P_{a,CO_2}, the CBF response for both the whole network and the central ROI, are calculated and are shown in Figure 6.7(a) and 6.7(b), respectively. The response dynamics for the change in the vessel calibre are shown in Figure 6.8 for both a downstream and an upstream arteriolar vessel, corresponding to short and long distances of the CVR electrical signal propagation, respectively. The change in ACh concentrations and the ensuing local changes in v_m at one of the terminal arterioles in shown in Figure 6.9.

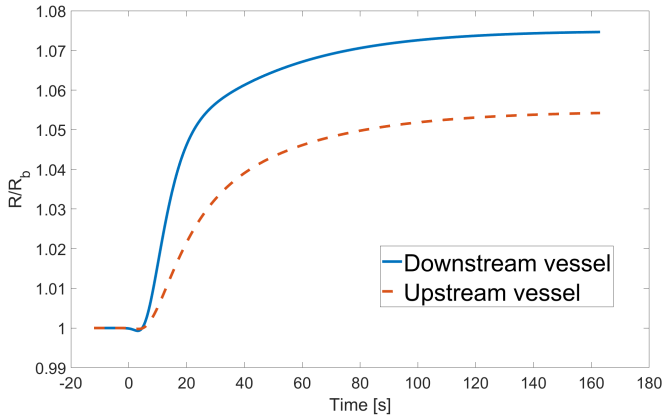

Figure 6.8: Changes in the vessel radius (relative to baseline) for an upstream and a downstream vessel in the multiscale network, representing a long and a short distance of electrical signal propagation, respectively, in response to a $1mmHg$ increase in P_{a,CO_2} at $t = 0s$. using the following parameter values for the CVR: $S_{ACh} = 2.5$, $\lambda = 2.5mm$, $\tau_M = 2.5s$, $\tau_{CVR} = 1.33s$.

Next, we examine the response of the multiscale network to different levels of P_{a,CO_2}. Figure 6.10(a) shows the final steady-state ROI perfusion for different values of P_{a,CO_2} in the range of $40 - 49mmHg$, while Figure 6.10(b) shows the same relationship but with the P_{a,CO_2} values restricted to a maximum of $44mmHg$, along with the linear best-fit line which indicates a cerebrovascular reactivity sensitivity of $2.3\%/mmHg$ for a value of $S_{ACh} = 2.5$. Figure 6.11(a)

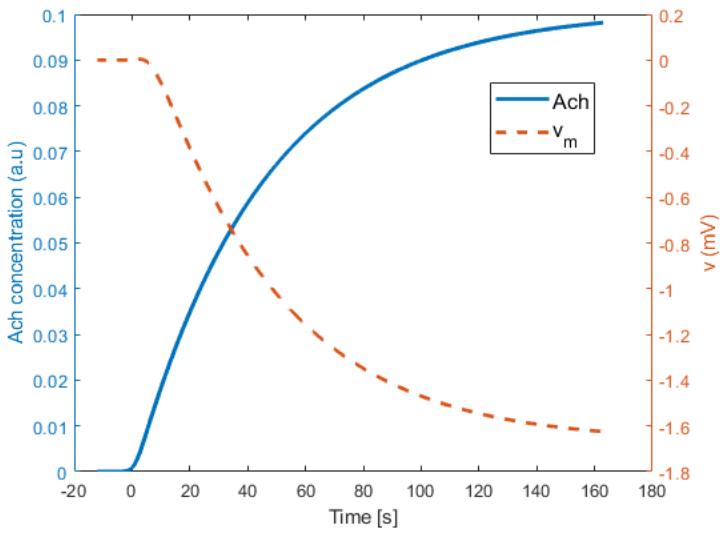

Figure 6.9: Changes in the ACh concentration and local membrane potential at a terminal arteriolar node in the multiscale network, in response to a $1mmHg$ increase in P_{a,CO_2} at $t = 0s$. using the following parameter values for the CVR: $S_{ACh} = 2.5$, $\lambda = 2.5mm$, $\tau_M = 2.5s$, $\tau_{CVR} = 1.33s$.

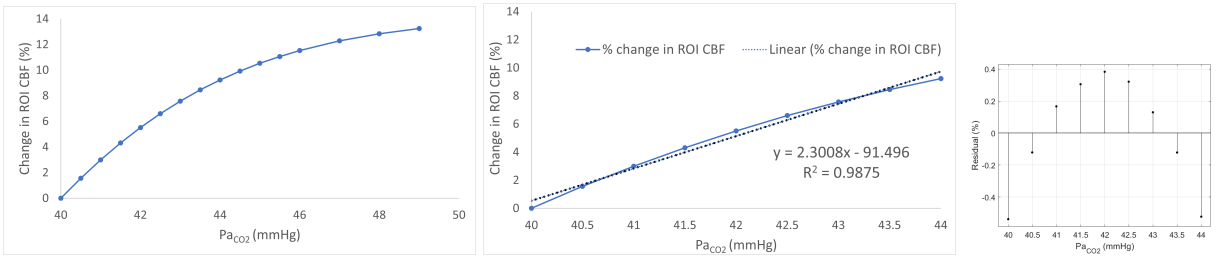

(a) (b) (c)

Figure 6.10: Relative changes in CBF in the multiscale network ROI from its baseline value for different values of P_{a,CO_2} (a), and the linear best fit ($R^2 = 0.9875$) (b), along with the residual plot (c) for P_{a,CO_2} up to $44mmHg$, above which increases in the inlet blood pressure might occur.

compares the time dynamics of the CBF response of the whole network when P_{a,CO_2} is raised by $5mmHg$ to when it is raised by $1mmHg$. If we were to define the net time constant as the time it takes from the hypercapnic stimulus initiation for the change in CBF to reach $1-1/e$ of its final value, then we can calculate the net time constants for different values of P_{a,CO_2}, which are plotted in Figure 6.11(b). Finally, to assess the impact of the myogenic and endothelial mechanisms on CBF under the hypercapnic response, Figure 6.12 compares the dynamic CBF profile in response to an increase of P_{a,CO_2} to $43mmHg$ when the myogenic and endothelial mechanisms are impaired, to when all three mechanisms are intact.

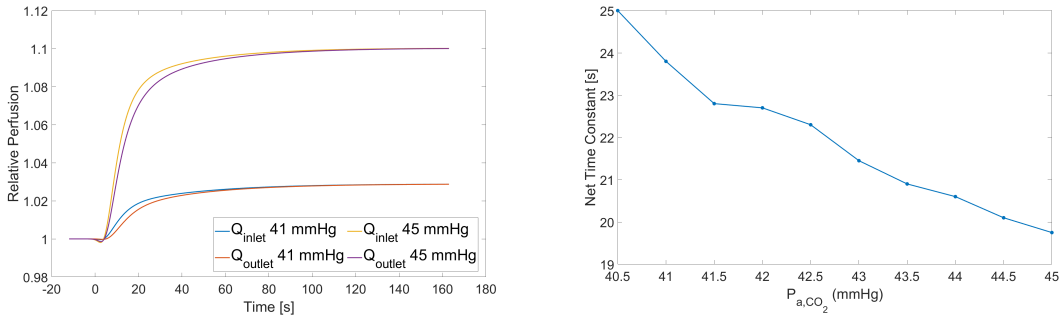

(a) (b)

Figure 6.11: Comparison between the response dynamics of the multiscale network CBF within the central ROI in response to increases in P_a, CO_2 at $t = 0$ by $1mmHg$ and by $5mmHg$ (a). The net time constants, defined as the time it takes from the hypercapnic stimulus initiation for the change in CBF to reach $1 - 1/e$ of its final value, for different values of P_{a,CO_2} (b).

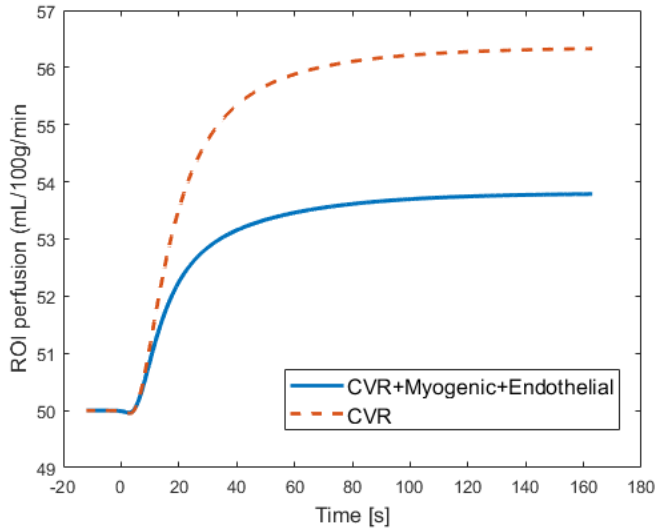

Figure 6.12: The CBF response to a $3mmHg$ increase in P_{a,CO_2} at $t = 0$ in the central ROI region of the multiscale network when all three myogenic, endothelial and CVR mechanisms are intact, and when only the CVR response is present. The following parameter values were used for the CVR: $S_{ACh} = 2.5$, $\lambda = 2.5mm$, $\tau_M = 2.5s$, $\tau_{CVR} = 1.33s$.

6.4 Discussion

It is well known that manipulation of $P_{a.CO_2}$ is routinely used both as a prognostic index to assess cerebrovascular vasomotor capacity,[398],[399] as well as a means of controlling ICP and adjusting CBF to metabolic requirement.[400],[401] Uncontrolled alterations in P_{a,CO_2} and ABP, however, can have a dramatic impact on CBF and ICP, leading to intracranial hypertension and cerebral ischaemia.[399] This study attempts to assemble a mathematical framework from constituent sub-models that is then used to explore the biophysical foundations and dynamics of the hypercapnic cerebrovascular reactivity response. The response is assumed to occur as a result of sequential signalling pathways, each of which is modelled based on experimental

data and knowledge of the chemical, structural, and electrical properties of the microvasculature. We obtain the model parameter space for each constituent signalling pathway, except for S_{ACh} and τ_{ACh} in Equation (6.6), by using the available experimental data to independently calibrate the parameter values for each of the constituent sub-models. We obtained the range of values for the S_{ACh} parameter in the simple bifurcating and the hybrid multiscale networks by ensuring that the percentage CBF increase in response to a $1mmHg$ increase in P_{a,CO_2} from baseline was within the experimentally measured range of $2-4\%$. We then assessed the overall response of the integrated model in the multiscale network by comparing the percentage CBF increase vs P_{a,CO_2} relationship obtained from the *in-silico* model to the experimentally observed trends in human subjects.

As shown in Figure 6.10(b) the CBF increase inside the central ROI of the multiscale network varies linearly ($R^2 = 0.9875$) with the P_{a,CO_2} in the range of $40 - 44$ mmHg, with a line of best-fit slope of $2.3\%/mmHg$ which very favourably compares with the linear trend with a sensitivity of $2-4\%$ observed experimentally.[286],[301],[302] It should be noted that normally there is a marked inhomogeneity in the cerebrovascular reactivity within the cerebral vasculature,[402],[403] as evident by the higher reactivity in grey matter vs white manner detected using arterial spin labelling,[7] and BOLD MRI maps.[92] The $2-4\%/mmHg$ sensitivity that is conventionally reported in the literature, which has been obtained from transcranial Doppler ultrasound measurements, can thus be understood as more of an average indicator of the CBF response over larger brain volumes.[92] Nonetheless, with no reported values for the cerebrovascular reactivity specifically within the cortical grey matter, we use the aforementioned sensitivity range to calibrate S_{Ach}, noting that higher values of S_{Ach} can be used in the dynamic simulations to achieve higher reactivities.

Above a value of $P_{a,CO_2} = 44.5mmHg$, cerebrovascular reactivity starts decreasing, as evident by the diminishing gradient of the CBF increase vs P_{a,CO_2} curve in Figure 6.10(a). This is in contrast to the linear trend reported in the experimental data. It is known that above a threshold value for P_{a,CO_2} in the range of $44-47mmHg$, blood pressure also starts increasing,[92],[286] which would also contribute to the increase in blood flow independently of the changes in cerebrovascular resistance. The reported cerebrovascular reactivity values for P_{a,CO_2} values above $44mmHg$ are thus likely to reflect the combined effects of reduced cerebrovascular resistance and increased blood pressure. The likely reason for the traditional lumping of both

effects into a single index is that complex modelling methods and well-controlled experiments may not be practical for clinical use.[404] Thus, if the cerebrovascular reactivity index was based purely on changes in the resistance, then the relationship between P_{a,CO_2} and the CBF increase would likely exhibit the trend shown in Figure 6.10(a).

Regarding the time dynamics, the CBF response to a hypercapnic step protocol has been previously reported to reach its peak value within 2 minutes of the start of the response,[287],[316] while Kontos et al.[299] and Shapiro et al.[309] reported that 4 and 5 minutes were adequate to achieve steady-state, respectively, the latter from the beginning of CO_2 inhalation. These time scales are generally in agreement with our simulation results (Figures 6.6, 6.7, and 6.11(a)). Note that the overall speed of the hypercapnic response in our simulations depends on the degree of P_{a,CO_2} increase, with an equivalent time constant in the range of $20 - 25s$ that decreases with P_{a,CO_2}, as demonstrated in Figure 6.11(b). This observed variability is in line with the earlier conclusions of authors who reported marked intra-subject variability in the response,[92] as well as the inability to fully and accurately characterise the response using a first-order model.[287] Note that the range obtained from the dynamic simulations for the hypercapnic response net time constant is lower than the experimentally reported value of 45s.[287] This could be due to the assumption of a fast ACh release ($\tau_{ACh} = 1$) used in this model in response to perturbations in tissue CO_2 concentrations. Given the lack of experimental data on the dynamics of ACh release in response to changes in tissue CO_2 concentration, we opted not to make any prior unwarranted assumptions about the speed of the response, and simply use a value of $\tau_{ACh} = 1s$ corresponding to an almost concomitant release. Accordingly, if the hypercapnic response were to be indeed mediated by local ACh release and the CVR, we speculate that the release of ACh would occur on a slightly slower timescale. As expected, a response dynamic with an equivalent time constant of 44s, as shown in Figure C2, that better matches the experimentally reported time constant, can be achieved by increasing the value of τ_{ACh}, for example, from 1s to 20s. This form of *in-silico* modelling can also help interpret the experimental data regarding the hypercapnic response, which, as discussed in Section 6.1.1, can at times appear contradictory, and can help explain the discrepancies between the reported values for the time constants, for instance, through *in-silico* replications of the experimental conditions by which blood CO_2 levels are increased.

Given that the time constants for the constituent signalling pathways all have relatively low

values ($\leq 2.5s$), it is worth investigating which of the signalling pathways dictates the timescale of the hypercapnic response with a net time constant $\approx 20-25s$. Firstly, we derive an expression for the time constant characterising the change in the tissue CO_2 concentrations from the first order-ODE in Equation (6.1): $\tau_{CO_2} = V_t/(\alpha Q_c)$. The resulting value for τ_{CO_2} in both the simple and multiscale networks under baseline flow conditions is $\approx 44.5s$, decreasing with increasing CBF, which matches the calculated time constant of $\approx 41.7s$ from Figure 6.5, even though the arteriolar CO_2 concentration increases via a rapid step response. This highlights the importance of accounting for the different response dynamics for the changes in CO_2 concentrations across the arteriolar and tissue microvascular components, rather than simply assuming steady-state equilibration of blood gas levels, and thus of choosing the appropriate breathing stimulus that matches the aims of the conducted experiments.[92],[312],[313]

Furthermore, as demonstrated in Figure 6.8, the upstream arteriolar vessels respond with much slower time dynamics compared to the downstream arteriolar vessels. Hence, even though the time constant used for the hyperpolarization signal propagation is only $\tau_m = 2.5s$, it takes time for the signal to travel upstream and it gets attenuated as it reaches the upstream arteriolar vessels. This could also explain why, in contrast to the generally non-discriminatory nature of hypocapnia-induced constriction, the smallest blood vessels are the ones that primarily dilate in response to elevations in CO_2 levels,[310] since the electrical signal gets progressively attenuated as it travels upstream. Hence, even though we have used the same parameter values, and thus assumed identical response dynamics, across the arteriolar vessel generations, we show that the segmental heterogeneity in the vascular response[122] could, in part, be a consequence of the attenuation and the time required for the signal to travel to the vessels upstream. This would also mean that the microvasculature network architecture and properties, such as vessel lengths, connectivity, and number of generations, can have a profound effect on the hypercapnic response and thus need to be accounted for in modelling studies. This complex relationship between the vessel location and ensuing diameter changes could also partially explain why no stable relation was observable between vessel diameter and P_{a,CO_2}.[307] In general, it seems that the overall speed of the response is primarily dictated by the rate of change of tissue CO_2 concentrations, the time required for the hyperpolarization signal to travel upstream, and the time dynamics of ACh release.

The local v_m response to a step increase in ACh concentration was obtained from the coupled

endothelial-VSM cellular model,[376],[377] and was then fit to a second-order exponential equation to obtain the values for the parameters in Table 6. The least absolute residuals method was used to fit the data points, coupled with the Levenberg-Marquardt algorithm in the Curve Fitter toolbox on MATLAB. This resulted in a very good fit for the data points for $t >= 2s$ from the time of the simulation (after accounting for the delay) but also resulted in the fitted curve not matching the first few data points for $t < 2s$ in Figure 6.2(a), as indicated by the high residual between the first three extracted simulation data points and the corresponding second-order exponential fit in Figure 6.2(b). Other combinations of non-linear least square methods and algorithms provided a better fit for the initial data points at the expense of a less matching fit for later data points. Ultimately, however, all non-linear least square optimizing schemes examined generally achieved a very good agreement ($R^2 = 0.99078$ for the current fit in Figure 6.2(a)), and provided a very similar range of values for the parameters shown in Table 6. Figure 6.9 shows the local v_m response at one of the terminal arterioles of the multiscale network to a $1mmHg$ increase in P_{a,CO_2}. In this case, v_m changed by 1.6mV, or 4.3% of the endothelial resting membrane potential of $V_m^\circ \approx -37mV$. The local V_m response at the terminal arterioles to the other P_{a,CO_2} input stimuli (in the range of $41 - 49mmHg$) was also within the experimentally reported physiological range of -35 to -55 mV.[386],[387]

It is important to note that cerebrovascular reactivity does not occur in isolation but rather occurs concomitantly with other dCA mechanisms.[405] The signalling pathways for the various control mechanisms generally converge towards the same end response; *i.e.* altering the intracellular Ca^{2+} concentration in VSM cells, which in turn affects the actin-myosin cross-bridge cycling and contraction.[2],[349]–[351],[394] Perhaps the most obvious demonstrations of this superposition effect are the use of the cerebrovascular reactivity response to assess the VSM overall dynamics and functionality, as well as the use of hypercapnia as a surrogate of impaired dCA, since it tends to saturate the vasodilatory capacity of the arteriole vessels, which, according to Equation (6.42) have a maximal change in compliance. This likely means that the cerebrovascular reactivity values reported in experiments, which are ostensibly attributed to changes in P_{a,CO_2}, are influenced by the myogenic tone and the other dCA mechanisms which are activated as a result of changes in vessel radius and downstream transmission of intravascular pressure. One benefit of *in-silico* experiments is that we can isolate the individual effects of the different control mechanisms (e.g. by setting the gain factor equal to 0) to better capture

the individual contributions to the total CBF response, as well as to investigate the dynamic interplay between the different mechanisms. Indeed, the discrepancy between the two CBF responses in Figure 6.12 highlights the significance of the other dCA control mechanisms, and indicates that such mechanisms must be borne in mind when assessing cerebrovascular reactivity in experimental and clinical settings.

This non-linear interaction between CO_2 reactivity and CA is documented in both experimental[310] and clinical[399] studies, giving rise to what is referred to as the 'inhibitory-facilitatory summation' effect.[122] Basically, as ABP decreases from its basal levels, vasoreactivity to CO_2 levels increases, indicating a 'facilitatory' overlapping of the two mechanisms. As ABP approaches the lower limit of dCA, however, the responsiveness to CO_2 diminishes, suggesting an 'inhibitory' overlapping between the hypercapnic response and the dCA mechanisms.[122] Both of these effects arising from the combined stimuli can be explained by the proposed model in this study. The non-linear interaction is accounted for in this model by mapping the summation of the activation factors into the static sigmoidal compliance relationship in Figure 3.1, which accounts for the natural bounds in VSM tension[122] regardless the stimuli, thereby echoing the general notion all feedback/control mechanisms share a common denominator; that is, regulating the levels of VSM intracellular calcium required for contraction.

When ABP decreases, so does the capillary blood flow, which leads to the accumulation of CO_2 in the tissue according to Equation (6.1); when coupled to the independently raised P_{a,CO_2} from the introduced hypercapnic stimulus, this augments the vasoreactivity response. Conversely, as ABP reaches the lower limit of dCA, capillary flow significantly decreases, which potentially leads to diminished ACh release and CVR-induced vasodilation as the levels of the ACh synthesis precursors become deficient, explaining the saturation of the hypercapnic response during the inhibitory phase. It would be interesting to use our model and attempt to replicate such interactive effects in the future. Nonetheless, in essence, both our model and the clinical results highlight the important point that, even though cerebrovascular reactivity serves as an important prognostic tool that is significantly correlated with clinical outcome, this analysis of this index in isolation can be misleading if not integrated with information on cerebral autoregulation status, ABP and CBF.[122] For example, hyperventilation as a manoeuvre is routinely and effectively used to control ICP in neurological patients; its effectiveness, however, depends on the CA and ABP status,[399] an important consideration

that should be borne in mind when clinicians are planning for surgical treatments.[122]

Next, we discuss some potential limitations of using the cable theory in Equation (6.24) to model the conducted vascular response. First of all, we note that the cable model homogenises the electrical and structural properties of the endothelial and VSM layers. This continuum approach thus neglects the effects of the orientation and morphology of the vascular wall cells, as well as that of vessel branching, which have been shown in *in-silico* simulations to distinctly shape the electrical conduction.[351],[406] Furthermore, the cable model assumes an ohmic behaviour for the gap and membrane junction electrical properties, as implied by the use of the space and time constants in Equation (6.28) that are derived from constant values for r_i and g_m in Equations (6.26) and (6.27). In reality, however, ion channels have time and voltage-dependent activation and inactivation properties.[377],[381] Nonetheless, the currents through the gap junctions of the membranes have been shown to exhibit a near-linear dependence on the membrane potential for small changes in the membrane potential from its resting value,[353],[382],[383] corresponding to $\pm 20mV$,[389],[407] which roughly conform to the changes in v_m encountered under normal physiological conditions.[386],[387] In addition, the junctions where the vessels meet are likely to constitute a structural obstacle from an electrical perspective due to the increased mass of cells at the branching points, resulting in an electrical decay[389] that is not accounted for in our model, where the terminal gridpoints of the vessels meeting at the junction are assumed to be equipotential.

The membrane proteins that form the homocellular and endothelial gap junctions are also subject to modulations and regulations from mechanical, electrical and endocrine signals, such as post-translational modifications[294],[406] which are not accounted for in our model. *In-silico* simulations using a two-layer model of the VSM and ECs[406] have demonstrated how alterations in gap channel conductance and ion channel properties can evoke distinct changes to the longitudinal and radial spread of charge, leading the authors to consider the CVR as 'pliant' to the current regulatory state and electrical environment. Finally, one of the major assumptions when applying the cable theory to model the CVR is that the endothelial and VSM layers can be regarded as a single isopotential syncytium. Some computational studies have demonstrated that the VSM and endothelial layers have distinct voltage profiles and thus cannot be treated as a single continuum.[351],[381] On the other hand an overwhelming number of both experimental and computational studies, which were examined in Section 6.2.3, have

shown that within the physiological membrane potential range, endothelial-initiated agonists elicit quasi-parallel electrical responses in endothelial and VSM layers, thereby supporting the notion that the two layers can be regarded as a single continuum. Such divergent views on the applicability of the syncytium approach may arise in part due to variability in the experimental conditions (ex different agonists, hyperpolarization vs depolarization) used to investigate the CVR.

Definite evidence of conduction deficit has been shown to be present in the pathological cases of sepsis, hypertension, and ageing (see[294] for an in-depth review). In all three pathological conditions, the limited blood flow delivery, especially during periods of enhanced metabolic demand, has been shown to occur for the most part as a result of diminished endothelial-endothelial conductance, which attenuates the conduction of the hyperpolarization signal. The cause of the increased resistance, however, is different for each case. There has been recent interest in how pharmacology could restore biological function; for instance, bolus injections of antioxidants do restore the conduction required for functional hyperemia in sepsis animals,[408],[409] in which the overproduction of reactive oxygen species is the underlying cause for the conduction deficit by impairing gap junction activity. These approaches, however, remain restricted and speculative,[294] and do not offer any viable predictions on how such interventions can potentially disrupt other aspects of the system dynamics. For instance, in the two-layer *in-silico* model by Hald and Welsh,[406] increased endothelial resistance impaired longitudinal but enhanced radial current spread to the VSM, thereby augmenting the local hyperpolarization and vasomotor responses. Given the potential interaction between impairments in the CVR during NVC and conditions under which brain ischaemia might occur,[319], and with the impact of disease on the CVR and cerebrovascular reactivity just starting to emerge, *in-silico* models like the one developed in this study can offer a fast and safe exploratory option for providing a preliminary assessment of the impact of different treatment options. By providing insight into the mechanisms underpinning the hypercapnic response, the *in-silico* model can also help identify druggable targets that could be used in future therapies for disorders implicated in an impaired hypercapnic response.

6.5 Conclusion

The current study was conducted to test whether the CVR plays a central role in mediating the cerebrovasculature's response to hypercapnia, using an *in-silico* experimental representation of the microvasculature, one that is physiologically grounded with *in-vivo* experimental data and knowledge. The results of the candidate model are consistent with the vascular manifestations of the hypercapnic response and suggest that the main signal initiating the hypercapnic response in the cerebral microvasculature is the increase in tissue CO_2 concentrations and that the local ACh release, the conduction of the hyperpolarization current upstream, and the corresponding vasomotor changes are all integral to the hypercapnic cerebrovascular reactivity response. The results do offer compelling evidence to support the hypothesis and provide a strong motivation to further examine the validity of the *in-silico* experimental results through *in-vivo* experiments, which are facilitated by the advancement of sophisticated imaging techniques like multiphoton microscopy that allow researchers to record responses deep within brain tissues, as well as those which allow for a spatially specific focal simulation of the brain arterioles, such as localized uncaging of Ca^{2+} or IP3 in a single or few cells.[319]

In that sense, the cerebrovascular sensitivity to tissue CO_2 concentrations would constitute an important component of the metabolic response, since it would allow the vasculature to respond to the accumulation of the local tissue metabolites, for instance, due to a discrepancy between the supply and demand of glucose and oxygen. Thus, this study offers an important addition to our understanding of the metabolic response. The CO_2 response would likely act in concert with other signalling pathways to ensure a robust metabolic response that is less susceptible to malfunctions or impairments in any single pathway. For example, some studies have shown that the cerebral vasculature is sensitive to hypoxia independently of an increase in blood CO_2 levels.[287],[410] Thus, in the future, other components of the metabolic response can be added into the present mathematical framework; for instance, through incorporating multiscale models of oxygen transport and diffusion.

Chapter 7

Conclusions and Future Work

7.1 Summary of the Models Developed

The primary aim of this thesis is to construct a multiscale model of CBF and control in the cortical microvasculature. This model could then be utilised as an *in-silico* platform for performing experiments and testing hypotheses that would be inaccessible in a conventional experimental context (such as exploring the mechanisms behind the hypercapnic response in Chapter 6) as well as for investigating the interplay between the CBF control mechanisms. The models developed in this thesis build upon one another: the dynamic network model developed in Chapter 3 is embedded into the dynamic multiscale model used in Chapter 4. The compliance feedback model used in these two chapters is then validated and its parameter space is calibrated in Chapter 5. The calibrated network and multiscale models are finally used in a case study in Chapter 6 where we demonstrate one of the potential uses of these models by numerically testing and providing insight into a plausible mechanistic pathway behind the hypercapnic cerebrovascular response.

In Chapter 3, we combine the three equations governing haemodynamic flow in a compliant autoregulatory microvessel, which are mass conservation, momentum conservation, and a tube law that accounts for the dCA mechanisms via a dynamically changing compliance, and then utilise perturbation techniques to derive an approximate analytical solution which characterises the flow in and out of the vessel in terms of the pressure profile at the vessel ends, as well as the vessel and blood properties. We incorporate the effects of the endothelial and myogenic mechanisms on the vessel stiffness via a first-order equation emulating low-pass filter dynamics, after which we non-linearly map the stiffness into the compliance through an asymmetrical sigmoidal function. Changes in the vessel compliance would then alter the pressure-radius relationship of the vessel. We link the vessels of the network together by assuming conditions of mass conservation and static pressure continuity at the nodes where vessels meet, giving rise to a first-order ODE system that characterises the pressure throughout the internal nodes of the microvasculature network.

Next, we apply the model to examine the response of the 13-generation network to a reduction in the ABP and find that the model captures the biphasic response that is characteristic of dCA. We also find that the model captures important flow dynamic features arising from the interaction of blood with the compliant vessel walls and thus the non-zero transit time distributions, which give rise to the transient discrepancies between the network inlet and outlet flows; these could have important implications, for instance when incorporating models of the contrast agent and tracer kinetics into the models of CBF, as discussed in Sections 3.5 and 7.2.2. We also benchmark-validate The derived model by comparing the results of the model with those obtained from a 1-D model of CBF in a network of compliant vessels and find that our model achieves very favourable agreement with a significantly lower computational cost compared to the 1-D model.

We also show how the model can be used to investigate the complex interplay of the dCA mechanisms across the different microvasculature generations. Finally, a variance-based, global parameter sensitivity analysis is conducted to assess the relative importance of the compliance feedback parameters. Even though the parameters have not been calibrated at this stage, the sensitivity analysis provides useful insights, such as the likely dominance of the myogenic response, and the weak impact of the parameters characterising the maximal and minimal changes in fractional compliance, which were in turn factor fixed in the calibration scheme in Chapter 5 to decrease the number of parameters that need calibration and thus improve the calibration process.

If the output of the microvasculature models were to be validated against macroscale clinical measurements, such as those of CBF, then the network structure needs to be upscaled (at least) to the size of an MRI voxel-sized network. Hence, in Chapter 4, we develop a multiscale model of CBF and control in the cortical microvasculature. A representative network the size of an MRI voxel is generated by embedding the statistically generated penetrating arteriole and venule penetrating trees into the homogenised capillary bed continuum. A hybrid CFD model is utilised, in which blood flow and control in the penetrating vessels is modelled based on the work in Chapter 3, while the capillary bed is treated as a porous medium and blood flow is modelled via the volume-averaged Darcy's law, and solved for using the FV method. This distinction and separation of scales was important since we lack both the anatomical data as well as the computational power to model the dense, complex web of capillary vessels, yet

we also need to preserve the hierarchical, fractal-like topology of the penetrating vessels. We assumed a distributed source flow formulation, in which the flow between the terminal penetrating vessels and the capillary bed FVs is restricted to a particular radius around the terminal nodes, in order to ensure a proper, numerically scale-invariant, and physically sound flow transition between the two media. We discretise the capillary domain using a non-uniform grid of cubes that ensures tighter meshing at the transition interface between terminal penetrating vessels and the capillary bed to ensure the numerical accuracy as well as the feasibility of the solver.

An implement an MCF scheme to efficiently derive the physiological range of values for the three parameters characterising flow at the mesoscopic scale, which are γ_a, γ_v, and K, from which useful insights, such as the weak impact of γ_a on the model output, as well as the reciprocal relationship between the permissible values of γ_v and K, were obtained. We also demonstrated the scale-invariance of our modelling formulation by showing how the voxel perfusion becomes independent of the FV size below a particular threshold. We constructed a statistically accurate multiscale network of the size of an MRI voxel, and examined the network's response to a drop in ABP, resulting in similar conclusions to those in Chapter 3. Given the higher computational costs of running simulations on the larger multiscale network compared to the simple small network in Chapter 3, we use the EE method to screen for the effects of the compliance feedback parameters. The sensitivity analysis results indicate myogenic dominance and the weak impact on the model outputs of the parameters characterising the maximal and minimal changes in fractional compliance, as before, but also highlight the non-linear effects arising from the interactions of the compliance feedback mechanisms.

In Chapter 5, we calibrate the model parameters of the myogenic and endothelial compliance feedback mechanisms based on experimental data that measure the diameter changes of individual isolated arteriole vessels to changes in the intraluminal pressure and the pressure gradient, in order to ensure that our model is both law (physics) and data-driven. At this stage, and in line with the experimental data, we first distinguish between the myogenic and endothelial time constants by modelling each activation factor separately in a first-order ODE emulating low-pass filter dynamics, before the two activation factors are summated and are non-linearly mapped into the vessel compliance. The myogenic response is also assumed to be elicited as a result of changes in wall tension rather than in intraluminal pressure since it

is the changes in the vessel wall tension that trigger the mechanistic pathway responsible for VSM relaxation or constriction. We also add a delay for the endothelial constriction based on our observation of the experimental data. We use an SMC ABC scheme for obtaining the parameter distributions. In an SMC scheme, a prior distribution of the parameters (as well as the initial conditions) is introduced and is used to create MC realizations, which are then used in the dynamic simulations to obtain the *in-silico* diameter traces. These traces are then compared to the original measurements carried under the same experimental conditions to calculate the error norms, which dictate whether a particular realization output is accepted or not. The accepted output realizations are mapped back into the input parameters to create a posterior distribution of the parameter space. The posterior distributions become the prior distributions for the next calibration iteration, and the error tolerances that control whether or not an MC realization is accepted are gradually reduced, thus achieving convergence towards the optimal parameter distributions.

The parameters are first calibrated for each experiment which measures the response of the individual vessels separately, before using the obtained parameter distributions to collectively calibrate all the experiments to obtain unified parameter distributions representative of all the data. Upon calibration, we obtain very good overall agreement between the simulation output and the diameter measurements for all experiments except one, for which the sources of discrepancies are very likely to be due to experimental artefacts and measurement errors, as explained in Section 5.8. The compliance tube law and feedback models are very computationally feasible, such that a simulation that traces the response of a microvessel over hundreds of seconds takes less than 5 seconds of computation time on a Desktop computer. Thus, the compliance model for characterising the response of the microvascular walls achieves a very good balance between accuracy, computational feasibility, and physiological informedness. The calibration scheme also reveals important mechanistic features of the autoregulatory response, such as the difference in timescales between the myogenic-induced dilation and constriction, which have been normally assumed to operate under the same time constant.

Finally, in Chapter 6 we put all the pieces together, and use the calibrated dynamic network and multiscale models in a case study that examines the biophysical origins of the hypercapnic cerebrovascular response. Drawing from information from various experimental data and observations, we propose a model in which the hypercapnic response is elicited by changes

in the local tissue CO_2 concentrations; these in turn, trigger the local release of the ACh neurotransmitter, which acts as an endothelial agonist that induces the local hyperpolarization of the ECs of the microvessels that are in close proximity to the affected tissue. The hyperpolarizing current gets conducted upstream of the network through the endothelial layers and is relayed from the ECs to the VSM cells via the myoendothelial gap junctions, resulting in VSM cell relaxation and hence vascular dilation. ACh is released in response to an increase in the local tissue CO_2 concentration above its baseline level. We derived a transfer function in the Laplace domain that relates the levels of local ACh release to the local changes in the membrane potential and calibrated it by examining the output of a coupled EC-VSM cell model that accounts for the constituent signalling pathways and traces the movement of the individual ions. We then transform the membrane potential output back into the time domain to obtain the analytical approximation of the membrane potential response to any ACh concentration.

We model the upstream conduction of the hyperpolarizing current using the cable model, and the resulting second-order parabolic PDE is spatiotemporal discretised using a hybrid CN-implicit scheme. We model the effects of the local decreases in the membrane potential on the VSM tone via an activation factor, along with the myogenic and endothelial responses, in line with the approach in Chapter 5. We non-linearly map the summation of the activation factors into the vessel compliance. We calibrate the parameters of the CVR model using a simple MC ABC scheme, in which experimental membrane potential and diameter measurements along the length of an arteriole vessel in response to the local administration of ACh are compared to the outputs of an *in-silico* representation of the experimental set-up. We first test the proposed model on the 13-generation network model in response to an increase in P_{a,CO_2} to obtain an approximate range of the parameter values for the S_{ACh} parameter characterising the amount of ACh released in response to local perturbations in tissue CO_2, before applying the electrophysiological model to the multiscale network, where the percentage increase in the CBF as a function of P_{a,CO_2} was found to be in very good agreement with the experimentally recorded trends.

Other important aspects that are featured in the model output include the attenuation and delay in the diameter changes as the CVR signal travels upstream, which could explain why the CVR response has been primarily identified in the downstream microvasculature vessels,

as well as the dependence of the cumulative time constant characterising the hypercapnic response on the level of P_{a,CO_2} increase, which could explain the marked experimental intersubject and intrasubject variability, as well as the inability to fit the experimental data to a simple model emulating a first-order low-pass filter dynamics. Furthermore, we demonstrate how the dCA mechanisms (the myogenic and endothelial responses), which are otherwise neglected in experiments measuring cerebrovascular reactivity, play an important role in shaping the cerebrovascular response. Overall, in this chapter, we have used the *in-silico* modelling framework developed in this thesis to provide compelling evidence for the CVR response as a mediator of the hypercapnic cerebrovascular reactivity, thereby complementing the available macroscale experimental data and prompting further *in-vivo* investigations. A better understanding of the mechanisms underpinning the hypercapnic response could lead to the development and administration of better-targeted drugs and treatment plans for impaired cerebrovascular reactivity, and the model developed in this chapter has the potential to be utilised as a safe and low-cost platform for screening and examining the impact of any treatment approaches before any real-life interventions.

7.2 Future Work

I hope that the models developed in this thesis become part of the fascinating cumulative work of many researchers spanning decades, which has and will continue to further our understanding of the complex and crucial network that is the cerebral microvasculature. For example, the network model in Chapter 3 was built on the model by Payne and El-Bouri,[79] which used as its vascular testing bed the 13-generation network by Payne and Lucas,[198] which itself was constructed based on measurements by Zweifach and Lipowsky[250],[251] in the 1970s. Furthermore, in the multiscale model of the cortical microvasculature that was generated in Chapter 4, we have relied on the statistically generated arteriole and venule penetrating tree structures by El-Bouri and Payne,[39] which were constructed based on the morphometric data recorded by Cassot et al.[38]; these, in turn, have been obtained from the detailed images of the cortical microvasculature, provided by Duvernoy et al.[37] in the 1980s. Similarly, the case study in Chapter 6 relied on the network and multiscale models developed in Chapters 3 and 4, respectively, as well as on experimental data, both old and very recent. The research in this thesis is indeed a testament to the cumulative nature of scientific work;

to this end, I propose future work that could build upon what was presented here to advance our understanding of the role of the microvasculature and the CBF control mechanisms in health and disease.

7.2.1 Combining the Micorcirculation and the Macrocirculation Models

The model developed here has the potential to be used as part of multiscale dynamic simulations of CBF and regulation over the entire brain or large segments of it. This could be important for understanding the impact of diseases or interventions on the whole-brain scale, and also to help with model validation and integration into clinical practice, since the measurements of CBF routinely made in clinical settings, as well as those recorded in experimental settings, tend to be mostly for the larger vessels. The human macrovasculature with diameters $\gtrapprox 0.8mm$ can be detected via clinical imaging data, and CBF through these vessels can be modelled using 1-D models, one example of which was derived and thoroughly discussed in Section 3.3. The models developed in Chapters 3 and 4 can then be used for modelling CBF and regulation in the microvasculature, since they are suitable for vessels with diameter $\lessapprox 1mm$. Accurate representations of the microvasculature can be obtained using statistically generated microvasculature networks like the ones used in this thesis, which match the morphometric properties of the human microvasculature that are available for vessels with diameter ($\lessapprox 50\mu m$). It would also be straightforward to adapt the models in this thesis to networks generated via other means, such as via constrained constructive optimization[43] and tissue metabolism-driven arterial tree generation,[44] or from the reconstructed *in-vivo* imaging of animals, subject to the appropriate scaling laws.

The final gap to fill would be to reconstruct the 'intermediate' pial vessels connecting the microvasculature that is visible in clinical images, to the cortical microvasculature, the statistical properties for which have been thoroughly documented and parameterized. These vessels have diameters below 1mm (and are thus not detectable using conventional clinical imaging), and also, unlike the cortical penetrating vessels, their anatomical and connective properties have not been, as far as I know, documented and parameterised. Recently, there has been some interesting and remarkable work in clinical imaging that was able to detect the pial arteries at this mesoscopic scale down to an isotropic resolution of 140 μm.[411] With

higher resolution future data obtained from advanced imaging techniques, potentially supplemented with the application of scaling laws,[412] accurate reconstructions and representations of those 'intermediate' vessels can be obtained and used in the models, thereby enabling multiscale dynamic simulations of CBF and regulation over large sections of the brain.

Each modelling approach within the multiscale model can be fittingly matched to the scale and zone of the vasculature it is used for. For instance, while the microcirculation model in Chapter 3 cannot be used for modelling CBF in the larger vasculature due to the restrictions imposed in the derivation (see for example Equation (3.13)), the longer vessel lengths of the macrovasculature mean that we do not need to resort to very small timesteps to meet the CFL stability condition (see Section3.3.3), which was the main computational deterrent from using 1-D models in the microvasculature. In the pial and penetrating arteries which exhibit fractal-like branching patterns that need to be accounted for, the network model developed in Chapter 3 would be the most suitable. Meanwhile, in the capillary bed, due to the mesh-like, isotropic and locally periodic topology of this complex network of vessels, as well as the collapse of the assumption of Newtonian flow mechanics at this micron-scale, a porous representation would be more appropriate. The penetrating vessels and the capillary bed can then be appropriately coupled, for instance via the distributed source term formulation described in Section 4.2.4. The 1-D models of the microvasculature and the branching microvasculature would also need to be strongly coupled via a formulation that meets the conditions of pressure continuity as well as mass and momentum conservation, which we have developed but not presented in this thesis. Figure 7.1 illustrates how the different length scales of the brain could be modelled using different modelling approaches developed and used in this thesis, which can then be combined into a single multiscale model.

7.2.2 Coupling with Multiscale Models of Mass Transport

The dynamic multiscale framework developed in this thesis for modelling CBF and regulation in the microvasculature can be coupled with other multiscale models of mass transport, such as those of O_2 transport and tissue perfusion, drug delivery, and tracer mechanics, to help better understand the effects of CBF dynamics and dCA impairments on their transport. As mentioned in Section 2.1, O_2 transport can occur both within the capillary bed as

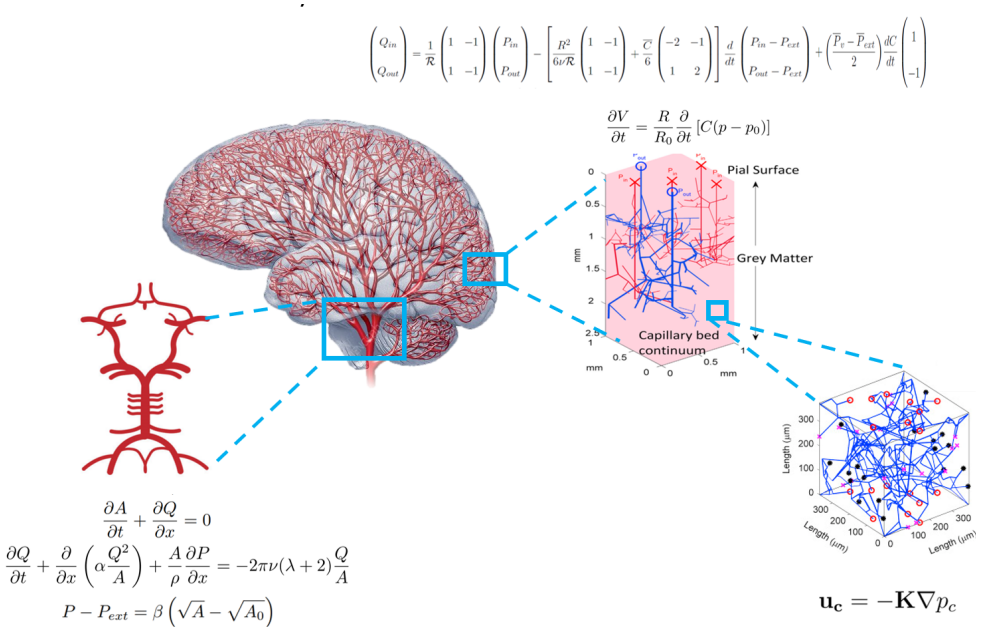

Figure 7.1: Multiscale modelling of CBF and regulation across the different length scales of the brain. The constituent images were reproduced from[41],[127] with permission.

well as through the walls of the penetrating arterioles,[65],[66] with different transport mechanisms (*ex.*, advection vs diffusion) dominating at the different length scales.[413] Models of oxygen transport across the different length scales have been constructed and coupled to simple haemodynamic models. These models have provided insights into the O_2 distribution in the microvasculature that are otherwise inaccessible in a conventional experimental context; for example, Hartung et al.[43] demonstrated how structural changes in the microvasculature induce hypoxic pockets in the aged brain, Sweeney et al.[320] showed how it is the vasoconstriction of smooth muscle actin-covered vessels, rather than pericyte-covered capillaries, that induces stable reductions in downstream intravascular capillary and tissue oxygenation, and Celaya-Alcala et al.[414] predicted the levels of reduction in perfusion or increase in oxygen demand that would result in tissue hypoxia.

So far, however, these studies have generally utilised simple, steady-state models of CBF that do not account for the flow dynamics or the dCA mechanisms. Combining the models of dynamic CBF control and regulation developed in this thesis with models of O_2 transport can provide valuable insights into how impairments in the autoregulatory mechanisms affect O_2 delivery, distribution and exchange across the different microvascular zones and regions; these, in turn, could enable a better understanding of the spatiotemporal patterns of ischaemic stroke, such as the ability to predict the location and volume of the infraction, and their inter-

play with the dCA mechanisms, which can ultimately lead to clinical breakthroughs.[133]

Similarly, the models here can be combined with models of drug transport to establish a better understanding of pharmaceutical interventions, especially under different disease conditions of the microvasculature architecture and dCA impairments, which would ultimately help achieve more targeted drug delivery. Another application of these models is to stimulate the movement of contrast agents and tracers used in clinical imaging, which are particularly sensitive to CBF dynamics and transit time distributions. These coupled models could, in turn, help in the development of more informed models of trace kinetics and hence achieve a better quantification of the measurements obtained from imaging data.

7.2.3 Investigating Additional Mechanisms and Impact of Diseases

Considering the modular manner by which the modelling framework in this work has been set up, the models in this thesis could provide a highly suitable *in-silico* modelling platform for incorporating additional features of varying degrees of complexity into the model, which could give rise to new mathematical modelling and experimental research. For example, in NVC, local CBF increases in response to increased neural activity. In addition, neuronal firing can also be affected by the levels of blood supply.[218] Incorporating models of NVC into the models of CBF regulation and control developed in this thesis, can help us explore the interplay between the dCA mechanisms and NVC and further our understanding of the NVC process for both health and disease. Another example would be to incorporate the effects of changes in intracranial pressure (which so far has been assumed to be constant in our model) as a result of changes in CBV, which has been done in compartmental models[105],[121] but not in network models where individual cortical penetrating vessels are resolved.

Finally, it would be very interesting and insightful to model the effects of penetrating vessel occlusion as a result of micro embolisms, similar to what has been done previously,[127] but now in the presence of the dCA mechanisms, in order to understand the role that dCA mechanisms could play in contributing towards reperfusion and alleviating the impact of vessel occlusion. This could help us discern, for instance, which regions and vessel generations in the microvasculature, or layers in the cortical tissue, are most 'susceptible' to the occlusions, and the impact the different treatment options have on restoring local CBF.

Appendices

A Appendix A

A.1 Compliance as a Function of Pressure

Assuming the material of the vessel wall to be linearly elastic, the circumferential strain ($\epsilon_{\theta\theta}$) and stress ($\sigma_{\theta\theta}$) in the vessel wall can be given by:

$$\epsilon_{\theta\theta} = \frac{R - R_{ref}}{(1-\nu^2)R_{ref}} \tag{A1}$$

$$\sigma_{\theta\theta} = E\epsilon_{\theta\theta} \tag{A2}$$

where ν is the Poisson's ratio. Next, Laplace's law for thin-walled cylinders, (where a thin-walled cylinder is defined by $\frac{h}{R_0} << \frac{P_t}{P_{ext}}$)[415] which is given by:

$$\sigma_{\theta\theta} = \frac{P_t R}{h} \tag{A3}$$

can be combined with Equations (A1) and (A2) to provide a function for the transmural pressure in terms of the radius:

$$P_t = \frac{Eh(R - R_{ref})}{(1-\nu^2)RR_{ref}} \tag{A4}$$

If h is approximated as constant, and the wall material is assumed incompressible ($\nu = 0.5$), then using the definition in Equation (3.5), then the compliance as a function of radius can be given by Equation (3.7). Also note that if $\frac{1}{R} \approx \frac{1}{R_{ref}}$, then we retrieve the non-linear tube law in Equation (3.3).

We can obtain the baseline Q and P throughout the network by solving the steady-state version of Equation (4.30). R_{ref} for each vessel can then be calculated from Equation (A4) using

the vessel P_t and R baseline conditions.

We can rearrange Equation (A4) to express R as a function of P_t, which can be inserted into Equation (3.7) to obtain a function for C in terms of P (in the absence of CA mechanisms):

$$C(P_t) = \frac{3\pi L}{2Eh}\left(\frac{EhR_{ref}}{Eh - \frac{3}{4}R_{ref}P_t}\right)^3 \tag{A5}$$

Figure A1 shows C as a function of P (assuming $P_{ext} = 0$) around baseline conditions for each vessel generation in the microvasculature network in Figure 3.3. For all microvessels except the capillaries, perturbations up to 15% in P_t result in $< 2.1\%$ change in C.

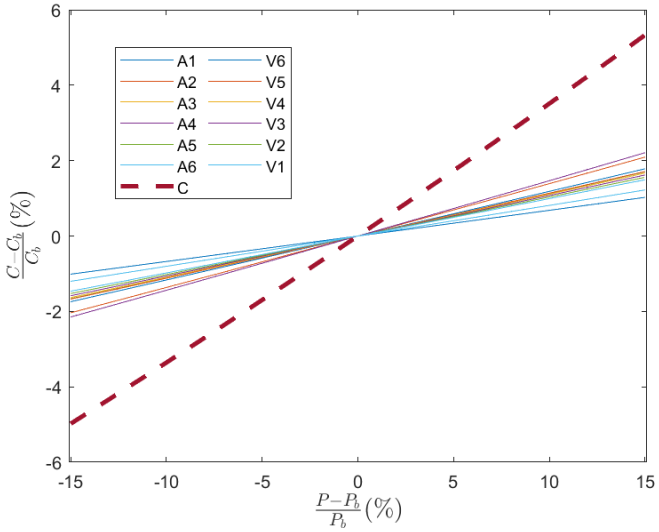

Figure A1: Changes in the Vessel compliance with changes in the vessel transmural pressure around baseline conditions for each vessel in the 13-generation network.

A.2 Combining the Governing Haemodynamic Equations

Equation (3.9) can be combined with Equation (3.1) to get:

$$\frac{\partial Q(x,t)}{\partial x} = -\frac{1}{L}\frac{\partial}{\partial t}\Big(C(t)P_t(x,t)\Big) \tag{A6}$$

which can then be transformed into the frequency domain to get:

$$\frac{\partial \hat{Q}(x,\omega)}{\partial x} = -\frac{i\omega}{L}\hat{C}(\omega) * \hat{P}_t(x,\omega) \tag{A7}$$

where $*$ denotes the linear convolution operator:

$$(\hat{C} * \hat{P}_t)(\omega) = \int_{-\infty}^{\infty} \hat{C}(\tau)\hat{P}_t(\omega - \tau)\, d\tau \tag{A8}$$

Differentiating Equations (3.10) and (3.11) we get:

$$\frac{\partial P_t(x,t)}{\partial t} \approx \frac{\partial \tilde{P}_t(x,t)}{\partial t} \tag{A9}$$

$$\frac{dC(t)}{\partial t} \approx \frac{d\tilde{C}(t)}{dt} \tag{A10}$$

Ignoring higher order terms ($\tilde{C}\tilde{P}_t \approx 0$), the tube law in Equation (3.9) can be written as

$$L\frac{\partial A(x,t)}{\partial t} = \overline{P_t}\frac{d\tilde{C}(t)}{dt} + \overline{C}\frac{\partial \tilde{P}_t(x,t)}{\partial t} \tag{A11}$$

Taking the Fourier transform of Equations (3.10) and (3.11) and dropping that hat notation we obtain:

$$P_t(x,\omega) = 2\pi\delta(\omega)\overline{P_t} + \tilde{P}_t(x,\omega) \tag{A12}$$

$$C(\omega) = 2\pi\delta(\omega)\overline{C} + \tilde{C}(\omega) \tag{A13}$$

which can then be inserted into the convolution integral in Equation (A8):

$$\begin{aligned}
&(C * P_t)(\omega) = \int_{-\infty}^{\infty} \Big(2\pi\delta(\tau)\overline{C} + \tilde{C(\tau)}\Big).\Big(2\pi\delta(\omega-\tau)\overline{P_t} + \tilde{P}_t(\omega-\tau)\Big)\, d\tau \\
&= 4\pi^2\overline{CP_t}\int_{-\infty}^{\infty}\delta(\tau)\delta(\omega-\tau)\, d\tau + 2\pi\Big(\overline{C}\int_{-\infty}^{\infty}\delta(\tau)\tilde{P}_t(\omega-\tau)\, d\tau\overline{P_t}\int_{-\infty}^{\infty}\tilde{C}(\tau)\delta(\omega-\tau)\, d\tau\Big) \\
&\cdot\int_{-\infty}^{\infty}\tilde{C}(\tau)\tilde{P}_t(\omega-\tau)\, d\tau = 4\pi^2\overline{CP_t}\big(\delta(\omega)*\delta(\omega)\big) + 2\pi(\overline{C}\tilde{P}_t + \overline{P_t}\tilde{C}) \\
&+ (\tilde{P}_t * \tilde{C})(\omega)4\pi^2\overline{CP_t}\delta(\omega) + 2\pi(\overline{C}\tilde{P}_t + \overline{P_t}\tilde{C})
\end{aligned}$$

where we have neglected the convolution of the higher order terms $\left(\mathcal{F}\left\{\tilde{C}(t)\tilde{P}_t(x,t)\right\} = \frac{1}{2\pi}(\tilde{P}_t * \tilde{C})(\omega) \approx 0\right)$. Inserting the expression above into Equation (A7), we obtain:

$$\frac{\partial Q(x,\omega)}{\partial x} = -\frac{1}{L}\left(\overline{C}(i\omega\tilde{P}_t) + \overline{P_t}(i\omega\tilde{C})\right) \tag{A14}$$

As proof, the same expression can be derived by taking the Fourier transform of Equation (A11). Equations (A9) and (A10) can then be inserted into Equation (A14) to obtain:

$$\frac{\partial Q(x,\omega)}{\partial x} = -\frac{1}{L}\left(\overline{C}(i\omega P_t) + \overline{P_t}(i\omega C)\right) \tag{A15}$$

Assuming that the external pressure is uniform around the microvessel (such that $\mathcal{F}\left\{\frac{\partial P_t(x,t)}{\partial x}\right\} = \mathcal{F}\left\{\frac{\partial P(x,t)}{\partial x}\right\}$), then Equation (3.2) can be written as:

$$Q(x,\omega) = -\frac{\overline{A}}{i\omega\rho}\left[1 - \frac{2J_1(i^{3/2}\alpha)}{i^{3/2}J_0(i^{3/2}\alpha)}\right]\frac{\partial P_t(x,\omega)}{\partial x} \tag{A16}$$

We differentiate Equation (A16) with respect to x, and insert into Equation (A15) to obtain the second order harmonic oscillator PDE for P_t in Equation (3.12).

A.3 Input-Output Scatter Plots for the Network Model

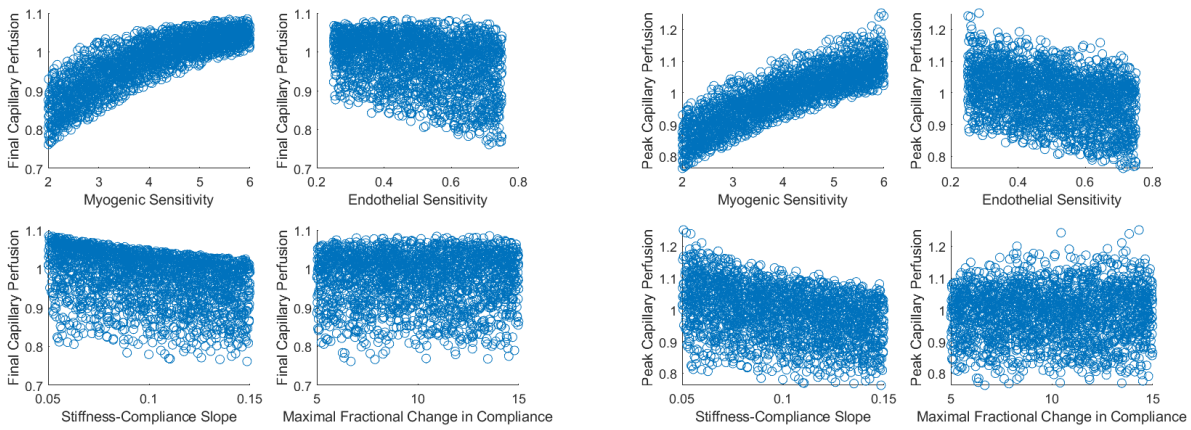

(a) (b)

Figure A2: Scatterplots for the final(a) and peak(b) perfusion versus the compliance model parameters.

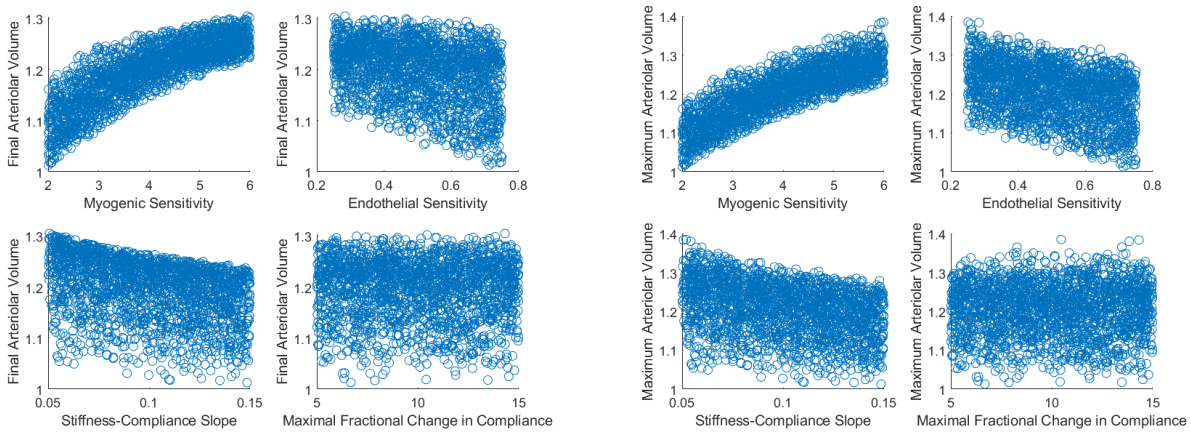

(a) (b)

Figure A3: Scatterplots for the final(a) and maximum(b) arteriolar CBV versus compliance model parameters.

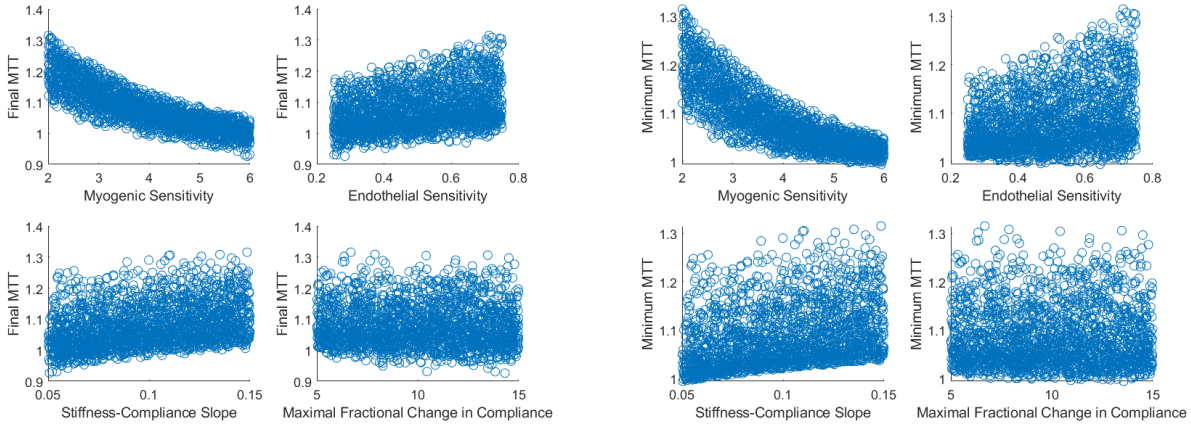

(a) (b)

Figure A4: Scatterplots for the final(a) and minimum(b) Mean Transit Time (MTT) versus compliance model parameters.

B Appendix B

B.1 Input Output Scatterplots for the Multiscale Model

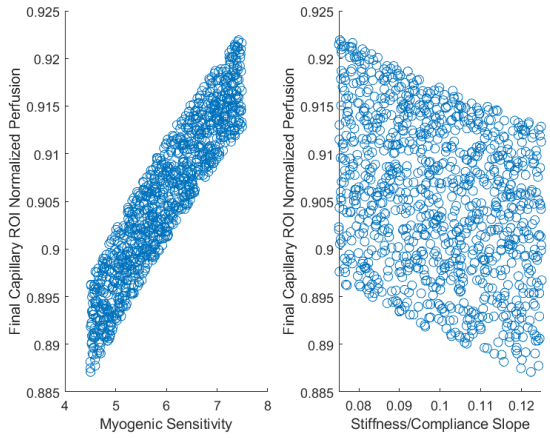

Figure B1: Scatterplots for the final perfusion (normalised to baseline perfusion) inside the capillary central ROI versus the myogenic sensitivity (S_α) and stiffness/compliance slope (G) compliance feedback parameters.

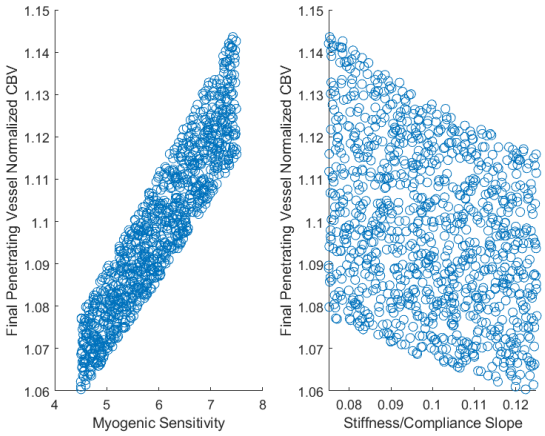

Figure B2: Scatterplots for the final volume of blood inside the penetrating vessels (normalised to baseline volume) inside the capillary central ROI versus the myogenic sensitivity (S_α) and stiffness/compliance slope (G) compliance feedback parameters.

B.2 Examining the Impact of the Radius of Support (ϵ) Value

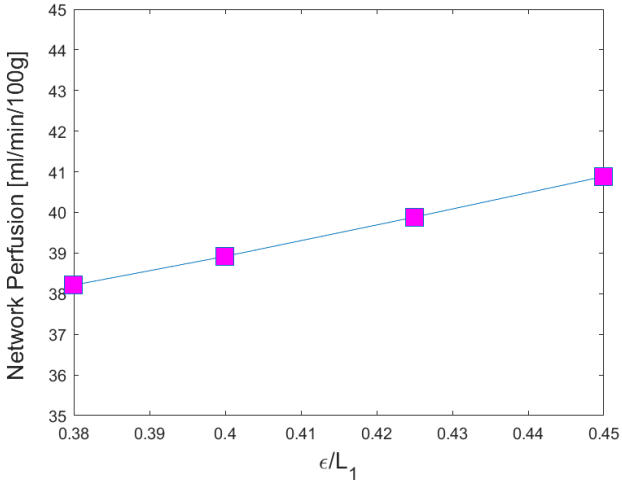

Figure B3: The steady-state perfusion of the network in Figure 4.2(d) using different values of ϵ within the permissible range of ϵ/L_1. The values of the other parameters were fixed to $K = 1.71 \times 10^{-12} m^3 s/kg$, $\gamma_v = 8.20 \times 10^{-16} m^4 s/kg$, and $\gamma_a = 1.17 \times 10^{-10} m^4 s/kg$.

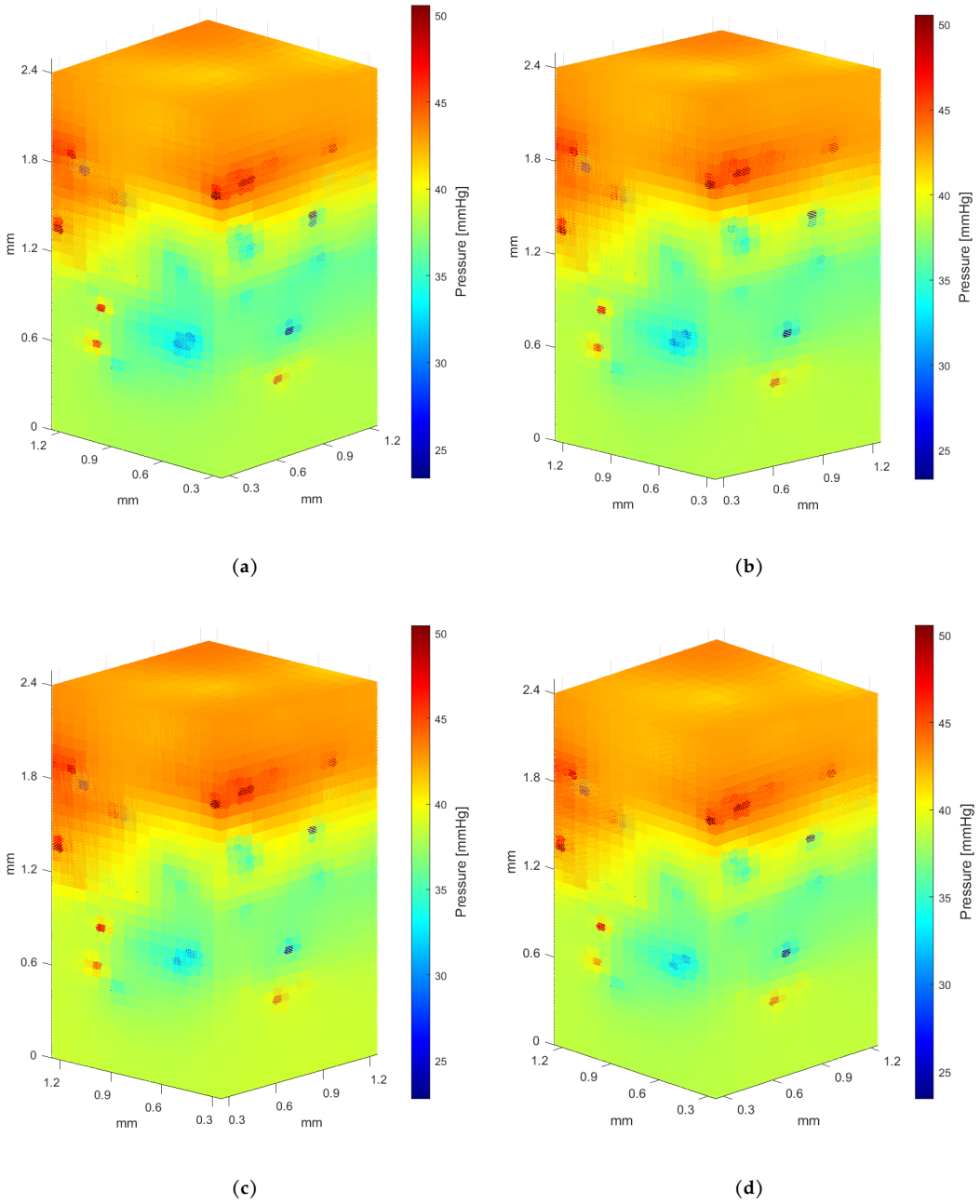

Figure B4: The steady-state pressure profile of the capillary bed inside the central ROI, for the network constructed in Figure 4.2(d), for the different values of ϵ within the permissible range: $\epsilon/L_1 = 0.45$ (a), $\epsilon/L_1 = 0.425$ (b), $\epsilon/L_1 = 0.40$ (c), and $\epsilon/L_1 = 0.38$ (d). The values of the remaining variables were fixed to: $K = 1.71 \times 10^{-12} m^3 s/kg$, $\gamma_v = 8.20 \times 10^{-16} m^4 s/kg$, and $\gamma_a = 1.17 \times 10^{-10} m^4 s/kg$. The values for the pressure were interpolated from the calculated capillary centroid pressure values using the nearest neighbour interpolation scheme in MATLAB.

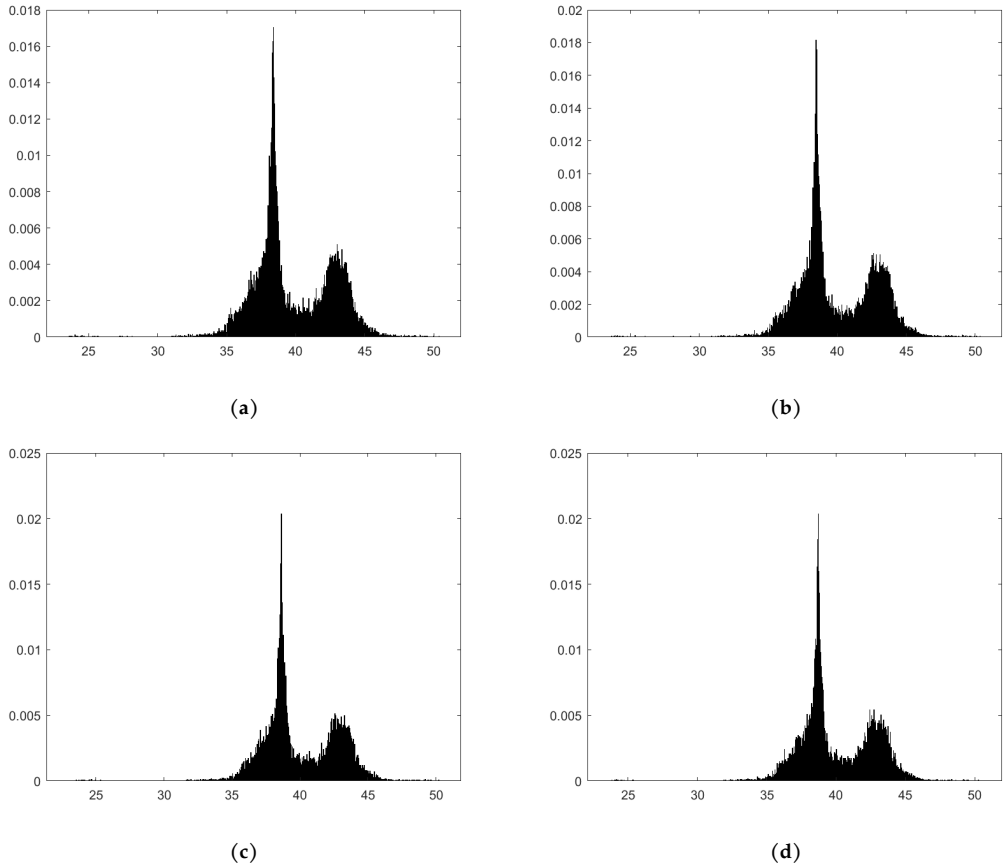

Figure B5: The PDF of the pressure distribution throughout the capillary bed, for the network constructed in Figure 4.2(d), for the different values of ϵ within the permissible range: $\epsilon/L_1 = 0.45$ (a), $\epsilon/L_1 = 0.425$ (b), $\epsilon/L_1 = 0.40$ (c), and $\epsilon/L_1 = 0.38$ (d). The values of the remaining variables were fixed to: $K = 1.71 \times 10^{-12} m^3 s/kg$, $\gamma_v = 8.20 \times 10^{-16} m^4 s/kg$, and $\gamma_a = 1.17 \times 10^{-10} m^4 s/kg$. The values for the pressure were interpolated from the calculated capillary centroid pressure values using the nearest neighbour interpolation scheme in MATLAB.

C Appendix C

C.1 Stability Analysis for the Conducted Hyperpolarization Signal

One major advantage of the CN method is that it is unconditionally stable, meaning that, unlike explicit methods that require resorting to cumbersomely small timesteps to achieve solution convergence, the simulation can be run with significantly larger timesteps, as long as Δt is sufficiently small compared to the smallest time constant (of $\approx 0.25s$; see Section 6.2.5), which is of great importance in terms of computational complexity and memory when the model is extended to a multiscale hybrid network-continuum representation of the microvasculature. Furthermore, the method is second-order accurate, such that, compared to the first-order accurate implicit (backwards) Euler method, a larger Δt can be used to achieve the same desired level of accuracy. However, one drawback of the CN method is that, depending on the network structure and the values of λ, τ_M, Δt and Δx, the solution can oscillate if there are sudden jumps in the initial and/or BCs, and these oscillations can propagate as weakly damped in time, thereby compromising the accuracy of the solution.[391] While such oscillations were not encountered with the symmetrical 13-generation network, for a stiff system that arises from the discretisation of the arteriolar network of the multiscale representation, some vessel gridpoints started exhibiting oscillations in v_m that lead to divergence in the solution for v_m which then emanated into the solution for the pressure and flow profiles.

To understand under what conditions these oscillations occur, it is instructive to use the Fourier transform approach as described in[391],[416]. Note that the analysis has been primarily conducted for the simple diffusion of the form:

$$\frac{\partial u}{\partial t} = b\frac{\partial^2 u}{\partial x^2} \tag{C1}$$

However, the cable model in Equation (6.28) can be written in a similar form:

$$\frac{\partial v_m}{\partial t} = \frac{\lambda^2}{\tau_M}\frac{\partial^2 v_m}{\partial x^2} - \frac{1}{\tau_M}v_m \tag{C2}$$

where b in Equation (C1) is equal to $\frac{\lambda^2}{\tau_M}$ for the cable model. Hence, for small values of v_m, the analysis derived in[391] is applicable to the cable model. The propagation of the FD solution from one timestep to another is governed by a growth factor $g(\phi)$, which for the CN method can be given by[391]:

$$g(\phi) = \frac{1 - 2b\mu sin^2\left(\frac{\phi}{2}\right)}{1 + 2b\mu sin^2\left(\frac{\phi}{2}\right)} \quad -\pi \leq \phi \leq \pi. \tag{C3}$$

where $\mu = \Delta t/\Delta x$. ϕ is the parameter in the frequency domain, with ϕ close to 0 corresponding to slowly varying components, and ϕ close to π corresponding to highly oscillatory components of the solution propagating to the next time step, which could arise due to discontinuities or jumps in the initial or BCs.[391] Since $|g(\phi)| \leq 1$, the CN scheme is unconditionally stable for all values of $b\mu$ and ϕ. However, for the high oscillatory components (*i.e.* when $\phi \approx \pm\pi$), then $g(\phi) \approx 1$ for large values of $b\mu$, resulting in the undamped propagation of oscillations in time. Using representative values of $\lambda = 2.5mm$, $\tau_m = 2.5s$, $\Delta t = 0.1s$ used in the simulations, and spatial discretisation of five equally spaced gridpoints for the arterioles in the multiscale network, which have lengths in the range of $39 - 930\mu m$, we get values for $b\mu$ in the range of $\approx 46 - 26950$, which produce a growth factor of $g(\pm\pi) \approx -1$ for the CN method. This explains the emergence of the oscillations and their amplification in time.

Considering the backward Euler implicit method, the growth factor can be given by[391]:

$$g(\phi) = \frac{1}{1 + 4b\mu sin^2\left(\frac{\phi}{2}\right)} \quad -\pi \leq \phi \leq \pi. \tag{C4}$$

Similar to the CN method, it can be easily seen that $|g(\phi)| \leq 1$, which implies unconditional stability. Interestingly, contrary to the CN method, the growth factor is small for the high oscillatory components of the solution for large values of $b\mu$, and decreases with increasing values of $b\mu$. This means that the components for which CN produces the most troublesome behaviour are the same components that are damped most by the implicit method, for sufficiently large values of $b\mu$. However, since the Euler method is first-order accurate, it requires smaller time steps than the CN to achieve the same level of accuracy. Therefore, the best possible way to proceed to achieve optimal computational feasibility and accuracy is to use

the CN method, combined with the backward Euler method with a smaller timestep in the time regions where such oscillations are likely to occur. In our case, when simulating the hypercapnic response by a sudden increase in P_{a,CO_2}, the implicit method can be used for the temporal range in the region encompassing the arteriolar CO_2 increase. This combination has been shown to eliminate the spurious oscillations arising from adopting a pure CN scheme.

C.2 Posterior CVR Model Parameter Distributions

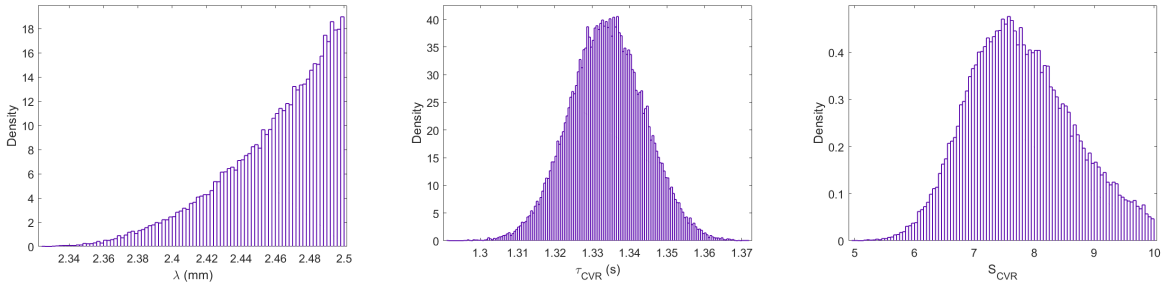

(a) (b) (c)

Figure C1: Final posterior distributions of the CVR model parameters obtained from Approximate Bayesian Computation (ABC) schemes.

C.3 Investigating the effect of increasing τ_{ACh}

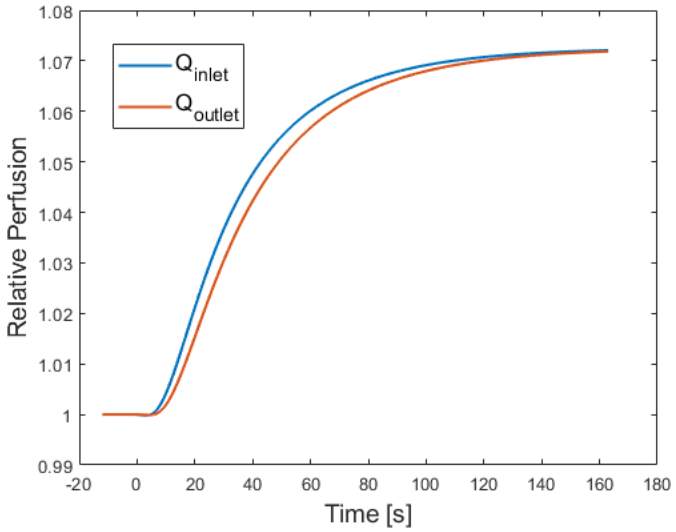

Figure C2: The CBF response to an $3mmHg$ increase in P_{a,CO_2} at $t = 0$ in the multiscale network, when τ_{ACh} is increased to 20s. The equivalent time constant, defined as the time it takes for the response to reach 1-1/e of its final value, is equal to 44s.

D Appendix D

Table D1: Comparison between the 1D Hyperbolic PDE Model and the 0D Microcirculation Model using Perturbation Methods for Blood Flow in a Vessel Network

		Hyperbolic Method	Perturbation Method
Governing Equations	Mass Conservation $\frac{\partial \rho}{\partial t} + \nabla \cdot (\rho \boldsymbol{v}) = 0$	$\frac{\partial A}{\partial t} + \frac{\partial Q}{\partial x} = 0$	$i\omega \hat{A} + \frac{\partial \hat{Q}}{\partial x} = 0$
	Momentum Conservation $\rho \frac{\partial \mathrm{v}}{\partial t} + \rho \boldsymbol{v}.(\nabla \boldsymbol{v})$ $+\nabla \mathrm{P} = \mu \cdot \nabla^2 \boldsymbol{v}$	$\frac{\partial Q}{\partial t} + \frac{\partial}{\partial x}\left(\alpha \frac{Q^2}{A}\right) + \frac{A}{\rho}\frac{\partial P}{\partial x}$ $= -2\pi\nu(\lambda + 2)\frac{Q}{A}$	$\hat{Q} = -\frac{\bar{A}}{i\omega\rho}\left[1 - \frac{2J_1(\epsilon)}{\epsilon J_0(\epsilon)}\right]\frac{\partial \hat{P}_t}{\partial x}$ $\epsilon = i^{3/2} R\sqrt{\frac{w}{\nu}}$
	Tube Law Elastic Wall/Laplace Law: $P = P_{ext} + \frac{Eh}{1-\nu^2}\frac{R - R_0}{RR_0}$	$P_t = \beta\left(\sqrt{A} - \sqrt{A_{ref}}\right)$ $\beta = \frac{Eh}{(1-\nu^2)\sqrt{\pi}R_{ref}^2}$	$\frac{dV}{dt} = \frac{d}{dt}(CP_t)$ $C_b = \frac{2\pi\,(1-\nu^2)R_0^3}{Eh}$
Single Vessel Model		Hyperbolic PDE system: $\frac{\partial \boldsymbol{U}}{\partial t} + \frac{\partial \boldsymbol{F}(\boldsymbol{U})}{\partial x} = \boldsymbol{S}(\boldsymbol{U})$ $\boldsymbol{U} = \begin{pmatrix} \boldsymbol{A} \\ \boldsymbol{Q} \end{pmatrix}$ $\boldsymbol{F} = \begin{pmatrix} \boldsymbol{Q} \\ \boldsymbol{\alpha}\frac{\boldsymbol{Q^2}}{\boldsymbol{A}} + \frac{\boldsymbol{\beta}}{\boldsymbol{3\rho}}\boldsymbol{A^{3/2}} \end{pmatrix}$ $\boldsymbol{S} = \begin{pmatrix} \boldsymbol{0} \\ \boldsymbol{-2\pi\nu(\lambda+2)\frac{Q}{A}} \end{pmatrix}$ Solved using 2nd order accurate (modified) MacCormack scheme (other FD, FV, or FE methods also applicable).	Harmonic oscillator equation for pressure in the frequency domain: $\frac{\partial^2 P_t}{\partial x^2} = \left[\frac{-w^2\rho}{\pi R^2 L\left[1 - \frac{2J_1(\epsilon)}{\epsilon J_0(\epsilon)}\right]}\right](\bar{C}P_t + C\bar{P_t})$ Use of Perturbation Methods and frequency-time analysis to arrive to the 0th dimensional solution for flow: $\begin{pmatrix} Q_{in} \\ Q_{out} \end{pmatrix} = \frac{1}{\mathcal{R}}\begin{pmatrix} 1 & -1 \\ 1 & -1 \end{pmatrix}\begin{pmatrix} P_{in} \\ P_{out} \end{pmatrix}$ $-\left[\frac{R^2}{6\nu\mathcal{R}}\begin{pmatrix} 1 & -1 \\ 1 & -1 \end{pmatrix}\right.$ $\left. + \frac{\bar{C}}{6}\begin{pmatrix} -2 & -1 \\ 1 & 2 \end{pmatrix}\right]\frac{d}{dt}\begin{pmatrix} P_{in} - P_{ext} \\ P_{out} - P_{ext} \end{pmatrix} + \frac{\bar{P}}{6}\frac{dC}{dt}\begin{pmatrix} 1 \\ -1 \end{pmatrix}$
Assumptions	Blood Properties	• Newtonian, incompressible fluid. • Viscosity modelled via empirical in-vivo model. • Negligible gravity.	
	Blood Flow Profile	• Axis-symmetric flow (hence laminar flow implicit assumption). • $\frac{R}{L}$ is sufficiently small, such that $v_x >> v_r$ and $\frac{\partial P}{\partial r} = 0$. • The vessel wall moves at the same velocity as the fluid at the interaction between them such that $v_x(R) = 0, v_r(R) = \frac{\partial R}{\partial t}$.	

	Velocity Profile	Power Law Velocity Profile Assumption: $V_x(r,x,t) = U(x,t)\Theta(r)$ $\Theta(r) = \frac{\lambda+2}{\lambda}\left[1-(\frac{r}{R})^{\lambda}\right]$ $\alpha = \frac{\lambda+2}{\lambda+1}$	A Womersley velocity profile is assumed.
	Vessel Dimensions	Long Wave assumption ((λ>>R)	Narrow vessels (R$\sqrt{\frac{\omega}{\nu}} << 1$)
	Advective Contributions	Incorporated: integration of momentum term over cross-sectional area is compensated for via the Coriolis coefficient α.	Advective Term Neglected.
	Laplace Law 'thin vessel' approximation	$\frac{h}{R_i} \ll \frac{\Delta P}{P_{ext}}$	
	Tube Law\Vessel Wall	• $\frac{1}{R} \sim \frac{1}{R_0}$ • $\frac{\partial \beta}{\partial x} = 0$ • $\frac{\partial A_0}{\partial x} = 0$ • β in quasi-steady-state.	• $\frac{\partial C}{\partial x} = 0$ • $R(x) \sim R_{avg}$ • C in quasi-steady-state. • R is in quasi-steady-state; the R in the harmonic oscillator equation used in perturbation analysis is the space and time averaged R; the R in the derived approximate analytical solution in the time domain is updated quasi-statically.
Boundary Conditions		Prescription of either the Q or P (but not both) at each boundary is permissible and required to ensure the analytical problem is well-posed. The other BC at each boundary as required for the numerical problem is obtained by enforcing the compatibility condition (spectral collocation approximation) on the outgoing characteristic.	Prescription of either Q or P (but not both) at each boundary is required.
Nodal Junctions Conditions	Mass (flow) Conservation from the (N) vessels connected to the node(j).	$\sum_{j \in N} \boldsymbol{q_j} = \mathbf{0}$	

	Pressure Continuity (ex. for a bifurcating node) $\mathbf{1} = \boldsymbol{parent\ vessel}$ $\boldsymbol{i} = \mathbf{2,3} = \boldsymbol{child\ vessels}$	Matching Total Pressure (Bernoulli Equation) $\boldsymbol{P_1} + \frac{1}{2}\boldsymbol{\rho}\left(\frac{\boldsymbol{Q_1}}{\boldsymbol{A_1}}\right)^2 = \boldsymbol{P_i} + \frac{1}{2}\boldsymbol{\rho}\left(\frac{\boldsymbol{Q_i}}{\boldsymbol{A_i}}\right)^2$	Matching Static Pressure $\boldsymbol{P_1} = \boldsymbol{P_i}$
	Information propagation from the interior domain of connecting vessels.	$\frac{\partial W_{outgoing}}{\partial t} + \lambda_{outgoing}\frac{\partial W_{outgoing}}{\partial x} + l_j^T S = 0,$ $j = \begin{cases} 1 & for\ vessel\ end \\ 2 & for\ vessel\ start \end{cases}$	$q_j = f\left(P, \frac{dP}{dt}, R, C\right)$
	Resulting System of Equations at each node.	6x6 non-linear square system (including 3 PDEs).	Linear ODE system of equations at each node.
Connecting the Network Together		At each timestep, variables of the vessel interior are updated via numerical solver, after which the terminal variables at the junctions are solved for via compatibility relation supplemented with conditions of mass conservation and pressure continuity.	All vessels in the network are connected into single ODE linear system to solve for the static pressure at the interior nodes: $\boldsymbol{A_{int}P_{int}} + \boldsymbol{B_{int}}\frac{\boldsymbol{dP_{int}}}{dt} = -\boldsymbol{GA_{ext}P_{ext}} - \boldsymbol{B_{ext}}\frac{\boldsymbol{dP_{ext}}}{dt}$ - **C**
Scheme Order Accuracy		2nd order in space and time overall: • Modified MacCormack scheme is 2nd order accurate in space and time. • Nodal Junction scheme is 2nd order accurate in time (trapezoidal) and >2nd order accurate in space.	Can be 2nd order (trapezoidal method) or 1st order accurate (Euler method).
Scheme Stability		Conditionally stable: • MacCormack scheme is explicit, nodal junction scheme is implicit, hence explicit scheme overall. • Lower (minimum) bound on stability (i.e., necessary but not sufficient* condition) is given by the CFL condition: $\Delta t \leq \frac{\Delta x}{max(\lvert U \rvert + c)}$ *The CFL condition is not sufficient because the problem is a non-linear PDE system of equations.	Unconditionally stable: • The first-order ODE system of equations is discretized and solved using a 'semi'-implicit scheme. • Δt is only bounded by accuracy limits (i.e., should be small enough to capture any perturbations).
Simulation Time (for 13-generation network)		1.037×10^6 seconds	58 seconds

References

[1] K.-A. Mardal, M. E. Rognes, T. B. Thompson, and L. M. Valnes, *Mathematical Modeling of the Human Brain: From Magnetic Resonance Images to Finite Element Simulation* (Simula SpringerBriefs on Computing), en. Cham: Springer International Publishing, 2022, vol. 10, ISBN: 9783030951351 9783030951368. DOI: 10.1007/978-3-030-95136-8.

[2] R. E. Klabunde, *Cardiovascular physiology concepts*, 2nd ed. Philadelphia, PA: Lippincott Williams & Wilkins/Wolters Kluwer, 2012, OCLC: ocn712765593, ISBN: 9781451113846.

[3] S. S. Kety and C. F. Schmidt, "THE EFFECTS OF ALTERED ARTERIAL TENSIONS OF CARBON DIOXIDE AND OXYGEN ON CEREBRAL BLOOD FLOW AND CEREBRAL OXYGEN CONSUMPTION OF NORMAL YOUNG MEN 1," *Journal of Clinical Investigation*, vol. 27, no. 4, pp. 484–492, Jul. 1948, ISSN: 0021-9738.

[4] T. P. Santisakultarm, N. R. Cornelius, N. Nishimura, *et al.*, "In vivo two-photon excited fluorescence microscopy reveals cardiac- and respiration-dependent pulsatile blood flow in cortical blood vessels in mice," en, *American Journal of Physiology-Heart and Circulatory Physiology*, vol. 302, no. 7, H1367–H1377, Apr. 2012, ISSN: 0363-6135, 1522-1539. DOI: 10.1152/ajpheart.00417.2011.

[5] N. Marina, I. N. Christie, A. Korsak, *et al.*, "Astrocytes monitor cerebral perfusion and control systemic circulation to maintain brain blood flow," en, *Nature Communications*, vol. 11, no. 1, p. 131, Dec. 2020, ISSN: 2041-1723. DOI: 10.1038/s41467-019-13956-y.

[6] K. Jackman and C. Iadecola, "Neurovascular Regulation in the Ischemic Brain," en, *Antioxidants & Redox Signaling*, vol. 22, no. 2, pp. 149–160, Jan. 2015, ISSN: 1523-0864, 1557-7716. DOI: 10.1089/ars.2013.5669.

[7] D. M. Mandell, J. S. Han, J. Poublanc, *et al.*, "Selective reduction of blood flow to white matter during hypercapnia corresponds with leukoaraiosis," eng, *Stroke*, vol. 39, no. 7, pp. 1993–1998, Jul. 2008, ISSN: 1524-4628. DOI: 10.1161/STROKEAHA.107.501692.

[8] R. B. Panerai, "Cerebral Autoregulation: From Models to Clinical Applications," en, *Cardiovascular Engineering*, vol. 8, no. 1, pp. 42–59, Mar. 2008, ISSN: 1567-8822, 1573-6806. DOI: 10.1007/s10558-007-9044-6.

[9] V. Novak, P. Novak, J. M. Spies, and P. A. Low, "Autoregulation of Cerebral Blood Flow in Orthostatic Hypotension," en, *Stroke*, vol. 29, no. 1, pp. 104–111, Jan. 1998, ISSN: 0039-2499, 1524-4628. DOI: 10.1161/01.STR.29.1.104.

[10] M. Reinhard, M. Roth, T. Müller, M. Czosnyka, J. Timmer, and A. Hetzel, "Cerebral Autoregulation in Carotid Artery Occlusive Disease Assessed From Spontaneous Blood Pressure Fluctuations by the Correlation Coefficient Index," en, *Stroke*, vol. 34, no. 9, pp. 2138–2144, Sep. 2003, ISSN: 0039-2499, 1524-4628. DOI: 10.1161/01.STR.0000087788.65566.AC.

[11] J. A. Claassen and R. Zhang, "Cerebral autoregulation in Alzheimer's disease," en, *Journal of Cerebral Blood Flow & Metabolism*, vol. 31, no. 7, pp. 1572–1577, Jul. 2011, ISSN: 0271-678X, 1559-7016. DOI: 10.1038/jcbfm.2011.69.

[12] J. Steinman, H.-S. Sun, and Z.-P. Feng, "Microvascular Alterations in Alzheimer's Disease," *Frontiers in Cellular Neuroscience*, vol. 14, p. 618 986, Jan. 2021, ISSN: 1662-5102. DOI: 10.3389/fncel.2020.618986.

[13] Z. Arvanitakis, A. W. Capuano, S. E. Leurgans, D. A. Bennett, and J. A. Schneider, "Relation of cerebral vessel disease to Alzheimer's disease dementia and cognitive function in elderly people: A cross-sectional study," eng, *The Lancet. Neurology*, vol. 15, no. 9, pp. 934–943, Aug. 2016, ISSN: 1474-4465. DOI: 10.1016/S1474-4422(16)30029-1.

[14] R. Tarawneh, "Microvascular Contributions to Alzheimer Disease Pathogenesis: Is Alzheimer Disease Primarily an Endotheliopathy?" en, *Biomolecules*, vol. 13, no. 5, p. 830, May 2023, ISSN: 2218-273X. DOI: 10.3390/biom13050830.

[15] J. M. Tarasoff-Conway, R. O. Carare, R. S. Osorio, *et al.*, "Clearance systems in the brain—implications for Alzheimer disease," en, *Nature Reviews Neurology*, vol. 11, no. 8, pp. 457–470, Aug. 2015, ISSN: 1759-4758, 1759-4766. DOI: 10.1038/nrneurol.2015.119.

[16] A. Deshpande, N. Jamilpour, B. Jiang, *et al.*, "Automatic segmentation, feature extraction and comparison of healthy and stroke cerebral vasculature," en, *NeuroImage: Clinical*, vol. 30, p. 102 573, 2021, ISSN: 22131582. DOI: 10.1016/j.nicl.2021.102573.

[17] E Bullitt, K Muller, I Jung, W Lin, and S Aylward, "Analyzing attributes of vessel populations," en, *Medical Image Analysis*, vol. 9, no. 1, pp. 39–49, Feb. 2005, ISSN: 13618415. DOI: 10.1016/j.media.2004.06.024.

[18] L. Østergaard, T. S. Engedal, F. Moreton, *et al.*, "Cerebral small vessel disease: Capillary pathways to stroke and cognitive decline," eng, *Journal of Cerebral Blood Flow and Metabolism: Official Journal of the International Society of Cerebral Blood Flow and Metabolism*, vol. 36, no. 2, pp. 302–325, Feb. 2016, ISSN: 1559-7016. DOI: 10.1177/0271678X15606723.

[19] J. C. Cruz Hernández, O. Bracko, C. J. Kersbergen, *et al.*, "Neutrophil adhesion in brain capillaries reduces cortical blood flow and impairs memory function in Alzheimer's disease mouse models," en, *Nature Neuroscience*, vol. 22, no. 3, pp. 413–420, Mar. 2019, ISSN: 1546-1726. DOI: 10.1038/s41593-018-0329-4.

[20] E. Farkas and P. G. Luiten, "Cerebral microvascular pathology in aging and Alzheimer's disease," eng, *Progress in Neurobiology*, vol. 64, no. 6, pp. 575–611, Aug. 2001, ISSN: 0301-0082. DOI: 10.1016/s0301-0082(00)00068-x.

[21] C. Iadecola, "Neurovascular regulation in the normal brain and in Alzheimer's disease," eng, *Nature Reviews. Neuroscience*, vol. 5, no. 5, pp. 347–360, May 2004, ISSN: 1471-003X. DOI: 10.1038/nrn1387.

[22] E. P. Meyer, A. Ulmann-Schuler, M. Staufenbiel, and T. Krucker, "Altered morphology and 3D architecture of brain vasculature in a mouse model for Alzheimer's disease," en, *Proceedings of the National Academy of Sciences*, vol. 105, no. 9, pp. 3587–3592, Mar. 2008, ISSN: 0027-8424, 1091-6490. DOI: 10.1073/pnas.0709788105.

[23] J. W. Baish, Y. Gazit, D. A. Berk, M. Nozue, L. T. Baxter, and R. K. Jain, "Role of Tumor Vascular Architecture in Nutrient and Drug Delivery: An Invasion Percolation-Based Network Model," en, *Microvascular Research*, vol. 51, no. 3, pp. 327–346, May 1996, ISSN: 00262862. DOI: 10.1006/mvre.1996.0031.

[24] D. A. Hartmann, A.-A. Berthiaume, R. I. Grant, *et al.*, "Brain capillary pericytes exert a substantial but slow influence on blood flow," eng, *Nature Neuroscience*, vol. 24, no. 5, pp. 633–645, May 2021, ISSN: 1546-1726. DOI: 10.1038/s41593-020-00793-2.

[25] J. M. Wardlaw, C. Smith, and M. Dichgans, "Mechanisms of sporadic cerebral small vessel disease: Insights from neuroimaging," en, *The Lancet Neurology*, vol. 12, no. 5, pp. 483–497, May 2013, ISSN: 14744422. DOI: 10.1016/S1474-4422(13)70060-7.

[26] F. Cassot, F. Lauwers, S. Lorthois, P. Puwanarajah, V. Cances-Lauwers, and H. Duvernoy, "Branching patterns for arterioles and venules of the human cerebral cortex," en, *Brain Research*, vol. 1313, pp. 62–78, Feb. 2010, ISSN: 00068993. DOI: 10.1016/j.brainres.2009.12.007.

[27] D. A. Hartmann, V. Coelho-Santos, and A. Y. Shih, "Pericyte Control of Blood Flow Across Microvascular Zones in the Central Nervous System," en, *Annual Review of Physiology*, vol. 84, no. 1, pp. 331–354, Feb. 2022, ISSN: 0066-4278, 1545-1585. DOI: 10.1146/annurev-physiol-061121-040127.

[28] L. O. Müller and E. F. Toro, "A global multiscale mathematical model for the human circulation with emphasis on the venous system," eng, *International Journal for Numerical Methods in Biomedical Engineering*, vol. 30, no. 7, pp. 681–725, Jul. 2014, ISSN: 2040-7947. DOI: 10.1002/cnm.2622.

[29] N. Xiao, J. Alastruey, and C. Alberto Figueroa, "A systematic comparison between 1-D and 3-D hemodynamics in compliant arterial models," eng, *International Journal for Numerical Methods in Biomedical Engineering*, vol. 30, no. 2, pp. 204–231, Feb. 2014, ISSN: 2040-7947. DOI: 10.1002/cnm.2598.

[30] R. M. Padmos, T. I. Józsa, W. K. El-Bouri, P. R. Konduri, S. J. Payne, and A. G. Hoekstra, "Coupling one-dimensional arterial blood flow to three-dimensional tissue perfusion models for *in silico* trials of acute ischaemic stroke," en, *Interface Focus*, vol. 11, no. 1, p. 20 190 125, Feb. 2021, ISSN: 2042-8898, 2042-8901. DOI: 10.1098/rsfs.2019.0125.

[31] J. Alastruey, K. H. Parker, and S. J. Sherwin, "Arterial pulse wave haemodynamics," English, *11th International Conference on Pressure Surges*, pp. 401–443, Oct. 2012.

[32] F. Liang, S. Takagi, R. Himeno, and H. Liu, "Multi-scale modeling of the human cardiovascular system with applications to aortic valvular and arterial stenoses," eng, *Medical & Biological Engineering & Computing*, vol. 47, no. 7, pp. 743–755, Jul. 2009, ISSN: 1741-0444. DOI: 10.1007/s11517-009-0449-9.

[33] J. P. Mynard and P. Nithiarasu, "A 1D arterial blood flow model incorporating ventricular pressure, aortic valve and regional coronary flow using the locally conservative Galerkin (LCG) method," en, *Communications in Numerical Methods in Engineering*, vol. 24, no. 5, pp. 367–417, Mar. 2008, ISSN: 10698299. DOI: 10.1002/cnm.1117.

[34] F. Piccioli, G. Bertaglia, A. Valiani, and V. Caleffi, "Modeling blood flow in networks of viscoelastic vessels with the 1-D augmented fluid–structure interaction system," *Journal of Computational Physics*, vol. 464, no. C, Sep. 2022, ISSN: 0021-9991. DOI: 10.1016/j.jcp.2022.111364.

[35] A. Quarteroni, A. Veneziani, and C. Vergara, "Geometric multiscale modeling of the cardiovascular system, between theory and practice," en, *Computer Methods in Applied Mechanics and Engineering*, vol. 302, pp. 193–252, Apr. 2016, ISSN: 0045-7825. DOI: 10.1016/j.cma.2016.01.007.

[36] F. Schmid, M. J. Barrett, P. Jenny, and B. Weber, "Vascular density and distribution in neocortex," en, *NeuroImage*, vol. 197, pp. 792–805, Aug. 2019, ISSN: 10538119. DOI: 10.1016/j.neuroimage.2017.06.046.

[37] H. Duvernoy, S. Delon, and J. Vannson, "Cortical blood vessels of the human brain," en, *Brain Research Bulletin*, vol. 7, no. 5, pp. 519–579, Nov. 1981, ISSN: 03619230. DOI: 10.1016/0361-9230(81)90007-1.

[38] F. Cassot, F. Lauwers, C. Fouard, S. Prohaska, and V. Lauwers-Cances, "A Novel Three-Dimensional Computer-Assisted Method for a Quantitative Study of Microvascular Networks of the Human Cerebral Cortex," en, *Microcirculation*, vol. 13, no. 1, pp. 1–18, Jan. 2006, ISSN: 1073-9688, 1549-8719. DOI: 10.1080/10739680500383407.

[39] W. K. El-Bouri and S. J. Payne, "A statistical model of the penetrating arterioles and venules in the human cerebral cortex," en, *Microcirculation*, vol. 23, no. 7, pp. 580–590, Oct. 2016, ISSN: 10739688. DOI: 10.1111/micc.12318.

[40] S.-W. Su, M. Catherall, and S. Payne, "The influence of network structure on the transport of blood in the human cerebral microvasculature," eng, *Microcirculation (New York, N.Y.: 1994)*, vol. 19, no. 2, pp. 175–187, Feb. 2012, ISSN: 1549-8719. DOI: 10.1111/j.1549-8719.2011.00148.x.

[41] W. El-Bouri and S. J. Payne, "Multi-scale homogenization of blood flow in 3-dimensional human cerebral microvascular networks," en, *Journal of Theoretical Biology*, vol. 380, pp. 40–47, Sep. 2015, ISSN: 00225193. DOI: 10.1016/j.jtbi.2015.05.011.

[42] J. Reichold, M. Stampanoni, A. L. Keller, A. Buck, P. Jenny, and B. Weber, "Vascular Graph Model to Simulate the Cerebral Blood Flow in Realistic Vascular Networks," en, *Journal of Cerebral Blood Flow & Metabolism*, vol. 29, no. 8, pp. 1429–1443, Aug. 2009, ISSN: 0271-678X, 1559-7016. DOI: 10.1038/jcbfm.2009.58.

[43] G. Hartung, S. Badr, M. Moeini, *et al.*, "Voxelized simulation of cerebral oxygen perfusion elucidates hypoxia in aged mouse cortex," en, *PLOS Computational Biology*, vol. 17, no. 1, R. M. Merks, Ed., e1008584, Jan. 2021, ISSN: 1553-7358. DOI: 10.1371/journal.pcbi.1008584.

[44] M. Schneider, J. Reichold, B. Weber, G. Székely, and S. Hirsch, "Tissue metabolism driven arterial tree generation," en, *Medical Image Analysis*, vol. 16, no. 7, pp. 1397–1414, Oct. 2012, ISSN: 13618415. DOI: 10.1016/j.media.2012.04.009.

[45] F. Schmid, P. S. Tsai, D. Kleinfeld, P. Jenny, and B. Weber, "Depth-dependent flow and pressure characteristics in cortical microvascular networks," en, *PLOS Computational Biology*, vol. 13, no. 2, J. J. Saucerman, Ed., e1005392, Feb. 2017, ISSN: 1553-7358. DOI: 10.1371/journal.pcbi.1005392.

[46] H. Shapiro, D. Stromberg, D. Lee, and C. Wiederhielm, "Dynamic pressures in the pial arterial microcirculation," en, *American Journal of Physiology-Legacy Content*, vol. 221, no. 1, pp. 279–283, Jul. 1971, ISSN: 0002-9513. DOI: 10.1152/ajplegacy.1971.221.1.279.

[47] S. L. Harper and H. G. Bohlen, "Microvascular adaptation in the cerebral cortex of adult spontaneously hypertensive rats.," en, *Hypertension*, vol. 6, no. 3, pp. 408–419, May 1984, ISSN: 0194-911X, 1524-4563. DOI: 10.1161/01.HYP.6.3.408.

[48] E. M. Hillman, "Coupling Mechanism and Significance of the BOLD Signal: A Status Report," en, *Annual Review of Neuroscience*, vol. 37, no. 1, pp. 161–181, Jul. 2014, ISSN: 0147-006X, 1545-4126. DOI: 10.1146/annurev-neuro-071013-014111.

[49] A. Quarteroni and L. Formaggia, "Mathematical Modelling and Numerical Simulation of the Cardiovascular System," en, in *Handbook of Numerical Analysis*, ser. Computational Models for the Human Body, vol. 12, Elsevier, Jan. 2004, pp. 3–127. DOI: 10.1016/S1570-8659(03)12001-7.

[50] S. Payne, T. I. Józsa, and W. K. El-Bouri, "Review of in silico models of cerebral blood flow in health and pathology," *Progress in Biomedical Engineering*, vol. 5, no. 2, p. 022 003, Apr. 2023, ISSN: 2516-1091. DOI: 10.1088/2516-1091/accc62.

[51] A. E. Van Rijssel, B. C. Stins, L. C. Beishon, *et al.*, "Effect of Antihypertensive Treatment on Cerebral Blood Flow in Older Adults: A Systematic Review and Meta-Analysis," en, *Hypertension*, vol. 79, no. 5, pp. 1067–1078, May 2022, ISSN: 0194-911X, 1524-4563. DOI: 10.1161/HYPERTENSIONAHA.121.18255.

[52] *Autoregulation-Oriented Blood Pressure Management in Acute Brain Injury*, en.

[53] M. Berg, Y. Davit, M. Quintard, and S. Lorthois, "Modelling solute transport in the brain microcirculation: Is it really well mixed inside the blood vessels?" en, *Journal of Fluid Mechanics*, vol. 884, A39, Feb. 2020, ISSN: 0022-1120, 1469-7645. DOI: 10.1017/jfm.2019.866.

[54] M. Y. Jen, M. Shahrokhi, and M. Varacallo, "Predictive Medicine," eng, in *StatPearls*, Treasure Island (FL): StatPearls Publishing, 2024.

[55] S. Payne, *Cerebral Autoregulation* (SpringerBriefs in Bioengineering). Cham: Springer International Publishing, 2016, ISBN: 9783319317830 9783319317847. DOI: 10.1007/978-3-319-31784-7.

[56] C. A. Taylor and M. T. Draney, "E XPERIMENTAL AND C OMPUTATIONAL M ETHODS IN C ARDIOVASCULAR F LUID M ECHANICS," en, *Annual Review of Fluid Mechanics*, vol. 36, no. 1, pp. 197–231, Jan. 2004, ISSN: 0066-4189, 1545-4479. DOI: 10.1146/annurev.fluid.36.050802.121944.

[57] M. Kelm, L. Goubergrits, J. Bruening, *et al.*, "Model-Based Therapy Planning Allows Prediction of Haemodynamic Outcome after Aortic Valve Replacement," en, *Scientific Reports*, vol. 7, no. 1, p. 9897, Aug. 2017, ISSN: 2045-2322. DOI: 10.1038/s41598-017-03693-x.

[58] H. Wang, H. Song, Y. Yang, *et al.*, "Hemodynamic testing using three-dimensional printing and computational fluid dynamics preoperatively may provide more information in mitral repair than traditional image dataset," *Annals of Translational Medicine*, vol. 9, no. 8, pp. 632–632, Apr. 2021, ISSN: 23055839, 23055847. DOI: 10.21037/atm-20-7960.

[59] T. M. J. Van Bakel, K. D. Lau, J. Hirsch-Romano, S. Trimarchi, A. L. Dorfman, and C. A. Figueroa, "Patient-Specific Modeling of Hemodynamics: Supporting Surgical Planning in a Fontan Circulation Correction," en, *Journal of Cardiovascular Translational Research*, vol. 11, no. 2, pp. 145–155, Apr. 2018, ISSN: 1937-5387, 1937-5395. DOI: 10.1007/s12265-017-9781-x.

[60] J. W. Thomas, *Numerical partial differential equations* (Texts in applied mathematics 22, 33). New York: Springer, 1995, ISBN: 9780387979991 9780387983462.

[61] H. Cheng, S. Vinci-Booher, J. Wang, *et al.*, "Denoising diffusion weighted imaging data using convolutional neural networks," en, *PLOS ONE*, vol. 17, no. 9, P.-T. Yap, Ed., e0274396, Sep. 2022, ISSN: 1932-6203. DOI: 10.1371/journal.pone.0274396.

[62] K. Azer and C. S. Peskin, "A one-dimensional model of blood flow in arteries with friction and convection based on the Womersley velocity profile," eng, *Cardiovascular Engineering (Dordrecht, Netherlands)*, vol. 7, no. 2, pp. 51–73, Jun. 2007, ISSN: 1567-8822. DOI: 10.1007/s10558-007-9031-y.

[63] *OpenStax*.

[64] A. F. H. McCaslin, B. R. Chen, A. J. Radosevich, B. Cauli, and E. M. C. Hillman, "*in vivo* 3D Morphology of Astrocyte—Vasculature Interactions in the Somatosensory Cortex: Implications for Neurovascular Coupling," en, *Journal of Cerebral Blood Flow & Metabolism*, vol. 31, no. 3, pp. 795–806, Mar. 2011, ISSN: 0271-678X, 1559-7016. DOI: 10.1038/jcbfm.2010.204.

[65] T. Köppl and B. Wohlmuth, "Optimal A Priori Error Estimates for an Elliptic Problem with Dirac Right-Hand Side," en, *SIAM Journal on Numerical Analysis*, vol. 52, no. 4, pp. 1753–1769, Jan. 2014, ISSN: 0036-1429, 1095-7170. DOI: 10.1137/130927619.

[66] S. Sakadžić, E. T. Mandeville, L. Gagnon, *et al.*, "Large arteriolar component of oxygen delivery implies a safe margin of oxygen supply to cerebral tissue," en, *Nature Communications*, vol. 5, no. 1, p. 5734, Dec. 2014, ISSN: 2041-1723. DOI: 10.1038/ncomms6734.

[67] I. G. Gould, P. Tsai, D. Kleinfeld, and A. Linninger, "The capillary bed offers the largest hemodynamic resistance to the cortical blood supply," en, *Journal of Cerebral Blood Flow & Metabolism*, vol. 37, no. 1, pp. 52–68, Jan. 2017, ISSN: 0271-678X, 1559-7016. DOI: 10.1177/0271678X16671146.

[68] N. Nishimura, C. B. Schaffer, B. Friedman, P. D. Lyden, and D. Kleinfeld, "Penetrating arterioles are a bottleneck in the perfusion of neocortex," en, *Proceedings of the National Academy of Sciences*, vol. 104, no. 1, pp. 365–370, Jan. 2007, ISSN: 0027-8424, 1091-6490. DOI: 10.1073/pnas.0609551104.

[69] F. Lauwers, F. Cassot, V. Lauwers-Cances, P. Puwanarajah, and H. Duvernoy, "Morphometry of the human cerebral cortex microcirculation: General characteristics and space-related profiles," en, *NeuroImage*, vol. 39, no. 3, pp. 936–948, Feb. 2008, ISSN: 10538119. DOI: 10.1016/j.neuroimage.2007.09.024.

[70] D. E. Sims, "The pericyte—A review," en, *Tissue and Cell*, vol. 18, no. 2, pp. 153–174, Jan. 1986, ISSN: 00408166. DOI: 10.1016/0040-8166(86)90026-1.

[71] S. Grubb, C. Cai, B. O. Hald, *et al.*, "Precapillary sphincters maintain perfusion in the cerebral cortex," en, *Nature Communications*, vol. 11, no. 1, p. 395, Jan. 2020, ISSN: 2041-1723. DOI: 10.1038/s41467-020-14330-z.

[72] R. I. Grant, D. A. Hartmann, R. G. Underly, A.-A. Berthiaume, N. R. Bhat, and A. Y. Shih, "Organizational hierarchy and structural diversity of microvascular pericytes in adult mouse cortex," en, *Journal of Cerebral Blood Flow & Metabolism*, vol. 39, no. 3, pp. 411–425, Mar. 2019, ISSN: 0271-678X, 1559-7016. DOI: 10.1177/0271678X17732229.

[73] X. Ji, T. Ferreira, B. Friedman, *et al.*, "Brain microvasculature has a common topology with local differences in geometry that match metabolic load," en, *Neuron*, vol. 109, no. 7, 1168–1187.e13, Apr. 2021, ISSN: 08966273. DOI: 10.1016/j.neuron.2021.02.006.

[74] A. Armulik, G. Genové, and C. Betsholtz, "Pericytes: Developmental, Physiological, and Pathological Perspectives, Problems, and Promises," en, *Developmental Cell*, vol. 21, no. 2, pp. 193–215, Aug. 2011, ISSN: 15345807. DOI: 10.1016/j.devcel.2011.07.001.

[75] R. Hill, L. Tong, P. Yuan, S. Murikinati, S. Gupta, and J. Grutzendler, "Regional Blood Flow in the Normal and Ischemic Brain Is Controlled by Arteriolar Smooth Muscle Cell Contractility and Not by Capillary Pericytes," en, *Neuron*, vol. 87, no. 1, pp. 95–110, Jul. 2015, ISSN: 08966273. DOI: 10.1016/j.neuron.2015.06.001.

[76] T. Lovick, L. Brown, and B. Key, "Neurovascular relationships in hippocampal slices: Physiological and anatomical studies of mechanisms underlying flow-metabolism coupling in intraparenchymal microvessels," en, *Neuroscience*, vol. 92, no. 1, pp. 47–60, Aug. 1999, ISSN: 03064522. DOI: 10.1016/S0306-4522(98)00737-4.

[77] C. M. Peppiatt, C. Howarth, P. Mobbs, and D. Attwell, "Bidirectional control of CNS capillary diameter by pericytes," en, *Nature*, vol. 443, no. 7112, pp. 700–704, Oct. 2006, ISSN: 0028-0836, 1476-4687. DOI: 10.1038/nature05193.

[78] N. Harel, S.-P. Lee, T. Nagaoka, D.-S. Kim, and S.-G. Kim, "Origin of Negative Blood Oxygenation Level—Dependent fMRI Signals," en, *Journal of Cerebral Blood Flow & Metabolism*, vol. 22, no. 8, pp. 908–917, Aug. 2002, ISSN: 0271-678X, 1559-7016. DOI: 10.1097/00004647-200208000-00002.

[79] S. J. Payne and W. K. El-Bouri, "Modelling dynamic changes in blood flow and volume in the cerebral vasculature," eng, *NeuroImage*, vol. 176, pp. 124–137, Aug. 2018, ISSN: 1095-9572. DOI: 10.1016/j.neuroimage.2018.04.037.

[80] R Aaslid, K. F. Lindegaard, W Sorteberg, and H Nornes, "Cerebral autoregulation dynamics in humans.," en, *Stroke*, vol. 20, no. 1, pp. 45–52, Jan. 1989, ISSN: 0039-2499, 1524-4628. DOI: 10.1161/01.STR.20.1.45.

[81] S. Payne, *Cerebral blood flow and metabolism: a quantitative approach*. New Jersey: World Scientific, 2018, ISBN: 9789813220560.

[82] S. Payne, "Identifying the myogenic and metabolic components of cerebral autoregulation," en, *Medical Engineering & Physics*, vol. 58, pp. 23–30, Aug. 2018, ISSN: 13504533. DOI: 10.1016/j.medengphy.2018.04.018.

[83] A. Silverman and N. H. Petersen, "Physiology, Cerebral Autoregulation," eng, in *StatPearls*, Treasure Island (FL): StatPearls Publishing, 2023.

[84] Y. C. Fung, *Biomechanics: circulation*, 2nd ed. New York: Springer, 1997, ISBN: 9780387943848.

[85] T. C. Gasser, *Vascular Biomechanics: Concepts, Models, and Applications*, en. Cham: Springer International Publishing, 2021, ISBN: 9783030709655 9783030709662. DOI: 10.1007/978-3-030-70966-2.

[86] B. Spronck, E. G. H. J. Martens, E. D. Gommer, and F. N. van de Vosse, "A lumped parameter model of cerebral blood flow control combining cerebral autoregulation and neurovascular coupling," en, *American Journal of Physiology-Heart and Circulatory Physiology*, vol. 303, no. 9, H1143–H1153, Nov. 2012, ISSN: 0363-6135, 1522-1539. DOI: 10.1152/ajpheart.00303.2012.

[87] A. A. Phillips, F. H. Chan, M. M. Z. Zheng, A. V. Krassioukov, and P. N. Ainslie, "Neurovascular coupling in humans: Physiology, methodological advances and clinical implications," en, *Journal of Cerebral Blood Flow & Metabolism*, vol. 36, no. 4, pp. 647–664, Apr. 2016, ISSN: 0271-678X, 1559-7016. DOI: 10.1177/0271678X15617954.

[88] R. Zhang, J. H. Zuckerman, K. Iwasaki, T. E. Wilson, C. G. Crandall, and B. D. Levine, "Autonomic Neural Control of Dynamic Cerebral Autoregulation in Humans," en, *Circulation*, vol. 106, no. 14, pp. 1814–1820, Oct. 2002, ISSN: 0009-7322, 1524-4539. DOI: 10.1161/01.CIR.0000031798.07790.FE.

[89] J. W. Hamner, C. O. Tan, Y.-C. Tzeng, and J. A. Taylor, "Cholinergic control of the cerebral vasculature in humans: Cholinergic control of the cerebral vasculature," en, *The Journal of Physiology*, vol. 590, no. 24, pp. 6343–6352, Dec. 2012, ISSN: 00223751. DOI: 10.1113/jphysiol.2012.245100.

[90] S. Ogoh, R. M. Brothers, W. L. Eubank, and P. B. Raven, "Autonomic Neural Control of the Cerebral Vasculature: Acute Hypotension," en, *Stroke*, vol. 39, no. 7, pp. 1979–1987, Jul. 2008, ISSN: 0039-2499, 1524-4628. DOI: 10.1161/STROKEAHA.107.510008.

[91] D. W. Busija and D. D. Heistad, "Factors involved in the physiological regulation of the cerebral circulation," en, in *Reviews of Physiology, Biochemistry and Pharmacology, Volume 86*, R. H. Adrian, E. Helmreich, H. Holzer, *et al.*, Eds., vol. 86, Berlin, Heidelberg: Springer Berlin Heidelberg, 1984, pp. 161–211, ISBN: 9783540094883 9783540352105. DOI: 10.1007/BFb0027696.

[92] P. N. Ainslie and J. Duffin, "Integration of cerebrovascular CO_2 reactivity and chemoreflex control of breathing: Mechanisms of regulation, measurement, and interpretation," en, *American Journal of Physiology-Regulatory, Integrative and Comparative Physiology*, vol. 296, no. 5, R1473–R1495, May 2009, ISSN: 0363-6119, 1522-1490. DOI: 10.1152/ajpregu.91008.2008.

[93] J. J. Van Lieshout and N. H. Secher, "Point:Counterpoint: Sympathetic activity does/does not influence cerebral blood flow," en, *Journal of Applied Physiology*, vol. 105, no. 4, pp. 1364–1366, Oct. 2008, ISSN: 8750-7587, 1522-1601. DOI: 10.1152/japplphysiol.90597.2008.

[94] L. Dean, "Blood and the cells it contains," en, in *Blood Groups and Red Cell Antigens* [*Internet*], National Center for Biotechnology Information (US), 2005.

[95] C. G. Caro, *The mechanics of the circulation*, English. Cambridge; New York: Cambridge University Press, 2012, OCLC: 1153535246.

[96] S. Reitsma, D. W. Slaaf, H. Vink, M. A. M. J. van Zandvoort, and M. G. A. oude Egbrink, "The endothelial glycocalyx: Composition, functions, and visualization," en, *Pflügers Archiv - European Journal of Physiology*, vol. 454, no. 3, pp. 345–359, Jun. 2007, ISSN: 1432-2013. DOI: 10.1007/s00424-007-0212-8.

[97] A. R. Pries and T. W. Secomb, "Microvascular blood viscosity in vivo and the endothelial surface layer," eng, *American Journal of Physiology. Heart and Circulatory Physiology*, vol. 289, no. 6, H2657–2664, Dec. 2005, ISSN: 0363-6135. DOI: 10.1152/ajpheart.00297.2005.

[98] R. Fåhræus and T. Lindqvist, "THE VISCOSITY OF THE BLOOD IN NARROW CAPILLARY TUBES," en, *American Journal of Physiology-Legacy Content*, vol. 96, no. 3, pp. 562–568, Mar. 1931, ISSN: 0002-9513. DOI: 10.1152/ajplegacy.1931.96.3.562.

[99] A. R. Pries, D. Neuhaus, and P. Gaehtgens, "Blood viscosity in tube flow: Dependence on diameter and hematocrit," en, *American Journal of Physiology-Heart and Circulatory Physiology*, vol. 263, no. 6, H1770–H1778, Dec. 1992, ISSN: 0363-6135, 1522-1539. DOI: 10.1152/ajpheart.1992.263.6.H1770.

[100] A Pries, "Biophysical aspects of blood flow in the microvasculature," en, *Cardiovascular Research*, vol. 32, no. 4, pp. 654–667, Oct. 1996, ISSN: 00086363. DOI: 10.1016/0008-6363(96)00065-X.

[101] R. Fåhraeus, "THE SUSPENSION STABILITY OF THE BLOOD," en, *Physiological Reviews*, vol. 9, no. 2, pp. 241–274, Apr. 1929, ISSN: 0031-9333, 1522-1210. DOI: 10.1152/physrev.1929.9.2.241.

[102] T.-R. Lee, S. S. Yoo, and J. Yang, "Generalized plasma skimming model for cells and drug carriers in the microvasculature," en, *Biomechanics and Modeling in Mechanobiology*, vol. 16, no. 2, pp. 497–507, Apr. 2017, ISSN: 1617-7940. DOI: 10.1007/s10237-016-0832-z.

[103] D. A. Boas, S. R. Jones, A. Devor, T. J. Huppert, and A. M. Dale, "A vascular anatomical network model of the spatio-temporal response to brain activation," en, *NeuroImage*, vol. 40, no. 3, pp. 1116–1129, Apr. 2008, ISSN: 10538119. DOI: 10.1016/j.neuroimage.2007.12.061.

[104] L. Grinberg, E. Cheever, T. Anor, J. R. Madsen, and G. E. Karniadakis, "Modeling blood flow circulation in intracranial arterial networks: A comparative 3D/1D simulation study," eng, *Annals of Biomedical Engineering*, vol. 39, no. 1, pp. 297–309, Jan. 2011, ISSN: 1573-9686. DOI: 10.1007/s10439-010-0132-1.

[105] M. Ursino and C. A. Lodi, "A simple mathematical model of the interaction between intracranial pressure and cerebral hemodynamics," en, *Journal of Applied Physiology*, vol. 82, no. 4, pp. 1256–1269, Apr. 1997, ISSN: 8750-7587, 1522-1601. DOI: 10.1152/jappl.1997.82.4.1256.

[106] E. Boileau, P. Nithiarasu, P. J. Blanco, *et al.*, "A benchmark study of numerical schemes for one-dimensional arterial blood flow modelling," eng, *International Journal for Numerical Methods in Biomedical Engineering*, vol. 31, no. 10, Oct. 2015, ISSN: 2040-7947. DOI: 10.1002/cnm.2732.

[107] K. S. Matthys, J. Alastruey, J. Peiró, *et al.*, "Pulse wave propagation in a model human arterial network: Assessment of 1-D numerical simulations against in vitro measurements," eng, *Journal of Biomechanics*, vol. 40, no. 15, pp. 3476–3486, 2007, ISSN: 0021-9290. DOI: 10.1016/j.jbiomech.2007.05.027.

[108] P. Reymond, F. Merenda, F. Perren, D. Rüfenacht, and N. Stergiopulos, "Validation of a one-dimensional model of the systemic arterial tree," en, *American Journal of Physiology-Heart and Circulatory Physiology*, vol. 297, no. 1, H208–H222, Jul. 2009, ISSN: 0363-6135, 1522-1539. DOI: 10.1152/ajpheart.00037.2009.

[109] X. Wang, "1D modeling of blood flow in networks : Numerical computing and applications," PhD Thesis, L'UNIVERSIT´E PIERRE ET MARIE CURIE - Paris VI, Paris, France, Oct. 2014.

[110] L. Formaggia, D. Lamponi, and A. Quarteroni, "One-dimensional models for blood flow in arteries," en, *Journal of Engineering Mathematics*, vol. 47, no. 3/4, pp. 251–276, Dec. 2003, ISSN: 0022-0833. DOI: 10.1023/B:ENGI.0000007980.01347.29.

[111] Y. Shi, P. Lawford, and R. Hose, "Review of Zero-D and 1-D Models of Blood Flow in the Cardiovascular System," *BioMedical Engineering OnLine*, vol. 10, no. 1, p. 33, Apr. 2011, ISSN: 1475-925X. DOI: 10.1186/1475-925X-10-33.

[112] S. Sorek, J. Bear, and Z. Karni, "Resistances and compliances of a compartmental model of the cerebrovascular system," en, *Annals of Biomedical Engineering*, vol. 17, no. 1, pp. 1–12, Jan. 1989, ISSN: 0090-6964, 1573-9686. DOI: 10.1007/BF02364270.

[113] K. Chatterjee, C. M. Carman-Esparza, and J. M. Munson, "Methods to measure, model and manipulate fluid flow in brain," en, *Journal of Neuroscience Methods*, vol. 333, p. 108 541, Mar. 2020, ISSN: 01650270. DOI: 10.1016/j.jneumeth.2019.108541.

[114] R. B. Buxton, K. Uludağ, D. J. Dubowitz, and T. T. Liu, "Modeling the hemodynamic response to brain activation," en, *NeuroImage*, vol. 23, S220–S233, Jan. 2004, ISSN: 10538119. DOI: 10.1016/j.neuroimage.2004.07.013.

[115] J. B. Mandeville, J. J. A. Marota, C. Ayata, *et al.*, "Evidence of a Cerebrovascular Postarteriole Windkessel with Delayed Compliance," en, *Journal of Cerebral Blood Flow & Metabolism*, vol. 19, no. 6, pp. 679–689, Jun. 1999, ISSN: 0271-678X, 1559-7016. DOI: 10.1097/00004647-199906000-00012.

[116] M. Banaji, I. Tachtsidis, D. Delpy, and S. Baigent, "A physiological model of cerebral blood flow control," en, *Mathematical Biosciences*, vol. 194, no. 2, pp. 125–173, Apr. 2005, ISSN: 00255564. DOI: 10.1016/j.mbs.2004.10.005.

[117] F. Kennedy McConnell and S. Payne, "The Dual Role of Cerebral Autoregulation and Collateral Flow in the Circle of Willis After Major Vessel Occlusion," *IEEE Transactions on Biomedical Engineering*, vol. 64, no. 8, pp. 1793–1802, Aug. 2017, ISSN: 0018-9294, 1558-2531. DOI: 10.1109/TBME.2016.2623710.

[118] R. Lampe, N. Botkin, V. Turova, T. Blumenstein, and A. Alves-Pinto, "Mathematical Modelling of Cerebral Blood Circulation and Cerebral Autoregulation: Towards Preventing Intracranial Hemorrhages in Preterm Newborns," en, *Computational and Mathematical Methods in Medicine*, vol. 2014, pp. 1–9, 2014, ISSN: 1748-670X, 1748-6718. DOI: 10.1155/2014/965275.

[119] S. Payne, "A model of the interaction between autoregulation and neural activation in the brain," en, *Mathematical Biosciences*, vol. 204, no. 2, pp. 260–281, Dec. 2006, ISSN: 00255564. DOI: 10.1016/j.mbs.2006.08.006.

[120] M. Ursino, "A mathematical study of human intracranial hydrodynamics part 1—The cerebrospinal fluid pulse pressure," en, *Annals of Biomedical Engineering*, vol. 16, no. 4, pp. 379–401, Jul. 1988, ISSN: 0090-6964, 1573-9686. DOI: 10.1007/BF02364625.

[121] M. Ursino and P. Di Giammarco, "A mathematical model of the relationship between cerebral blood volume and intracranial pressure changes: The generation of plateau waves," en, *Annals of Biomedical Engineering*, vol. 19, no. 1, pp. 15–42, Jan. 1991, ISSN: 1573-9686. DOI: 10.1007/BF02368459.

[122] M. Ursino and C. A. Lodi, "Interaction among autoregulation, CO_2 reactivity, and intracranial pressure: A mathematical model," en, *American Journal of Physiology-Heart and Circulatory Physiology*, vol. 274, no. 5, H1715–H1728, May 1998, ISSN: 0363-6135, 1522-1539. DOI: 10.1152/ajpheart.1998.274.5.H1715.

[123] M. Ursino, A. Ter Minassian, C. A. Lodi, and L. Beydon, "Cerebral hemodynamics during arterial and CO_2 pressure changes: In vivo prediction by a mathematical model," en, *American Journal of Physiology-Heart and Circulatory Physiology*, vol. 279, no. 5, H2439–H2455, Nov. 2000, ISSN: 0363-6135, 1522-1539. DOI: 10.1152/ajpheart.2000.279.5.H2439.

[124] J. Yang, J. W. Clark, R. M. Bryan, and C. S. Robertson, "The myogenic response in isolated rat cerebrovascular arteries: Vessel model," en, *Medical Engineering & Physics*, vol. 25, no. 8, pp. 711–717, Oct. 2003, ISSN: 13504533. DOI: 10.1016/S1350-4533(03)00101-2.

[125] C. Francis, L. Frederic, L. Sylvie, P. Prasanna, and D. Henri, "Scaling Laws for Branching Vessels of Human Cerebral Cortex," en, *Microcirculation*, vol. 16, no. 4, pp. 331–344, Jan. 2009, ISSN: 1073-9688, 1549-8719. DOI: 10.1080/10739680802662607.

[126] S. Lorthois, F. Cassot, and F. Lauwers, "Simulation study of brain blood flow regulation by intra-cortical arterioles in an anatomically accurate large human vascular network: Part I: Methodology and baseline flow," en, *NeuroImage*, vol. 54, no. 2, pp. 1031–1042, Jan. 2011, ISSN: 10538119. DOI: 10.1016/j.neuroimage.2010.09.032.

[127] W. K. El-Bouri and S. J. Payne, "Investigating the effects of a penetrating vessel occlusion with a multi-scale microvasculature model of the human cerebral cortex," en, *NeuroImage*, vol. 172, pp. 94–106, May 2018, ISSN: 10538119. DOI: 10.1016/j.neuroimage.2018.01.049.

[128] R. J. Shipley and S. J. Chapman, "Multiscale Modelling of Fluid and Drug Transport in Vascular Tumours," en, *Bulletin of Mathematical Biology*, vol. 72, no. 6, pp. 1464–1491, Aug. 2010, ISSN: 0092-8240, 1522-9602. DOI: 10.1007/s11538-010-9504-9.

[129] T. I. Józsa, R. M. Padmos, W. K. El-Bouri, A. G. Hoekstra, and S. J. Payne, "On the Sensitivity Analysis of Porous Finite Element Models for Cerebral Perfusion Estimation," en, *Annals of Biomedical Engineering*, vol. 49, no. 12, pp. 3647–3665, Dec. 2021, ISSN: 1573-9686. DOI: 10.1007/s10439-021-02808-w.

[130] S. Lorthois and F. Cassot, "Fractal analysis of vascular networks: Insights from morphogenesis," en, *Journal of Theoretical Biology*, vol. 262, no. 4, pp. 614–633, Feb. 2010, ISSN: 00225193. DOI: 10.1016/j.jtbi.2009.10.037.

[131] A. F. Smith, V. Doyeux, M. Berg, *et al.*, "Brain Capillary Networks Across Species: A few Simple Organizational Requirements Are Sufficient to Reproduce Both Structure and Function," *Frontiers in Physiology*, vol. 10, 2019, ISSN: 1664-042X.

[132] P. Blinder, P. S. Tsai, J. P. Kaufhold, P. M. Knutsen, H. Suhl, and D. Kleinfeld, "The cortical angiome: An interconnected vascular network with noncolumnar patterns of blood flow," en, *Nature Neuroscience*, vol. 16, no. 7, pp. 889–897, Jul. 2013, ISSN: 1097-6256, 1546-1726. DOI: 10.1038/nn.3426.

[133] M. Peyrounette, Y. Davit, M. Quintard, and S. Lorthois, "Multiscale modelling of blood flow in cerebral microcirculation: Details at capillary scale control accuracy at the level of the cortex," en, *PLOS ONE*, vol. 13, no. 1, J. Boltze, Ed., e0189474, Jan. 2018, ISSN: 1932-6203. DOI: 10.1371/journal.pone.0189474.

[134] B. J. Kim, S. M. Kim, D.-W. Kang, S. U. Kwon, D. C. Suh, and J. S. Kim, "Vascular Tortuosity May Be Related to Intracranial Artery Atherosclerosis," en, *International Journal of Stroke*, vol. 10, no. 7, pp. 1081–1086, Oct. 2015, ISSN: 1747-4930, 1747-4949. DOI: 10.1111/ijs.12525.

[135] A. Deshpande, J. Elliott, N. Kari, *et al.*, "Novel imaging markers for altered cerebrovascular morphology in aging, stroke, and Alzheimer's disease," eng, *Journal of Neuroimaging: Official Journal of the American Society of Neuroimaging*, vol. 32, no. 5, pp. 956–967, Sep. 2022, ISSN: 1552-6569. DOI: 10.1111/jon.13023.

[136] J. Gutierrez, K. Cheung, A. Bagci, *et al.*, "Brain Arterial Diameters as a Risk Factor for Vascular Events," en, *Journal of the American Heart Association*, vol. 4, no. 8, e002289, Aug. 2015, ISSN: 2047-9980. DOI: 10.1161/JAHA.115.002289.

[137] A. Ergul, W. Li, M. M. Elgebaly, A. Bruno, and S. C. Fagan, "Hyperglycemia, diabetes and stroke: Focus on the cerebrovasculature," *Vascular Pharmacology*, vol. 51, no. 1, pp. 44–49, Jul. 2009, ISSN: 1537-1891. DOI: 10.1016/j.vph.2009.02.004.

[138] S. B. Cox, T. A. Woolsey, and C. M. Rovainen, "Localized Dynamic Changes in Cortical Blood Flow with Whisker Stimulation Corresponds to Matched Vascular and Neuronal Architecture of Rat Barrels," en, *Journal of Cerebral Blood Flow & Metabolism*, vol. 13, no. 6, pp. 899–913, Nov. 1993, ISSN: 0271-678X, 1559-7016. DOI: 10.1038/jcbfm.1993.113.

[139] A. Devor, P. Tian, N. Nishimura, *et al.*, "Suppressed Neuronal Activity and Concurrent Arteriolar Vasoconstriction May Explain Negative Blood Oxygenation Level-Dependent Signal," en, *Journal of Neuroscience*, vol. 27, no. 16, pp. 4452–4459, Apr. 2007, ISSN: 0270-6474, 1529-2401. DOI: 10.1523/JNEUROSCI.0134-07.2007.

[140] A. Shmuel, E. Yacoub, J. Pfeuffer, *et al.*, "Sustained Negative BOLD, Blood Flow and Oxygen Consumption Response and Its Coupling to the Positive Response in the Human Brain," en, *Neuron*, vol. 36, no. 6, pp. 1195–1210, Dec. 2002, ISSN: 08966273. DOI: 10.1016/S0896-6273(02)01061-9.

[141] S. N. Jespersen and L. Østergaard, "The Roles of Cerebral Blood Flow, Capillary Transit Time Heterogeneity, and Oxygen Tension in Brain Oxygenation and Metabolism," en, *Journal of Cerebral Blood Flow & Metabolism*, vol. 32, no. 2, pp. 264–277, Feb. 2012, ISSN: 0271-678X, 1559-7016. DOI: 10.1038/jcbfm.2011.153.

[142] B. Li, T. V. Esipova, I. Sencan, *et al.*, "More homogeneous capillary flow and oxygenation in deeper cortical layers correlate with increased oxygen extraction," en, *eLife*, vol. 8, e42299, Jul. 2019, ISSN: 2050-084X. DOI: 10.7554/eLife.42299.

[143] S. F. Eskildsen, L. Gyldensted, K. Nagenthiraja, *et al.*, "Increased cortical capillary transit time heterogeneity in Alzheimer's disease: A DSC-MRI perfusion study," en, *Neurobiology of Aging*, vol. 50, pp. 107–118, Feb. 2017, ISSN: 01974580. DOI: 10.1016/j.neurobiolaging.2016.11.004.

[144] M. Arango-Lievano, B. Boussadia, L. D. T. De Terdonck, *et al.*, "Topographic Reorganization of Cerebrovascular Mural Cells under Seizure Conditions," en, *Cell Reports*, vol. 23, no. 4, pp. 1045–1059, Apr. 2018, ISSN: 22111247. DOI: 10.1016/j.celrep.2018.03.110.

[145] J.-M. Fullana and S. Zaleski, "A branched one-dimensional model of vessel networks," en, *Journal of Fluid Mechanics*, vol. 621, pp. 183–204, Feb. 2009, ISSN: 1469-7645, 0022-1120. DOI: 10.1017/S0022112008004771.

[146] D. Burkhoff, J. Alexander, and J. Schipke, "Assessment of Windkessel as a model of aortic input impedance," en, *American Journal of Physiology-Heart and Circulatory Physiology*, vol. 255, no. 4, H742–H753, Oct. 1988, ISSN: 0363-6135, 1522-1539. DOI: 10.1152/ajpheart.1988.255.4.H742.

[147] A. S. Olufsen, *Modeling the arterial system with reference to an anesthesia simulator* (Tekster fra IMFUFA). Roskilde: Roskilde Universitet, 1998.

[148] M. S. Olufsen, "Structured tree outflow condition for blood flow in larger systemic arteries," en, *American Journal of Physiology-Heart and Circulatory Physiology*, vol. 276, no. 1, H257–H268, Jan. 1999, ISSN: 0363-6135, 1522-1539. DOI: 10.1152/ajpheart.1999.276.1.H257.

[149] A. P. Avolio, "Multi-branched model of the human arterial system," en, *Medical and Biological Engineering and Computing*, vol. 18, no. 6, pp. 709–718, Nov. 1980, ISSN: 1741-0444. DOI: 10.1007/BF02441895.

[150] Y. Zheng, D. Johnston, J. Berwick, D. Chen, S. Billings, and J. Mayhew, "A three-compartment model of the hemodynamic response and oxygen delivery to brain," en, *NeuroImage*, vol. 28, no. 4, pp. 925–939, Dec. 2005, ISSN: 10538119. DOI: 10.1016/j.neuroimage.2005.06.042.

[151] T. J. Huppert, M. S. Allen, H. Benav, P. B. Jones, and D. A. Boas, "A Multicompartment Vascular Model for Inferring Baseline and Functional Changes in Cerebral Oxygen Metabolism and Arterial Dilation," en, *Journal of Cerebral Blood Flow & Metabolism*, vol. 27, no. 6, pp. 1262–1279, Jun. 2007, ISSN: 0271-678X, 1559-7016. DOI: 10.1038/sj.jcbfm.9600435.

[152] H. F. Frasch, J. Y. Kresh, and A. Noordergraaf, "Two-port analysis of microcirculation: An extension of windkessel," en, *American Journal of Physiology-Heart and Circulatory Physiology*, vol. 270, no. 1, H376–H385, Jan. 1996, ISSN: 0363-6135, 1522-1539. DOI: 10.1152/ajpheart.1996.270.1.H376.

[153] S. Epstein, M. Willemet, P. J. Chowienczyk, and J. Alastruey, "Reducing the number of parameters in 1D arterial blood flow modeling: Less is more for patient-specific simulations," en, *American Journal of Physiology-Heart and Circulatory Physiology*, vol. 309, no. 1, H222–H234, Jul. 2015, ISSN: 0363-6135, 1522-1539. DOI: 10.1152/ajpheart.00857.2014.

[154] H. A. Kontos, E. P. Wei, R. M. Navari, J. E. Levasseur, W. I. Rosenblum, and J. L. Patterson, "Responses of cerebral arteries and arterioles to acute hypotension and hypertension," eng, *The American Journal of Physiology*, vol. 234, no. 4, H371–383, Apr. 1978, ISSN: 0002-9513. DOI: 10.1152/ajpheart.1978.234.4.H371.

[155] L. Kuo, W. M. Chilian, and M. J. Davis, "Interaction of pressure- and flow-induced responses in porcine coronary resistance vessels," *American Journal of Physiology-Heart and Circulatory Physiology*, vol. 261, no. 6, H1706–H1715, Dec. 1991, ISSN: 0363-6135. DOI: 10.1152/ajpheart.1991.261.6.H1706.

[156] F. A. Garcia, D. L. Spavieri, and A. Linninger, "Cerebral hemodynamics: A mathematical model including autoregulation, baroreflex and extracranial peripheral circulation," Journal Article, Jun. 2021.

[157] G. L. Baumbach and D. D. Heistad, "Regional, segmental, and temporal heterogeneity of cerebral vascular autoregulation," en, *Annals of Biomedical Engineering*, vol. 13, no. 3-4, pp. 303–310, May 1985, ISSN: 0090-6964, 1573-9686. DOI: 10.1007/BF02584248.

[158] A. R. Pries, T. W. Secomb, and P. Gaehtgens, "Structure and hemodynamics of microvascular networks: Heterogeneity and correlations," en, *American Journal of Physiology-Heart and Circulatory Physiology*, vol. 269, no. 5, H1713–H1722, Nov. 1995, ISSN: 0363-6135, 1522-1539. DOI: 10.1152/ajpheart.1995.269.5.H1713.

[159] L. Gagnon, A. F. Smith, D. A. Boas, A. Devor, T. W. Secomb, and S. Sakadžić, "Modeling of Cerebral Oxygen Transport Based on In vivo Microscopic Imaging of Microvascular Network Structure, Blood Flow, and Oxygenation," *Frontiers in Computational Neuroscience*, vol. 10, Aug. 2016, ISSN: 1662-5188. DOI: 10.3389/fncom.2016.00082.

[160] M. A. Horsfield, J. L. Jara, N. P. Saeed, R. B. Panerai, and T. G. Robinson, "Regional Differences in Dynamic Cerebral Autoregulation in the Healthy Brain Assessed by Magnetic Resonance Imaging," *PLoS ONE*, vol. 8, no. 4, e62588, Apr. 2013, ISSN: 1932-6203. DOI: 10.1371/journal.pone.0062588.

[161] E. T. MacKenzie, S Strandgaard, D. I. Graham, J. V. Jones, A. M. Harper, and J. K. Farrar, "Effects of acutely induced hypertension in cats on pial arteriolar caliber, local cerebral blood flow, and the blood-brain barrier.," en, *Circulation Research*, vol. 39, no. 1, pp. 33–41, Jul. 1976, ISSN: 0009-7330, 1524-4571. DOI: 10.1161/01.RES.39.1.33.

[162] E. T. MacKenzie, J. K. Farrar, W Fitch, D. I. Graham, P. C. Gregory, and A. M. Harper, "Effects of hemorrhagic hypotension on the cerebral circulation. I. Cerebral blood flow and pial arteriolar caliber.," en, *Stroke*, vol. 10, no. 6, pp. 711–718, Nov. 1979, ISSN: 0039-2499, 1524-4628. DOI: 10.1161/01.STR.10.6.711.

[163] L. Gagnon, S. Sakad i , F. Lesage, *et al.*, "Quantifying the Microvascular Origin of BOLD-fMRI from First Principles with Two-Photon Microscopy and an Oxygen-Sensitive Nanoprobe," en, *Journal of Neuroscience*, vol. 35, no. 8, pp. 3663–3675, Feb. 2015, ISSN: 0270-6474, 1529-2401. DOI: 10.1523/JNEUROSCI.3555-14.2015.

[164] R. Chaudhry, J. H. Miao, and A. Rehman, "Physiology, Cardiovascular," eng, in *StatPearls*, Treasure Island (FL): StatPearls Publishing, 2022.

[165] S. Milanovic, K. Shaw, C. Hall, and S. Payne, "Investigating the role of pericytes in cerebral autoregulation: A modeling study," *Physiological Measurement*, vol. 42, no. 5, p. 054 003, May 2021, ISSN: 0967-3334, 1361-6579. DOI: 10.1088/1361-6579/abfb0a.

[166] F. M. Faraci and D. D. Heistad, "Regulation of the Cerebral Circulation: Role of Endothelium and Potassium Channels," en, *Physiological Reviews*, vol. 78, no. 1, pp. 53–97, Jan. 1998, ISSN: 0031-9333, 1522-1210. DOI: 10.1152/physrev.1998.78.1.53.

[167] B. Folkow, "DESCRIPTION OF THE MYOGENIC HYPOTHESIS," eng, *Circulation Research*, vol. 15, SUPPL:279–287, Aug. 1964, ISSN: 0009-7330.

[168] S. CaniC and E. H. Kim, "Mathematical analysis of the quasilinear effects in a hyperbolic model blood flow through compliant axi-symmetric vessels," en, *Mathematical Methods in the Applied Sciences*, vol. 26, no. 14, pp. 1161–1186, Sep. 2003, ISSN: 0170-4214, 1099-1476. DOI: 10.1002/mma.407.

[169] J. Flores, J. Alastruey, and E. Corvera Poiré, "A Novel Analytical Approach to Pulsatile Blood Flow in the Arterial Network," eng, *Annals of Biomedical Engineering*, vol. 44, no. 10, pp. 3047–3068, Oct. 2016, ISSN: 1573-9686. DOI: 10.1007/s10439-016-1625-3.

[170] M. S. Olufsen, C. S. Peskin, W. Y. Kim, E. M. Pedersen, A. Nadim, and J. Larsen, "Numerical Simulation and Experimental Validation of Blood Flow in Arteries with Structured-Tree Outflow Conditions," en, *Annals of Biomedical Engineering*, vol. 28, no. 11, pp. 1281–1299, Nov. 2000, ISSN: 1573-9686. DOI: 10.1114/1.1326031.

[171] R. Absi, "Revisiting the pressure-area relation for the flow in elastic tubes: Application to arterial vessels," English, *Series on Biomechanics, Bulgarian Academy of Sciences*, vol. 32, no. 1, pp. 47–59, 2018.

[172] S. Sherwin, V. Franke, J. Peiró, and K. Parker, "One-dimensional modelling of a vascular network in space-time variables," en, *Journal of Engineering Mathematics*, vol. 47, no. 3, pp. 217–250, Dec. 2003, ISSN: 1573-2703. DOI: 10.1023/B:ENGI.0000007979.32871.e2.

[173] V. E. Franke, K. H. Parker, L. Y. Wee, N. M. Fisk, and S. J. Sherwin, "Time domain computational modelling of 1D arterial networks in monochorionic placentas," en, *ESAIM: Mathematical Modelling and Numerical Analysis*, vol. 37, no. 4, pp. 557–580, Jul. 2003, ISSN: 0764-583X, 1290-3841. DOI: 10.1051/m2an:2003047.

[174] J. Alastruey Arimon, "Numerical modelling of pulse wave propagation in the cardiovascular system : Development, validation and clinical applications," eng, Jan. 2006.

[175] J. Alastruey, K. H. Parker, J. Peiró, S. M. Byrd, and S. J. Sherwin, "Modelling the circle of Willis to assess the effects of anatomical variations and occlusions on cerebral flows," eng, *Journal of Biomechanics*, vol. 40, no. 8, pp. 1794–1805, 2007, ISSN: 0021-9290. DOI: 10.1016/j.jbiomech.2006.07.008.

[176] M. Ursino, A. Fiorenzi, and E. Belardinelli, "The role of pressure pulsatility in the carotid baroreflex control: A computer simulation study," eng, *Computers in Biology and Medicine*, vol. 26, no. 4, pp. 297–314, Jul. 1996, ISSN: 0010-4825. DOI: 10.1016/0010-4825(96)00012-1.

[177] M. Chappell and S. Payne, *Physiology for engineers: applying engineering methods to physiological systems* (Biosystems & biorobotics Volume 13), eng. Cham: Springer, 2016, OCLC: 1011682652, ISBN: 9783319261959 9783319261973.

[178] Y. C. Fung, *Biomechanics: mechanical properties of living tissues*. New York: Springer-Verlag, 1981, ISBN: 9780387904726.

[179] G. Clough, P. A. Fraser, and L. H. Smaje, "Proceedings: Compliance measurement in single capillaries of the cat mesentery," eng, *The Journal of Physiology*, vol. 240, no. 2, 9P–11P, Jul. 1974, ISSN: 0022-3751.

[180] M. E. Murphy and P. C. Johnson, "Possible contribution of basement membrane to the structural rigidity of blood capillaries," en, *Microvascular Research*, vol. 9, no. 2, pp. 242–245, Mar. 1975, ISSN: 00262862. DOI: 10.1016/0026-2862(75)90084-9.

[181] L. H. Smaje, P. A. Fraser, and G. Clough, "The distensibility of single capillaries and venules in the cat mesentery," en, *Microvascular Research*, vol. 20, no. 3, pp. 358–370, Nov. 1980, ISSN: 0026-2862. DOI: 10.1016/0026-2862(80)90064-3.

[182] Q. Pan, R. Wang, B. Reglin, *et al.*, "A One-Dimensional Mathematical Model for Studying the Pulsatile Flow in Microvascular Networks," en, *Journal of Biomechanical Engineering*, vol. 136, no. 1, p. 011 009, Jan. 2014, ISSN: 0148-0731, 1528-8951. DOI: 10.1115/1.4025879.

[183] J. Seki, "Flow pulsation and network structure in mesenteric microvasculature of rats," en, *American Journal of Physiology-Heart and Circulatory Physiology*, vol. 266, no. 2, H811–H821, Feb. 1994, ISSN: 0363-6135, 1522-1539. DOI: 10.1152/ajpheart.1994.266.2.H811.

[184] A. G. Salotto, L. F. Muscarella, J. Melbin, J. K.-J. Li, and A. Noordergraaf, "Pressure pulse transmission into vascular beds," en, *Microvascular Research*, vol. 32, no. 2, pp. 152–163, Sep. 1986, ISSN: 00262862. DOI: 10.1016/0026-2862(86)90051-8.

[185] L. Formaggia, F. Nobile, A. Quarteroni, and A. Veneziani, "Multiscale modelling of the circulatory system: A preliminary analysis," en, *Computing and Visualization in Science*, vol. 2, no. 2, pp. 75–83, Dec. 1999, ISSN: 1433-0369. DOI: 10.1007/s007910050030.

[186] M. Saito, "One-dimensional modeling of pulse wave for a human artery model," Universite Pierre et Marie-Curie, Paris, France, Tech. Rep.

[187] R. W. MacCormack, "The Effect of Viscosity in Hypervelocity Impact Cratering," *Journal of Spacecraft and Rockets*, vol. 40, no. 5, pp. 757–763, 2003, ISSN: 0022-4650. DOI: 10.2514/2.6901.

[188] D. Griffiths and D. J. Higham, "MacCormack's method for advection-reaction equations," 2001.

[189] C. C. Mei, *Mathematical Analysis in Engineering: How to Use the Basic Tools*. Cambridge: Cambridge University Press, 1995, ISBN: 9780521587983. DOI: 10.1017/CBO9780511810749.

[190] L. C. Evans, *Partial differential equations* (Graduate studies in mathematics v. 19), 2nd ed. Providence, R.I: American Mathematical Society, 2010, OCLC: ocn465190110, ISBN: 9780821849743.

[191] J. W Thomas, *Numerical Partial Differential Equations: Conservation Laws and Elliptic Equations.* English. New York, NY: Springer, 2013, OCLC: 1076234752, ISBN: 9781461205692.

[192] A. Quarteroni and A. Valli, *Numerical approximation of partial differential equations: with 17 tables* (Springer series in computational mathematics 23), eng, 1. softcover printing. Berlin Heidelberg: Springer Series in Computational Mathematics, 1991, ISBN: 3540571116.

[193] A. G. Guaily and M. Epstein, "Boundary conditions for hyperbolic systems of partial differentials equations," en, *Journal of Advanced Research*, vol. 4, no. 4, pp. 321–329, Jul. 2013, ISSN: 2090-1232. DOI: 10.1016/j.jare.2012.05.006.

[194] E. Godlewski and P.-A. Raviart, *Numerical approximation of hyperbolic systems of conservation laws* (Applied mathematical sciences 118), English. Springer-Verlag, 1996, OCLC: 1159596324, ISBN: 0387945296.

[195] E. F. Toro, *Riemann solvers and numerical methods for fluid dynamics: a practical introduction*, 3rd ed. Dordrecht ; New York: Springer, 2009, OCLC: ocn401321914, ISBN: 9783540252023 9783540498346.

[196] R. J. LeVeque, *Finite Volume Methods for Hyperbolic Problems* (Cambridge Texts in Applied Mathematics). Cambridge: Cambridge University Press, 2002, ISBN: 9780521009249. DOI: 10.1017/CBO9780511791253.

[197] F. Dubois and P. Le Floch, "Boundary conditions for nonlinear hyperbolic systems of conservation laws," en, *Journal of Differential Equations*, vol. 71, no. 1, pp. 93–122, Jan. 1988, ISSN: 0022-0396. DOI: 10.1016/0022-0396(88)90040-X.

[198] S. J. Payne and C. Lucas, "Oxygen delivery from the cerebral microvasculature to tissue is governed by a single time constant of approximately 6 seconds," eng, *Microcirculation (New York, N.Y.: 1994)*, vol. 25, no. 2, Feb. 2018, ISSN: 1549-8719. DOI: 10.1111/micc.12428.

[199] D. Gottlieb, M. Gunzburger, and E. Turkel, "On Numerical Boundary Treatment of Hyperbolic Systems for Finite Difference and Finite Element Methods," *SIAM Journal on Numerical Analysis*, vol. 19, no. 4, pp. 671–682, Aug. 1982, ISSN: 0036-1429. DOI: 10.1137/0719047.

[200] C. Canuto and A. Quarteroni, "On the boundary treatment in spectral methods for hyperbolic systems," en, *Journal of Computational Physics*, vol. 71, no. 1, pp. 100–110, Jul. 1987, ISSN: 0021-9991. DOI: 10.1016/0021-9991(87)90021-0.

[201] T. Hagstrom and S. I. Hariharan, "Accurate boundary conditions for exterior problems in gas dynamics," en, *Mathematics of Computation*, vol. 51, no. 184, pp. 581–597, 1988, ISSN: 0025-5718, 1088-6842. DOI: 10.1090/S0025-5718-1988-0935075-7.

[202] C. Canuto, M. Y. Hussaini, A. Quarteroni, and T. A. Zang, *Spectral Methods in Fluid Dynamics*. Berlin, Heidelberg: Springer, 1988, ISBN: 9783540522058 9783642841088. DOI: 10.1007/978-3-642-84108-8.

[203] C. Grossmann, H.-G. Roos, and M. Stynes, *Numerical treatment of partial differential equations* (Universitext), eng. Berlin New York: Springer, 2007, ISBN: 9783540715849.

[204] A. Saltelli, M. Ratto, T. Andres, *et al.*, *Global Sensitivity Analysis: The Primer*, en. John Wiley & Sons, Feb. 2008, Google-Books-ID: wAssmt2vumgC, ISBN: 9780470725177.

[205] A. Saltelli, "Making best use of model evaluations to compute sensitivity indices," en, *Computer Physics Communications*, vol. 145, no. 2, pp. 280–297, May 2002, ISSN: 0010-4655. DOI: 10.1016/S0010-4655(02)00280-1.

[206] T. H. Jochimsen, R. D. Newbould, S. T. Skare, *et al.*, "Identifying systematic errors in quantitative dynamic-susceptibility contrast perfusion imaging by high-resolution multi-echo parallel EPI," *NMR in biomedicine*, vol. 20, no. 4, pp. 429–438, Jun. 2007, ISSN: 0952-3480. DOI: 10.1002/nbm.1107.

[207] G. Zaharchuk, "Theoretical Basis of Hemodynamic MR Imaging Techniques to Measure Cerebral Blood Volume, Cerebral Blood Flow, and Permeability," *AJNR: American Journal of Neuroradiology*, vol. 28, no. 10, pp. 1850–1858, Nov. 2007, ISSN: 0195-6108. DOI: 10.3174/ajnr.A0831.

[208] A. Mehndiratta, F. Calamante, B. J. MacIntosh, D. E. Crane, S. J. Payne, and M. A. Chappell, "Modeling and correction of bolus dispersion effects in dynamic susceptibility contrast MRI," en, *Magnetic Resonance in Medicine*, vol. 72, no. 6, pp. 1762–1774, Dec. 2014, ISSN: 0740-3194, 1522-2594. DOI: 10.1002/mrm.25077.

[209] J. Yang, J. W. Clark, R. M. Bryan, and C. Robertson, "The myogenic response in isolated rat cerebrovascular arteries: Smooth muscle cell model," en, *Medical Engineering & Physics*, vol. 25, no. 8, pp. 691–709, Oct. 2003, ISSN: 13504533. DOI: 10.1016/S1350-4533(03)00100-0.

[210] Y. Tardy, J. J. Meister, F. Perret, H. R. Brunner, and M. Arditi, "Non-invasive estimate of the mechanical properties of peripheral arteries from ultrasonic and photoplethysmographic measurements," eng, *Clinical Physics and Physiological Measurement: An Official Journal of the Hospital Physicists' Association, Deutsche Gesellschaft Fur Medizinische Physik and the European Federation of Organisations for Medical Physics*, vol. 12, no. 1, pp. 39–54, Feb. 1991, ISSN: 0143-0815. DOI: 10.1088/0143-0815/12/1/003.

[211] R. Fogliardi, M. Di Donfrancesco, and R. Burattini, "Comparison of linear and nonlinear formulations of the three-element windkessel model," eng, *The American Journal of Physiology*, vol. 271, no. 6 Pt 2, H2661–2668, Dec. 1996, ISSN: 0002-9513. DOI: 10.1152/ajpheart.1996.271.6.H2661.

[212] P. Segers, N. Stergiopulos, P. Verdonck, and R. Verhoeven, "Assessment of distributed arterial network models," eng, *Medical & Biological Engineering & Computing*, vol. 35, no. 6, pp. 729–736, Nov. 1997, ISSN: 0140-0118. DOI: 10.1007/BF02510985.

[213] T. Partington and A. Farmery, "Intracranial pressure and cerebral blood flow," English, *Anaesthesia & Intensive Care Medicine*, vol. 15, no. 4, pp. 189–194, Apr. 2014, ISSN: 1472-0299, 1878-7584. DOI: 10.1016/j.mpaic.2014.02.002.

[214] R. Guibert, C. Fonta, and F. Plouraboué, "Cerebral Blood Flow Modeling in Primate Cortex," en, *Journal of Cerebral Blood Flow & Metabolism*, vol. 30, no. 11, pp. 1860–1873, Nov. 2010, ISSN: 0271-678X, 1559-7016. DOI: 10.1038/jcbfm.2010.105.

[215] A. R. Pries, B. Reglin, and T. W. Secomb, "Structural response of microcirculatory networks to changes in demand: Information transfer by shear stress," en, *American Journal of Physiology-Heart and Circulatory Physiology*, vol. 284, no. 6, H2204–H2212, Jun. 2003, ISSN: 0363-6135, 1522-1539. DOI: 10.1152/ajpheart.00757.2002.

[216] E. Baraghis, V. Bolduc, J. Lefebvre, *et al.*, "Measurement of cerebral microvascular compliance in a model of atherosclerosis with optical coherence tomography," *Biomedical Optics Express*, vol. 2, no. 11, pp. 3079–3093, Oct. 2011, ISSN: 2156-7085. DOI: 10.1364/BOE.2.003079.

[217] E. Hodneland, E. Hanson, O. Sævareid, *et al.*, "A new framework for assessing subject-specific whole brain circulation and perfusion using MRI-based measurements and a multi-scale continuous flow model," en, *PLOS Computational Biology*, vol. 15, no. 6, e1007073, Jun. 2019, ISSN: 1553-7358. DOI: 10.1371/journal.pcbi.1007073.

[218] L. Chen, Y. Hannawi, and D. Terman, "Modeling the effect of cerebral capillary blood flow on neuronal firing," en, *Journal of Theoretical Biology*, vol. 537, p. 111 018, Mar. 2022, ISSN: 0022-5193. DOI: 10.1016/j.jtbi.2022.111018.

[219] Y. Zhao, C. Jiang, and A. Yang, "Towards a Generic Simulation Environment for Multiscale Modelling based on Tool Integration," en, in *Computer Aided Chemical Engineering*, ser. 21 European Symposium on Computer Aided Process Engineering, E. N. Pistikopoulos, M. C. Georgiadis, and A. C. Kokossis, Eds., vol. 29, Elsevier, Jan. 2011, pp. 76–80. DOI: 10.1016/B978-0-444-53711-9.50016-X.

[220] L. Formaggia, J. Gerbeau, F. Nobile, and A. Quarteroni, "On the coupling of 3D and 1D Navier–Stokes equations for flow problems in compliant vessels," en, *Computer Methods in Applied Mechanics and Engineering*, vol. 191, no. 6-7, pp. 561–582, Dec. 2001, ISSN: 00457825. DOI: 10.1016/S0045-7825(01)00302-4.

[221] H. Jasak, "Error analysis and estimation for the finite volume method with applications to fluid flows," eng, Ph.D. Imperial College London (University of London), 1996.

[222] N. Wang, M. Li, R. Ma, and L. Zhang, "Accuracy analysis of gradient reconstruction on isotropic unstructured meshes and its effects on inviscid flow simulation," *Advances in Aerodynamics*, vol. 1, no. 1, p. 18, Sep. 2019, ISSN: 2524-6992. DOI: 10.1186/s42774-019-0020-9.

[223] N. I. Grashchenkov, B. N. Klosovskii, E. N. Kosmarskaia, and L. N. Siskin, "Soviet investigations in the field of the vascular supply of the brain," eng, *Archives of Internal Medicine*, vol. 106, pp. 532–570, Oct. 1960, ISSN: 0003-9926. DOI: 10.1001/archinte.1960.03820040070008.

[224] J.-L. Auriault, "Heterogeneous periodic and random media. Are the equivalent macroscopic descriptions similar?" en, *International Journal of Engineering Science*, vol. 49, no. 8, pp. 806–808, Aug. 2011, ISSN: 00207225. DOI: 10.1016/j.ijengsci.2011.01.005.

[225] M. H. Holmes, *Introduction to perturbation methods* (Texts in applied mathematics 20), 2nd ed. New York: Springer, 2013, OCLC: ocn839305658, ISBN: 9781461454762.

[226] L. Risser, F. Plouraboué, P. Cloetens, and C. Fonta, "A 3D-investigation shows that angiogenesis in primate cerebral cortex mainly occurs at capillary level," en, *International Journal of Developmental Neuroscience*, vol. 27, no. 2, pp. 185–196, Apr. 2009, ISSN: 0736-5748, 1873-474X. DOI: 10.1016/j.ijdevneu.2008.10.006.

[227] B. Weber, A. L. Keller, J. Reichold, and N. K. Logothetis, "The Microvascular System of the Striate and Extrastriate Visual Cortex of the Macaque," en, *Cerebral Cortex*, vol. 18, no. 10, pp. 2318–2330, Oct. 2008, ISSN: 1460-2199, 1047-3211. DOI: 10.1093/cercor/bhm259.

[228] F. Moukalled, L. Mangani, and D. Mohammed, *The Finite Volume Method in Computational Fluid Dynamics*, en. Switzerland: Springer, 2016, vol. 113, ISBN: 978-3-319-16874-6.

[229] J. Guerrero, "A Crash Introduction to the Finite Volume Method and Discretization Schemes in OpenFOAM," Arlington, VA, USA: OpenFOAM, Jun. 2020.

[230] S. GmbH, *Mesh Quality | Mesh Visualization Tips*, en, publisher: SimScale GmbH, 2021.

[231] J. Wu and P. Traoré, "Similarity and Comparison of Three Finite-Volume Methods for Diffusive Fluxes Computation on Nonorthogonal Meshes," *Numerical Heat Transfer, Part B: Fundamentals*, vol. 64, no. 2, pp. 118–146, Aug. 2013, ISSN: 1040-7790. DOI: 10.1080/10407790.2013.784146.

[232] M. Kobayashi, J. Pereira, and J. Pereira, "A Second-Order Upwind Least-Squares Scheme for Incompressible Flows on Unstructured Hybrid Grids," *Numerical Heat Transfer, Part B: Fundamentals*, vol. 34, no. 1, pp. 39–60, Jul. 1998, ISSN: 1040-7790. DOI: 10.1080/10407799808915047.

[233] J. H. Ferziger and M. Perić, *Computational Methods for Fluid Dynamics*, en. Berlin, Heidelberg: Springer Berlin Heidelberg, 2002, ISBN: 9783540420743 9783642560262. DOI: 10.1007/978-3-642-56026-2.

[234] W. Choi and S. Lee, "Optimal error estimate of elliptic problems with Dirac sources for discontinuous and enriched Galerkin methods," en, *Applied Numerical Mathematics*, vol. 150, pp. 76–104, Apr. 2020, ISSN: 0168-9274. DOI: 10.1016/j.apnum.2019.09.010.

[235] T. Apel, J. Pfefferer, and A. Rösch, "Finite element error estimates for Neumann boundary control problems on graded meshes," en, *Computational Optimization and Applications*, vol. 52, no. 1, pp. 3–28, May 2012, ISSN: 1573-2894. DOI: 10.1007/s10589-011-9427-x.

[236] *Density » IT'IS Foundation*.

[237] M. D. Morris, "Factorial Sampling Plans for Preliminary Computational Experiments," en, *Technometrics*, vol. 33, no. 2, pp. 161–174, May 1991, ISSN: 0040-1706, 1537-2723. DOI: 10.1080/00401706.1991.10484804.

[238] F. Campolongo, J. Cariboni, and A. Saltelli, "An effective screening design for sensitivity analysis of large models," en, *Environmental Modelling & Software*, Modelling, computer-assisted simulations, and mapping of dangerous phenomena for hazard assessment, vol. 22, no. 10, pp. 1509–1518, Oct. 2007, ISSN: 1364-8152. DOI: 10.1016/j.envsoft.2006.10.004.

[239] a. Ventura-Antunes and S. Herculano-Houzel, "Energy supply per neuron is constrained by capillary density in the mouse brain," *Frontiers in Integrative Neuroscience*, vol. 16, 2022, ISSN: 1662-5145.

[240] J. Helenius, J. Perkiö, L. Soinne, *et al.*, "Cerebral Hemodynamics in a Healthy Population Measured by Dynamic Susceptibility Contrast Mr Imaging," *Acta Radiologica*, vol. 44, no. 5, pp. 538–546, Jan. 2003, ISSN: 0284-1851. DOI: 10.1080/j.1600-0455.2003.00104.x.

[241] A. N. Cookson, J. Lee, C. Michler, *et al.*, "A novel porous mechanical framework for modelling the interaction between coronary perfusion and myocardial mechanics," en, *Journal of Biomechanics*, Special Issue on Cardiovascular Solid Mechanics, vol. 45, no. 5, pp. 850–855, Mar. 2012, ISSN: 0021-9290. DOI: 10.1016/j.jbiomech.2011.11.026.

[242] A. N. Cookson, J. Lee, C. Michler, *et al.*, "A spatially-distributed computational model to quantify behaviour of contrast agents in MR perfusion imaging," en, *Medical Image Analysis*, vol. 18, no. 7, pp. 1200–1216, Oct. 2014, ISSN: 1361-8415. DOI: 10.1016/j.media.2014.07.002.

[243] S. P. Sourbron and D. L. Buckley, "Classic models for dynamic contrast-enhanced MRI: CLASSIC MODELS FOR DCE-MRI," en, *NMR in Biomedicine*, vol. 26, no. 8, pp. 1004–1027, Aug. 2013, ISSN: 09523480. DOI: 10.1002/nbm.2940.

[244] E. Rohan, V. Lukeš, and A. Jonášová, "Modeling of the contrast-enhanced perfusion test in liver based on the multi-compartment flow in porous media," en, *Journal of Mathematical Biology*, vol. 77, no. 2, pp. 421–454, Aug. 2018, ISSN: 1432-1416. DOI: 10.1007/s00285-018-1209-y.

[245] D. D. Stromberg and J. R. Fox, "Pressures in the Pial Arterial Microcirculation of the Cat during Changes in Systemic Arterial Blood Pressure," en, *Circulation Research*, vol. 31, no. 2, pp. 229–239, Aug. 1972, ISSN: 0009-7330, 1524-4571. DOI: 10.1161/01.RES.31.2.229.

[246] A. W. Toga and J. C. Mazziotta, *Brain Mapping: The Methods: the Methods*, English. 2002, OCLC: 932057096, ISBN: 9780080528281.

[247] M. J. Cipolla, "The Cerebral Circulation," en, *Colloquium Series on Integrated Systems Physiology: From Molecule to Function*, vol. 1, no. 1, pp. 1–59, Jan. 2009, ISSN: 2154-560X, 2154-5626. DOI: 10.4199/C00005ED1V01Y200912ISP002.

[248] J. Grüner, R. Paamand, L. Højgaard, and I. Law, "Brain perfusion CT compared with15O-H2O-PET in healthy subjects," en, *EJNMMI Research*, vol. 1, no. 1, p. 28, 2011, ISSN: 2191-219X. DOI: 10.1186/2191-219X-1-28.

[249] A. A. Linninger, I. G. Gould, T. Marinnan, C.-Y. Hsu, M. Chojecki, and A. Alaraj, "Cerebral Microcirculation and Oxygen Tension in the Human Secondary Cortex," en, *Annals of Biomedical Engineering*, vol. 41, no. 11, pp. 2264–2284, Nov. 2013, ISSN: 0090-6964, 1573-9686. DOI: 10.1007/s10439-013-0828-0.

[250] B. W. Zweifach, "Quantitative studies of microcirculatory structure and function. I. Analysis of pressure distribution in the terminal vascular bed in cat mesentery," eng, *Circulation Research*, vol. 34, no. 6, pp. 843–857, Jun. 1974, ISSN: 0009-7330.

[251] B. W. Zweifach and H. H. Lipowsky, "Quantitative studies of microcirculatory structure and function. III. Microvascular hemodynamics of cat mesentery and rabbit omentum.," en, *Circulation Research*, vol. 41, no. 3, pp. 380–390, Sep. 1977, ISSN: 0009-7330, 1524-4571. DOI: 10.1161/01.RES.41.3.380.

[252] H. Fukasawa, "Hemodynamical Studies of Cerebral Arteries by Means of Mathematical Analysis of Arterial Casts," en, *The Tohoku Journal of Experimental Medicine*, vol. 99, no. 3, pp. 255–268, 1969, ISSN: 0040-8727, 1349-3329. DOI: 10.1620/tjem.99.255.

[253] P. J. Blanco, L. O. Müller, and J. D. Spence, "Blood pressure gradients in cerebral arteries: A clue to pathogenesis of cerebral small vessel disease," en, *Stroke and Vascular Neurology*, vol. 2, no. 3, pp. 108–117, Sep. 2017, ISSN: 2059-8688, 2059-8696. DOI: 10.1136/svn-2017-000087.

[254] D. Dieckhoff and E. Kanzow, "□On the location of the flow resistance in the cerebral circulation," de, *Pflugers Archive European Journal of Physiology*, vol. 310, no. 1, pp. 75–85, 1969, ISSN: 0031-6768, 1432-2013. DOI: 10.1007/BF00586876.

[255] G. Hasle, K.-A. Lie, and E. Quak, *Geometric Modelling, Numerical Simulation, and Optimization: Applied Mathematics at SINTEF*, eng. Berlin Heidelberg: Springer e-books, 2007, ISBN: 9783540687832.

[256] M. Shashkov and S. Steinberg, "Solving Diffusion Equations with Rough Coefficients in Rough Grids," *Journal of Computational Physics*, vol. 129, pp. 383–405, Dec. 1996, ADS Bibcode: 1996JCoPh.129..383S, ISSN: 0021-9991. DOI: 10.1006/jcph.1996.0257.

[257] F. Hermeline, "A Finite Volume Method for the Approximation of Diffusion Operators on Distorted Meshes," en, *Journal of Computational Physics*, vol. 160, no. 2, pp. 481–499, May 2000, ISSN: 00219991. DOI: 10.1006/jcph.2000.6466.

[258] J. Breil and P.-H. Maire, "A cell-centered diffusion scheme on two-dimensional unstructured meshes," en, *Journal of Computational Physics*, vol. 224, no. 2, pp. 785–823, Jun. 2007, ISSN: 0021-9991. DOI: 10.1016/j.jcp.2006.10.025.

[259] Z. Sheng and G. Yuan, "A Finite Volume Scheme for Diffusion Equations on Distorted Quadrilateral Meshes," *Transport Theory and Statistical Physics*, vol. 37, no. 2-4, pp. 171–207, Dec. 2008, ISSN: 0041-1450. DOI: 10.1080/00411450802526533.

[260] S. Anil Lal, R. V. Reji, and K. S. Santhosh, "Evaluation of diffusive flux across faces of arbitrary shaped finite volume cells," en, *Computers & Fluids*, vol. 57, pp. 225–236, Mar. 2012, ISSN: 0045-7930. DOI: 10.1016/j.compfluid.2012.01.001.

[261] W. A. Copen, M. H. Lev, and O. Rapalino, "Brain perfusion: Computed tomography and magnetic resonance techniques," eng, *Handbook of Clinical Neurology*, vol. 135, pp. 117–135, 2016, ISSN: 0072-9752. DOI: 10.1016/B978-0-444-53485-9.00006-4.

[262] P. Barabas, J. Augustine, J. A. Fernández, J. G. McGeown, M. K. McGahon, and T. M. Curtis, "Chapter Seven - Ion channels and myogenic activity in retinal arterioles," en, in *Current Topics in Membranes*, ser. Ion Channels and Calcium Signaling in the Microcirculation, W. F. Jackson, Ed., vol. 85, Academic Press, Jan. 2020, pp. 187–226. DOI: 10.1016/bs.ctm.2020.01.008.

[263] P. Jeppesen, P. A. Gregersen, and T. Bek, "The age-dependent decrease in the myogenic response of retinal arterioles as studied with the Retinal Vessel Analyzer," eng, *Graefe's Archive for Clinical and Experimental Ophthalmology = Albrecht Von Graefes Archiv Fur Klinische Und Experimentelle Ophthalmologie*, vol. 242, no. 11, pp. 914–919, Nov. 2004, ISSN: 0721-832X. DOI: 10.1007/s00417-004-0945-4.

[264] N. Patton, T. Aslam, T. MacGillivray, A. Pattie, I. J. Deary, and B. Dhillon, "Retinal vascular image analysis as a potential screening tool for cerebrovascular disease: A rationale based on homology between cerebral and retinal microvasculatures," en, *Journal of Anatomy*, vol. 206, no. 4, p. 319, Apr. 2005, ISSN: 1469-7580. DOI: 10.1111/j.1469-7580.2005.00395.x.

[265] E. Courtie, T. Veenith, A. Logan, A. K. Denniston, and R. J. Blanch, "Retinal blood flow in critical illness and systemic disease: A review," *Annals of Intensive Care*, vol. 10, p. 152, Nov. 2020, ISSN: 2110-5820. DOI: 10.1186/s13613-020-00768-3.

[266] A. S. M. Salinet, T. G. Robinson, and R. B. Panerai, "Cerebral blood flow response to neural activation after acute ischemic stroke: A failure of myogenic regulation?" eng, *Journal of Neurology*, vol. 260, no. 10, pp. 2588–2595, Oct. 2013, ISSN: 1432-1459. DOI: 10.1007/s00415-013-7022-z.

[267] L. Kuo, M. J. Davis, and W. M. Chilian, "Endothelium-dependent, flow-induced dilation of isolated coronary arterioles," eng, *The American Journal of Physiology*, vol. 259, no. 4 Pt 2, H1063–1070, Oct. 1990, ISSN: 0002-9513. DOI: 10.1152/ajpheart.1990.259.4.H1063.

[268] T. Toni, D. Welch, N. Strelkowa, A. Ipsen, and M. P. Stumpf, "Approximate Bayesian computation scheme for parameter inference and model selection in dynamical systems," en, *Journal of The Royal Society Interface*, vol. 6, no. 31, pp. 187–202, Feb. 2009, ISSN: 1742-5689, 1742-5662. DOI: 10.1098/rsif.2008.0172.

[269] M. A. Black, N. T. Cable, D. H. J. Thijssen, and D. J. Green, "Importance of measuring the time course of flow-mediated dilatation in humans," eng, *Hypertension (Dallas, Tex.: 1979)*, vol. 51, no. 2, pp. 203–210, Feb. 2008, ISSN: 1524-4563. DOI: 10.1161/HYPERTENSIONAHA.107.101014.

[270] M. C. Corretti, T. J. Anderson, E. J. Benjamin, *et al.*, "Guidelines for the ultrasound assessment of endothelial-dependent flow-mediated vasodilation of the brachial artery," en, *Journal of the American College of Cardiology*, vol. 39, no. 2, pp. 257–265, Jan. 2002, ISSN: 07351097. DOI: 10.1016/S0735-1097(01)01746-6.

[271] M. Kelm, "Nitric oxide metabolism and breakdown," en, *Biochimica et Biophysica Acta (BBA) - Bioenergetics*, vol. 1411, no. 2, pp. 273–289, May 1999, ISSN: 0005-2728. DOI: 10.1016/S0005-2728(99)00020-1.

[272] J. K. Pritchard, M. T. Seielstad, A. Perez-Lezaun, and M. W. Feldman, "Population growth of human Y chromosomes: A study of Y chromosome microsatellites," eng, *Molecular Biology and Evolution*, vol. 16, no. 12, pp. 1791–1798, Dec. 1999, ISSN: 0737-4038. DOI: 10.1093/oxfordjournals.molbev.a026091.

[273] P. Marjoram, J. Molitor, V. Plagnol, and S. Tavaré, "Markov chain Monte Carlo without likelihoods," en, *Proceedings of the National Academy of Sciences*, vol. 100, no. 26, pp. 15 324–15 328, Dec. 2003, ISSN: 0027-8424, 1091-6490. DOI: 10.1073/pnas.0306899100.

[274] S. A. Sisson, Y. Fan, and M. M. Tanaka, "Sequential Monte Carlo without likelihoods," en, *Proceedings of the National Academy of Sciences*, vol. 104, no. 6, pp. 1760–1765, Feb. 2007, ISSN: 0027-8424, 1091-6490. DOI: 10.1073/pnas.0607208104.

[275] N. Toda and T. Okamura, "Cerebral Vasodilators," en, *Japanese Journal of Pharmacology*, vol. 76, no. 4, pp. 349–367, 1998, ISSN: 00215198. DOI: 10.1254/jjp.76.349.

[276] E. Lanzarone, P. Liani, G. Baselli, and M. L. Costantino, "Model of arterial tree and peripheral control for the study of physiological and assisted circulation," eng, *Medical Engineering & Physics*, vol. 29, no. 5, pp. 542–555, Jun. 2007, ISSN: 1350-4533. DOI: 10.1016/j.medengphy.2006.08.004.

[277] D. McDonald and E. Arnold, *Blood Flow in Arteries*. London: Physiological Society, 1974.

[278] R. Rockwell, M. Anliker, and J. Elsner, "Model studies of the pressure and flow pulses in a viscoelastic arterial conduit," en, *Journal of the Franklin Institute*, vol. 297, no. 5, pp. 405–427, May 1974, ISSN: 00160032. DOI: 10.1016/0016-0032(74)90042-8.

[279] J. E. Brian, F. M. Faraci, and D. D. Heistad, "Recent insights into the regulation of cerebral circulation," eng, *Clinical and Experimental Pharmacology & Physiology*, vol. 23, no. 6-7, pp. 449–457, 1996, ISSN: 0305-1870. DOI: 10.1111/j.1440-1681.1996.tb02760.x.

[280] A. Almanza-Hurtado, C. Polanco Guerra, M. C. Martínez-Ávila, D. Borré-Naranjo, T. Rodríguez-Yanez, and C. Dueñas-Castell, "Hypercapnia from Physiology to Practice," eng, *International Journal of Clinical Practice*, vol. 2022, p. 2 635 616, 2022, ISSN: 1742-1241. DOI: 10.1155/2022/2635616.

[281] A. D. Wijnhoud, P. J. Koudstaal, and D. W. J. Dippel, "Relationships of transcranial blood flow Doppler parameters with major vascular risk factors: TCD study in patients with a recent TIA or nondisabling ischemic stroke," eng, *Journal of clinical ultrasound: JCU*, vol. 34, no. 2, pp. 70–76, Feb. 2006, ISSN: 0091-2751. DOI: 10.1002/jcu.20193.

[282] S. Atwi, H. Shao, D. E. Crane, *et al.*, "BOLD-based cerebrovascular reactivity vascular transfer function isolates amplitude and timing responses to better characterize cerebral small vessel disease," eng, *NMR in biomedicine*, vol. 32, no. 3, e4064, Mar. 2019, ISSN: 1099-1492. DOI: 10.1002/nbm.4064.

[283] D. Kim, T. M. Hughes, M. E. Lipford, *et al.*, "Relationship Between Cerebrovascular Reactivity and Cognition Among People With Risk of Cognitive Decline," *Frontiers in Physiology*, vol. 12, p. 645 342, May 2021, ISSN: 1664-042X. DOI: 10.3389/fphys.2021.645342.

[284] L. Glodzik, C. Randall, H. Rusinek, and M. J. de Leon, "Cerebrovascular reactivity to carbon dioxide in Alzheimer's disease," eng, *Journal of Alzheimer's disease: JAD*, vol. 35, no. 3, pp. 427–440, 2013, ISSN: 1875-8908. DOI: 10.3233/JAD-122011.

[285] M. Younes, M. Ostrowski, R. Atkar, J. Laprairie, A. Siemens, and P. Hanly, "Mechanisms of breathing instability in patients with obstructive sleep apnea," eng, *Journal of Applied Physiology (Bethesda, Md.: 1985)*, vol. 103, no. 6, pp. 1929–1941, Dec. 2007, ISSN: 8750-7587. DOI: 10.1152/japplphysiol.00561.2007.

[286] A Battisti-Charbonney, J Fisher, and J Duffin, "The cerebrovascular response to carbon dioxide in humans," *The Journal of Physiology*, vol. 589, no. Pt 12, pp. 3039–3048, Jun. 2011, ISSN: 0022-3751. DOI: 10.1113/jphysiol.2011.206052.

[287] M. J. Poulin, P. J. Liang, and P. A. Robbins, "Dynamics of the cerebral blood flow response to step changes in end-tidal PCO2 and PO2 in humans," eng, *Journal of Applied Physiology (Bethesda, Md.: 1985)*, vol. 81, no. 3, pp. 1084–1095, Sep. 1996, ISSN: 8750-7587. DOI: 10.1152/jappl.1996.81.3.1084.

[288] P. Liu, J. B. De Vis, and H. Lu, "Cerebrovascular reactivity (CVR) MRI with CO2 challenge: A technical review," en, *NeuroImage*, vol. 187, pp. 104–115, Feb. 2019, ISSN: 10538119. DOI: 10.1016/j.neuroimage.2018.03.047.

[289] M. G. Berger, C. Vandier, P. Bonnet, W. F. Jackson, and N. J. Rusch, "Intracellular acidosis differentially regulates KV channels in coronary and pulmonary vascular muscle," eng, *The American Journal of Physiology*, vol. 275, no. 4, H1351–1359, Oct. 1998, ISSN: 0002-9513. DOI: 10.1152/ajpheart.1998.275.4.H1351.

[290] H. Xu, N. Cui, Z. Yang, *et al.*, "Direct activation of cloned K(atp) channels by intracellular acidosis," eng, *The Journal of Biological Chemistry*, vol. 276, no. 16, pp. 12 898–12 902, Apr. 2001, ISSN: 0021-9258. DOI: 10.1074/jbc.M009631200.

[291] T. Kitazono, F. M. Faraci, H. Taguchi, and D. D. Heistad, "Role of potassium channels in cerebral blood vessels," eng, *Stroke*, vol. 26, no. 9, pp. 1713–1723, Sep. 1995, ISSN: 0039-2499. DOI: 10.1161/01.str.26.9.1713.

[292] M. T. Nelson and J. M. Quayle, "Physiological roles and properties of potassium channels in arterial smooth muscle," eng, *The American Journal of Physiology*, vol. 268, no. 4 Pt 1, pp. C799–822, Apr. 1995, ISSN: 0002-9513. DOI: 10.1152/ajpcell.1995.268.4.C799.

[293] H. Kinoshita and Z. S. Katusic, "Role of potassium channels in relaxations of isolated canine basilar arteries to acidosis," eng, *Stroke*, vol. 28, no. 2, 433–437; discussion 437–438, Feb. 1997, ISSN: 0039-2499. DOI: 10.1161/01.str.28.2.433.

[294] D. G. Welsh, C. H. T. Tran, B. O. Hald, and M. Sancho, "The Conducted Vasomotor Response: Function, Biophysical Basis, and Pharmacological Control," eng, *Annual Review of Pharmacology and Toxicology*, vol. 58, pp. 391–410, Jan. 2018, ISSN: 1545-4304. DOI: 10.1146/annurev-pharmtox-010617-052623.

[295] A. Zechariah, C. H. T. Tran, B. O. Hald, *et al.*, "Intercellular Conduction Optimizes Arterial Network Function and Conserves Blood Flow Homeostasis During Cerebrovascular Challenges," en, *Arteriosclerosis, Thrombosis, and Vascular Biology*, vol. 40, no. 3, pp. 733–750, Mar. 2020, ISSN: 1079-5642, 1524-4636. DOI: 10.1161/ATVBAHA.119.313391.

[296] A. R. Fathi, C. Yang, K. D. Bakhtian, M. Qi, R. R. Lonser, and R. M. Pluta, "Carbon dioxide influence on nitric oxide production in endothelial cells and astrocytes: Cellular mechanisms," *Brain research*, vol. 1386, pp. 50–57, Apr. 2011, ISSN: 0006-8993. DOI: 10.1016/j.brainres.2011.02.066.

[297] H. L. Xu, H. M. Koenig, S. Ye, D. L. Feinstein, and D. A. Pelligrino, "Influence of the glia limitans on pial arteriolar relaxation in the rat," eng, *American Journal of Physiology. Heart and Circulatory Physiology*, vol. 287, no. 1, H331–339, Jul. 2004, ISSN: 0363-6135. DOI: 10.1152/ajpheart.00831.2003.

[298] R. C. Ziegelstein, L. Cheng, P. S. Blank, *et al.*, "Modulation of calcium homeostasis in cultured rat aortic endothelial cells by intracellular acidification," eng, *The American Journal of Physiology*, vol. 265, no. 4 Pt 2, H1424–1433, Oct. 1993, ISSN: 0002-9513. DOI: 10.1152/ajpheart.1993.265.4.H1424.

[299] H. A. Kontos, E. P. Wei, A. J. Raper, and J. L. Patterson, "Local mechanism of CO2 action of cat pial arterioles," eng, *Stroke*, vol. 8, no. 2, pp. 226–229, 1977, ISSN: 0039-2499. DOI: 10.1161/01.str.8.2.226.

[300] D Heistad and H. Kontos, *Handbook of Physiology Section 2 Peripheral Circulation and Organ Blood Flow - AbeBooks*, en. 1983, vol. 3.

[301] M. Reivich, "ARTERIAL PCO2 AND CEREBRAL HEMODYNAMICS," eng, *The American Journal of Physiology*, vol. 206, pp. 25–35, Jan. 1964, ISSN: 0002-9513. DOI: 10.1152/ajplegacy.1964.206.1.25.

[302] R. L. Grubb, M. E. Raichle, J. O. Eichling, and M. M. Ter-Pogossian, "The effects of changes in PaCO2 on cerebral blood volume, blood flow, and vascular mean transit time," eng, *Stroke*, vol. 5, no. 5, pp. 630–639, 1974, ISSN: 0039-2499. DOI: 10.1161/01.str.5.5.630.

[303] K. J. Cummings, M. Swart, and P. N. Ainslie, "Morning attenuation in cerebrovascular CO2 reactivity in healthy humans is associated with a lowered cerebral oxygenation and an augmented ventilatory response to CO2," eng, *Journal of Applied Physiology (Bethesda, Md.: 1985)*, vol. 102, no. 5, pp. 1891–1898, May 2007, ISSN: 8750-7587. DOI: 10.1152/japplphysiol.01437.2006.

[304] K. Ide, M. Eliasziw, and M. J. Poulin, "Relationship between middle cerebral artery blood velocity and end-tidal PCO2 in the hypocapnic-hypercapnic range in humans," eng, *Journal of Applied Physiology (Bethesda, Md.: 1985)*, vol. 95, no. 1, pp. 129–137, Jul. 2003, ISSN: 8750-7587. DOI: 10.1152/japplphysiol.01186.2002.

[305] A. Xie, J. B. Skatrud, B. Morgan, *et al.*, "Influence of cerebrovascular function on the hypercapnic ventilatory response in healthy humans," *The Journal of Physiology*, vol. 577, no. Pt 1, pp. 319–329, Nov. 2006, ISSN: 0022-3751. DOI: 10.1113/jphysiol.2006.110627.

[306] A. Xie, J. B. Skatrud, S. R. Barczi, *et al.*, "Influence of cerebral blood flow on breathing stability," eng, *Journal of Applied Physiology (Bethesda, Md.: 1985)*, vol. 106, no. 3, pp. 850–856, Mar. 2009, ISSN: 8750-7587. DOI: 10.1152/japplphysiol.90914.2008.

[307] L. Auerr, "Pial arterial reactions to hyper- and hypocapnia: A dynamic experimental study in cats," eng, *European Neurology*, vol. 17, no. 6, pp. 351–362, 1978, ISSN: 0014-3022. DOI: 10.1159/000114974.

[308] J. W. Severinghaus and N. Lassen, "Step hypocapnia to separate arterial from tissue PCO2 in the regulation of cerebral blood flow," eng, *Circulation Research*, vol. 20, no. 2, pp. 272–278, Feb. 1967, ISSN: 0009-7330. DOI: 10.1161/01.res.20.2.272.

[309] W. SHAPIRO, A. J. WASSERMAN, and J. L. PATTERSON JR., "Human Cerebrovascular Response Time to Elevation of Arterial Carbon Dioxide Tension," *Archives of Neurology*, vol. 13, no. 2, pp. 130–138, Aug. 1965, ISSN: 0003-9942. DOI: 10.1001/archneur.1965.00470020020003.

[310] E. P. Wei, H. A. Kontos, and J. L. Patterson, "Dependence of pial arteriolar response to hypercapnia on vessel size," eng, *The American Journal of Physiology*, vol. 238, no. 5, pp. 697–703, May 1980, ISSN: 0002-9513. DOI: 10.1152/ajpheart.1980.238.5.H697.

[311] P. N. Ainslie, L. Celi, K. McGrattan, K. Peebles, and S. Ogoh, "Dynamic cerebral autoregulation and baroreflex sensitivity during modest and severe step changes in arterial PCO2," eng, *Brain Research*, vol. 1230, pp. 115–124, Sep. 2008, ISSN: 0006-8993. DOI: 10.1016/j.brainres.2008.07.048.

[312] V. Fencl, "Acid-Base Balance in Cerebral Fluids," en, in *Comprehensive Physiology*, R. Terjung, Ed., 1st ed., Wiley, Dec. 1986, pp. 115–140, ISBN: 9780470650714. DOI: 10.1002/cphy.cp030204.

[313] K. Peebles, L. Celi, K. McGrattan, C. Murrell, K. Thomas, and P. N. Ainslie, "Human cerebrovascular and ventilatory CO_2 reactivity to end-tidal, arterial and internal jugular vein P_{CO2}: Cerebrovascular and ventilatory CO_2 reactivity to arterial and brain P_{CO2}," en, *The Journal of Physiology*, vol. 584, no. 1, pp. 347–357, Oct. 2007, ISSN: 00223751. DOI: 10.1113/jphysiol.2007.137075.

[314] W Shapiro, A. J. Wasserman, and J. L. Patterson, "Mechanism and pattern of human cerebrovascular regulation after rapid changes in blood CO2 tension.," *Journal of Clinical Investigation*, vol. 45, no. 6, pp. 913–922, Jun. 1966, ISSN: 0021-9738.

[315] P. C. Njemanze, "Critical limits of pressure-flow relation in the human brain," eng, *Stroke*, vol. 23, no. 12, pp. 1743–1747, Dec. 1992, ISSN: 0039-2499. DOI: 10.1161/01.str.23.12.1743.

[316] I. Ellingsen, A. Hauge, G. Nicolaysen, M. Thoresen, and L. Walløe, "Changes in human cerebral blood flow due to step changes in PAO2 and PACO2," eng, *Acta Physiologica Scandinavica*, vol. 129, no. 2, pp. 157–163, Feb. 1987, ISSN: 0001-6772. DOI: 10.1111/j.1748-1716.1987.tb08054.x.

[317] A. Vis and H. Folgering, "The dynamic effect of PETCO, on vertebral bloodflow in cats," eng, *Respiration Physiology*, vol. 42, no. 2, pp. 131–143, Nov. 1980, ISSN: 0034-5687. DOI: 10.1016/0034-5687(80)90110-3.

[318] A. Xie, J. B. Skatrud, R. Khayat, J. A. Dempsey, B. Morgan, and D. Russell, "Cerebrovascular response to carbon dioxide in patients with congestive heart failure," eng, *American Journal of Respiratory and Critical Care Medicine*, vol. 172, no. 3, pp. 371–378, Aug. 2005, ISSN: 1073-449X. DOI: 10.1164/rccm.200406-807OC.

[319] L. J. Jensen and N.-H. Holstein-Rathlou, "The vascular conducted response in cerebral blood flow regulation," *Journal of Cerebral Blood Flow & Metabolism*, vol. 33, no. 5, pp. 649–656, May 2013, ISSN: 0271-678X. DOI: 10.1038/jcbfm.2013.25.

[320] P. W. Sweeney, S. Walker-Samuel, and R. J. Shipley, "Insights into cerebral haemodynamics and oxygenation utilising in vivo mural cell imaging and mathematical modelling," en, *Scientific Reports*, vol. 8, no. 1, p. 1373, Jan. 2018, ISSN: 2045-2322. DOI: 10.1038/s41598-017-19086-z.

[321] D. A. Van Riper and J. A. Bevan, "Electrical field stimulation-mediated relaxation of rabbit middle cerebral artery. Evidence of a cholinergic endothelium-dependent component," eng, *Circulation Research*, vol. 70, no. 6, pp. 1104–1112, Jun. 1992, ISSN: 0009-7330. DOI: 10.1161/01.res.70.6.1104.

[322] A. Sato and Y. Sato, "Cholinergic neural regulation of regional cerebral blood flow," eng, *Alzheimer Disease and Associated Disorders*, vol. 9, no. 1, pp. 28–38, 1995, ISSN: 0893-0341. DOI: 10.1097/00002093-199505000-00007.

[323] O. U. Scremin and D. J. Jenden, "Cholinergic control of cerebral blood flow in stroke, trauma and aging," eng, *Life Sciences*, vol. 58, no. 22, pp. 2011–2018, 1996, ISSN: 0024-3205. DOI: 10.1016/0024-3205(96)00192-0.

[324] F. Zhang, S. Xu, and C. Iadecola, "Role of nitric oxide and acetylcholine in neocortical hyperemia elicited by basal forebrain stimulation: Evidence for an involvement of endothelial nitric oxide," eng, *Neuroscience*, vol. 69, no. 4, pp. 1195–1204, Dec. 1995, ISSN: 0306-4522. DOI: 10.1016/0306-4522(95)00302-y.

[325] P. Lacombe, R. Sercombe, C. Verrecchia, V. Philipson, E. T. MacKenzie, and J. Seylaz, "Cortical blood flow increases induced by stimulation of the substantia innominata in the unanesthetized rat," eng, *Brain Research*, vol. 491, no. 1, pp. 1–14, Jul. 1989, ISSN: 0006-8993. DOI: 10.1016/0006-8993(89)90083-8.

[326] A. A. Rovere, O. U. Scremin, M. R. Beresi, A. C. Raynald, and A. Giardini, "Cholinergic mechanism in the cerebrovascular action of carbon dioxide," eng, *Stroke*, vol. 4, no. 6, pp. 969–972, 1973, ISSN: 0039-2499. DOI: 10.1161/01.str.4.6.969.

[327] D. M. Hudson, D. J. Jenden, O. U. Scremin, and R. R. Sonnenschein, "Cortical acetylcholine efflux with hypercapnia and nociceptive stimulation," eng, *Brain Research*, vol. 338, no. 2, pp. 267–272, Jul. 1985, ISSN: 0006-8993. DOI: 10.1016/0006-8993(85)90156-8.

[328] O. U. Scremin, E. H. Rubinstein, and R. R. Sonnenschein, "Cerebrovascular CO2 reactivity: Role of a cholinergic mechanism modulated by anesthesia," eng, *Stroke*, vol. 9, no. 2, pp. 160–165, 1978, ISSN: 0039-2499. DOI: 10.1161/01.str.9.2.160.

[329] F. Eckenstein and H. Thoenen, "Cholinergic neurons in the rat cerebral cortex demonstrated by immunohistochemical localization of choline acetyltransferase," eng, *Neuroscience Letters*, vol. 36, no. 3, pp. 211–215, Apr. 1983, ISSN: 0304-3940. DOI: 10.1016/0304-3940(83)90002-2.

[330] O. U. Scremin, A. A. Rovere, A. C. Raynald, and A. Giardini, "Cholinergic control of blood flow in the cerebral cortex of the rat," eng, *Stroke*, vol. 4, no. 2, pp. 233–239, 1973, ISSN: 0039-2499.

[331] M. Yamada, K. G. Lamping, A. Duttaroy, *et al.*, "Cholinergic dilation of cerebral blood vessels is abolished in M(5) muscarinic acetylcholine receptor knockout mice," eng, *Proceedings of the National Academy of Sciences of the United States of America*, vol. 98, no. 24, pp. 14 096–14 101, Nov. 2001, ISSN: 0027-8424. DOI: 10.1073/pnas.251542998.

[332] R. T. R. Huckstepp, E. Llaudet, and A. V. Gourine, "CO2-Induced ATP-Dependent Release of Acetylcholine on the Ventral Surface of the Medulla Oblongata," *PLoS ONE*, vol. 11, no. 12, e0167861, Dec. 2016, ISSN: 1932-6203. DOI: 10.1371/journal.pone.0167861.

[333] B. Metz, "Hypercapnia and acetylcholine release from the cerebral cortex and medulla," eng, *The Journal of Physiology*, vol. 186, no. 2, pp. 321–332, Oct. 1966, ISSN: 0022-3751. DOI: 10.1113/jphysiol.1966.sp008037.

[334] W. M. Zhu, A. Neuhaus, D. J. Beard, B. A. Sutherland, and G. C. DeLuca, "Neurovascular coupling mechanisms in health and neurovascular uncoupling in Alzheimer's disease," eng, *Brain: A Journal of Neurology*, vol. 145, no. 7, pp. 2276–2292, Jul. 2022, ISSN: 1460-2156. DOI: 10.1093/brain/awac174.

[335] W. J. Powers, I. B. Hirsch, and P. E. Cryer, "Effect of stepped hypoglycemia on regional cerebral blood flow response to physiological brain activation," eng, *The American Journal of Physiology*, vol. 270, no. 2 Pt 2, H554–559, Feb. 1996, ISSN: 0002-9513. DOI: 10.1152/ajpheart.1996.270.2.H554.

[336] T. Wolf, U. Lindauer, A. Villringer, and U. Dirnagl, "Excessive oxygen or glucose supply does not alter the blood flow response to somatosensory stimulation or spreading depression in rats," eng, *Brain Research*, vol. 761, no. 2, pp. 290–299, Jul. 1997, ISSN: 0006-8993. DOI: 10.1016/s0006-8993(97)00354-5.

[337] N. Bertrand, H. Ishii, A. Beley, and M. Spatz, "Biphasic striatal acetylcholine release during and after transient cerebral ischemia in gerbils," eng, *Journal of Cerebral Blood Flow and Metabolism: Official Journal of the International Society of Cerebral Blood Flow and Metabolism*, vol. 13, no. 5, pp. 789–795, Sep. 1993, ISSN: 0271-678X. DOI: 10.1038/jcbfm.1993.100.

[338] M. Ueno, T. Itakura, H. Yokote, H. Imai, T. Okuno, and N. Komai, "[Dynamics of extracellular acetylcholine of the gerbil striatum during cerebral ischemia monitored by intracerebral microdialysis]," jpn, *No to Shinkei = Brain and Nerve*, vol. 43, no. 5, pp. 467–472, May 1991, ISSN: 0006-8969.

[339] Y. Kumagae and Y. Matsui, "Output, tissue levels, and synthesis of acetylcholine during and after transient forebrain ischemia in the rat," eng, *Journal of Neurochemistry*, vol. 56, no. 4, pp. 1169–1173, Apr. 1991, ISSN: 0022-3042. DOI: 10.1111/j.1471-4159.1991.tb11407.x.

[340] O. U. Scremin and D. J. Jenden, "Focal ischemia enhances choline output and decreases acetylcholine output from rat cerebral cortex," eng, *Stroke*, vol. 20, no. 1, pp. 92–95, Jan. 1989, ISSN: 0039-2499. DOI: 10.1161/01.str.20.1.92.

[341] J Rícný and S Tucek, "Relation between the content of acetyl-coenzyme A and acetylcholine in brain slices.," *Biochemical Journal*, vol. 188, no. 3, pp. 683–688, Jun. 1980, ISSN: 0264-6021.

[342] G. G. Emerson and S. S. Segal, "Electrical Coupling Between Endothelial Cells and Smooth Muscle Cells in Hamster Feed Arteries: Role in Vasomotor Control," en, *Circulation Research*, vol. 87, no. 6, pp. 474–479, Sep. 2000, ISSN: 0009-7330, 1524-4571. DOI: 10.1161/01.RES.87.6.474.

[343] Y. Yamamoto, K. Imaeda, and H. Suzuki, "Endothelium-dependent hyperpolarization and intercellular electrical coupling in guinea-pig mesenteric arterioles," *The Journal of Physiology*, vol. 514, no. Pt 2, pp. 505–513, Jan. 1999, ISSN: 0022-3751. DOI: 10.1111/j.1469-7793.1999.505ae.x.

[344] G. Y. Mironova, P. M. Kowalewska, M. El-Lakany, *et al.*, "The conducted vasomotor response and the principles of electrical communication in resistance arteries," eng, *Physiological Reviews*, vol. 104, no. 1, pp. 33–84, Jan. 2024, ISSN: 1522-1210. DOI: 10.1152/physrev.00035.2022.

[345] G. G. Emerson and S. S. Segal, "Endothelial cell pathway for conduction of hyperpolarization and vasodilation along hamster feed artery," eng, *Circulation Research*, vol. 86, no. 1, pp. 94–100, Jan. 2000, ISSN: 0009-7330. DOI: 10.1161/01.res.86.1.94.

[346] P. Bagher and S. S. Segal, "Regulation of blood flow in the microcirculation: Role of conducted vasodilation," eng, *Acta Physiologica (Oxford, England)*, vol. 202, no. 3, pp. 271–284, Jul. 2011, ISSN: 1748-1716. DOI: 10.1111/j.1748-1716.2010.02244.x.

[347] S. S. Segal and B. R. Duling, "Flow control among microvessels coordinated by intercellular conduction," eng, *Science (New York, N.Y.)*, vol. 234, no. 4778, pp. 868–870, Nov. 1986, ISSN: 0036-8075. DOI: 10.1126/science.3775368.

[348] G. G. Emerson, T. O. Neild, and S. S. Segal, "Conduction of hyperpolarization along hamster feed arteries: Augmentation by acetylcholine," en, *American Journal of Physiology-Heart and Circulatory Physiology*, vol. 283, no. 1, H102–H109, Jul. 2002, ISSN: 0363-6135, 1522-1539. DOI: 10.1152/ajpheart.00038.2002.

[349] W. C. Cole and D. G. Welsh, "Role of myosin light chain kinase and myosin light chain phosphatase in the resistance arterial myogenic response to intravascular pressure," eng, *Archives of Biochemistry and Biophysics*, vol. 510, no. 2, pp. 160–173, Jun. 2011, ISSN: 1096-0384. DOI: 10.1016/j.abb.2011.02.024.

[350] M. Mita, H. Yanagihara, S. Hishinuma, M. Saito, and M. P. Walsh, "Membrane depolarization-induced contraction of rat caudal arterial smooth muscle involves Rho-associated kinase.," *Biochemical Journal*, vol. 364, no. Pt 2, pp. 431–440, Jun. 2002, ISSN: 0264-6021. DOI: 10.1042/BJ20020191.

[351] H. K. Diep, E. J. Vigmond, S. S. Segal, and D. G. Welsh, "Defining electrical communication in skeletal muscle resistance arteries: A computational approach," eng, *The Journal of Physiology*, vol. 568, no. Pt 1, pp. 267–281, Oct. 2005, ISSN: 0022-3751. DOI: 10.1113/jphysiol.2005.090233.

[352] T. Horiuchi, H. H. Dietrich, K. Hongo, and R. G. Dacey, "Mechanism of extracellular K+-induced local and conducted responses in cerebral penetrating arterioles," eng, *Stroke*, vol. 33, no. 11, pp. 2692–2699, Nov. 2002, ISSN: 1524-4628. DOI: 10.1161/01.str.0000034791.52151.6b.

[353] Y. Yamamoto, M. F. Klemm, F. R. Edwards, and H. Suzuki, "Intercellular electrical communication among smooth muscle and endothelial cells in guinea-pig mesenteric arterioles," *The Journal of Physiology*, vol. 535, no. Pt 1, pp. 181–195, Aug. 2001, ISSN: 0022-3751. DOI: 10.1111/j.1469-7793.2001.00181.x.

[354] C. Iadecola, G. Yang, T. J. Ebner, and G. Chen, "Local and propagated vascular responses evoked by focal synaptic activity in cerebellar cortex," eng, *Journal of Neurophysiology*, vol. 78, no. 2, pp. 651–659, Aug. 1997, ISSN: 0022-3077. DOI: 10.1152/jn.1997.78.2.651.

[355] P. O'Herron, P. Y. Chhatbar, M. Levy, *et al.*, "Neural correlates of single-vessel haemodynamic responses in vivo," en, *Nature*, vol. 534, no. 7607, pp. 378–382, Jun. 2016, ISSN: 1476-4687. DOI: 10.1038/nature17965.

[356] B. R. Chen, M. G. Kozberg, M. B. Bouchard, M. A. Shaik, and E. M. C. Hillman, "A critical role for the vascular endothelium in functional neurovascular coupling in the brain," eng, *Journal of the American Heart Association*, vol. 3, no. 3, e000787, Jun. 2014, ISSN: 2047-9980. DOI: 10.1161/JAHA.114.000787.

[357] R. L. Rungta, E. Chaigneau, B.-F. Osmanski, and S. Charpak, "Vascular Compartmentalization of Functional Hyperemia from the Synapse to the Pia," eng, *Neuron*, vol. 99, no. 2, 362–375.e4, Jul. 2018, ISSN: 1097-4199. DOI: 10.1016/j.neuron.2018.06.012.

[358] T. David, S. Alzaidi, and H. Farr, "Coupled autoregulation models in the cerebro-vasculature," en, *Journal of Engineering Mathematics*, vol. 64, no. 4, pp. 403–415, Aug. 2009, ISSN: 1573-2703. DOI: 10.1007/s10665-009-9274-2.

[359] J. Petersson and R. W. Glenny, "Gas exchange and ventilation–perfusion relationships in the lung," en, *European Respiratory Journal*, vol. 44, no. 4, pp. 1023–1041, Oct. 2014, ISSN: 0903-1936, 1399-3003. DOI: 10.1183/09031936.00037014.

[360] A. L. Urback, B. J. MacIntosh, and B. I. Goldstein, "Cerebrovascular reactivity measured by functional magnetic resonance imaging during breath-hold challenge: A systematic review," en, *Neuroscience & Biobehavioral Reviews*, vol. 79, pp. 27–47, Aug. 2017, ISSN: 01497634. DOI: 10.1016/j.neubiorev.2017.05.003.

[361] J Fierstra, O Sobczyk, A Battisti-Charbonney, *et al.*, "Measuring cerebrovascular reactivity: What stimulus to use?" *The Journal of Physiology*, vol. 591, no. Pt 23, pp. 5809–5821, Dec. 2013, ISSN: 0022-3751. DOI: 10.1113/jphysiol.2013.259150.

[362] E. Sleight, M. S. Stringer, I. Marshall, J. M. Wardlaw, and M. J. Thrippleton, "Cerebrovascular Reactivity Measurement Using Magnetic Resonance Imaging: A Systematic Review," *Frontiers in Physiology*, vol. 12, p. 643 468, Feb. 2021, ISSN: 1664-042X. DOI: 10.3389/fphys.2021.643468.

[363] S. Patel, J. H. Miao, E. Yetiskul, A. Anokhin, and S. H. Majmundar, "Physiology, Carbon Dioxide Retention," eng, in *StatPearls*, Treasure Island (FL): StatPearls Publishing, 2023.

[364] B. Lukitsch, P. Ecker, M. Elenkov, *et al.*, "Suitable CO2 Solubility Models for Determination of the CO2 Removal Performance of Oxygenators," *Bioengineering*, vol. 8, no. 3, p. 33, Mar. 2021, ISSN: 2306-5354. DOI: 10.3390/bioengineering8030033.

[365] A. C. Guyton and J. E. Hall, *Textbook of Medical Physiology*, en. Elsevier Saunders, 2006, Google-Books-ID: 0mdqAAAAMAAJ, ISBN: 9780721602400.

[366] J. E. Colt, "The computation and reporting of dissolved gas levels," *Water Research*, vol. 17, no. 8, pp. 841–849, Jan. 1983, ISSN: 0043-1354. DOI: 10.1016/0043-1354(83)90157-4.

[367] L. J.A., U. Luft, and E. Fletcher, "Quantitative description of whole blood CO2 dissociation curve and Haldane effect," en, *Respiration Physiology*, vol. 51, no. 2, pp. 167–181, Feb. 1983, ISSN: 00345687. DOI: 10.1016/0034-5687(83)90038-5.

[368] H. Kazemi and J. C. Mithoefer, "CO2 DISSOCIATION CURVE OF DOG BRAIN," eng, *The American Journal of Physiology*, vol. 205, pp. 598–600, Sep. 1963, ISSN: 0002-9513. DOI: 10.1152/ajplegacy.1963.205.3.598.

[369] B. J. McGuire and T. W. Secomb, "A theoretical model for oxygen transport in skeletal muscle under conditions of high oxygen demand," eng, *Journal of Applied Physiology (Bethesda, Md.: 1985)*, vol. 91, no. 5, pp. 2255–2265, Nov. 2001, ISSN: 8750-7587. DOI: 10.1152/jappl.2001.91.5.2255.

[370] R. L. Hester and L. W. Hammer, "Venular-arteriolar communication in the regulation of blood flow," eng, *American Journal of Physiology. Regulatory, Integrative and Comparative Physiology*, vol. 282, no. 5, R1280–1285, May 2002, ISSN: 0363-6119. DOI: 10.1152/ajpregu.00744.2001.

[371] C. Rink and S. Khanna, "Significance of Brain Tissue Oxygenation and the Arachidonic Acid Cascade in Stroke," *Antioxidants & Redox Signaling*, vol. 14, no. 10, pp. 1889–1903, May 2011, ISSN: 1523-0864. DOI: 10.1089/ars.2010.3474.

[372] C. Noblet, G. Delpon, S. Supiot, V. Potiron, F. Paris, and S. Chiavassa, "A new tissue segmentation method to calculate 3D dose in small animal radiation therapy," en, *Radiation Oncology*, vol. 13, no. 1, pp. 1–8, Dec. 2018, ISSN: 1748-717X. DOI: 10.1186/s13014-018-0971-8.

[373] M. C. McKenna, G. A. Dienel, U. Sonnewald, H. S. Waagepetersen, and A. Schousboe, "Chapter 11 - Energy Metabolism of the Brain," in *Basic Neurochemistry (Eighth Edition)*, S. T. Brady, G. J. Siegel, R. W. Albers, and D. L. Price, Eds., New York: Academic Press, Jan. 2012, pp. 200–231, ISBN: 9780123749475. DOI: 10.1016/B978-0-12-374947-5.00011-0.

[374] A. J. Wasserman and J. L. Patterson, "THE CEREBRAL VASCULAR RESPONSE TO REDUCTION IN ARTERIAL CARBON DIOXIDE TENSION*," *Journal of Clinical Investigation*, vol. 40, no. 7, pp. 1297–1303, Jul. 1961, ISSN: 0021-9738.

[375] H. Angleys and L. Østergaard, "Krogh's capillary recruitment hypothesis, 100 years on: Is the opening of previously closed capillaries necessary to ensure muscle oxygenation during exercise?" en, *American Journal of Physiology-Heart and Circulatory Physiology*, vol. 318, no. 2, H425–H447, Feb. 2020, ISSN: 0363-6135, 1522-1539. DOI: 10.1152/ajpheart.00384.2019.

[376] A. Rego, "How Do Brain Vessels Respond to a Stimulus Far Away?" English, M.S. thesis, University of Oxford, Oxford, UK, 2018.

[377] A. Kapela, A. Bezerianos, and N. M. Tsoukias, "A mathematical model of vasoreactivity in rat mesenteric arterioles: I. Myoendothelial communication," *Microcirculation (New York, N.Y. : 1994)*, vol. 16, no. 8, pp. 694–713, Nov. 2009, ISSN: 1073-9688. DOI: 10.3109/10739680903177539.

[378] H. S. Silva, A. Kapela, and N. M. Tsoukias, "A mathematical model of plasma membrane electrophysiology and calcium dynamics in vascular endothelial cells," eng, *American Journal of Physiology. Cell Physiology*, vol. 293, no. 1, pp. C277–293, Jul. 2007, ISSN: 0363-6143. DOI: 10.1152/ajpcell.00542.2006.

[379] A. Kapela, A. Bezerianos, and N. M. Tsoukias, "A mathematical model of Ca2+ dynamics in rat mesenteric smooth muscle cell: Agonist and NO stimulation," eng, *Journal of Theoretical Biology*, vol. 253, no. 2, pp. 238–260, Jul. 2008, ISSN: 1095-8541. DOI: 10.1016/j.jtbi.2008.03.004.

[380] T. D. Carter and D. Ogden, "Acetylcholine-stimulated changes of membrane potential and intracellular Ca2+ concentration recorded in endothelial cells in situ in the isolated rat aorta," eng, *Pflugers Archiv: European Journal of Physiology*, vol. 428, no. 5-6, pp. 476–484, Oct. 1994, ISSN: 0031-6768. DOI: 10.1007/BF00374568.

[381] B. O. Hald, L. J. Jensen, P. G. Sørensen, N.-H. Holstein-Rathlou, and J. C. B. Jacobsen, "Applicability of cable theory to vascular conducted responses," eng, *Biophysical Journal*, vol. 102, no. 6, pp. 1352–1362, Mar. 2012, ISSN: 1542-0086. DOI: 10.1016/j.bpj.2012.01.055.

[382] T. F. Weiss, *Cellular Biophysics: Electrical Properties*, English. Cambridge, US: MIT Press, Mar. 1996, ISBN: 9780262529570.

[383] G. D. Hirst and T. O. Neild, "An analysis of excitatory junctional potentials recorded from arterioles," eng, *The Journal of Physiology*, vol. 280, pp. 87–104, Jul. 1978, ISSN: 0022-3751. DOI: 10.1113/jphysiol.1978.sp012374.

[384] C. H. T. Tran, E. J. Vigmond, D. Goldman, F. Plane, and D. G. Welsh, "Electrical communication in branching arterial networks," *American Journal of Physiology - Heart and Circulatory Physiology*, vol. 303, no. 6, H680–H692, Sep. 2012, ISSN: 0363-6135. DOI: 10.1152/ajpheart.00261.2012.

[385] B. Hald, D. Welsh, N.-H. Holstein-Rathlou, and J. Jacobsen, "Gap Junctions Suppress Electrical but Not [Ca2+] Heterogeneity in Resistance Arteries," *Biophysical Journal*, vol. 107, no. 10, pp. 2467–2476, Nov. 2014, ISSN: 0006-3495. DOI: 10.1016/j.bpj.2014.09.036.

[386] J. Yamazaki and K. Kitamura, "Intercellular electrical coupling in vascular cells present in rat intact cerebral arterioles," eng, *Journal of Vascular Research*, vol. 40, no. 1, pp. 11–27, 2003, ISSN: 1018-1172. DOI: 10.1159/000068934.

[387] H. J. Knot and M. T. Nelson, "Regulation of arterial diameter and wall [Ca2+] in cerebral arteries of rat by membrane potential and intravascular pressure," *The Journal of Physiology*, vol. 508, no. Pt 1, pp. 199–209, Apr. 1998, ISSN: 0022-3751. DOI: 10.1111/j.1469-7793.1998.199br.x.

[388] B. O. Hald, J. C. B. Jacobsen, S. L. Sandow, N. Holstein-Rathlou, and D. G. Welsh, "Less is more: Minimal expression of myoendothelial gap junctions optimizes cell–cell communication in virtual arterioles," en, *The Journal of Physiology*, vol. 592, no. 15, pp. 3243–3255, Aug. 2014, ISSN: 0022-3751, 1469-7793. DOI: 10.1113/jphysiol.2014.272815.

[389] B. O. Hald, "A generative modeling approach to connectivity—Electrical conduction in vascular networks," *Journal of Theoretical Biology*, vol. 399, pp. 1–12, Jun. 2016, ISSN: 0022-5193. DOI: 10.1016/j.jtbi.2016.03.032.

[390] B. R. Chen, M. B. Bouchard, A. F. H. McCaslin, S. A. Burgess, and E. M. C. Hillman, "High-speed vascular dynamics of the hemodynamic response," *NeuroImage*, vol. 54, no. 2, pp. 1021–1030, Jan. 2011, ISSN: 1053-8119. DOI: 10.1016/j.neuroimage.2010.09.036.

[391] O. Østerby, "Five Ways of Reducing the Crank–Nicolson Oscillations," en, *BIT Numerical Mathematics*, vol. 43, no. 4, pp. 811–822, Nov. 2003, ISSN: 1572-9125. DOI: 10.1023/B:BITN.0000009942.00540.94.

[392] E. M. Golding, S. P. Marrelli, J. You, and R. M. Bryan, "Endothelium-derived hyperpolarizing factor in the brain: A new regulator of cerebral blood flow?" eng, *Stroke*, vol. 33, no. 3, pp. 661–663, Mar. 2002, ISSN: 1524-4628.

[393] W. F. Jackson, "Potassium channels in the peripheral microcirculation," eng, *Microcirculation (New York, N.Y.: 1994)*, vol. 12, no. 1, pp. 113–127, 2005, ISSN: 1073-9688. DOI: 10.1080/10739680590896072.

[394] R. C. Webb, "SMOOTH MUSCLE CONTRACTION AND RELAXATION," en, *Advances in Physiology Education*, vol. 27, no. 4, pp. 201–206, Dec. 2003, ISSN: 1043-4046, 1522-1229. DOI: 10.1152/advan.00025.2003.

[395] B. L. Ginsborg, "*From Neuron to Brain*, 2nd edition. Edited by S. W. Kuffler, J. G. Nicholls and A. R. Martin. Pp. 651. (Blackwell Scientific Publications, 1984.) £14.80 Paperback," en, *Quarterly Journal of Experimental Physiology*, vol. 70, no. 3, pp. 469–469, Jul. 1985, ISSN: 01448757. DOI: 10.1113/expphysiol.1985.sp002931.

[396] J. Xia, T. L. Little, and B. R. Duling, "Cellular pathways of the conducted electrical response in arterioles of hamster cheek pouch in vitro," eng, *The American Journal of Physiology*, vol. 269, no. 6 Pt 2, H2031–2038, Dec. 1995, ISSN: 0002-9513. DOI: 10.1152/ajpheart.1995.269.6.H2031.

[397] S. S. Segal, D. N. Damon, and B. R. Duling, "Propagation of vasomotor responses coordinates arteriolar resistances," eng, *The American Journal of Physiology*, vol. 256, no. 3 Pt 2, H832–837, Mar. 1989, ISSN: 0002-9513. DOI: 10.1152/ajpheart.1989.256.3.H832.

[398] G. E. Cold, "Measurements of CO2 reactivity and barbiturate reactivity in patients with severe head injury," en, *Acta Neurochirurgica*, vol. 98, no. 3-4, pp. 153–163, Sep. 1989, ISSN: 0001-6268, 0942-0940. DOI: 10.1007/BF01407342.

[399] E. M. Enevoldsen and F. T. Jensen, "Autoregulation and CO2 responses of cerebral blood flow in patients with acute severe head injury," *Journal of Neurosurgery*, vol. 48, no. 5, pp. 689–703, May 1978, ISSN: 0022-3085. DOI: 10.3171/jns.1978.48.5.0689.

[400] J. P. Muizelaar, H. G. Van Der Poel, Z. Li, H. A. Kontos, and J. E. Levasseur, "Pial arteriolar vessel diameter and CO2 reactivity during prolonged hyperventilation in the rabbit," *Journal of Neurosurgery*, vol. 69, no. 6, pp. 923–927, Dec. 1988, ISSN: 0022-3085. DOI: 10.3171/jns.1988.69.6.0923.

[401] O. B. Paulson, J. Olesen, and M. S. Christensen, "Restoration of autoregulation of cerebral blood flow by hypocapnia," en, *Neurology*, vol. 22, no. 3, pp. 286–286, Mar. 1972, ISSN: 0028-3878, 1526-632X. DOI: 10.1212/WNL.22.3.286.

[402] U. Nöth, F. Kotajima, R. Deichmann, R. Turner, and D. R. Corfield, "Mapping of the cerebral vascular response to hypoxia and hypercapnia using quantitative perfusion MRI at 3 T," eng, *NMR in biomedicine*, vol. 21, no. 5, pp. 464–472, Jun. 2008, ISSN: 0952-3480. DOI: 10.1002/nbm.1210.

[403] S. K. Piechnik, P. A. Chiarelli, and P. Jezzard, "Modelling vascular reactivity to investigate the basis of the relationship between cerebral blood volume and flow under CO2 manipulation," eng, *NeuroImage*, vol. 39, no. 1, pp. 107–118, Jan. 2008, ISSN: 1053-8119. DOI: 10.1016/j.neuroimage.2007.08.022.

[404] J. A. H. R. Claassen, R. Zhang, Q. Fu, S. Witkowski, and B. D. Levine, "Transcranial Doppler estimation of cerebral blood flow and cerebrovascular conductance during modified rebreathing," *Journal of applied physiology*, vol. 102, no. 3, pp. 870–877, Mar. 2007, ISSN: 8750-7587. DOI: 10.1152/japplphysiol.00906.2006.

[405] S. Yoon, M. Zuccarello, and R. M. Rapoport, "pCO2 and pH regulation of cerebral blood flow," *Frontiers in Physiology*, vol. 3, p. 365, Sep. 2012, ISSN: 1664-042X. DOI: 10.3389/fphys.2012.00365.

[406] B. O. Hald and D. G. Welsh, "Conceptualizing conduction as a pliant electrical response: Impact of gap junctions and ion channels," eng, *American Journal of Physiology. Heart and Circulatory Physiology*, vol. 319, no. 6, H1276–H1289, Dec. 2020, ISSN: 1522-1539. DOI: 10.1152/ajpheart.00285.2020.

[407] R. Vogel and R. Weingart, "The electrophysiology of gap junctions and gap junction channels and their mathematical modelling," eng, *Biology of the Cell*, vol. 94, no. 7-8, pp. 501–510, Nov. 2002, ISSN: 0248-4900. DOI: 10.1016/s0248-4900(02)00022-9.

[408] F. Wu, J. X. Wilson, and K. Tyml, "Ascorbate inhibits iNOS expression and preserves vasoconstrictor responsiveness in skeletal muscle of septic mice," eng, *American Journal of Physiology. Regulatory, Integrative and Comparative Physiology*, vol. 285, no. 1, R50–56, Jul. 2003, ISSN: 0363-6119. DOI: 10.1152/ajpregu.00564.2002.

[409] J. Armour, K. Tyml, D. Lidington, and J. X. Wilson, "Ascorbate prevents microvascular dysfunction in the skeletal muscle of the septic rat," eng, *Journal of Applied Physiology (Bethesda, Md.: 1985)*, vol. 90, no. 3, pp. 795–803, Mar. 2001, ISSN: 8750-7587. DOI: 10.1152/jappl.2001.90.3.795.

[410] S. Ogoh and P. N. Ainslie, "Regulatory mechanisms of cerebral blood flow during exercise: New concepts," eng, *Exercise and Sport Sciences Reviews*, vol. 37, no. 3, pp. 123–129, Jul. 2009, ISSN: 1538-3008. DOI: 10.1097/JES.0b013e3181aa64d7.

[411] S. Bollmann, H. Mattern, M. Bernier, *et al.*, "Imaging of the pial arterial vasculature of the human brain in vivo using high-resolution 7T time-of-flight angiography," en, *eLife*, vol. 11, e71186, Apr. 2022, ISSN: 2050-084X. DOI: 10.7554/eLife.71186.

[412] T. F. Sherman, "On connecting large vessels to small. The meaning of Murray's law.," en, *The Journal of general physiology*, vol. 78, no. 4, pp. 431–453, Oct. 1981, ISSN: 0022-1295, 1540-7748. DOI: 10.1085/jgp.78.4.431.

[413] W. El-Bouri and S. Payne, "Multi-Scale Homogenization of the Mass Transport Equation in Periodic Capillary Networks," Paris, Jun. 2015.

[414] J. T. Celaya-Alcala, G. V. Lee, A. F. Smith, *et al.*, "Simulation of oxygen transport and estimation of tissue perfusion in extensive microvascular networks: Application to cerebral cortex," eng, *Journal of Cerebral Blood Flow and Metabolism: Official Journal of the International Society of Cerebral Blood Flow and Metabolism*, vol. 41, no. 3, pp. 656–669, Mar. 2021, ISSN: 1559-7016. DOI: 10.1177/0271678X20927100.

[415] F. Costanzo and J. G. Brasseur, "The invalidity of the Laplace law for biological vessels and of estimating elastic modulus from total stress vs. strain: A new practical method," eng, *Mathematical medicine and biology: a journal of the IMA*, vol. 32, no. 1, pp. 1–37, Mar. 2015, ISSN: 1477-8602. DOI: 10.1093/imammb/dqt020.

[416] J. Strikwerda, *Finite Difference Schemes and Partial Differential Equations*. Pacific Grove, California: Wadsworthand Brooks/Cole, 1989.